MULTISCALE MATHEMATICAL MODELING OF OCULAR BLOOD FLOW AND OXYGENATION AND THEIR RELEVANCE TO GLAUCOMA

A Dissertation
Submitted to the Faculty
of
Purdue University
by
Lucia Carichino

In Partial Fulfillment of the
Requirements for the Degree
of
Doctor of Philosophy

August 2016
Purdue University
Indianapolis, Indiana

Al nostro viaggio insieme

To our journey together

ACKNOWLEDGMENTS

Firstly, I would like to thank my advisor Prof. Guidoboni for her guidance during my Ph.D, for her passion, encouragement and perseverance. Thank you for being an excellent mentor and, at the same time, a friend.

My sincere thanks goes to my co-advisors: Prof. Harris for his open mindedness and insightful comments, and Prof. Arciero for her enthusiasm and motivation. I would like to thank Prof. Szopos and Prof. Prud'homme for giving me the opportunity to join their team in Strasbourg and to study new topics, and Prof. Sacco for his immense knowledge and for believing in me since the beginning.

I would like to thank my friends, near and far, for making this experience at IUPUI extraordinary with their support and help. I would like to express my sincere gratitude to my travel companion Simone: I would have never made it without him, we complete each other. Un grazie enorme alla mia famiglia per tutto il loro sostegno durante questa avventura, superando la tristezza della lontananza.

TABLE OF CONTENTS

Page

LIST OF TABLES

LIST OF FIGURES

ABBREVIATIONS

ATP	Adenosine triphosphate
C	Capillaries
CCC	Concordance correlation coefficient
CDI	Color Doppler imaging
CI	Confidence interval
CSFp	Cerebrospinal fluid pressure
CRA	Central retinal artery
CRV	Central retinal vein
DAD/T	Normalized distance between ascending and descending
DNV	Dicrotic notch velocity
DOPP	Diastolic ocular perfusion pressure
DP	Diastolic pressure
DTI	Diastolic time interval
EDV	End diastolic velocity
HR	Heart rate
IA	Impaired autoregulation
ICH	Intracranial hypertension
IOP	Intraocluar pressure
LA	Large arterioles
LC	Lamina cribrosa
LV	Large venules
MAP	Mean arterial pressure
MD	Mean defect
MOPP	Mean ocular perfusion pressure

NTG	Normal tension glaucoma
OA	Ophthalmic artery
OPP	Ocular perfusion pressure
POAG	Primary open-angle glaucoma
PSV	Peak systolic velocity
RI	Resistive index
RLTp	Retrolaminar tissue pressure
SA	Small arterioles
SD	Standard deviation
SEVR	Subendocardial viability ratio
SOPP	Systolic ocular perfusion pressure
SP	Systolic pressure
STI	Systolic time interval
SV	Small venules
TLpD	Translaminar pressure difference
WPs	Waveform parameters
0D	Zero dimensional

ABSTRACT

Carichino, Lucia PhD, Purdue University, August 2016. Multiscale Mathematical Modeling of Ocular Blood Flow and Oxygenation and Their Relevance to Glaucoma. Major Professor: Giovanna Guidoboni.

Glaucoma is a multifactorial ocular disease progressively leading to irreversible blindness. There is clear evidence of correlations between alterations in ocular hemodynamics and glaucoma; however, the mechanisms giving rise to these correlations are still elusive. The objective of this thesis is to develop mathematical models and methods to help elucidate these mechanisms. First, we develop a mathematical model that describes the deformation of ocular structures and ocular blood flow using a reduced-order fluid-structure interaction model. This model is used to investigate the relevance of mechanical and vascular factors in glaucoma. As a first step in expanding this model to higher dimensions, we propose a novel energy-based technique for coupling partial and ordinary differential equations in blood flow, using operator splitting. Next, we combine clinical data and model predictions to propose possible explanations for the increase in venous oxygen saturation in advanced glaucoma patients. We develop a computer-aided manipulation process of color Doppler images to extract novel waveform parameters to distinguish between healthy and glaucomatous individuals. The results obtained in this work suggest that: 1) the increase in resistance of the retinal microcirculation contributes to the influence of intraocular pressure on retinal hemodynamics; 2) the influence of cerebrospinal fluid pressure on retinal hemodynamics is mediated by associated changes in blood pressure; 3) the increase in venous oxygen saturation levels observed among advanced glaucoma patients depends on the value of the patients' intraocular pressure; 4) the normalized distance between the ascending and descending limb of the ophthalmic artery velocity profile is significantly higher in glaucoma patients than in healthy individuals.

1. INTRODUCTION

Glaucoma is a neurodegenerative disease affecting the eye and is the second cause of blindness worldwide. Elevated *intraocular pressure* (IOP) has been known as a risk factor for glaucoma for more than 150 years [1]. However, a high percentage of individuals with elevated IOP never develop glaucoma [2], and many glaucoma patients continue to experience disease progression despite lowering IOP to target levels, condition called *normal tension glaucoma* (NTG) [3]. This suggests that, in addition to elevated IOP, there are other important risk factors associated with glaucoma onset and progression.

Ocular hemodynamics has been shown to contribute to the pathophysiology of glaucoma [4–8]. Despite this evidence linking blood flow alterations with glaucoma, it is still unknown whether vascular changes occur primary or secondary to vision loss. If *primary*, vascular changes would lead to tissue damage with subsequent vision loss. If *secondary*, vascular changes would be the result of tissue damage and vision loss.

Understanding the mechanisms relating alterations in retinal hemodynamics and visual function could lead to significant improvement in the clinical management of patients and also aid the potential development of therapies targeting the modulation of ocular blood flow [9]. Mathematical modeling can help elucidate these mechanisms via theoretical investigations and data analysis.

The overall objective of this thesis is to introduce new mathematical models and methods to study the vascular component in glaucoma. To provide context for those models, we begin by describing the eye anatomy, defining glaucoma and the main challenges in modeling ocular blood flow. Finally, we outline the main objectives that will be addressed in Chapters 3, 4 and 5.

1.1 Anatomy of the eye

The eye is a complex organ with a multi-layer structure: the *sclera* is the outer layer, also called the white of the eye, the *choroid* is the middle vascular layer, that receives approximately 80% of the total ocular blood flow, and the *retina* is the inner layer, that is light sensitive. The *retinal ganglion cells* are neurons located in the retina that are responsible for the transmission of the visual information from the retina to the brain via the optic nerve.

The *ophthalmic artery* (OA) is the primary source of blood to the eye and is located close to the *optic nerve*, Figure 1.1. The *central retinal artery* (CRA) branches off the OA and penetrates the optic nerve approximately 10 mm behind the globe. The CRA runs within the central portion of the optic nerve canal parallel to the *central retina vein* (CRV). Blood is supplied to the retina via the CRA and is drained by the CRV, as described below

- the CRA emerges from the optic nerve into the globe, at the *optic nerve head* (also called *optic disc*), and branches into four major arteries, each of which supplies one quadrant of the retina;
- the four retinal arteries branch into smaller arterioles, which branch into retinal capillaries, to supply nutrients to the retinal tissue;
- the retinal blood is drained by four major retinal veins, one for each quadrant;
- the blood drains from the four retinal veins into the CRV, which exits the eye via the optic nerve.

Retinal arteries, capillaries and veins together form the *retinal microcirculation*, which is depicted in Figure 1.1.

The optic nerve tissue and the eye globe are a pressurized system; the pressure difference between the *retrolaminar tissue pressure* (RLTp) in the optic nerve tissue (baseline value 7-10 mmHg) and the IOP inside the eye globe (baseline value 12-15 mmHg) is maintained by the *lamina cribrosa* (LC), a collagen structure that is pierced by the central retinal vessels approximately in its center, Figure 1.1. The CRA and CRV are exposed to the RLTp

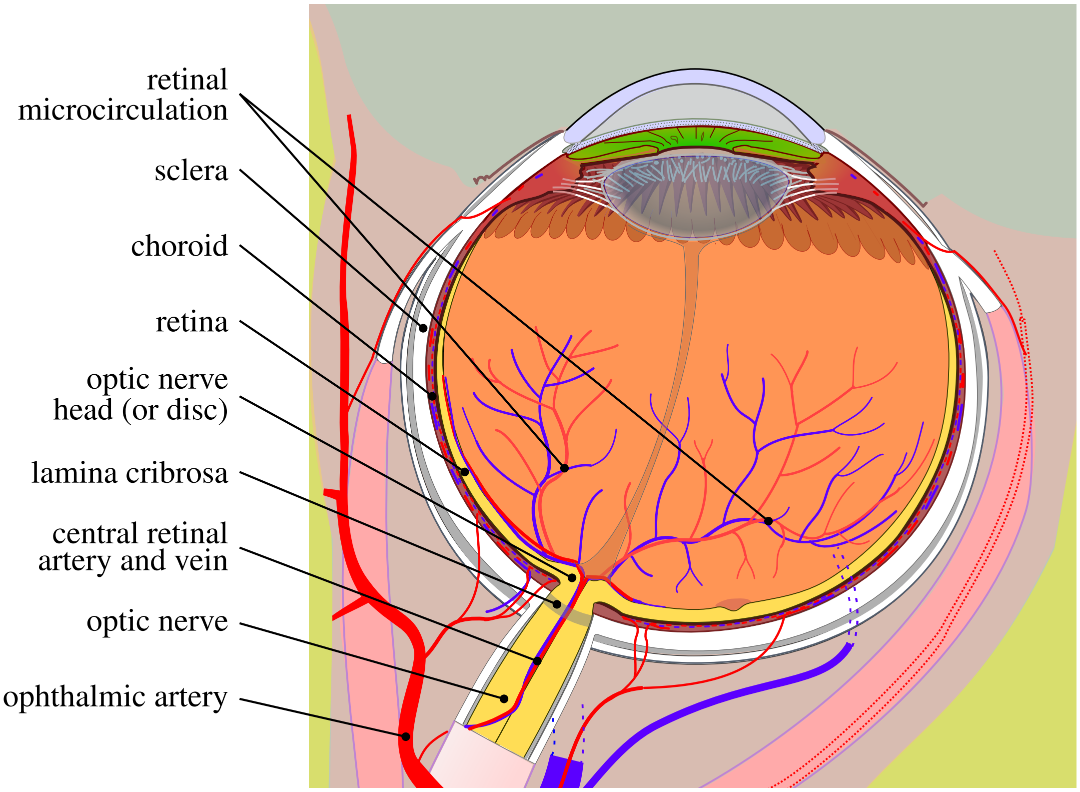

Fig. 1.1.: Anatomy of the right human eye, adapted from [10].

in the optic nerve canal and are exposed to the IOP once they enter the eye globe. The visual information is transmitted via the retinal ganglion cell axons that extend from the eye to the brain via the optic nerve, passing through the lamina cribrosa. For more details on the eye anatomy and ocular blood flow, we refer to [11].

The eye, as well as many other organs in the body, has the capacity to maintain a constant nutrient supply to the tissue despite changes in local parameters. This ability is called *autoregulation* and is defined as the ability of vessels to change in diameter in order to maintain a relatively constant blood flow despite changes in pressure, while meeting the metabolic demands of the tissue, see Figure 1.2. The dilation or contraction of the vessels is due to changes in smooth muscle tone in response to different signals, including pressure, oxygen and carbon dioxide concentrations [12].

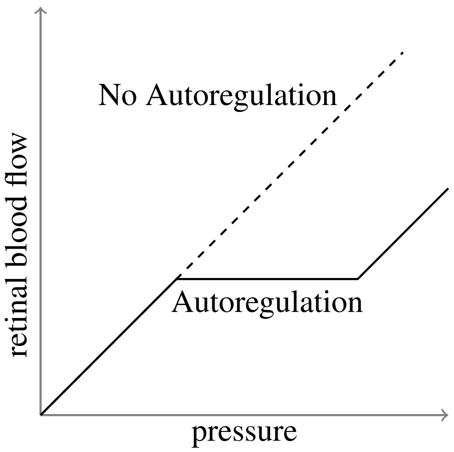

Fig. 1.2.: Graph of retinal blood flow versus pressure in the presence of autoregulation (solid line) and in the absence of autoregulation (dashed line).

The blood flow as well as the morphology and functionality of the vascular system in the retina can be observed and measured non-invasively in humans *in vivo* utilizing appropriate technologies, including fluorescein angiography, color Doppler imaging, laser Doppler flowmetry, Doppler optical coherence tomography and retinal oximetry [11, 13–15]. In particular, color Doppler imaging (CDI) is used to measure the time profile of blood velocity in the OA, CRA and CRV, Figure 1.3(a), and retinal oximetry is used to measure hemoglobin oxygen saturation and vessel diameter in the retina microcirculation, Figure 1.3(b).

1.2 Glaucoma and ocular bood flow modeling

Glaucoma is characterized by the degeneration of the optic nerve and loss of retinal ganglion cells, resulting in progressive and irreversible blindness. For more than 150 years elevated IOP has been considered to be the main risk factor in glaucoma; however, NTG patients continue to experience disease progression despite lowering IOP to target levels.

Recent studies have suggested that the difference between IOP and *cerebrospinal fluid pressure* (CSFp) could be a relevant factor to be considered in glaucoma patients beyond

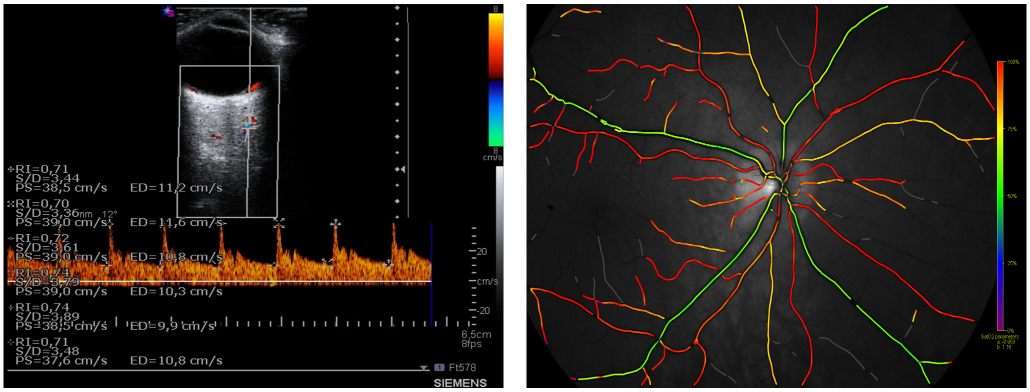

(a) color Doppler imaging

(b) retinal oximetry

Fig. 1.3.: Color Doppler image of the ophthalmic artery (a) and retinal oxygen saturation image (b) in a healthy individual.

the value of IOP itself [16, 17]. The pressure difference between IOP and CSFp is usually referred to as *translamina cribrosa pressure difference* (TLpD), assuming that the RLTp and the CSFp are approximately equal [18]. Increased TLpD could be due to IOP elevation and/or CSFp reduction. Recently, low CSFp has been identified as a relevant factor in glaucoma [19–21].

Although pressure is an important risk factor in glaucoma, several studies and clinical correlations have indicated a multitude of other risk factors, with ocular blood flow being among the most important. Many factors influence the blood flow in the retina, including the values of IOP and CSFp [22–24], and this makes the clinical interpretation of flow and velocity measurements extremely challenging. Mathematical modeling could help quantify the influence of changes in IOP and CSFp on retinal hemodynamics.

Building models of the eye is very challenging since it involves deformations of pressurized ambients, fluid-structure interactions, complex microvascular systems and vascular autoregulation. Several detailed models of the deformation of the optic nerve tissues, including the lamina cribrosa, have been proposed in recent years [25–34]. However, only a few investigators have attempted to model the retinal vasculature and autoregulation [35–40], and the models did not account for structural deformations.

Direct simulations of three-dimensional fluid-structure interaction problems in the ocular circulation are limited by the complexity of the vasculature and by the numerical cost of the simulations. To overcome this issue, which has also been encountered in modeling other parts of the cardiovascular system [41–43], reduced-order models have been introduced. These models can be adapted to simplify various aspects of the ocular vasculature, leading to the coupling of multiscale mathematical models.

1.3 Aim of this thesis

The main objectives of this thesis are

1. To summarize the continuum mechanics assumptions used to derive the conservation laws, to describe and compare one-dimensional and zero-dimensional reduced models for fluid-structure interaction in compliant vessels, and to discuss the challenges in coupling the fluid flow in two or three-dimensional domains to zero-dimensional reduced models (Chapter 2).
2. To develop the first multiscale mathematical model that combines the mechanical deformation of the lamina cribrosa with the blood flow in the central retinal vessels and in the retinal microcirculation (Chapter 3, Sections 3.1-3.4).
3. To estimate and quantify the mechanical factors that contribute to the influence of IOP and CSFp on central retinal vessels and retinal hemodynamics, and to compare the effect of changes in IOP and CSFp (Chapter 3, Sections 3.5-3.6).
4. To develop a stable energy-based technique for coupling systems of partial and ordinary differential equations for blood flow simulations using operator splitting (Chapter 4).

5. To combine clinical data and mathematical predictions to propose possible explanations for the increases in venous oxygen saturation observed in advanced glaucoma patients (Chapter 5, Section 5.1).

6. To develop a computer-aided manipulation process of ophthalmic artery CDI images that enables the extraction of a novel set of waveform parameters and study the statistical relevance of these parameters in characterizing the disease status in glaucoma (Chapter 5, Section 5.2).

2. MATHEMATICAL FOUNDATIONS

In this Chapter we provide a summary of the mathematical concepts and formulations used in Chapters 3, 4 and 5.

In Section 2.1, we describe the motion and deformation of a continuum body in a general curvilinear coordinates system, emphasizing the difference between Lagrangian and Eulerian descriptions. We also define the conservations laws of mass, linear momentum and angular momentum in Lagrangian and Eulerian descriptions, and the constitutive equations of a Newtonian viscous fluid and of a linear elastic solid. In Section 2.2, we study the intrinsic behavior of the operators in the conservation laws of a Newtonian viscous fluid and of a linear elastic solid from the energy point of view. In Section 2.3, we study the fluid-structure interaction problem involving the coupling between a fluid inside a cylindrical domain and a cylindrical structure surrounding it. Two models for the structure are considered: the linear elastic thick shell model and the linear elastic thin Koiter shell model. In Section 2.4, we present and compare two one-dimensional modeling reduction techniques for fluid-structure interaction problems in cylindrical domains: the cross-sectional averaging technique and the dimensional analysis technique. In the comparison tests we consider both shell models presented in Section 2.3. In Section 2.5, a zero-dimensional reduced model for fluid-structure interaction based on the analogy between vascular beds and electrical circuits is presented, together with the resistance formulas for rigid or compliant vessels. In Section 2.6, we discuss the modeling and numerical challenges that arise when coupling the fluid flow in a two or three-dimensional domain to a zero-dimensional reduced model.

2.1 Continuum mechanics

In this section, we summarize the main continuum mechanics concepts behind the description of motion and deformation of a continuum body in a general curvilinear coordinates system, emphasizing the difference between Lagrangian and Eulerian descriptions. For further details we refer to [44, 45].

A body $\mathcal{B} \subset \mathbb{R}^3$ is by definition a *continuum* if it fills the entire region of space it occupies and its properties are continuously distributed in space. Precisely, let $\Omega_t \subset \mathbb{R}^3$ be the region occupied by $\mathcal{B}$ at time $t \geq 0$, and assume that its boundary $\partial\Omega_t$ is smooth enough to admit an outward normal unit vector at any point and at any time. Given a spatial point in Ω_t, its position vector is denoted as $\underline{\boldsymbol{r}} \in \Omega_t$. Note that, in reality, we are assuming that $\underline{\boldsymbol{r}}$ is the position of the barycenter of an infinitesimal volume called *material particle*. Given the position vector $\underline{\boldsymbol{r}}$ of a material particle at time t in Ω_t, let $\underline{\boldsymbol{R}} \in \Omega_0$ be the position vector of the same material particle at time $t = 0$. Then, the motion of the body $\mathcal{B}$ is determined by a family of maps $\boldsymbol{\psi}(\cdot, t)$ defined as

$$\begin{aligned} \boldsymbol{\psi}(\cdot, t): \quad \Omega_0 &\rightarrow \Omega_t \\ \underline{\boldsymbol{R}} &\mapsto \underline{\boldsymbol{r}} = \boldsymbol{\psi}\left(\underline{\boldsymbol{R}}, t\right), \end{aligned} \tag{2.1}$$

for every $t \geq 0$, Figure 2.1.

The body $\mathcal{B}$ is a continuum if

1. any macroscopic quantity that describes a property of $\mathcal{B}$ is an absolutely continuous function on each material particle;
2. if $\boldsymbol{\psi}$ is a diffeomorphism, i.e. $\boldsymbol{\psi}$ is invertible and differentiable, and $\boldsymbol{\psi}^{-1}(\underline{\boldsymbol{r}}, t) = \underline{\boldsymbol{R}}$ is differentiable as well.

Let $\mathcal{V}_{\underline{\boldsymbol{R}}}$ a subset of Ω_0, then, at any time $t > 0$, the image of $\mathcal{V}_{\underline{\boldsymbol{R}}}$ throughout the diffeomorphism $\boldsymbol{\psi}(\cdot, t)$ is $\mathcal{V}_{\underline{\boldsymbol{r}}} \subset \Omega_t$ such that $\mathcal{V}_{\underline{\boldsymbol{r}}} = \boldsymbol{\psi}(\mathcal{V}_{\underline{\boldsymbol{R}}}, t)$, and it is called *material domain*, Figure 2.1.

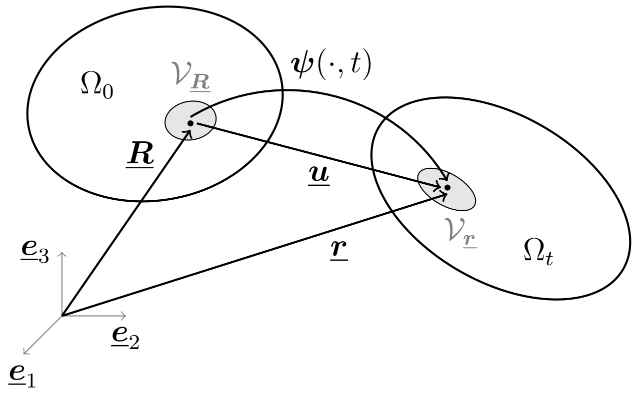

Fig. 2.1.: Sketch of the motion of a continuum body that occupies the region Ω_0 at time $t = 0$ and the region Ω_t at time $t > 0$. $\underline{\boldsymbol{r}} \in \Omega_t$ is the position vector of a material particle at time t, and $\underline{\boldsymbol{R}} \in \Omega_0$ is the position vector of the same material particle at time $t = 0$, and they are related throughout the diffeomorphism $\boldsymbol{\psi}(\cdot,t)$. $\mathcal{V}_{\underline{\boldsymbol{R}}}$ is a subset of Ω_0 and $\mathcal{V}_{\underline{\boldsymbol{r}}} = \boldsymbol{\psi}(\mathcal{V}_{\underline{\boldsymbol{R}}},t)$ is the corresponding material domain in Ω_t. $\underline{\boldsymbol{u}}$ is the displacement of a material particle moving from $\underline{\boldsymbol{R}}$ to $\underline{\boldsymbol{r}}$.

2.1.1 Curvilinear coordinates

Let $\underline{\boldsymbol{x}} = \left\{x^1, x^2, x^3\right\}$ be the set of cartesian coordinates, and let $\underline{\boldsymbol{e}}_1$, $\underline{\boldsymbol{e}}_2$, $\underline{\boldsymbol{e}}_3$ be the standard basis vectors. Any vector $\underline{\boldsymbol{w}} \in \mathbb{R}^3$ can be expressed as a linear combination of the standard basis vectors as

$$\underline{\boldsymbol{w}} = \Sigma_{L=1}^3 w^L \underline{\boldsymbol{e}}_L = w^L \underline{\boldsymbol{e}}_L, \tag{2.2}$$

where w^1, w^2 and w^3 are its components with respect to the standard basis. In (2.2), the Einstein summation convention has been adopted, where summations over repeated indices are implicitly assumed.

Introducing a set of curvilinear coordinates $\underline{\boldsymbol{\xi}} = \left\{\xi^1, \xi^2, \xi^3\right\}$, we can define two other bases for $\mathbb{R}^3$ beyond the standard basis

- the *covariant basis vectors*

$$\underline{\boldsymbol{g}}_i := \frac{\partial \underline{\boldsymbol{x}}}{\partial \xi^i} = \frac{\partial x^L}{\partial \xi^i} \underline{\boldsymbol{e}}_L \quad \text{for} \quad i = 1,2,3; \tag{2.3}$$

- the *contravariant basis vectors*

$$\underline{\boldsymbol{g}}^j := \frac{\partial \xi^j}{\partial \underline{\boldsymbol{x}}} = \frac{\partial \xi^j}{\partial x^L} \underline{\boldsymbol{e}}_L \quad \text{for} \quad j = 1, 2, 3. \tag{2.4}$$

Covariant and contravariant basis vectors are orthogonal since

$$\underline{\boldsymbol{g}}_i \cdot \underline{\boldsymbol{g}}^j = \frac{\partial x^L}{\partial \xi^i} \frac{\partial \xi^j}{\partial x^L} = \delta_i^j := \begin{cases} 1 & \text{if} \quad i = j, \\ 0 & \text{otherwise.} \end{cases} \tag{2.5}$$

Note that the cartesian coordinates are a particular case of curvilinear coordinates where covariant and contravariant basis vectors coincide, namely $\underline{\boldsymbol{e}}_L = \underline{\boldsymbol{e}}^L$, and are orthonormal, namely $\underline{\boldsymbol{e}}_L \cdot \underline{\boldsymbol{e}}^K = \delta_L^K$. Here, we adopt the notation in which

- uppercase indices correspond to cartesian coordinates;
- lowercase indices correspond to covariant and contravariant coordinates.

Any vector $\underline{\boldsymbol{w}} \in \mathbb{R}^3$ can be expressed as a linear combination of the standard basis vectors, as in (2.2), and also of the covariant basis vectors and contravariant basis vectors as follows

$$\underline{\boldsymbol{w}} = w_L \underline{\boldsymbol{e}}^L = w^L \underline{\boldsymbol{e}}_L = w^i \underline{\boldsymbol{g}}_i = w_j \underline{\boldsymbol{g}}^j, \tag{2.6}$$

where the w^i are the *covariant coordinates* and w_j are the *contravariant coordinates*, defined as

$$w^i := \underline{\boldsymbol{w}} \cdot \underline{\boldsymbol{g}}^i \quad \text{and} \quad w_j := \underline{\boldsymbol{w}} \cdot \underline{\boldsymbol{g}}_j. \tag{2.7}$$

In the particular case of cartesian coordinates, since $\underline{\boldsymbol{e}}_L = \underline{\boldsymbol{e}}^L$, then $w_L = w^L$.

Given $\underline{\boldsymbol{w}}, \underline{\boldsymbol{y}} \in \mathbb{R}^3$, the scalar product between $\underline{\boldsymbol{w}}$ and $\underline{\boldsymbol{y}}$ is defined as

$$\underline{\boldsymbol{w}} \cdot \underline{\boldsymbol{y}} := w^L y^L = w^i y_i. \tag{2.8}$$

Note that, even though the covariant and contarvariant basis vectors are not orthogonal sets, they are, however, mutually orthogonal, see (2.5). Then the scalar product between two vectors results in the sum of the products of covariant and contravariant coordinates.

The *covariant, contravariant* and *mixed metric tensors* are defined as

- covariant metric tensor $g_{ij} := \underline{\boldsymbol{g}}_i \cdot \underline{\boldsymbol{g}}_j = \dfrac{\partial x^L}{\partial \xi^i}\dfrac{\partial x^L}{\partial \xi^j}$;
- contravariant metric tensor $g^{ij} := \underline{\boldsymbol{g}}^i \cdot \underline{\boldsymbol{g}}^j = \dfrac{\partial \xi^i}{\partial x^L}\dfrac{\partial \xi^j}{\partial x^L}$;
- mixed metric tensor $g^i_j := \underline{\boldsymbol{g}}^i \cdot \underline{\boldsymbol{g}}_j = \delta^i_j$.

All the three metric tensors are symmetric.

The covariant and contravariant metric tensors equations are used to pass from the covariant components of a vector to the contravariant components and vice versa, since

$$\underline{\boldsymbol{g}}^i = g^{ij}\underline{\boldsymbol{g}}_j \quad \text{and} \quad \underline{\boldsymbol{g}}_i = g_{ij}\underline{\boldsymbol{g}}^j. \tag{2.9}$$

Hence, given a vector $\underline{\boldsymbol{w}}$,

$$w_i := g_{ij}w^j \quad \text{and} \quad w^i := g^{ij}w_j. \tag{2.10}$$

Let $\underline{\underline{\boldsymbol{M}}} \in \mathbb{R}^{3\times 3}$ be a second order tensor and consider the associated linear transformation

$$\begin{aligned} \mathcal{L}\underline{\underline{\boldsymbol{M}}}: \ \mathbb{R}^3 &\to \mathbb{R}^3 \\ \underline{\boldsymbol{y}} &\mapsto \underline{\boldsymbol{w}} = \underline{\underline{\boldsymbol{M}}}\,\underline{\boldsymbol{y}}. \end{aligned} \tag{2.11}$$

Depending on the choice of coordinates for the vectors

$$\underline{\boldsymbol{w}} = w_L\underline{\boldsymbol{e}}_L = w^i\underline{\boldsymbol{g}}_i = w_i\underline{\boldsymbol{g}}^i \quad \text{and} \quad \underline{\boldsymbol{y}} = y_K\underline{\boldsymbol{e}}_K = y^j\underline{\boldsymbol{g}}_j = y_j\underline{\boldsymbol{g}}^j, \tag{2.12}$$

we have that

$$w_L = M_{LK}y_K, \quad w^i = M^i_j y^j, \quad w^i = M^{ij}y_j, \quad w_i = M_i^j y_j, \quad w_i = M_{ij}y^j, \tag{2.13}$$

where $M_{LK} := \underline{\boldsymbol{e}}_L \cdot \underline{\underline{\boldsymbol{M}}}\,\underline{\boldsymbol{e}}_K$ and

$$\begin{aligned} M^i_j &:= \frac{\partial \xi^i}{\partial x^L}M_{LK}\frac{\partial x^K}{\partial \xi^j}, \quad M^{ij} := \frac{\partial \xi^i}{\partial x^L}M_{LK}\frac{\partial \xi^j}{\partial x^K}, \\ M_i^j &:= \frac{\partial x^L}{\partial \xi^i}M_{LK}\frac{\partial \xi^j}{\partial x^K}, \quad M_{ij} := \frac{\partial x^L}{\partial \xi^i}M_{LK}\frac{\partial x^K}{\partial \xi^j}. \end{aligned} \tag{2.14}$$

Thus far, we have considered the differences between the scalar product and the tensor-vector product in curvilinear coordinates with respect to cartesian coordinates. We can also study the differences in the derivative, gradient and divergence. Contrary to the standard basis vectors, the vectors $\underline{\boldsymbol{g}}_i$ and $\underline{\boldsymbol{g}}^i$ do depend on the curvilinear coordinates ξ^i, as shown by (2.3) and (2.4). Precisely, we can write

$$\frac{\partial \underline{\boldsymbol{g}}_i}{\partial \xi^j} = \Gamma^k_{ij}\underline{\boldsymbol{g}}_k \quad \text{and} \quad \frac{\partial \underline{\boldsymbol{g}}^i}{\partial \xi^j} = -\Gamma^i_{kj}\underline{\boldsymbol{g}}^k, \tag{2.15}$$

where $\Gamma_{ijl} := \dfrac{\partial^2 x^L}{\partial \xi^i \partial \xi^j}\dfrac{\partial x^L}{\partial \xi^l}$ are the first kind Christoffel symbols and $\Gamma^k_{ij} := \Gamma_{ijl} g^{lk}$ are the second kind Christoffel symbols.

Now, let f be a scalar function $f : \mathbb{R}^3 \to \mathbb{R}$, let $\underline{\boldsymbol{f}}$ be a vector function $\underline{\boldsymbol{f}} : \mathbb{R}^3 \to \mathbb{R}^3$, and let $\underline{\underline{\boldsymbol{M}}}$ be a second order tensor in $\mathbb{R}^{3\times 3}$, then

- the derivative of the scalar function f with respect to ξ^i can be written as

$$\frac{\partial f}{\partial \xi^i} = \frac{\partial x^L}{\partial \xi^i}\frac{\partial f}{\partial x^L}; \tag{2.16}$$

- the derivative of the vector function $\underline{\boldsymbol{f}}$ with respect to ξ^i can be written as

$$\frac{\partial \underline{\boldsymbol{f}}}{\partial \xi^i} = f^l|_i \underline{\boldsymbol{g}}_l = f_l|_i \underline{\boldsymbol{g}}^l, \tag{2.17}$$

  where $f^l|_j := \left(\dfrac{\partial f^l}{\partial \xi^j} + \Gamma^l_{ij} f^i\right)$ is the *covariant derivative* and $f_l|_j := \left(\dfrac{\partial f_l}{\partial \xi^j} - \Gamma^i_{jl} f_i\right)$ is the *contravariant derivative*. Note that $f^K|_L = f_K|_L = \dfrac{\partial f^K}{\partial x^L}$;

- the gradient of the scalar function f can be written as

$$\boldsymbol{\nabla} f = \frac{\partial f}{\partial x^L}\underline{\boldsymbol{e}^L} = \frac{\partial f}{\partial \xi^i}\underline{\boldsymbol{g}}^i = \frac{\partial f}{\partial \xi^i} g^{ij}\underline{\boldsymbol{g}}_j; \tag{2.18}$$

- the gradient of the vector function $\underline{\boldsymbol{f}}$ is a tensor and its components can be written as

$$\left(\boldsymbol{\nabla}\underline{\boldsymbol{f}}\right)_{ij} = f_j|_i; \tag{2.19}$$

- the divergence of the vector function $\underline{\boldsymbol{f}}$ can be written as

$$\boldsymbol{\nabla} \cdot \underline{\boldsymbol{f}} = \frac{\partial f^L}{\partial x^L} = f^i|_i; \tag{2.20}$$

- the divergence of the tensor $\underline{\underline{\boldsymbol{M}}}$ can be written as

$$\boldsymbol{\nabla}\cdot\underline{\underline{\boldsymbol{M}}} = \frac{\partial M^{KL}}{\partial x^{L}}\underline{\boldsymbol{e}}_K = M^{ji}|_j\underline{\boldsymbol{g}}_i, \tag{2.21}$$

where

$$M^{ji}|_j = \left(\frac{\partial M^{ji}}{\partial \xi_j} + \Gamma^i_{jk}M^{jk} + \Gamma^k_{kj}M^{ji}\right). \tag{2.22}$$

Finally, we can generalize the Divergence Theorem to curvilinear coordinates.

Theorem 1 *Divergence Theorem: Suppose that $\mathcal{V}\subset\mathbb{R}^3$ is compact and has a piecewise smooth boundary $\partial\mathcal{V}$. If $\underline{\boldsymbol{f}}$ is a continuously differentiable vector function defined on a neighborhood of $\mathcal{V}$, then*

$$\int_{\mathcal{V}}\boldsymbol{\nabla}\cdot\underline{\boldsymbol{f}}d\mathcal{V} = \int_{\mathcal{V}} f^i|_i d\mathcal{V} = \int_{\partial\mathcal{V}} f^i n_i d\left(\partial\mathcal{V}\right) = \int_{\partial\mathcal{V}}\underline{\boldsymbol{f}}\cdot\underline{\boldsymbol{n}}d\left(\partial\mathcal{V}\right), \tag{2.23}$$

where $\underline{\boldsymbol{n}} = n_i\underline{\boldsymbol{g}}^i$ is the outward unit normal to $\partial\mathcal{V}$.

Example 1 *Cylindrical coordinates.*

Consider the change of coordinates from cartesian coordinates $\underline{\boldsymbol{x}} = \{x^1, x^2, x^3\}$ to cylindrical coordinates $\underline{\boldsymbol{\xi}} = \{r,\theta,z\}$. We can express $\underline{\boldsymbol{x}}$ as functions of $\underline{\boldsymbol{\xi}}$ and vice versa as

$$\begin{cases} x^1 &= r\cos\theta,\\ x^2 &= r\sin\theta,\\ x^3 &= z,\end{cases}\qquad \begin{cases} r &= \sqrt{(x^1)^2+(x^2)^2},\\ \theta &= \tan^{-1}\left(\dfrac{x^2}{x^1}\right),\\ z &= x^3.\end{cases} \tag{2.24}$$

Using these relationships and the definition of covariant and contravariant basis vectors, we obtain

$$\begin{aligned} \underline{\boldsymbol{g}}_1 &= \cos\theta\underline{\boldsymbol{e}}_1 + \sin\theta\underline{\boldsymbol{e}}_2, & \underline{\boldsymbol{g}}^1 &= \cos\theta\underline{\boldsymbol{e}}_1 + \sin\theta\underline{\boldsymbol{e}}_2,\\ \underline{\boldsymbol{g}}_2 &= -r\sin\theta\underline{\boldsymbol{e}}_1 + r\cos\theta\underline{\boldsymbol{e}}_2, & \underline{\boldsymbol{g}}_2 &= -\frac{1}{r}\sin\theta\underline{\boldsymbol{e}}_1 + \frac{1}{r}\cos\theta\underline{\boldsymbol{e}}_2,\\ \underline{\boldsymbol{g}}_3 &= \underline{\boldsymbol{e}}_3, & \underline{\boldsymbol{g}}^3 &= \underline{\boldsymbol{e}}_3. \end{aligned} \tag{2.25}$$

Note that in cylindrical coordinates, not only are covariant and contravariant basis mutually orthogonal, i.e. $\underline{\boldsymbol{g}}_i\cdot\underline{\boldsymbol{g}}^j = \delta^j_i$, but they are also orthogonal bases, i.e $\underline{\boldsymbol{g}}_i\cdot\underline{\boldsymbol{g}}_j = 0$ and $\underline{\boldsymbol{g}}^i\cdot\underline{\boldsymbol{g}}^j = 0$

for $i \neq j$. However, the covariant and contravariant bases are not orthonormal, since the vectors $\underline{\boldsymbol{g}}_2$ and $\underline{\boldsymbol{g}}^2$ are not unitary, i.e. $\underline{\boldsymbol{g}}_2 \cdot \underline{\boldsymbol{g}}_2 = r^2$ and $\underline{\boldsymbol{g}}^2 \cdot \underline{\boldsymbol{g}}^2 = \frac{1}{r^2}$. Thus, the cylindrical basis vectors $\underline{\boldsymbol{e}}_r$, $\underline{\boldsymbol{e}}_\theta$,$\underline{\boldsymbol{e}}_z$ are often introduced, where

$$\underline{\boldsymbol{e}}_r = \underline{\boldsymbol{g}}_1, \qquad \underline{\boldsymbol{e}}_\theta = \frac{1}{r}\underline{\boldsymbol{g}}_2 = r\underline{\boldsymbol{g}}^2, \qquad \underline{\boldsymbol{e}}_z = \underline{\boldsymbol{e}}_3. \tag{2.26}$$

This basis is now orthonormal.

For any vector $\underline{\boldsymbol{w}} \in \mathbb{R}^3$, then $\underline{\boldsymbol{w}} = w^i \underline{\boldsymbol{g}}_i = w_i \underline{\boldsymbol{g}}^i$ and $\underline{\boldsymbol{w}} = w_r \underline{\boldsymbol{e}}_r + w_\theta \underline{\boldsymbol{e}}_\theta + w_z \underline{\boldsymbol{e}_z}$, where

$$w_r = w^1 = w_1, \qquad w_\theta = r w^2 = \frac{1}{r} w_2, \qquad w_z = w^3 = w_3. \tag{2.27}$$

As defined in Equations (2.18), (2.20) and (2.22), the gradient in cylindrical coordinates of a scalar function f can be expressed as

$$\begin{aligned} \boldsymbol{\nabla} f &= \frac{\partial f}{\partial r}\underline{\boldsymbol{g}}_1 + \frac{1}{r^2}\frac{\partial f}{\partial \theta}\underline{\boldsymbol{g}}_2 + \frac{\partial f}{\partial z}\underline{\boldsymbol{g}}_3 \\ &= \frac{\partial f}{\partial r}\underline{\boldsymbol{g}}^1 + \frac{\partial f}{\partial \theta}\underline{\boldsymbol{g}}^2 + \frac{\partial f}{\partial z}\underline{\boldsymbol{g}}^3 \\ &= \frac{\partial f}{\partial r}\underline{\boldsymbol{e}}_r + \frac{1}{r}\frac{\partial f}{\partial \theta}\underline{\boldsymbol{e}}_\theta + \frac{\partial f}{\partial z}\underline{\boldsymbol{e}}_z, \end{aligned} \tag{2.28}$$

the divergence of a vectorial function $\underline{\boldsymbol{f}}$ in cylindrical coordinates can be expressed as

$$\begin{aligned} \boldsymbol{\nabla} \cdot \underline{\boldsymbol{f}} &= \frac{\partial f^1}{\partial r} + \frac{1}{r} f^1 + \frac{\partial f^2}{\partial \theta} + \frac{\partial f^3}{\partial z} \\ &= \frac{\partial f_r}{\partial r} + \frac{1}{r} f_r + \frac{1}{r}\frac{\partial f_\theta}{\partial \theta} + \frac{\partial f_z}{\partial z} \\ &= \frac{1}{r}\frac{\partial}{\partial r}(r f_r) + \frac{1}{r}\frac{\partial f_\theta}{\partial \theta} + \frac{\partial f_z}{\partial z}, \end{aligned} \tag{2.29}$$

and the divergence of a tensor $\underline{\underline{\boldsymbol{M}}}$ in cylindrical coordinates can be expressed as

$$\begin{aligned} \boldsymbol{\nabla} \cdot \underline{\underline{\boldsymbol{M}}} &= \left(\frac{1}{r}M^{11} - rM^{22} + \frac{\partial M^{11}}{\partial r} + \frac{\partial M^{21}}{\partial \theta} + \frac{\partial M^{31}}{\partial z}\right)\underline{\boldsymbol{g}}_1 \\ &+ \left(\frac{2M^{12} + M^{21}}{r} + \frac{\partial M^{12}}{\partial r} + \frac{\partial M^{22}}{\partial \theta} + \frac{\partial M^{32}}{\partial z}\right)\underline{\boldsymbol{g}}_2 \\ &+ \left(\frac{1}{r}M^{13} + \frac{\partial M^{13}}{\partial r} + \frac{\partial M^{23}}{\partial \theta} + \frac{\partial M^{33}}{\partial z}\right)\underline{\boldsymbol{g}}_3 \\ &= \left(\frac{M_{rr} - M_{\theta\theta}}{r} + \frac{\partial M_{rr}}{\partial r} + \frac{1}{r}\frac{\partial M_{\theta r}}{\partial \theta} + \frac{\partial M_{zr}}{\partial z}\right)\underline{\boldsymbol{e}}_r \\ &+ \left(\frac{M_{r\theta} + M_{\theta r}}{r} + \frac{\partial M_{r\theta}}{\partial r} + \frac{1}{r}\frac{\partial M_{\theta\theta}}{\partial \theta} + \frac{\partial M_{z\theta}}{\partial z}\right)\underline{\boldsymbol{e}}_\theta \\ &+ \left(\frac{M_{rz}}{r} + \frac{\partial M_{rz}}{\partial sr} + \frac{1}{s}\frac{\partial M_{\theta z}}{\partial \theta} + \frac{\partial M_{zz}}{\partial z}\right)\underline{\boldsymbol{e}}_z. \end{aligned} \tag{2.30}$$

Let us now consider the gradient of a vectorial function $\underline{\boldsymbol{f}}$ (2.19), its components $\left(\boldsymbol{\nabla}\underline{\boldsymbol{f}}\right)_{ij}$ can be expressed as

$$\boldsymbol{\nabla}\underline{\boldsymbol{f}} = \begin{bmatrix} \dfrac{\partial f_1}{\partial r} & \dfrac{\partial f_2}{\partial r} - \dfrac{1}{r} f_2 & \dfrac{\partial f_3}{\partial r} \\ \dfrac{\partial f_1}{\partial \theta} - \dfrac{1}{r} f_2 & \dfrac{\partial f_2}{\partial \theta} + r f_1 & \dfrac{\partial f_3}{\partial \theta} \\ \dfrac{\partial f_1}{\partial z} & \dfrac{\partial f_2}{\partial z} & \dfrac{\partial f_3}{\partial z} \end{bmatrix}, \tag{2.31}$$

and its components in the cylindrical orthonormal basis $\underline{\boldsymbol{e}}_r$, $\underline{\boldsymbol{e}}_\theta$,$\underline{\boldsymbol{e}}_z$, can be expressed as

$$\boldsymbol{\nabla}\underline{\boldsymbol{f}} = \begin{bmatrix} \dfrac{\partial f_r}{\partial r} & \dfrac{\partial f_\theta}{\partial r} & \dfrac{\partial f_z}{\partial r} \\ \dfrac{1}{r}\dfrac{\partial f_r}{\partial \theta} - \dfrac{1}{r} f_\theta & \dfrac{1}{r}\left(\dfrac{\partial f_\theta}{\partial \theta} + f_r\right) & \dfrac{1}{r}\dfrac{\partial f_z}{\partial \theta} \\ \dfrac{\partial f_r}{\partial z} & \dfrac{\partial f_\theta}{\partial z} & \dfrac{\partial f_3}{\partial z} \end{bmatrix}. \tag{2.32}$$

Note that, in the second part of Equations (2.30) and (2.32), we have used the fact that

$$\begin{aligned} &M_{rr} = M^{11} = M_{11}, && M_{r\theta} = rM^{12} = \frac{1}{r}M_{12}, && M_{rz} = M^{13} = M_{13}, \\ &M_{\theta r} = rM^{21} = \frac{1}{r}M_{21}, && M_{\theta\theta} = r^2 M^{22} = \frac{1}{r^2}M_{22}, && M_{\theta z} = rM^{23} = \frac{1}{r}M_{23}, \\ &M_{zr} = M^{31} = M_{31}, && M_{z\theta} = rM^{32} = \frac{1}{r}M_{32}, && M_{zz} = M^{33} = M_{33}. \end{aligned} \tag{2.33}$$

2.1.2 Lagrangian and Eulerian description of motion

For the description of motion of a continuum body, given the existence of the diffeomorphism $\boldsymbol{\psi}$ between $\underline{\boldsymbol{R}} \in \Omega_0$ and $\underline{\boldsymbol{r}} \in \Omega_t$

1. we can choose to treat $\underline{\boldsymbol{R}}$ and t as independent variables and express the current position as a function of the original position at any time, i.e. $\underline{\boldsymbol{r}} = \underline{\boldsymbol{r}}(\underline{\boldsymbol{R}}, t) = \boldsymbol{\psi}(\underline{\boldsymbol{R}}, t)$. This is called the *Lagrangian* or *material description* and it is commonly used in solid mechanics;

2. we can choose to treat $\underline{\boldsymbol{r}}$ and t as independent variables and express the original position as a function of the current position at any time, i.e. $\underline{\boldsymbol{R}} = \underline{\boldsymbol{R}}(\underline{\boldsymbol{r}}, t) = \boldsymbol{\psi}^{-1}(\underline{\boldsymbol{r}}, t)$.

> This is called the *Eulerian* or *spacial description* and it is commonly used in fluid mechanics.

We define now the time derivative, displacement, velocity and acceleration in the Lagrangian and Eulerian descriptions, and introduce curvilinear coordinates in both descriptions.

Lagrangian description

In the Lagrangian description, the coordinates of a material point $\underline{\boldsymbol{R}}$ do not change in time. Thus, given a scalar function $f(\underline{\boldsymbol{R}}, t)$ the derivative of f with respect to time at a fixed position $\underline{\boldsymbol{R}}$, also called *material derivative*, is

$$\frac{Df(\underline{\boldsymbol{R}}, t)}{Dt} := \left.\frac{\partial f}{\partial t}\right|_{\underline{\boldsymbol{R}}\ \text{fixed}} = \frac{\partial f}{\partial t}, \tag{2.34}$$

which simply corresponds to the partial derivative of f with respect to time.

The displacement $\underline{\boldsymbol{U}}$ is defined as the difference between the current position $\underline{\boldsymbol{r}}$ and the original position $\underline{\boldsymbol{R}}$, where the current position is expressed in terms of $\underline{\boldsymbol{R}}$ and t

$$\underline{\boldsymbol{U}}(\underline{\boldsymbol{R}}, t) := \underline{\boldsymbol{r}}(\underline{\boldsymbol{R}}, t) - \underline{\boldsymbol{R}}. \tag{2.35}$$

The velocity $\underline{\boldsymbol{V}}$ of a material point $\underline{\boldsymbol{R}}$ is the rate of change of the position vector $\underline{\boldsymbol{r}}$ with respect to time

$$\underline{\boldsymbol{V}}(\underline{\boldsymbol{R}}, t) := \left.\frac{\partial \underline{\boldsymbol{r}}(\underline{\boldsymbol{R}}, t)}{\partial t}\right|_{\underline{\boldsymbol{R}}} = \left.\frac{\partial \underline{\boldsymbol{U}}(\underline{\boldsymbol{R}}, t)}{\partial t}\right|_{\underline{\boldsymbol{R}}}. \tag{2.36}$$

The acceleration of a material point $\underline{\boldsymbol{R}}$ is the rate of change of its velocity in time

$$\underline{\boldsymbol{A}}(\underline{\boldsymbol{R}}, t) := \left.\frac{\partial \underline{\boldsymbol{V}}(\underline{\boldsymbol{R}}, t)}{\partial t}\right|_{\underline{\boldsymbol{R}}} = \left.\frac{\partial^2 \underline{\boldsymbol{r}}(\underline{\boldsymbol{R}}, t)}{\partial t^2}\right|_{\underline{\boldsymbol{R}}}. \tag{2.37}$$

Let $\underline{\boldsymbol{\xi}} = \left\{\xi^1, \xi^2, \xi^3\right\}$ be a set of Lagrangian curvilinear coordinates, let $\underline{\boldsymbol{G}}_i := \dfrac{\partial \underline{\boldsymbol{R}}}{\partial \xi^i}$ be the Lagrangian covariant basis vectors in the initial configuration, let

$$\underline{\boldsymbol{g}}_i := \frac{\partial \underline{\boldsymbol{r}}}{\partial \xi^i} = \frac{\partial \left(\underline{\boldsymbol{R}} + \underline{\boldsymbol{U}}\right)}{\partial \xi^i} = \underline{\boldsymbol{G}}_i + \frac{\partial \underline{\boldsymbol{U}}}{\partial \xi^i} \tag{2.38}$$

be the Lagrangian covariant basis vectors in the current configuration, and let $\underline{\boldsymbol{G}}^i$ and $\underline{\boldsymbol{g}}^i$ be the corresponding contravariant bases. Then, in the Lagrangian description, any vector $\underline{\boldsymbol{w}} \in \mathbb{R}^3$ can be expressed as $\underline{\boldsymbol{w}} = W^j \underline{\boldsymbol{G}}_j = w^j \underline{\boldsymbol{g}}_j$ and, similarly, its derivative with respect to ξ^j is

$$\frac{\partial \underline{\boldsymbol{w}}}{\partial \xi^j} = W^l|_j \underline{\boldsymbol{G}}_l = w^l||_j \underline{\boldsymbol{g}}_l, \tag{2.39}$$

where $W^l|_j$ is the Lagrangian covariant derivative, Equation (2.17), in the initial configuration, and $w^l||_j$ is the Lagrangian covariant derivative in the current configuration.

Eulerian description

In the Eulerian description, we focus our attention on a specific point in space; at any instant in time, a different material particle will pass through that point. So, given a scalar function $f(\underline{\boldsymbol{r}}, t)$, to compute the derivative of f with respect to time for a fixed material point $\underline{\boldsymbol{R}}$, we need to retrieve the current coordinates of the material point at every instant, i.e. $\underline{\boldsymbol{r}} = \underline{\boldsymbol{r}}(\underline{\boldsymbol{R}}, t)$. Hence, the *material derivative* of f in the Eulerian description is

$$\frac{Df(\underline{\boldsymbol{r}}, t)}{Dt} := \left. \frac{\partial f(\underline{\boldsymbol{r}}(\underline{\boldsymbol{R}}, t), t)}{\partial t} \right|_{\underline{\boldsymbol{R}}} = \left. \frac{\partial f}{\partial t} \right|_{\underline{\boldsymbol{r}}} + \left. \frac{\partial \underline{\boldsymbol{r}}}{\partial t} \right|_{\underline{\boldsymbol{R}}} \cdot \left. \frac{\partial f}{\partial \underline{\boldsymbol{r}}} \right|_t = \frac{\partial f}{\partial t} + \underline{\boldsymbol{v}} \cdot \boldsymbol{\nabla}_{\underline{\boldsymbol{r}}} f, \tag{2.40}$$

where $\boldsymbol{\nabla}_{\underline{\boldsymbol{r}}} f$ represents the gradient of f with respect to the spacial coordinates in the current configuration.

The displacement $\underline{\boldsymbol{u}}$ is defined as the difference between the current position $\underline{\boldsymbol{r}}$ and the original position $\underline{\boldsymbol{R}}$, where the original position is expressed in terms of the current position $\underline{\boldsymbol{r}}$ and t

$$\underline{\boldsymbol{u}}(\underline{\boldsymbol{r}}, t) := \underline{\boldsymbol{r}} - \underline{\boldsymbol{R}}(\underline{\boldsymbol{r}}, t). \tag{2.41}$$

The velocity $\underline{\boldsymbol{v}}$ of a material point $\underline{\boldsymbol{R}}$ in the Eulerian description is the material derivative of its displacement

$$\underline{\boldsymbol{v}}(\underline{\boldsymbol{r}}, t) := \left. \frac{\partial \underline{\boldsymbol{r}}}{\partial t} \right|_{\underline{\boldsymbol{R}}} = \frac{D\underline{\boldsymbol{u}}(\underline{\boldsymbol{r}}, t)}{Dt} = \underline{\boldsymbol{V}}(\underline{\boldsymbol{R}}(\underline{\boldsymbol{r}}, t), t). \tag{2.42}$$

The acceleration $\underline{\boldsymbol{a}}$ of a material point $\underline{\boldsymbol{R}}$ in the Eulerian description is the material derivative of its velocity

$$\underline{\boldsymbol{a}}(\underline{\boldsymbol{r}}, t) := \frac{D\underline{\boldsymbol{v}}(\underline{\boldsymbol{r}}(\underline{\boldsymbol{R}}, t), t)}{Dt} = \left.\frac{\partial \underline{\boldsymbol{v}}(\underline{\boldsymbol{r}}(\underline{\boldsymbol{R}}, t), t)}{\partial t}\right|_{\underline{\boldsymbol{R}}} = \frac{\partial \underline{\boldsymbol{v}}}{\partial t} + \underline{\boldsymbol{v}} \cdot \boldsymbol{\nabla}_{\underline{\boldsymbol{r}}} \underline{\boldsymbol{v}}. \tag{2.43}$$

Let $\underline{\overline{\boldsymbol{\xi}}} = \left\{ \overline{\xi}^1, \overline{\xi}^2, \overline{\xi}^3 \right\}$ be a set of Eulerian curvilinear coordinates, let $\underline{\overline{\boldsymbol{G}}}_i := \dfrac{\partial \underline{\boldsymbol{R}}(\underline{\boldsymbol{r}}, t)}{\partial \overline{\xi}^i}$ be the Eulerian covariant basis vectors in the initial configuration, let

$$\underline{\overline{\boldsymbol{g}}}_i := \frac{\partial \underline{\boldsymbol{r}}}{\partial \overline{\xi}^i} = \underline{\overline{\boldsymbol{G}}}_i + \frac{\partial \underline{\boldsymbol{u}}}{\partial \overline{\xi}^i} \tag{2.44}$$

be the Eulerian covariant basis vectors in the current configuration, and let $\underline{\overline{\boldsymbol{G}}}^i$ and $\underline{\overline{\boldsymbol{g}}}^i$ be the corresponding contravariant bases. Then, in the Eulerian description, any vector $\underline{\boldsymbol{w}} \in \mathbb{R}^3$ can be expressed as $\underline{\boldsymbol{w}} = \overline{W}^j \underline{\overline{\boldsymbol{G}}}_j = \overline{w}^j \underline{\overline{\boldsymbol{g}}}_j$ and, similarly, its derivative with respect to $\overline{\xi}^j$ is

$$\frac{\partial \underline{\boldsymbol{w}}}{\partial \xi^j} = \overline{W^l|}_j \underline{\overline{\boldsymbol{G}}}_l = \overline{w^l||}_j \underline{\overline{\boldsymbol{g}}}_l, \tag{2.45}$$

where $\overline{W^l|}_j$ is the Eulerian covariant derivative, Equation (2.17), in the initial configuration, and $\overline{w^l||}_j$ is the Eulerian covariant derivative in the current configuration.

2.1.3 Deformation

The *deformation gradient* $\underline{\underline{\boldsymbol{F}}}$ measures how the distances between two material points change in time; $\underline{\underline{\boldsymbol{F}}}$ is defined as the Jacobian of the map ψ

$$\underline{\underline{\boldsymbol{F}}} := \frac{\partial \underline{\boldsymbol{r}}}{\partial \underline{\boldsymbol{R}}} = \frac{\partial \psi\left(\underline{\boldsymbol{R}}, t\right)}{\partial \underline{\boldsymbol{R}}} = \boldsymbol{\nabla}_{\underline{\boldsymbol{R}}} \psi\left(\underline{\boldsymbol{R}}, t\right). \tag{2.46}$$

Let J be the determinant of the Jacobian of the map ψ, i.e. $J = \det(\underline{\underline{\boldsymbol{F}}})$. The fact that ψ is a diffeomorphism implies that $J \neq 0$. The deformation gradient can be also expressed in terms of the displacement $\underline{\boldsymbol{U}}$ using Equation (2.35)

$$\underline{\underline{\boldsymbol{F}}} = \frac{\partial \underline{\boldsymbol{r}}}{\partial \underline{\boldsymbol{R}}} = \frac{\partial \left(\underline{\boldsymbol{U}} + \underline{\boldsymbol{R}}\right)}{\partial \underline{\boldsymbol{R}}} = \boldsymbol{\nabla}_{\underline{\boldsymbol{R}}} \underline{\boldsymbol{U}} + \underline{\underline{\boldsymbol{I}}}, \tag{2.47}$$

where $\underline{\underline{\boldsymbol{I}}}$ is the identity tensor.

The Green-Lagrange *strain tensor* provides another measure of the evolution of distances between material points and is defined as

$$\gamma_{ij} := \frac{1}{2}\left(g_{ij} - G_{ij}\right). \tag{2.48}$$

More precisely, this strain tensor is a measure of the difference between the Lagrangian covariant metric tensor in the deformed configuration and the Lagrangian covariant metric tensor in the reference configuration. It can be also expressed in terms of the displacement $\underline{\boldsymbol{U}}$ using Equation (2.38)

$$\gamma_{ij} = \frac{1}{2}\left(U_i|_j + U_j|_i + U^k|_i U_k|_j\right), \tag{2.49}$$

where $\underline{\boldsymbol{U}} = U^i \underline{\boldsymbol{G}}_i = U_i \underline{\boldsymbol{G}}^i$.

Measures of deformation that do not depend on the choice of coordinate systems are the *strain scalar invariants*

$$I_1 := g^i_i, \qquad I_2 := \frac{1}{2}\left(g^i_i g^j_j - g^i_j g^j_i\right), \qquad I_3 := \frac{\det|g_{ij}|}{\det|G_{ij}|}, \tag{2.50}$$

where g^i_j and g_{ij} are the Lagrangian mixed and covariant metric tensors in the current configuration and G_{ij} is the Lagrangian covariant metric tensor in the original configuration. The first invariant is a measure of stretch in the principal directions. The second invariant is a measure of changes in orientation. The third invariant is a measure of volumetric changes, since the changes in volume in the original configuration $d\mathcal{V}_0$ are related to the changes in volume in the current configuration $d\mathcal{V}_t$ as follows

$$d\mathcal{V}_t = \sqrt{I_3}\, d\mathcal{V}_0. \tag{2.51}$$

It can be specified that $\sqrt{I_3} = J$, thus leading to

$$d\mathcal{V}_t = J d\mathcal{V}_0. \tag{2.52}$$

2.1.4 Stress tensors

The internal forces in an infinitesimal volume of a continuum body are represented by the *traction* on its surface, and, by Cauchy's postulate, the traction is assumed to depend only on the normal to the surface. Note that the traction is defined as a force per unit of area. Given the normal to a surface, the traction can be expressed via the stress tensor. Different stress tensors can be defined depending on whether the traction per unit of area is expressed in the original or current configuration, and depending on whether the normal vector is expressed in the basis for the original or current configuration. The *Nanson's formula* provides a relation between area elements in the current and original configuration. Let $d\Sigma$ be an infinitesimal area in the original configuration, let $d\sigma$ be the corresponding infinitesimal area in the current configuration, let $\underline{\boldsymbol{N}}$ be the normal to $d\Sigma$ and let $\underline{\boldsymbol{n}}$ be the normal to $d\sigma$, then Nanson's formula can be expressed as

$$\underline{\boldsymbol{n}} d\sigma = J \underline{\underline{\boldsymbol{F}}}^{-T} \underline{\boldsymbol{N}} d\Sigma. \tag{2.53}$$

The different stress tensors are defined as

- the *Cauchy stress tensor* $\overline{T}^{ij}$ represents the traction per unit of area in the current configuration when the normal is expressed as a linear combination of Eulerian covariant basis vectors $\underline{\overline{\boldsymbol{g}}}_j$;
- the *body stress tensor* $T^{sl} = \dfrac{\partial \xi^s}{\partial \overline{\xi}^i} \overline{T}^{ij} \dfrac{\partial \xi^l}{\partial \overline{\xi}^j}$ represents the traction per unit of area in the current configuration when the normal is expressed as a linear combination of the Lagrangian covariant basis vectors $\underline{\boldsymbol{g}}_j$;
- the *first Piola-Kirchhoff stress tensor* $P^{jk} = J \overline{T}^{ij} \dfrac{\partial \xi^k}{\partial \overline{\xi}^i}$ represents the traction per unit of area in the original configuration when the normal is expressed as a linear combination of the Eulerian covariant basis vectors $\underline{\overline{\boldsymbol{g}}}_j$;
- the *second Piola-Kirchhoff stress tensor* $S^{kl} = P^{jk} \dfrac{\partial \xi^l}{\partial \overline{\xi}^j} = J T^{kl} = J \dfrac{\partial \xi^k}{\partial \overline{\xi}^i} \overline{T}^{ij} \dfrac{\partial \xi^l}{\partial \overline{\xi}^j}$ represents the traction per unit of area in the original configuration when the normal is expressed as a linear combination of the Lagrangian covariant basis vectors $\underline{\boldsymbol{g}}_j$.

The Cauchy stress tensor, the body stress tensor, and the second Piola-Kirchhoff stress tensor are symmetric, whereas the first Piola-Kirchhoff stress tensor is not.

2.1.5 Conservation laws

In this section we summarize the conservation laws for mass, linear momentum and angular momentum in the Lagrangian and Eulerian descriptions. For the detailed derivation of these laws we refer to [45]. The conservations laws reported below are derived in the isothermal case, under the assumption that the mass body is preserved, i.e. there are no body sinks or sources.

Lagrangian description

- *Conservation of mass*

$$\begin{aligned} \rho(\underline{\boldsymbol{R}}, 0) &= \rho_0(\underline{\boldsymbol{R}}) \\ &= J\rho(\underline{\boldsymbol{r}}(\underline{\boldsymbol{R}}, t), t); \end{aligned} \tag{2.54}$$

- *Conservation of linear momentum*

$$\rho_0 \frac{\partial \underline{\boldsymbol{V}}}{\partial t} = \boldsymbol{\nabla}_{\underline{\boldsymbol{R}}} \cdot \underline{\underline{\boldsymbol{H}}} + \rho_0 \underline{\boldsymbol{F}}, \tag{2.55}$$

  or in component form in the basis $\underline{\boldsymbol{G}}_i$

$$\rho_0 \frac{\partial V^i}{\partial t} = H^{ji}|_j + \rho_0 F^i, \tag{2.56}$$

  where $\underline{\boldsymbol{F}}$ is the resultant of external body forces per unit of volume and

$$H^{jk} \underline{\boldsymbol{G}}_j = P^{jk} \underline{\overline{\boldsymbol{g}}_{\boldsymbol{j}}}. \tag{2.57}$$

  Note that only in cartesian coordinates $\underline{\underline{\boldsymbol{H}}} = \underline{\underline{\boldsymbol{P}}}$;

- *Conservation of angular momentum*

$$\underline{\underline{\boldsymbol{S}}} = \underline{\underline{\boldsymbol{S}}}^T \qquad S^{kl} = S^{lk}. \tag{2.58}$$

Eulerian description

- *Conservation of mass*

$$\frac{D\rho}{Dt} + \rho \boldsymbol{\nabla}_{\underline{\boldsymbol{r}}} \cdot \underline{\boldsymbol{v}} = 0, \tag{2.59}$$

or in component form in the basis $\underline{\overline{\boldsymbol{g}}}_i$

$$\frac{\partial \rho}{\partial t} + \overline{v}^i \frac{\partial \rho}{\partial \overline{\xi}^i} + \rho \overline{v^i \|}_i = 0; \tag{2.60}$$

- *Conservation of linear momentum*

$$\rho \frac{D\underline{\boldsymbol{v}}}{Dt} = \boldsymbol{\nabla}_{\underline{\boldsymbol{r}}} \cdot \underline{\underline{\boldsymbol{T}}} + \rho \underline{\boldsymbol{f}}, \tag{2.61}$$

or in component form in the basis $\underline{\overline{\boldsymbol{g}}}_i$

$$\rho \left(\frac{d\overline{v}^i}{dt} + \overline{v}^j \overline{v^i \|}_j \right) = \overline{T^{ji} \|}_j + \rho \overline{f}^i, \tag{2.62}$$

where $\underline{\boldsymbol{f}}$ is the resultant of external body forces per unit of volume;

- *Conservation of angular momentum*

$$\underline{\underline{\boldsymbol{T}}} = \underline{\underline{\boldsymbol{T}}}^T \qquad \overline{T}^{ij} = \overline{T}^{ji}. \tag{2.63}$$

2.1.6 Constitutive equation

As discussed in the previous section, a Lagrangian description of body motion is often used in solid mechanics, and an Eulerian description of motion is often used in fluid mechanics. Constitutive equations of the stress tensors are necessary to close the system of conservation laws summarized in Section 2.1.5. In this section we provide examples of constitutive equations for a Newtonian viscous fluid and a linear elastic solid.

Newtonian viscous fluid

In the case of a Newtonian viscous fluid, we choose the Eulerian description and we assume that the Cauchy stress tensor is the sum of two terms. The fist term is due to the isotropic contribution of the fluid pressure p, and the second term is due to the viscous dissipation of the fluid, namely

$$\underline{\underline{\boldsymbol{T}}} := -p\underline{\underline{\boldsymbol{I}}} + 2\mu \underline{\underline{\boldsymbol{D}}}, \tag{2.64}$$

where $\mu > 0$ is the fluid viscosity and

$$\underline{\underline{\boldsymbol{D}}} := \frac{1}{2}\left(\boldsymbol{\nabla}_{\underline{\boldsymbol{r}}}\underline{\boldsymbol{v}} + \boldsymbol{\nabla}^{T}_{\underline{\boldsymbol{r}}}\underline{\boldsymbol{v}}\right) \tag{2.65}$$

is the symmetric part of the Eulerian velocity gradient tensor, also known as the *rate-of-strain tensor*. $\underline{\underline{\boldsymbol{T}}}$ is symmetric by definition so that the conservation of angular momentum, Equation 2.63, is satisfied. Component-wise Equations (2.64) and (2.65) can be written in the Eulerian covariant basis vectors $\underline{\overline{\boldsymbol{g}}}_i$ as

$$\overline{T}^{ij} = \left(-p\overline{g}^{ij} + 2\mu\overline{D}^{ij}\right) \quad \text{and} \quad \overline{D}^{ij} = \frac{1}{2}\left(\overline{g}^{kj}\overline{v}^{i}\overline{||}_{k} + \overline{g}^{ki}v^{j}\overline{||}_{k}\right). \tag{2.66}$$

Moreover, if we assume that the fluid is homogeneous, i.e. the density ρ is constant in space and time, namely $\rho(\underline{\boldsymbol{r}}(\underline{\boldsymbol{R}}, t), t) = \rho_0(\underline{\boldsymbol{R}})$, then the conservation of mass (2.59) becomes

$$\boldsymbol{\nabla}_{\underline{\boldsymbol{r}}} \cdot \underline{\boldsymbol{v}} = \overline{v}^{i}\overline{||}_{i} = 0. \tag{2.67}$$

Let us introduce the Leibnitz transport Theorem.

Theorem 2 *Leibnitz transport Theorem: Suppose that $\mathcal{V}_{\underline{\boldsymbol{r}}} \subset \Omega_t$ is a compact material domain and that $f(\underline{\boldsymbol{r}}, t)$ is a scalar function in the Eulerian description of motion. If f is*

- *a Lebesgue-integrable function on $\mathcal{V}_{\underline{\boldsymbol{r}}}$ at any time t;*
- *differentiable with respect to $\underline{\mathbf{r}}$ at any time t and the derivative is Lebesgue-integrable;*

then

$$\frac{d}{dt}\int_{\mathcal{V}_{\underline{\boldsymbol{r}}}} f(\underline{\boldsymbol{r}}, t)d\mathcal{V} = \int_{\mathcal{V}_{\underline{\boldsymbol{r}}}} \left(\left.\frac{\partial f}{\partial t}\right|_{\underline{\boldsymbol{r}}} + \boldsymbol{\nabla}_{\underline{\boldsymbol{r}}} \cdot (f\underline{\boldsymbol{v}})\right) d\mathcal{V}. \tag{2.68}$$

The volume of the fluid is defined as

$$vol = \int_{\Omega_t} d\Omega_t, \tag{2.69}$$

and, using the Leibnitz transport Theorem (2.68), the body volume variation in time can be expressed as

$$\frac{d\,(vol)}{dt} = \frac{d}{dt}\int_{\Omega_t} d\Omega_t = \int_{\Omega_t} \boldsymbol{\nabla}_{\underline{\boldsymbol{r}}} \cdot \underline{\boldsymbol{v}} d\Omega_t. \tag{2.70}$$

Hence, the constraint on the Eulerian velocity to have zero divergence, that follows from the homogeneity of the fluid, implies that the fluid volume is constant, i.e. the fluid is incompressible. In this case, the conservation of mass and the balance of linear momentum for a homogenous Newtonian viscous fluid are

$$\nabla_{\underline{r}} \cdot \underline{v} = 0, \tag{2.71a}$$

$$\rho \frac{\partial \underline{v}}{\partial t} + \rho \left(\underline{v} \cdot \nabla_{\underline{r}} \right) \underline{v} = \nabla_{\underline{r}} \cdot \underline{\underline{T}} + \rho \underline{f}, \tag{2.71b}$$

where

$$\nabla_{\underline{r}} \cdot \underline{\underline{T}} = -\nabla_{\underline{r}}\, p + \mu \nabla^2_{\underline{r}}\, \underline{v}, \tag{2.72}$$

also called the *Navier-Stokes equations*. In the case of laminar flow, the convection term $\left(\underline{v} \cdot \nabla_{\underline{r}} \right) \underline{v}$ is negligible, and (2.71) becomes

$$\nabla \cdot \underline{v} = 0, \tag{2.73a}$$

$$\rho \frac{\partial \underline{v}}{\partial t} = \nabla_{\underline{r}} \cdot \underline{\underline{T}} + \rho \underline{f}, \tag{2.73b}$$

also called *Stokes equations*.

Conversely, if we assume that the fluid is incompressible, then Equation (2.70) implies that $\nabla_{\underline{r}} \cdot \underline{v} = 0$, so that the conservation of mass (2.59) becomes $\frac{D\rho}{Dt} = 0$; hence the density of a material point is constant in time. Note that this implies that the fluid is homogenous at time t, only if it was homogeneous in the initial configuration.

Example 2 *Navier-Stokes equations and Stokes equations in cylindrical coordinates.*

Let us consider the cylindrical coordinates $\underline{\xi} = \{r, \theta, z\}$ with Eulerian curvilinear coordinates and the cylindrical basis $\underline{e}_r$, $\underline{e}_\theta$ and $\underline{e}_z$, defined in Equation (2.26). To simplify the notation we omit the over-bar sign and the subscript to the gradient. Then, with respect to the chosen basis and using (2.32), the components of $\underline{\underline{\boldsymbol{D}}}$ are

$$\underline{\underline{\boldsymbol{D}}} = \begin{bmatrix} \dfrac{\partial v_r}{\partial r} & \dfrac{1}{2}\left[r\dfrac{\partial}{\partial r}\left(\dfrac{v_\theta}{r}\right) + \dfrac{1}{r}\dfrac{\partial v_r}{\partial \theta}\right] & \dfrac{1}{2}\left(\dfrac{\partial v_r}{\partial z} + \dfrac{\partial v_z}{\partial r}\right) \\ \dfrac{1}{2}\left[r\dfrac{\partial}{\partial r}\left(\dfrac{v_\theta}{r}\right) + \dfrac{1}{r}\dfrac{\partial v_r}{\partial \theta}\right] & \dfrac{1}{r}\left(\dfrac{\partial v_\theta}{\partial \theta} + v_r\right) & \dfrac{1}{2}\left(\dfrac{\partial v_\theta}{\partial z} + \dfrac{1}{r}\dfrac{\partial v_z}{\partial \theta}\right) \\ \dfrac{1}{2}\left(\dfrac{\partial v_r}{\partial z} + \dfrac{\partial v_z}{\partial r}\right) & \dfrac{1}{2}\left(\dfrac{\partial v_\theta}{\partial z} + \dfrac{1}{r}\dfrac{\partial v_z}{\partial \theta}\right) & \dfrac{\partial v_z}{\partial z} \end{bmatrix}, \tag{2.74}$$

the Navier-Stokes equations (2.71) can be written as

$$\begin{cases} \dfrac{1}{r}\dfrac{\partial}{\partial r}(rv_r) + \dfrac{1}{r}\dfrac{\partial v_\theta}{\partial \theta} + \dfrac{\partial v_z}{\partial z} & = 0, \\ \rho\left(\dfrac{\partial v_r}{\partial t} + v_r\dfrac{dv_r}{dr} + \dfrac{v_\theta}{r}\dfrac{\partial v_r}{\partial \theta} + v_z\dfrac{\partial v_r}{\partial z} - \dfrac{v_\theta^2}{r}\right) & = -\dfrac{\partial p}{\partial r} \\ & +\mu\left(\Delta v_r - \dfrac{v_r}{r^2} - \dfrac{2}{r^2}\dfrac{\partial v_\theta}{\partial \theta}\right) + \rho f_r, \\ \rho\left(\dfrac{\partial v_\theta}{\partial t} + v_r\dfrac{\partial v_\theta}{\partial r} + \dfrac{v_\theta v_r}{r} + \dfrac{v_\theta}{r}\dfrac{\partial v_\theta}{\partial \theta} + v_z\dfrac{\partial v_\theta}{\partial z}\right) & = -\dfrac{1}{r}\dfrac{\partial p}{\partial \theta} \\ & +\mu\left(\Delta v_\theta - \dfrac{v_\theta}{r^2} + \dfrac{2}{r^2}\dfrac{dv_r}{d\theta}\right) + \rho f_\theta, \\ \rho\left(\dfrac{\partial v_z}{\partial t} + v_r\dfrac{\partial v_z}{\partial r} + \dfrac{v_\theta}{r}\dfrac{\partial v_z}{\partial \theta} + v_z\dfrac{\partial v_z}{\partial z}\right) & = -\dfrac{\partial p}{\partial z} + \mu\Delta v_z + \rho f_z, \end{cases} \tag{2.75}$$

and the Stokes equations (2.73) can be written as

$$\begin{cases} \dfrac{1}{r}\dfrac{\partial}{\partial r}(rv_r) + \dfrac{1}{r}\dfrac{\partial v_\theta}{\partial \theta} + \dfrac{\partial v_z}{\partial z} = 0, \\ \rho\dfrac{\partial v_r}{\partial t} = -\dfrac{\partial p}{\partial r} + \mu\left(\Delta v_r - \dfrac{v_r}{r^2} - \dfrac{2}{r^2}\dfrac{\partial v_\theta}{\partial \theta}\right) + \rho f_r, \\ \rho\dfrac{\partial v_\theta}{\partial t} = -\dfrac{1}{r}\dfrac{\partial p}{\partial \theta} + \mu\left(\Delta v_\theta - \dfrac{v_\theta}{r^2} + \dfrac{2}{r^2}\dfrac{dv_r}{d\theta}\right) + \rho f_\theta, \\ \rho\dfrac{\partial v_z}{\partial t} = -\dfrac{\partial p}{\partial z} + \mu\Delta v_z + \rho f_z, \end{cases} \tag{2.76}$$

where $\Delta(\cdot) = \dfrac{1}{r}\dfrac{\partial}{\partial r}\left(r\dfrac{\partial(\cdot)}{\partial r}\right) + \dfrac{1}{r^2}\dfrac{\partial^2(\cdot)}{\partial \theta^2} + \dfrac{\partial^2(\cdot)}{\partial z^2}$.

Linear elastic solid

In the case of a purely elastic material, we adopt the Lagrangian description and we assume that there exists a strain energy function $\mathcal{W}$ that depends only on the strain tensor $\underline{\underline{\gamma}}$, such that

$$S^{ij} := \frac{\partial \mathcal{W}}{\partial \gamma_{ij}}. \tag{2.77}$$

Moreover, we assume that the dependence of $\mathcal{W}$ on the strain is through the scalar strain invariants, i.e. $\mathcal{W} = \mathcal{W}\left(I_1, I_2, I_3\right)$.

Consider the case of infinitesimal deformations, also referred to as the small deformation case, where there exists $0 < \varepsilon \ll 1$ such that $\underline{\boldsymbol{r}} = \underline{\boldsymbol{R}} + \underline{\boldsymbol{U}} = \underline{\boldsymbol{r}} + \varepsilon \underline{\tilde{\boldsymbol{U}}}$ and $\underline{\tilde{\boldsymbol{U}}}$ is $\mathcal{O}(1)$. Now, expanding the Green-Lagrangian strain tensor, Equation (2.49), in terms of ε and neglecting the terms multiplied by ε^2, we obtain

$$\gamma_{ij} \simeq \frac{1}{2}\left(U_i|_j + U_j|_i\right) =: E_{ij}. \tag{2.78}$$

Here,

$$\underline{\underline{\boldsymbol{E}}} := \frac{1}{2}\left(\boldsymbol{\nabla}_{\underline{\boldsymbol{R}}}\underline{\boldsymbol{u}} + \boldsymbol{\nabla}^T_{\underline{\boldsymbol{R}}}\underline{\boldsymbol{u}}\right) \tag{2.79}$$

is the *linearized strain tensor* and it is equal to the symmetric part of the Lagrangian displacement gradient tensor. If we expand also J with respect to ε, we obtain that $J = 1 + \mathcal{O}(\varepsilon)$. If we neglect the terms multiplied by ε, then $J \simeq 1$ and this implies that

1. the solid is incompressible, since the deformation preserves the volumes, see Equation (2.52);

2. the solid is homogeneous, since the conservation of mass implies that $\rho = \rho_0$, see Equation (2.54).

Moreover, if we expand the stress tensors defined in Section 2.1.4 with respect to ε, we obtain that all of them have the same leading terms, implying that $\underline{\underline{\boldsymbol{S}}} \simeq \underline{\underline{\boldsymbol{P}}} \simeq \underline{\underline{\boldsymbol{T}}}$.

Finally, if we assume that the material has a linear elastic constitutive equation, namely that $\mathcal{W}$ depends linearly on the strain tensor, we can write

$$\underline{\underline{\boldsymbol{S}}} = \frac{\partial \mathcal{W}}{\partial \gamma_{ij}} := \lambda \operatorname{tr}\left(\underline{\underline{\gamma}}\right) \underline{\underline{\boldsymbol{I}}} + 2\mu \underline{\underline{\gamma}}, \tag{2.80}$$

where λ and μ are positive constants also known as Lamé parameters. That, in the case of small deformations, becomes

$$\underline{\underline{\boldsymbol{S}}} = \lambda \operatorname{tr}\left(\underline{\underline{\boldsymbol{E}}}\right) \underline{\underline{\boldsymbol{I}}} + 2\mu \underline{\underline{\boldsymbol{E}}}. \tag{2.81}$$

Under these assumptions, the Lagrangian conservation of linear momentum, Equation(2.55), for a linear elastic solid in the regime of infinitesimal deformations becomes

$$\rho_0 \frac{\partial^2 \underline{\boldsymbol{U}}}{\partial t^2} = \boldsymbol{\nabla}_{\underline{\boldsymbol{R}}} \cdot \underline{\underline{\boldsymbol{S}}} + \rho_0 \underline{\boldsymbol{F}}, \tag{2.82}$$

or, component-wise in the Lagrangian covariant basis $\underline{\boldsymbol{G}}_i$, we can write

$$\rho_0 \frac{\partial^2 U^i}{\partial t^2} = \left(\lambda G^{ji} E^k_k + 2\mu E^{ji}\right)|_j + \rho_0 F^i. \tag{2.83}$$

Note that the symmetry of $\underline{\underline{\boldsymbol{E}}}$ implies that $\underline{\underline{\boldsymbol{S}}}$ is also symmetric; hence the conservation of linear momentum, Equation (2.55), is satisfied.

Example 3 *Linear elastic solid in regime of small deformations in cylindrical coordinates.*

Let us consider the cylindrical coordinates $\underline{\boldsymbol{\xi}} = \{s, \vartheta, \zeta\}$ as Lagrangian curvilinear coordinates and the cylindrical basis $\underline{\boldsymbol{e}}_s$, $\underline{\boldsymbol{e}}_\vartheta$ and $\underline{\boldsymbol{e}}_\zeta$.Then, with respect to the chosen basis, the components of the second Piola-Kirchooff stress tensor can be written as

$$\underline{\underline{\boldsymbol{S}}} = \begin{bmatrix} \lambda \boldsymbol{\nabla} \cdot \underline{\boldsymbol{U}} + 2\mu \frac{\partial U_s}{\partial s} & \mu\left(s\frac{\partial}{\partial s}\left(\frac{U_\vartheta}{s}\right) + \frac{1}{s}\frac{\partial U_s}{\partial \vartheta}\right) & \mu\left(\frac{\partial U_s}{\partial \zeta} + \frac{\partial U_\zeta}{\partial s}\right) \\ \mu\left(s\frac{\partial}{\partial s}\left(\frac{U_\vartheta}{s}\right) + \frac{1}{s}\frac{\partial U_s}{\partial \vartheta}\right) & \lambda \boldsymbol{\nabla} \cdot \underline{\boldsymbol{U}} + \frac{2\mu}{s}\left(\frac{\partial U_\vartheta}{\partial \vartheta} + U_s\right) & \mu\left(\frac{\partial U_\vartheta}{\partial \zeta} + \frac{1}{s}\frac{\partial U_\zeta}{\partial \vartheta}\right) \\ \mu\left(\frac{\partial U_s}{\partial \zeta} + \frac{\partial U_\zeta}{\partial s}\right) & \mu\left(\frac{\partial U_\vartheta}{\partial \zeta} + \frac{1}{s}\frac{\partial U_\zeta}{\partial \vartheta}\right) & \lambda \boldsymbol{\nabla} \cdot \underline{\boldsymbol{U}} + 2\mu \frac{\partial U_\zeta}{\partial \zeta} \end{bmatrix}, \tag{2.84}$$

where $\boldsymbol{\nabla} \cdot \underline{\boldsymbol{U}} = \frac{1}{s}\frac{d}{ds}(sU_s) + \frac{1}{s}\frac{dU_\vartheta}{d\vartheta} + \frac{dU_\zeta}{d\zeta}$, and the conservation of linear momentum, Equation (2.82), can be written as

$$\begin{cases} \rho_0 \frac{\partial^2 U_s}{\partial t^2} &= \frac{S_{ss} - S_{\vartheta\vartheta}}{s} + \frac{\partial S_{ss}}{\partial s} + \frac{1}{s}\frac{\partial S_{\vartheta s}}{\partial \vartheta} + \frac{\partial S_{\zeta s}}{\partial \zeta} + \rho_0 F_s, \\ \rho_0 \frac{\partial^2 U_\vartheta}{\partial t^2} &= \frac{S_{s\vartheta} + S_{\vartheta s}}{s} + \frac{\partial S_{s\vartheta}}{\partial s} + \frac{1}{s}\frac{\partial S_{\vartheta\vartheta}}{\partial \vartheta} + \frac{\partial S_{\zeta\vartheta}}{\partial \zeta} + \rho_0 F_\vartheta, \\ \rho_0 \frac{\partial^2 U_\zeta}{\partial t^2} &= \frac{S_{s\zeta}}{s} + \frac{\partial S_{s\zeta}}{\partial s} + \frac{1}{s}\frac{\partial S_{\vartheta\zeta}}{\partial \vartheta} + \frac{\partial S_{\zeta\zeta}}{\partial \zeta} + \rho_0 F_\zeta. \end{cases} \tag{2.85}$$

2.2 Energy identities

In this section we study the intrinsic behavior of the operators in the conservation laws of a incompressible homogenous Newtonian viscous fluid and of a linear elastic solid from the energy point of view. For simplicity, we present the results in cartesian coordinates, but the same results hold in any curvilinear coordinates.

Fist of all, we list some definitions that will be used in the present and next sections, where we consider $\Omega \subset \mathbb{R}^d$, for $d = 2, 3$.

Definition 1 *Let f be a scalar function $f : \Omega \to \mathbb{R}$, define the L^2 space as*

$$L^2(\Omega) = \left\{ f : \Omega \to \mathbb{R} \;\middle|\; \int_\Omega f^2 \, d\Omega < \infty \right\}, \tag{2.86}$$

with the norm

$$\|f\|_{L^2(\Omega)} = \sqrt{\int_\Omega |f|^2 d\Omega}. \tag{2.87}$$

Let $\underline{\boldsymbol{f}}$ be a vectorial function $\underline{\boldsymbol{f}} : \Omega \to \mathbb{R}^d$, for $d = 2, 3$, define

$$\mathbf{L}^2(\Omega) = \left(L^2(\Omega)\right)^d, \tag{2.88}$$

with the norm

$$\|\underline{\boldsymbol{f}}\|_{L^2(\Omega)} = \sqrt{\int_\Omega |\underline{\boldsymbol{f}}|^2 d\Omega} = \sqrt{\int_\Omega \underline{\boldsymbol{f}} \cdot \underline{\boldsymbol{f}} \, d\Omega}. \tag{2.89}$$

Let $\underline{\underline{\boldsymbol{A}}}$ be a second order tensor $\underline{\underline{\boldsymbol{A}}} \in \mathbb{R}^{d \times d}$, define the norm

$$\|\underline{\underline{\boldsymbol{A}}}\|_{L^2(\Omega)} = \sqrt{\int_\Omega \underline{\underline{\boldsymbol{A}}} : \underline{\underline{\boldsymbol{A}}} \, d\Omega}, \tag{2.90}$$

where $\underline{\underline{\boldsymbol{A}}} : \underline{\underline{\boldsymbol{B}}} = A_{IJ} B_{IJ}$.

Definition 2 *Let f be a scalar function $f : \Omega \to \mathbb{R}$, define the H^1 space as*

$$H^1(\Omega) = \left\{ f : \Omega \to \mathbb{R} \;\middle|\; \int_\Omega \left(f^2 + |\boldsymbol{\nabla} f|^2 \right) d\Omega < \infty \right\}, \tag{2.91}$$

with the seminorm

$$|f|_{H^1(\Omega)} = \sqrt{\|\boldsymbol{\nabla} f\|^2_{L^2(\Omega)}}, \tag{2.92}$$

and norm

$$\|f\|_{H^1(\Omega)} = \sqrt{\|f\|^2_{L^2(\Omega)} + |f|^2_{H^1(\Omega)}}. \tag{2.93}$$

Let $\underline{\boldsymbol{f}}$ *be a vectorial function* $\underline{\boldsymbol{f}} : \Omega \rightarrow \mathbb{R}^d$*, for* $d = 2, 3$*, define*

$$\mathbf{H}^1(\Omega) = \left(H^1(\Omega)\right)^d, \tag{2.94}$$

with the seminorm

$$|\underline{\boldsymbol{f}}|_{H^1(\Omega)} = \sqrt{\|\boldsymbol{\nabla}\underline{\boldsymbol{f}}\|^2_{L^2(\Omega)}}, \tag{2.95}$$

and norm

$$\|\underline{\boldsymbol{f}}\|_{H^1(\Omega)} = \sqrt{\|\underline{\boldsymbol{f}}\|^2_{L^2(\Omega)} + |\underline{\boldsymbol{f}}|^2_{H^1(\Omega)}}. \tag{2.96}$$

Definition 3 *Let* f *be a scalar function* $f : \Omega \rightarrow \mathbb{R}$*, define the* H^2 *space as*

$$H^2(\Omega) = \left\{ f : \Omega \rightarrow \mathbb{R}^3 \;\middle|\; \int_\Omega \left(f^2 + |\boldsymbol{\nabla} f|^2 + \underline{\underline{\boldsymbol{\mathcal{H}}}}(f) : \underline{\underline{\boldsymbol{\mathcal{H}}}}(f) \right) d\Omega < \infty \right\}, \tag{2.97}$$

with the norm

$$\|f\|_{H^2(\Omega)} = \sqrt{\|f\|^2_{L^2(\Omega)} + \|\boldsymbol{\nabla} f\|^2_{L^2(\Omega)} + \|\underline{\underline{\boldsymbol{\mathcal{H}}}}(f)\|^2_{L^2(\Omega)}}, \tag{2.98}$$

where $\underline{\underline{\boldsymbol{\mathcal{H}}}}(f)$ *is the Hessian of* f*.*

Definition 4 *For functions depending on time and space, given a functional space* $\mathbf{V}$*, define the following spaces*

$$L^2(0, T; \mathbf{V}) = \left\{ \mathbf{h} : (0, T) \rightarrow \mathbf{V} \;\middle|\; \int_0^T \|\mathbf{h}(t)\|^2_V dt < \infty \right\} \tag{2.99}$$

and

$$L^\infty(0, T; \mathbf{V}) = \left\{ \mathbf{h} : (0, T) \rightarrow \mathbf{V} \;\middle|\; \operatorname*{ess\,sup}_{t \in (0,T)} \|\mathbf{h}(t)\|_V < \infty \right\}, \tag{2.100}$$

where, depending on $\mathbf{V}$*,* $\mathbf{h}$ *is a scalar or a vectorial function in space.*

We consider the case of homogenous Dirichlet boundary conditions in the absence of body forces, this implies that the time evolution of the system is solely driven by a nonzero initial condition. Under these assumptions, we identify two main types of energy identities.

Case 1 Non-dissipative system

$$\frac{d}{dt}\mathcal{E}(t) = 0, \tag{2.101}$$

where $\mathcal{E}(t)$ is a non-negative functional describing the energy of the system. In a non-dissipative system, the energy is constant, i.e. $\mathcal{E}(t) = \mathcal{E}(0)$ for all $t \in (0, T)$, so the energy is conserved. An example of a non-dissipative system is the motion of a linear elastic solid.

Case 2 Dissipative system

$$\frac{d}{dt}\mathcal{E}(t) = -\mathcal{D}(t), \tag{2.102}$$

where $\mathcal{E}(t)$ and $\mathcal{D}(t)$ are non-negative functional describing the energy and the dissipation of the system, respectively. The energy is dissipated, namely $\mathcal{E}(t) \leq \mathcal{E}(0)$ for all $t \in (0, T)$. An example of a dissipative system is the flow of a incompressible homogenous Newtonian viscous fluids.

2.2.1 Newtonian viscous fluid

Consider the Navier-Stokes Equations (2.71), in a fixed bounded domain $\Omega \subset \mathbb{R}^3$, and $t \in (0, T)$, with a nonzero initial condition $\underline{\boldsymbol{v}}(t = 0) = \underline{\boldsymbol{v}}_0$ and homogenous Dirichlet boundary conditions $\underline{\boldsymbol{v}} = \underline{\mathbf{0}}$ on $\partial\Omega$. If we multiply the balance of linear momentum (2.71b) by $\underline{\boldsymbol{v}}$ in $\mathbf{L}^2(\Omega)$, for every t

$$\int_\Omega \rho \frac{\partial \underline{\boldsymbol{v}}}{\partial t} \cdot \underline{\boldsymbol{v}} d\Omega + \int_\Omega \rho \left(\underline{\boldsymbol{v}} \cdot \nabla\right) \underline{\boldsymbol{v}} \cdot \underline{\boldsymbol{v}} d\Omega = \int_\Omega \left(\nabla \cdot \underline{\underline{\boldsymbol{T}}}\right) \cdot \underline{\boldsymbol{v}} d\Omega. \tag{2.103}$$

Since the fluid is homogeneous and Ω does not depend on time, the first term on the left-hand side of Equation (2.103) yields

$$\int_\Omega \rho \frac{\partial \underline{\boldsymbol{v}}}{\partial t} \cdot \underline{\boldsymbol{v}} d\Omega = \frac{\rho}{2} \int_\Omega \frac{\partial \underline{\boldsymbol{v}}^2}{\partial t} d\Omega = \frac{1}{2}\frac{d}{dt}\left(\rho \int_\Omega \underline{\boldsymbol{v}}^2 d\Omega\right) = \frac{1}{2}\frac{d}{dt}\left(\rho \|\underline{\boldsymbol{v}}\|^2_{L^2(\Omega)}\right), \tag{2.104}$$

where $\dfrac{\partial}{\partial t}$ represents the partial derivative, and $\dfrac{d}{dt}$ the total derivative with respect to time. Using the Divergence theorem (2.23), the incompressibility condition and the boundary conditions, the second term on the left-hand side of Equation (2.103) is

$$\begin{aligned}
\int_\Omega \rho\left(\underline{\boldsymbol{v}}\cdot\nabla\right)\underline{\boldsymbol{v}}\cdot\underline{\boldsymbol{v}}d\Omega &= \rho\int_\Omega v_I\,\frac{\partial v_J}{\partial x_I}d\Omega = \frac{\rho}{2}\int_\Omega v_I\,\frac{\partial\left(v_J^2\right)}{\partial x_I}d\Omega\\
&= \frac{\rho}{2}\int_\Omega\left(\underline{\boldsymbol{v}}\cdot\nabla\right)\underline{\boldsymbol{v}}^2 d\Omega = \frac{\rho}{2}\int_\Omega\nabla\cdot\left(\underline{\boldsymbol{v}}^2\,\underline{\boldsymbol{v}}\right)d\Omega - \cancel{\frac{\rho}{2}\int_\Omega\underline{\boldsymbol{v}}\nabla\cdot\underline{\boldsymbol{v}}d\Omega}\\
&= \cancel{\frac{\rho}{2}\int_{\partial\Omega}\underline{\boldsymbol{v}}^2\,\underline{\boldsymbol{v}}\cdot\underline{\boldsymbol{n}}\,d\left(\partial\Omega\right)} = 0,
\end{aligned}\tag{2.105}$$

and the term on the right-hand side of Equation (2.103) is

$$\begin{aligned}
\int_\Omega\left(\nabla\cdot\underline{\underline{\boldsymbol{T}}}\right)\cdot\underline{\boldsymbol{v}}d\Omega &= \int_\Omega\frac{\partial T_{IJ}}{\partial x_J}v_I d\Omega = \int_\Omega\frac{\partial\left(T_{IJ}v_I\right)}{\partial x_J}d\Omega - \int_\Omega T_{IJ}\frac{\partial v_I}{\partial x_J}d\Omega\\
&= \int_\Omega v_I T_{IJ} n_J\,d\Omega - \int_\Omega T_{IJ}\left(\nabla\underline{\boldsymbol{v}}\right)_{IJ}d\Omega\\
&= \cancel{\int_{\partial\Omega}\underline{\boldsymbol{v}}\cdot\underline{\underline{\boldsymbol{T}}}\cdot\underline{\boldsymbol{n}}\,d\left(\partial\Omega\right)} - \int_\Omega\underline{\underline{\boldsymbol{T}}}:\nabla\underline{\boldsymbol{v}}\,d\Omega\\
&= -\int_\Omega\underline{\underline{\boldsymbol{T}}}:\nabla\underline{\boldsymbol{v}}\,d\Omega.
\end{aligned}\tag{2.106}$$

Now, using the constitutive equation of the stress tensor for a incompressible homogenous Newtonian viscous fluid (2.64)-(2.65), assuming that μ is constant, and using the fact that $\underline{\underline{\boldsymbol{D}}}(\underline{\boldsymbol{v}})$ is the symmetric part of $\boldsymbol{\nabla}\underline{\boldsymbol{v}}$, we obtain

$$\begin{aligned}
\int_\Omega\underline{\underline{\boldsymbol{T}}}:\nabla\underline{\boldsymbol{v}}\,d\Omega &= -\int_\Omega p\underline{\underline{\boldsymbol{I}}}:\nabla\underline{\boldsymbol{v}}d\Omega + \int_\Omega 2\mu\underline{\underline{\boldsymbol{D}}}(\underline{\boldsymbol{v}}):\nabla\underline{\boldsymbol{v}}d\Omega\\
&= \cancel{-\int_\Omega p\nabla\cdot\underline{\boldsymbol{v}}d\Omega} + \textstyle\int_\Omega 2\mu\,\underline{\underline{\boldsymbol{D}}}(\underline{\boldsymbol{v}}):\underline{\underline{\boldsymbol{D}}}(\underline{\boldsymbol{v}})d\Omega\\
&= 2\mu\|\mathbf{D}(\underline{\boldsymbol{v}})\|^2_{L^2(\Omega)}.
\end{aligned}\tag{2.107}$$

Substituting Equations (2.104)-(2.107) in Equation (2.103), we obtain the energy identity for the Navier-Stokes equations (2.71)

$$\frac{d}{dt}\left(\frac{\rho}{2}\|\underline{\boldsymbol{v}}\|^2_{L^2(\Omega)}\right) = -2\mu\|\underline{\underline{\boldsymbol{D}}}(\underline{\boldsymbol{v}})\|^2_{L^2(\Omega)}.\tag{2.108}$$

Hence, this is a dissipative system (2.102) where

$$\mathcal{E}(t) = \frac{\rho}{2}\|\underline{\boldsymbol{v}}\|^2_{L^2(\Omega)} \qquad \text{and} \qquad \mathcal{D}(t) = 2\mu\|\underline{\underline{\boldsymbol{D}}}(\underline{\boldsymbol{v}})\|^2_{L^2(\Omega)}.\tag{2.109}$$

The energy functional $\mathcal{E}(t)$ corresponds to the fluid kinetic energy that comes from the velocity contribution. The energy dissipates due to the viscous dissipation and depends on the fluid viscosity μ.

2.2.2 Linear elastic solid

Consider a linear elastic solid in a fixed bounded domain $\Omega \subset \mathbb{R}^3$, and $t \in (0, T)$, with a nonzero initial condition $\underline{\boldsymbol{U}}(t = 0) = \underline{\boldsymbol{U}}_0$ and homogenous Dirichlet boundary conditions $\underline{\boldsymbol{U}} = \underline{\mathbf{0}}$ on $\partial\Omega$. If we multiply the balance of linear momentum, Equation (2.82), by $\dfrac{\partial \underline{\boldsymbol{U}}}{\partial t}$ in $\mathbf{L}^2(\Omega)$, for every t

$$\int_\Omega \rho \frac{\partial^2 \underline{\boldsymbol{U}}}{\partial t^2} \cdot \frac{\partial \underline{\boldsymbol{U}}}{\partial t} d\Omega = \int_\Omega \left(\nabla \cdot \underline{\underline{\boldsymbol{S}}}\right) \cdot \frac{\partial \underline{\boldsymbol{U}}}{\partial t} d\Omega. \tag{2.110}$$

Following a similar procedure to that one used to simplify Equations (2.104) and (2.106), we obtain

$$\frac{d}{dt}\left(\frac{\rho}{2}\left\|\frac{\partial \underline{\boldsymbol{U}}}{\partial t}\right\|^2_{L^2(\Omega)}\right) = -\int_\Omega \underline{\underline{\boldsymbol{S}}} : \nabla\left(\frac{\partial \underline{\boldsymbol{U}}}{\partial t}\right) d\Omega. \tag{2.111}$$

Now, using the constitutive equation for linearly elastic materials (2.78) and (2.81), assuming that λ and μ are constants, using the fact that Ω does not depends on time, and assuming that $\underline{\boldsymbol{U}}$ is smooth and regular enough so that the temporal and spatial derivatives can be exchanged, then, the right-hand side of Equation (2.111), can be written as

$$\begin{aligned}
\int_\Omega \underline{\underline{\boldsymbol{S}}} : \nabla\left(\frac{\partial \underline{\boldsymbol{U}}}{\partial t}\right) d\Omega &= \lambda \int_\Omega \boldsymbol{\nabla} \cdot \underline{\boldsymbol{U}}\, \boldsymbol{\nabla} \cdot \left(\frac{\partial \underline{\boldsymbol{U}}}{\partial t}\right) d\Omega + 2\mu \int_\Omega \underline{\underline{\boldsymbol{E}}}(\underline{\boldsymbol{U}}) : \nabla\left(\frac{\partial \underline{\boldsymbol{U}}}{\partial t}\right) d\Omega \\
&= \lambda \int_\Omega \boldsymbol{\nabla} \cdot \underline{\boldsymbol{U}} \frac{\partial}{\partial t}\left(\boldsymbol{\nabla} \cdot \underline{\boldsymbol{U}}\right) d\Omega + 2\mu \int_\Omega \underline{\underline{\boldsymbol{E}}}(\underline{\boldsymbol{U}}) : \frac{\partial}{\partial t}\left(\boldsymbol{\nabla} \underline{\boldsymbol{U}}\right) d\Omega \\
&= \frac{\lambda}{2} \int_\Omega \frac{\partial}{\partial t}\left(\boldsymbol{\nabla} \cdot \underline{\boldsymbol{U}}\right)^2 d\Omega + \mu \int_\Omega \frac{\partial}{\partial t}\left(\underline{\underline{\boldsymbol{E}}}(\underline{\boldsymbol{U}}) : \underline{\underline{\boldsymbol{E}}}(\underline{\boldsymbol{U}})\right) d\Omega \\
&= \frac{1}{2}\frac{d}{dt}\left(\lambda \|\boldsymbol{\nabla} \cdot \underline{\boldsymbol{U}}\|^2_{L^2(\Omega)} + 2\mu \|\underline{\underline{\boldsymbol{E}}}(\underline{\boldsymbol{U}})\|^2_{L^2(\Omega)}\right).
\end{aligned} \tag{2.112}$$

Substituting Equation (2.112) into Equation (2.111) we obtain the following energy identity for a linear elastic material

$$\frac{d}{dt}\left(\frac{\rho}{2}\left\|\frac{\partial \underline{\boldsymbol{U}}}{\partial t}\right\|^2_{L^2(\Omega)} + \frac{\lambda}{2}\|\boldsymbol{\nabla} \cdot \underline{\boldsymbol{U}}\|^2_{L^2(\Omega)} + \mu \|\underline{\underline{\boldsymbol{E}}}(\underline{\boldsymbol{U}})\|^2_{L^2(\Omega)}\right) = 0, \tag{2.113}$$

This is a conservative system (2.101) where the energy of the system is given by

$$\mathcal{E}(t) = \frac{\rho}{2}\left\|\frac{\partial \underline{\boldsymbol{U}}}{\partial t}\right\|^2_{L^2(\Omega)} + \frac{\lambda}{2}\|\boldsymbol{\nabla}\cdot\underline{\boldsymbol{U}}\|^2_{L^2(\Omega)} + \mu\|\underline{\underline{\boldsymbol{E}}}(\underline{\boldsymbol{U}})\|^2_{L^2(\Omega)}, \tag{2.114}$$

that consists of a sum of a kinetic part, since the velocity is $\underline{\boldsymbol{V}} = \dfrac{D\underline{\boldsymbol{U}}}{Dt}$, and a potential part, that depends on the elastic properties of the material, i.e. the Lamé parameters λ and μ.

2.3 Fluid-structure interaction in a cylindrical domain

Modeling blood flow in blood vessels involves *fluid-structure interaction* problems, where the fluid is represented by the blood passing through the vessel and the structure is represented by the vessel wall that deforms due to the fluid motion inside it. In this section we study the coupling between the fluid in a cylindrical domain and the structure occupying a cylindrical shell around it. We adopt the Eulerian description for the fluid motion and the Lagrangian description for the structure deformation, both in cylindrical coordinates.

Let $\underline{\boldsymbol{x}} = (r\cos\theta, r\sin\theta, z)$ be a point in the fluid domain

$$\Omega^f(t) := \left\{\underline{\boldsymbol{x}} \in \mathbb{R}^3 | r \in [0, \gamma(\theta, z, t)), \theta \in [0, 2\pi), z \in (0, L)\right\}, \tag{2.115}$$

where $\{r, \theta, z\}$ are the radial, azimuthal and axial Eulerian coordinates, respectively. L is the length of the domain and γ is the deformed radius, that might depend on θ, z and time t, see Figure 2.2. The boundary of $\Omega^f(t)$ is the union of three different surfaces

$$\partial\Omega^f = \Sigma^f_0(t) \cup \Sigma^f_L(t) \cup \Sigma^f_{lat}(t), \tag{2.116a}$$

where

- $\Sigma^f_0(t)$ is the fluid inlet surface, defined as

$$\Sigma^f_0(t) := \left\{\underline{\boldsymbol{x}} \in \mathbb{R}^3 | r \in [0, \gamma(\theta, z, t)), \theta \in [0, 2\pi), z = 0\right\}; \tag{2.116b}$$

- $\Sigma^f_L(t)$ is the fluid outlet surface, defined as

$$\Sigma^f_L(t) := \left\{\underline{\boldsymbol{x}} \in \mathbb{R}^3 | r \in [0, \gamma(\theta, z, t)), \theta \in [0, 2\pi), z = L\right\}; \tag{2.116c}$$

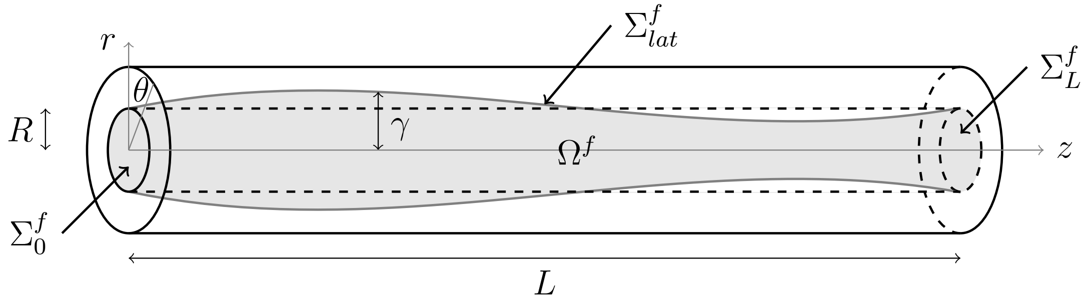

Fig. 2.2.: Fluid-structure interaction in a cylindrical domain: fluid domain Ω^f in cylindrical coordinates $\{r, \theta, z\}$. R is the reference radius of the domain, γ is the deformed radius and L is its length. Σ^f_0, Σ^f_L and Σ^f_{lat} are the inlet, outlet and lateral surfaces of Ω^f, respectively.

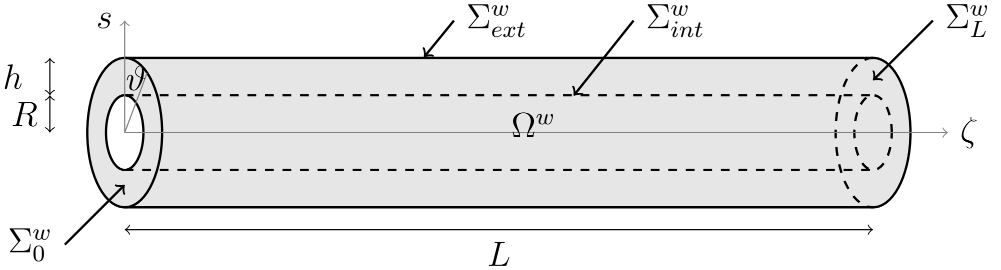

Fig. 2.3.: Fluid-structure interaction in a cylindrical domain: vessel wall domain Ω^w in cylindrical coordinates $\{s, \vartheta, \zeta\}$. R is the reference radius of the fluid domain and L is its length, and h is the thickness of the wall. Σ^w_0, Σ^w_L, Σ^w_{ext} and Σ^w_{int} are the inlet, outlet, external and internal surfaces of Ω^f, respectively.

- $\Sigma^f_{lat}(t)$ is the fluid lateral surface, defined as

$$\Sigma^f_{lat}(t) := \left\{ \underline{\boldsymbol{x}} \in \mathbb{R}^3 | r = \gamma(\theta, z, t), \theta \in [0, 2\pi), z \in (0, L) \right\}, \tag{2.116d}$$

  that represents the fluid-structure interface in the Eulerian description.

Note that, since we have chosen the Eulerian description for the fluid motion, the domain $\Omega^f(t)$ and its boundary $\partial\Omega^f(t)$ change with time.

Let $\underline{\boldsymbol{X}} = (s\cos\vartheta, s\sin\vartheta, \zeta)$ be a point in the wall domain Ω^w, which is defined as

$$\Omega^w := \left\{ \underline{\boldsymbol{X}} \in \mathbb{R}^3 | s \in (R, R+h), \vartheta \in [0, 2\pi), \zeta \in (0, L) \right\}, \tag{2.117}$$

where $\{s, \vartheta, \zeta\}$ are the radial, azimuthal and axial Lagrangian coordinates, respectively. R is the reference radius of the fluid domain and h is the reference thickness of the wall, see Figure 2.3. The boundary of Ω^w is the union of four distinct surfaces

$$\partial\Omega^w = \Sigma_0^w \cup \Sigma_L^w \cup \Sigma_{ext}^w \cup \Sigma_{int}^w, \tag{2.118a}$$

where

- Σ_0^w is the wall inlet surface, defined as

$$\Sigma_0^w := \left\{ \underline{\boldsymbol{X}} \in \mathbb{R}^3 | s \in (R, R+h), \vartheta \in [0, 2\pi), \zeta = 0 \right\}; \tag{2.118b}$$

- Σ_L^w is the wall outlet surface, defined as

$$\Sigma_L^w := \left\{ \underline{\boldsymbol{X}} \in \mathbb{R}^3 | s \in (R, R+h), \vartheta \in [0, 2\pi), \zeta = L \right\}; \tag{2.118c}$$

- Σ_{ext}^w is the wall external surface, defined as

$$\Sigma_{ext}^w := \left\{ \underline{\boldsymbol{X}} \in \mathbb{R}^3 | s = R+h, \vartheta \in [0, 2\pi), \zeta \in (0, L) \right\}; \tag{2.118d}$$

- Σ_{int}^w is the wall internal surface, defined as

$$\Sigma_{int}^w := \left\{ \underline{\boldsymbol{X}} \in \mathbb{R}^3 | s = R, \vartheta \in [0, 2\pi), \zeta \in (0, L) \right\}, \tag{2.118e}$$

  that represents the fluid-structure interface in the Lagrangian description.

Note that, since we have chosen the Lagrangian description for the wall deformation, the domain Ω^w and its boundary $\partial\Omega^w$ are fixed in time.

Given a material point $\underline{\boldsymbol{X}} = (R\cos\vartheta, R\sin\vartheta, \zeta) \in \Sigma_{int}^w$, the corresponding spatial point $\underline{\boldsymbol{x}} = (\gamma\cos\theta, \gamma\sin\theta, z) \in \Sigma_{lat}^f$ can be retrieved via the displacement

$$\underline{\boldsymbol{U}} = \underline{\boldsymbol{x}} - \underline{\boldsymbol{X}} = U_s \underline{\boldsymbol{e}}_s + U_\vartheta \underline{\boldsymbol{e}}_\vartheta + U_\zeta \underline{\boldsymbol{e}}_\zeta \tag{2.119}$$

as follows

$$\gamma = R + U_s, \qquad \theta = \vartheta + U_\vartheta \qquad \text{and} \qquad z = \zeta + U_\zeta. \tag{2.120}$$

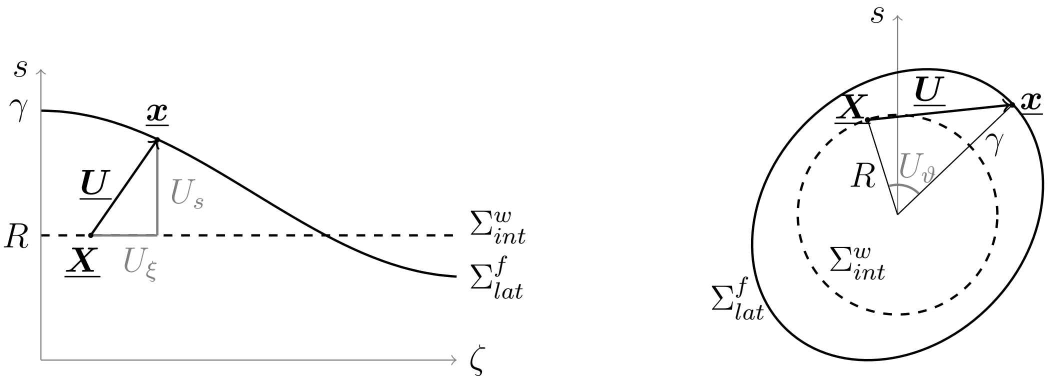

Fig. 2.4.: A sketch of the coupling between $\underline{\boldsymbol{x}} \in \Sigma^f_{lat}(t)$ and $\underline{\boldsymbol{X}} \in \Sigma^w_{int}$ via the displacement $\underline{\boldsymbol{U}} = \underline{\boldsymbol{x}} - \underline{\boldsymbol{X}}$. The projection of $\underline{\boldsymbol{U}}$ on the $s\zeta$-plane is sketched on the left, and the projection on a cross section is sketched on the right. U_s, U_ζ and U_ϑ are the radial, axial and angular components of the displacement. R is the reference radius of the fluid domain and γ is the deformed radius of the fluid domain.

Figure 2.4 shows a sketch of the components of the displacement. The radial component U_s and axial component U_ζ of the displacement can be extracted by projecting $\underline{\boldsymbol{U}}$ on the $s\zeta$-plane, Figure 2.4 (left). The angular component U_ϑ can be extracted by projecting $\underline{\boldsymbol{U}}$ on a cross section, i.e. for ζ fixed, Figure 2.4 (right).

The fluid motion in $\Omega^f(t)$ is coupled with the wall deformation in Ω^w via the following kinematic and dynamic interface conditions.

Kinematic condition: we impose the velocity of the fluid $\underline{\boldsymbol{v}}$ at $\underline{\boldsymbol{x}} \in \Sigma^f_{lat}(t)$ to be equal to the velocity of the wall $\underline{\boldsymbol{V}}$ on the corresponding point $\underline{\boldsymbol{X}} \in \Sigma^w_{int}$. Since, by definition (2.36), the wall velocity is equal to the partial derivative of the displacement with respect to time, the kinematic interface condition can be expressed as

$$\underline{\boldsymbol{v}}(\underline{\boldsymbol{x}}, t)\Big|_{\underline{\boldsymbol{x}} \in \Sigma^f_{lat}(t)} = \left.\frac{\partial \underline{\boldsymbol{U}}(\underline{\boldsymbol{X}}, t)}{\partial t}\right|_{\underline{\boldsymbol{X}} \in \Sigma^w_{int}}, \tag{2.121}$$

where $\underline{\boldsymbol{x}} = \underline{\boldsymbol{U}} + \underline{\boldsymbol{X}}$.

Dynamic condition: we impose continuity of forces on the fluid-structure interface. As described in Section 2.1.4, the internal forces in a continuum are represented by the surface traction, that can be expressed with the stress tensor and the normal to the surface. Let $d\Sigma$ be an infinitesimal area on Σ^w_{int} and let $d\sigma$ be the corresponding infinitesimal area in $\Sigma^f_{lat}(t)$, let $\underline{\boldsymbol{N}}$ be the normal to $d\Sigma$ and let $\underline{\boldsymbol{n}}$ be the normal to $d\sigma$; then, the equilibrium of forces on fluid-structure interface can be expressed as

$$\underline{\underline{\boldsymbol{S}}}\,\underline{\boldsymbol{N}}\,d\Sigma = \underline{\underline{\boldsymbol{T}}}\,\underline{\boldsymbol{n}}\,d\sigma. \tag{2.122}$$

Using Nanson's relation (2.53), the right-hand side of Equation (2.122) becomes

$$\underline{\underline{\boldsymbol{T}}}\,\underline{\boldsymbol{n}}\,d\sigma = \underline{\underline{\boldsymbol{T}}}\,J\,\underline{\underline{\boldsymbol{F}}}^{-T}\,\underline{\boldsymbol{N}}\,d\Sigma. \tag{2.123}$$

Moreover, substituting Equation (2.123) into Equation (2.122), the conservation of forces can be expressed as

$$\underline{\underline{\boldsymbol{S}}}\,\underline{\boldsymbol{N}}\,d\Sigma = \underline{\underline{\boldsymbol{T}}}\,J\,\underline{\underline{\boldsymbol{F}}}^{-T}\,\underline{\boldsymbol{N}}\,d\Sigma \qquad \forall\, d\Sigma \subset \Sigma^w_{int}, \tag{2.124}$$

that simplifies to

$$\underline{\underline{\boldsymbol{S}}}\Big|_{\underline{\boldsymbol{X}}\in\Sigma^w_{int}}\underline{\boldsymbol{N}} = \; J\underline{\underline{\boldsymbol{T}}}\Big|_{\underline{\boldsymbol{x}}\in\Sigma^f_{lat}(t)}\underline{\underline{\boldsymbol{F}}}^{-T}\underline{\boldsymbol{N}}. \tag{2.125}$$

We consider two mathematical models for the mechanics of the wall: a linear elastic *thick shell* model and a linear elastic *thin Koiter shell* model. In the case of a thick shell, Section 2.3.1, the thickness is not negligible, thus we study the deformation of the whole three-dimensional domain. In the case of a thin shell, Section 2.3.2, the thickness is negligible and the deformation of the shell can be approximated by the deformation of its middle surface. Axial symmetry is assumed and thus the angular components of the fluid velocity and solid displacement are null, namely $v_\theta = 0$ and $U_\vartheta = 0$, and there is no dependence on θ and ϑ of any other variable. Note that the axial symmetry assumption implies that the cross-section of the fluid and wall domains remain circular at all times.

2.3.1 Linear elastic axially symmetric thick shell

Let us consider an incompressible homogenous Newtonian viscous fluid running through $\Omega^f(t)$ (2.115) and a linear elastic solid that occupies Ω^w (2.117). Under the assumption of axial symmetry, the Cauchy stress tensor (2.64) in the cylindrical basis $\underline{\boldsymbol{e}}_r$, $\underline{\boldsymbol{e}}_\theta$ and $\underline{\boldsymbol{e}}_z$ simplifies to

$$\underline{\underline{\boldsymbol{T}}} = \begin{bmatrix} -p + 2\mu_f \dfrac{\partial v_r}{\partial r} & 0 & \mu_f \left(\dfrac{\partial v_r}{\partial z} + \dfrac{\partial v_z}{\partial r} \right) \\ 0 & -p + 2\mu_f \dfrac{v_r}{r} & 0 \\ \mu_f \left(\dfrac{\partial v_r}{\partial z} + \dfrac{\partial v_z}{\partial r} \right) & 0 & -p + 2\mu_f \dfrac{\partial v_z}{\partial z} \end{bmatrix}, \tag{2.126}$$

where μ_f is the fluid viscosity. Similarly, the second Piola-Kirchhoff stress tensor (2.84) in the cylindrical basis $\underline{\boldsymbol{e}}_s$, $\underline{\boldsymbol{e}}_\vartheta$ and $\underline{\boldsymbol{e}}_\zeta$ simplifies to

$$\underline{\underline{\boldsymbol{S}}} = \begin{bmatrix} \lambda_w \boldsymbol{\nabla} \cdot \underline{\boldsymbol{U}} + 2\mu_w \dfrac{\partial U_s}{\partial s} & 0 & \mu_w \left(\dfrac{\partial U_s}{\partial \zeta} + \dfrac{\partial U_\zeta}{\partial s} \right) \\ 0 & \lambda_w \boldsymbol{\nabla} \cdot \underline{\boldsymbol{U}} + 2\mu_w \dfrac{U_s}{s} & 0 \\ \mu_w \left(\dfrac{\partial U_s}{\partial \zeta} + \dfrac{\partial U_\zeta}{\partial s} \right) & 0 & \lambda_w \boldsymbol{\nabla} \cdot \underline{\boldsymbol{U}} + 2\mu_w \dfrac{\partial U_\zeta}{\partial \zeta} \end{bmatrix}, \tag{2.127}$$

where λ_w and μ_w are the wall Lamé parameters and $\boldsymbol{\nabla} \cdot \underline{\boldsymbol{U}} = \dfrac{1}{s}\dfrac{d}{ds}(sU_s) + \dfrac{dU_\zeta}{d\zeta}$. The deformation gradient $\underline{\underline{\boldsymbol{F}}}$ can be expressed as

$$\underline{\underline{\boldsymbol{F}}} = \underline{\underline{\boldsymbol{I}}} + \boldsymbol{\nabla}\underline{\boldsymbol{U}} = \begin{bmatrix} 1 + \dfrac{\partial U_s}{\partial s} & 0 & \dfrac{\partial U_s}{\partial \zeta} \\ 0 & 1 + \dfrac{U_s}{s} & 0 \\ \dfrac{\partial U_s}{\partial \zeta} & 0 & 1 + \dfrac{\partial U_\zeta}{\partial \zeta}. \end{bmatrix}. \tag{2.128}$$

Thus, in the case of a thick linear elastic shell, the dynamic coupling condition (2.125) can be written as

$$\begin{cases} \lambda_w \boldsymbol{\nabla} \cdot \underline{\boldsymbol{U}} + 2\mu_w \dfrac{\partial U_s}{\partial s} & = \left(-p + 2\mu_f \dfrac{\partial v_r}{\partial r} \right) \left(1 + \dfrac{U_s}{s} \right) \left(1 + \dfrac{\partial U_\zeta}{\partial \zeta} \right) \\ & \quad -\mu_f \left(\dfrac{\partial v_r}{\partial z} + \dfrac{\partial v_z}{\partial r} \right) \left(1 + \dfrac{U_s}{s} \right) \dfrac{\partial U_s}{\partial \zeta}, \\ \mu_w \left(\dfrac{\partial U_s}{\partial \zeta} + \dfrac{\partial U_\zeta}{\partial s} \right) & = \mu_f \left(\dfrac{\partial v_r}{\partial z} + \dfrac{\partial v_z}{\partial r} \right) \left(1 + \dfrac{U_s}{s} \right) \left(1 + \dfrac{\partial U_\zeta}{\partial \zeta} \right) \\ & \quad - \left(-p + 2\mu_f \dfrac{\partial v_z}{\partial z} \right) \left(1 + \dfrac{U_s}{s} \right) \dfrac{\partial U_s}{\partial \zeta}. \end{cases} \tag{2.129}$$

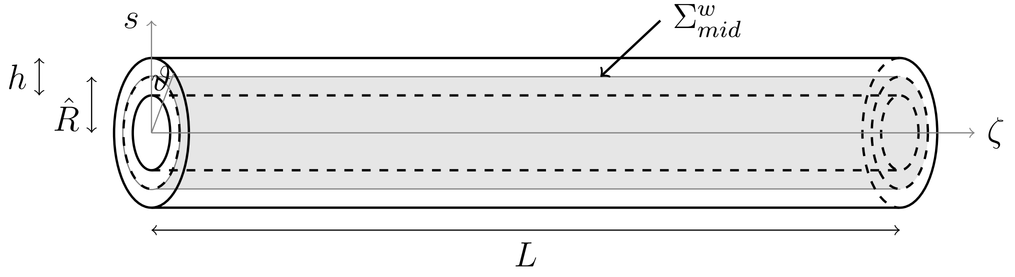

Fig. 2.5.: Fluid-structure interaction in a cylindrical domain: wall middle surface Σ^w_{mid} in cylindrical coordinates $\{s, \vartheta, \zeta\}$, where $\hat{R}$ is the radius of the middle surface, L is its length, and h is the thickness of the wall.

2.3.2 Linear elastic axially symmetric thin Koiter shell

Let us consider the case of the thin shell model in which $h/\hat{R} \ll 1$, where h is the shell thickness and $\hat{R}$ is the shell middle surface radius. Then, the wall mechanics can be approximated by studying the deformation of the middle surface

$$\Sigma^w_{mid} = \left\{ \underline{\boldsymbol{X}} = (\hat{R}\cos\vartheta, \hat{R}\cos\vartheta, z) \in \mathbb{R}^3 | \vartheta \in [0, 2\pi), \zeta \in (0, L) \right\} \tag{2.130}$$

represented in Figure 2.5. The fluid occupies the same domain defined in Equations (2.115)-(2.116) with $R = \hat{R}$.

Below we list the main assumptions under which the linear elastic Koiter shell method holds:

- thin shell, $h/\hat{R} \ll 1$;
- small strains, although large deflection is allowed;
- approximately plane state of stress;
- linear elastic homogenous solid.

For a complete derivation of the Koiter shell model we refer to [46, 47].

The forces in a thin shell are represented by the vector $\underline{\boldsymbol{\mathcal{S}}}$, defined as the surface density of the forces applied to the shell. Under the assumption of axial symmetry, the components of $\underline{\boldsymbol{\mathcal{S}}}$ can be expressed as

$$\begin{cases} \mathcal{S}_\zeta &:= -\dfrac{hE}{1-\nu^2}\left(\dfrac{\partial^2 U_\zeta}{\partial \zeta^2} + \dfrac{\nu}{\hat{R}}\dfrac{\partial U_s}{\partial \zeta}\right) + \rho_w h \dfrac{\partial^2 U_\zeta}{\partial t^2}, \\ \mathcal{S}_s &:= \dfrac{h^3 E}{12(1-\nu^2)}\left(\dfrac{\partial^4 U_s}{\partial \zeta^4} - 2\dfrac{\nu}{\hat{R}^2}\dfrac{\partial^2 U_s}{\partial \zeta^2} + \dfrac{U_s}{\hat{R}^4}\right) \\ & \quad + \dfrac{hE}{\hat{R}(1-\nu^2)}\left(\nu\dfrac{\partial U_\zeta}{\partial \zeta} + \dfrac{U_s}{\hat{R}}\right) + \rho_w h \dfrac{\partial^2 U_s}{\partial t^2}, \end{cases} \tag{2.131}$$

where

$$E = \frac{\mu_w(3\lambda_w + 2\mu_w)}{\lambda_w + \mu_w} \qquad \text{and} \qquad \nu = \frac{\lambda_w}{2(\lambda_w + \mu_w)} \tag{2.132}$$

are the Young's modulus and the Poisson's ratio, respectively. In the regime of small deformations in the axial direction, namely $|U_\zeta| \ll 1$,

$$\mathcal{S}_\zeta \simeq 0, \tag{2.133a}$$

$$\mathcal{S}_s = \rho_w h \frac{\partial^2 U_s}{\partial t^2} + C_0 U_s - C_1 \frac{\partial^2 U_s}{\partial \zeta^2} + C_2 \frac{\partial^4 U_s}{\partial \zeta^4}, \tag{2.133b}$$

where

$$C_0 = \frac{h}{\hat{R}^2}\frac{E}{1-\nu^2}\left(1 + \frac{h^2}{12\hat{R}^2}\right), \tag{2.134a}$$

$$C_1 = 2\frac{h^3}{12\hat{R}^2}\frac{E\nu}{1-\nu^2}, \tag{2.134b}$$

$$C_2 = \frac{h^3}{12}\frac{E}{1-\nu^2}. \tag{2.134c}$$

For a full derivation of $\underline{\boldsymbol{\mathcal{S}}}$ we refer to [42].

For a thin shell, the continuity of forces (2.125) at the coupling interface converts to the continuity of surface density forces, that is imposed weakly as

$$\int_{\Sigma^w_{mid}} (\underline{\boldsymbol{\mathcal{S}}} + P_e \underline{\boldsymbol{N}}) \cdot \underline{\boldsymbol{w}} d\Sigma = -\int_{\Sigma^f_{lat}(t)} \left(\underline{\underline{\boldsymbol{T}}}\, \underline{\boldsymbol{n}}\right) \cdot \underline{\boldsymbol{w}} d\sigma, \tag{2.135}$$

for any test $\underline{\boldsymbol{w}} \in \mathbf{H}^1(0, L) \times \mathbf{H}^2(0, L)$ and null on any clamped boundary. $P_e(\zeta, t)$ represents the external pressure acting on the shell. Using Nanson's relation (2.53) and choosing $\underline{\boldsymbol{w}} = w_s \underline{\boldsymbol{e}}_s$, Equation (2.135) can be written as

$$\int_{\Sigma^w_{mid}} \left(\mathcal{S}_s + P_e\right) w_s d\Sigma = - \int_{\Sigma^w_{mid}} \left(\left(\underline{\underline{\boldsymbol{T}}}\underline{\boldsymbol{n}}\right)\Big|_{\underline{\boldsymbol{x}} \in \Sigma^f_{lat}} \cdot \underline{\boldsymbol{e_s}} \left(1 + \frac{U_s}{\hat{R}}\right) \sqrt{1 + \left(\frac{\partial U_s}{\partial \zeta}\right)^2} \right) w_s d\Sigma, \tag{2.136}$$

which simplifies to

$$\mathcal{S}_s + P_e = \left(p\underline{\underline{\boldsymbol{I}}} - 2\mu_f \underline{\underline{\boldsymbol{D}}}\right)\Big|_{\underline{\boldsymbol{x}} \in \Sigma^f_{lat}} \underline{\boldsymbol{n}} \cdot \underline{\boldsymbol{e_s}} \left(1 + \frac{U_s}{\hat{R}}\right) \sqrt{1 + \left(\frac{\partial U_s}{\partial \zeta}\right)^2} \tag{2.137}$$

in the case of a homogenous incompressible Newtonian viscous fluid.

2.4 One-dimensional reduced model for fluid-structure interaction

To simplify the numerical simulations of fluid-structure interaction problems in vascular beds, various modeling reduction techniques have been proposed. Even if reduced models are derived under specific simplified model assumptions, they are able to capture the main physical phenomena governing the system and, at the same time, can be studied at a lower computational cost. In this section we consider two techniques of model reduction

1. the cross-sectional averaging technique;
2. the dimensional analysis technique.

In Section 2.4.1 and 2.4.2, we present the two modeling reduction techniques. In Section 2.4.3 and 2.4.4, we compare the two techniques for the Stokes flow inside a linear elastic thin Koiter shell (Test Case 1) or inside a linear elastic thick shell (Test Case 2). In all the Test Cases we assume no body forces.

2.4.1 Cross-sectional averaging technique

The cross-sectional averaging reduction technique, presented in [48,49], averages the conservation equations on the domain cross-section to obtain a system of equations where the independent variables depend only on the axial coordinate. Thus, the problem is reduced from three-dimensions to one-dimension.

The main assumptions under which this reduction technique holds are

1. cylindrical domain;
2. axial symmetry;
3. viscous effects are relevant only near the boundaries;
4. constant fluid pressure in each cross-section, namely $p = p(z,t)$;
5. radial component of the velocity v_r negligible with respect to the axial component v_z, thus $v_r \simeq 0$;
6. axial component of the velocity v_z can be expressed as

   $$v_z(r,z,t) = \overline{v}(z,t)\,\mathrm{s}\left(\frac{r}{\gamma(z,t)}\right), \tag{2.138}$$

   where $\overline{v}$ is the mean axial velocity on the cross-section and

   $$\begin{aligned} \mathrm{s}:\mathbb{R} &\rightarrow \mathbb{R} \\ r &\mapsto \mathrm{s}\left(\frac{r}{\gamma(z,t)}\right) \end{aligned} \tag{2.139}$$

   is the velocity profile in the radial direction, also called the *profile law*, that is assumed to be given a priori.

A possible form for the profile law is

$$\mathrm{s}\left(\frac{r}{\gamma(z,t)}\right) := \frac{\tau+2}{\tau}\left(1-\left(\frac{r}{\gamma(z,t)}\right)^{\tau}\right), \tag{2.140}$$

where the value of the parameter $\tau > 0$ defines the shape of the velocity profile in the radial direction. For example, for $\tau = 2$ the velocity has the parabolic shape typical of Poiseuille flow, and for $\tau = 8$, it has a flatter profile, see Figure 2.6.

Let $\mathcal{P}$ be the portion of the domain $\Omega^f(t)$ between $\hat{z} - dz/2$ and $\hat{z} + dz/2$, with $\hat{z} \in (0, L)$ and dz small enough so that $\hat{z} - dz/2 > 0$ and $\hat{z} + dz/2 < L$, as sketched in

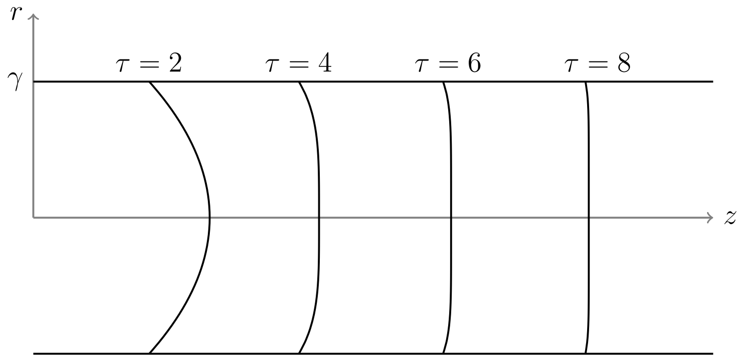

Fig. 2.6.: Shape of the profile law $\mathrm{s}(r/\gamma)$ for different values of the parameter $\tau = 2, 4, 6, 8$.

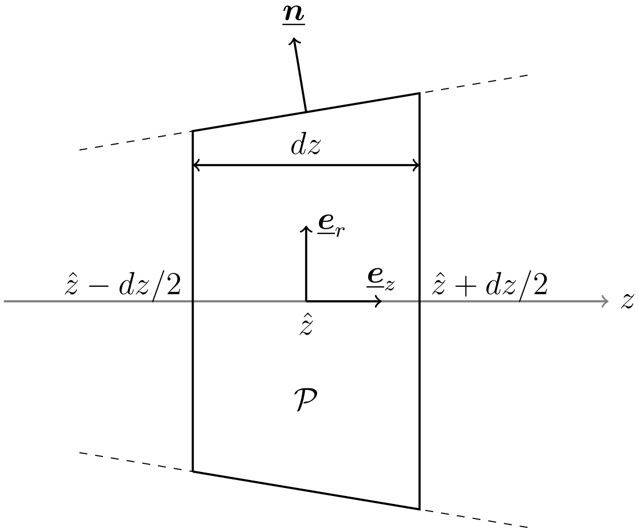

Fig. 2.7.: Sketch of the portion $\mathcal{P}$ of the domain $\Omega^f(t)$ between $\hat{z} - dz/2$ and $\hat{z} + dz/2$, with $\hat{z} \in (0, L)$ and dz small enough so that $\hat{z} - dz/2 > 0$ and $\hat{z} + dz/2 < L$.

Figure 2.7. The reduced model is derived by integrating the Navier-Stokes equations (2.71) on $\mathcal{P}$ and then passing to the limit for $dz \to 0$, under the assumption that all the quantities are smooth enough.

For any value of $z \in (0, L)$ and at any instant of time t, let us define

- $\Sigma(z, t)$ to be fluid domain cross-section;

- $A(z,t)$ to be the fluid cross-sectional area, expressed as

  $$\mathcal{A}(z,t) = \int_{\Sigma(z,t)} d\sigma = \pi\gamma(z,t)^2, \tag{2.141}$$

  since the assumption of axial symmetry ensures that the cross-section remains circular at any instant of time;

- $\mathcal{Q}(z,t)$ to be the average flow rate, expressed as

  $$\mathcal{Q}(z,t) = \int_{\Sigma(z,t)} v_z(r,z,t)d\sigma = \overline{v}(z,t)\mathcal{A}(z,t). \tag{2.142}$$

Then, $\mathcal{A}$, $\mathcal{Q}$ and p are the independent variables in the following reduced Stokes equations obtained with the reduction method just described

$$\left\{ \begin{array}{rl} \dfrac{\partial \mathcal{A}(z,t)}{\partial t} + \dfrac{\partial \mathcal{Q}(z,t)}{\partial z} & = 0 \\ \dfrac{\partial \mathcal{Q}(z,t)}{\partial t} + \dfrac{\mathcal{A}(z,t)}{\rho_f}\dfrac{dp(z,t)}{dz} + k_R\dfrac{\mathcal{Q}(z,t)}{\mathcal{A}(z,t)} & = 0 \end{array} \right. \qquad z \in (0,L), \forall t, \tag{2.143}$$

where ρ_f is the fluid density and

$$k_R = -2\pi\frac{\mu_f}{\rho_f}\frac{ds}{dr}\bigg|_{r=\gamma}. \tag{2.144}$$

For a detailed derivation of the reduced model we refer to [48]. System (2.143) is a system of two equations in three variables; thus, an additional condition is needed to close the system.

In literature, this reduction technique has been usually adopted in the case of fluids that are coupled with structures modeled as thin shells. If we consider the linear elastic Koiter thin shell case, described in Section 2.3.2, system (2.143) is closed by condition (2.137), that provides a relationship between $\mathcal{A}$ and p (see Section 2.4.3).

2.4.2 Dimensional analysis technique

The dimensional analysis technique for model reduction, presented in [42, 43], consists of performing a dimensional analysis on the conservation equations based on the small parameter $\varepsilon = \dfrac{R}{L}$, where R is the reference radius of the fluid domain and L is the reference length.

The main assumptions under which this reduction technique holds are

1. cylindrical domain;
2. axial symmetry;
3. small ratio $\varepsilon = \dfrac{R}{L} \ll 1$;
4. radial component of the velocity v_r is one order of magnitude less than the axial component v_z with respect to the asymptotic expansion in ε.

Consider the Stokes equations in the fluid domain $\Omega^f(t)$ (2.115); under these assumptions, the first step to derive the reduced conservation equations is to non-dimensionalize the equations by introducing the relations

$$\begin{gathered} r = R\tilde{r}, \quad z = L\tilde{z}, \quad t = T\tilde{t}, \\ v_r = V_r\tilde{v}_r, \quad v_z = V_z\tilde{v}_z, \quad p = P\tilde{p}, \quad \gamma = R\tilde{\gamma}, \end{gathered} \tag{2.145}$$

where the non-dimensional variables are denoted with a tilde and the characteristic quantities are denoted with uppercase letters. Then, the non-dimensional form of the Stokes equations in cylindrical coordinates (2.76) can be written as

$$\left\{ \begin{aligned} \frac{V_r L}{V_z R}\frac{1}{\tilde{r}}\frac{\partial}{\partial \tilde{r}}(\tilde{r}\tilde{v}_r) + \frac{\partial \tilde{v}_z}{\partial \tilde{z}} &= 0, \\ \frac{\rho_f V_r}{T}\frac{\partial \tilde{v}_r}{\partial \tilde{t}} + \frac{P}{R}\frac{\partial \tilde{p}}{\partial \tilde{r}} - \frac{\mu_f V_r}{R^2}\left(\Delta_{\tilde{r}}\tilde{v}_r - \frac{\tilde{v}_r}{\tilde{r}^2}\right) - \frac{\mu_f V_r}{L^2}\frac{\partial^2 \tilde{v}_r}{\partial \tilde{z}^2} &= 0, \\ \frac{\rho_f V_z}{T}\frac{\partial \tilde{v}_z}{\partial \tilde{t}} + \frac{P}{L}\frac{\partial \tilde{p}}{\partial \tilde{z}} - \frac{\mu_f V_z}{R^2}\Delta_{\tilde{r}}\tilde{v}_z - \frac{\mu_f V_z}{L^2}\frac{\partial^2 \tilde{v}_z}{\partial \tilde{z}^2} &= 0, \end{aligned} \right. \tag{2.146}$$

for $\tilde{r} \in [0, \tilde{\gamma})$ and $\tilde{z} \in (0, 1)$, where $\Delta_{\tilde{r}}(\cdot) = \dfrac{1}{\tilde{r}}\dfrac{\partial}{\partial \tilde{r}}\left(\tilde{r}\dfrac{\partial(\cdot)}{\partial \tilde{r}}\right)$.

Assumption 4 translates into the following relation between the radial and axial characteristic velocities

$$V_r = \varepsilon V_z. \tag{2.147}$$

Similarly, we have to choose a relation between P, T and the other characteristic quantities. These relations might vary depending on the mathematical model chosen for the mechanics of the structure. We will discuss two possible choices for the scaling of P in Sections 2.4.3 and 2.4.4. For an example of scaling for T we refer to [42].

At this point, we expand the variables with respect to ε as follows

$$\begin{aligned} v_z = V_z\tilde{v}_z = V_z\left(\tilde{v}_r^0 + \varepsilon\tilde{v}_r^1 + \dots\right), \quad & v_r = V_r\tilde{v}_r = \varepsilon V_z\left(\tilde{v}_r^1 + \dots\right), \\ p = P\tilde{p} = P\left(\tilde{p}^0 + \varepsilon\tilde{p}^1 + \dots\right), \quad & \gamma = R\left(\tilde{\gamma}^0 + \varepsilon\tilde{\gamma}^1 + \dots\right). \end{aligned} \tag{2.148}$$

Note that, due to (2.147), the leading order of the expansion of v_r with respect to ε is one, not zero, as for v_z. Substituting these expansions in the non-dimensional Stokes equations (2.146), and neglecting the terms multiplied by any power of ε, we obtain the reduced *0-th order* Stokes problem.

In literature, this reduction technique has been adopted in the case of fluids that are coupled with structures modeled both as thin or thick shells.

2.4.3 Test Case 1: linear elastic thin Koiter shell

In this section we will compare the two reduction techniques presented in Sections 2.4.1 and 2.4.2 in the case of Stokes equations (2.76) coupled with a linear elastic thin Koiter shell model. Let us consider the stationary case, i.e. no dependence on time, and let us assume that $U_\zeta \simeq 0$, implying that $\zeta = z$.

In the stationary case, the kinematic condition (2.121) on Σ_{lat}^f can be expressed as

$$v_r = 0 \quad \text{and} \quad v_z = 0 \quad \text{for} \quad r = \gamma,\ z \in (0, L). \tag{2.149}$$

The dynamic condition (2.137) can be expressed as

$$\mathcal{S}_s + P_e = \left[p - 2\mu_f \frac{\partial v_r}{\partial r} + \mu_f \frac{dU_s}{dz}\left(\frac{\partial v_r}{\partial z} + \frac{\partial v_z}{\partial r}\right)\right]\Bigg|_{r=\gamma} \left(1 + \frac{U_s}{R}\right), \tag{2.150}$$

since the normal $\underline{\boldsymbol{n}}$ to Σ_{lat}^f is

$$\underline{\boldsymbol{n}} = \left(1 + \left(\frac{\partial U_s}{\partial z}\right)^2\right)^{-1/2} \left(\underline{\boldsymbol{e}}_r - \frac{\partial U_s}{\partial z}\underline{\boldsymbol{e}}_z\right). \tag{2.151}$$

Using the expression of $\mathcal{S}_s$ for a stationary linear elastic thin Koiter shell (2.133b) and (2.134) in Equation (2.150), the dynamic coupling condition becomes

$$C_0 U_s - C_1 \frac{d^2 U_s}{dz^2} + C_2 \frac{d^4 U_s}{dz^4} + P_e = \left[p - 2\mu_f \frac{\partial v_r}{\partial r} + \mu_f \frac{\partial U_s}{\partial z} \left(\frac{\partial v_r}{\partial z} + \frac{\partial v_z}{\partial r} \right) \right] \Bigg|_{r=\gamma} \left(1 + \frac{U_s}{R} \right). \quad (2.152)$$

Here, we assume that the external pressure P_e is constant.

Cross-sectional averaging technique

The stationary form of the reduced Stokes equations (2.143) is

$$\begin{cases} \dfrac{\partial \mathcal{Q}(z)}{\partial z} &= 0 \\ \dfrac{\mathcal{A}(z)}{\rho_f} \dfrac{dp(z)}{dz} + k_R \dfrac{\mathcal{Q}(z)}{\mathcal{A}(z)} &= 0 \end{cases} \quad z \in (0, L), \quad (2.153)$$

where $\mathcal{A}$, $\mathcal{Q}$ and k_R depend on $\overline{v}(z)$ and on the profile law $\mathrm{s}(r/\gamma)$ chosen, see (2.141), (2.142) and (2.144).

As in [48], we consider the purely elastic dynamic interface condition

$$p(z) - P_e = C_0 U_s(z) = C_0 \left(\gamma(z) - R \right), \quad (2.154)$$

that can be obtained from (2.152) by neglecting all the axial derivatives and assuming that $\left(1 + \frac{U_s}{R} \right) \simeq 1$. Since $\mathcal{A} = \pi \gamma^2$, the dynamic interface condition can be expressed as

$$p(z) - P_e = C_0 R^2 \sqrt{\pi} \frac{\sqrt{\mathcal{A}(z)} - \sqrt{A_{ref}}}{A_{ref}}, \quad (2.155)$$

where $\mathcal{A}_{ref} = \pi R^2$ is the reference cross-sectional area. This relationship between p and $\mathcal{A}$, together with the boundary conditions

$$p(0) = P_0, \qquad \overline{v}(0) = V_0, \quad (2.156)$$

close system (2.153).

The solution of the reduced Stokes equations can be computed explicitly as

$$\mathcal{Q} = \left(\frac{(P_0 - P_e)A_{ref}}{C_0 R^2 \sqrt{\pi}} + \sqrt{A_{ref}}\right)^2 V_0, \tag{2.157a}$$

$$\mathcal{A}(z) = \left(\left(\frac{(P_0 - P_e)A_{ref}}{C_0 R^2 \sqrt{\pi}} + \sqrt{A_{ref}}\right)^5 - 5\frac{k_R \rho_f \mathcal{A}_{ref} Q}{\beta}\, z\right)^{2/5}, \tag{2.157b}$$

$$p(z) = P_e + C_0 R^2 \sqrt{\pi}\frac{\sqrt{\mathcal{A}(z)} - \sqrt{A_{ref}}}{A_{ref}}, \tag{2.157c}$$

$$\gamma(z) = \sqrt{\frac{A(z)}{\pi}}, \tag{2.157d}$$

$$v_z(r,z) = \frac{Q}{A(z)}\mathrm{s}\left(\frac{r}{\gamma(z)}\right), \tag{2.157e}$$

$$U_s(z) = \sqrt{\frac{A(z)}{\pi}} - R, \tag{2.157f}$$

for $z \in (0, L)$ and $r \in [0, \gamma)$.

Dimensional analysis technique

The stationary form of the non-dimensional Stokes equations (2.146) is

$$\begin{cases} \dfrac{1}{\tilde{r}}\dfrac{\partial}{\partial \tilde{r}}(\tilde{r}\tilde{v}_r) + \dfrac{\partial \tilde{v}_z}{\partial \tilde{z}} &= 0, \\ \dfrac{\partial \tilde{p}}{\partial \tilde{r}} - \varepsilon\dfrac{\mu_f V_z}{RP}\left(\Delta_{\tilde{r}}\tilde{v}_r - \dfrac{\tilde{v}_r}{\tilde{r}^2}\right) - \varepsilon\dfrac{\mu_f V_z R}{L^2 P}\dfrac{\partial^2 \tilde{v}_r}{\partial \tilde{z}^2} &= 0, \\ \dfrac{R^2 P}{\mu_f V_z L}\dfrac{\partial \tilde{p}}{\partial \tilde{z}} - \Delta_{\tilde{r}}\tilde{v}_z - \varepsilon^2\dfrac{\partial^2 \tilde{v}_z}{\partial \tilde{z}^2} &= 0, \end{cases} \tag{2.158}$$

for $\tilde{r} \in [0, \tilde{\gamma})$ and $\tilde{z} \in (0, 1)$, where we have already included the assumption that $V_r = \varepsilon V_z$.

Let us define the non-dimensional variables for the Koiter shell as

$$s = R\tilde{s}, \qquad \zeta = z = L\tilde{z}, \qquad U_s = W\tilde{U}_s. \tag{2.159}$$

and for the external pressure

$$P_e = P\tilde{P}_e. \tag{2.160}$$

We consider the small deformation regime, thus

$$\delta = \frac{W}{R} \simeq \mathcal{O}(\varepsilon). \tag{2.161}$$

Note that $\gamma = R + U_s$ implies that

$$\tilde{\gamma} = \frac{\gamma}{R} = \frac{R + W\tilde{U}_s}{R} = 1 + \delta\tilde{U}_s. \tag{2.162}$$

The non-dimensional version of the dynamic interface condition (2.152) can be written as

$$\begin{aligned}\tilde{P}_e + \frac{\delta}{\varepsilon}\frac{C_0 R^2}{PL}\tilde{U}_s - \delta\varepsilon\frac{C_1}{PL}\frac{d^2\tilde{U}_s}{d\tilde{z}^2} + \delta\varepsilon\frac{C_2}{PL^3}\frac{d^4\tilde{U}_s}{d\tilde{z}^4} &= \\ \left[\tilde{p} - \varepsilon\frac{2\mu_f V_z}{PR}\frac{\partial\tilde{v}_r}{\partial\tilde{r}} + \delta\frac{\mu_f V_z}{LP}\frac{\partial\tilde{U}_s}{\partial\tilde{z}}\left(\varepsilon^2\frac{\partial\tilde{v}_r}{\partial\tilde{z}} + \frac{\partial\tilde{v}_z}{\partial\tilde{r}}\right)\right]&\left(1 + \delta\tilde{U}_s\right),\end{aligned} \tag{2.163}$$

for $\tilde{r} = \tilde{\gamma} = 1 + \delta\tilde{U}_s$.

In other to have a 0-th order coupling condition similar to that used for the other reduction technique, i.e. Equation (2.154), we choose

$$P = \frac{\delta}{\varepsilon}\frac{C_0 R^2}{L}. \tag{2.164}$$

With this choice for the characteristic pressure P, the non-dimensional Stokes equations (2.158) becomes

$$\begin{cases} \dfrac{1}{\tilde{r}}\dfrac{\partial}{\partial\tilde{r}}(\tilde{r}\tilde{v}_r) + \dfrac{\partial\tilde{v}_z}{\partial\tilde{z}} &= 0, \\ \dfrac{\partial\tilde{p}}{\partial\tilde{r}} - \varepsilon^2\beta\left(\Delta_{\tilde{r}}\tilde{v}_r - \dfrac{\tilde{v}_r}{\tilde{r}^2}\right) - \varepsilon^3\beta\dfrac{\partial^2\tilde{v}_r}{\partial\tilde{z}^2} &= 0, \\ \dfrac{\partial\tilde{p}}{\partial\tilde{z}} - \beta\Delta_{\tilde{r}}\tilde{v}_z - \beta\varepsilon^2\dfrac{\partial^2\tilde{v}_z}{\partial\tilde{z}^2} &= 0, \end{cases} \tag{2.165}$$

for $\tilde{r} \in [0, 1 + \delta\tilde{U}_s)$ and $\tilde{z} \in (0, 1)$, where

$$\beta = \frac{\mu_f V_z L}{PR^2}. \tag{2.166}$$

Assuming that $1 > \beta > \mathcal{O}(\varepsilon)$ and following the procedure described in Section 2.4.2, the 0-th approximation of the fluid-structure interaction problem is

$$\begin{cases} \dfrac{1}{\tilde{r}}\dfrac{\partial}{\partial\tilde{r}}(\tilde{r}\tilde{v}_r^1) + \dfrac{\partial\tilde{v}_z^0}{\partial\tilde{z}} &= 0 \\ -\dfrac{\partial\tilde{p}^0}{\partial\tilde{r}} &= 0 \\ -\dfrac{\partial\tilde{p}^0}{\partial\tilde{z}} + \beta\Delta_{\tilde{r}}\tilde{v}_z^0 &= 0 \end{cases} \quad \text{for} \quad \tilde{r} \in [0, \tilde{\gamma}^0),\ \tilde{z} \in (0, 1). \tag{2.167}$$

The fluid-structure coupling conditions

$$\tilde{v}_z^0 = \tilde{v}_r^0 = 0 \quad \text{and} \quad \tilde{p}^0 - \tilde{P}_e = \tilde{U}_s^0 \quad \text{for} \quad \tilde{r} = \tilde{\gamma}^0 = 1 + \delta \tilde{U}_s^0, \tag{2.168}$$

together with the boundary conditions

$$\tilde{p} = \tilde{P}_0 \quad \text{for} \quad \tilde{z} = 0, \tag{2.169a}$$

$$\tilde{p} = \tilde{P}_L \quad \text{for} \quad \tilde{z} = 1, \tag{2.169b}$$

close system (2.167).

The dimensional solution for the 0-th oder problem can be computed explicitly as

$$p^0(z) = C_0(N - Mz)^{1/5} - RC_0 + P_e, \tag{2.170a}$$

$$\gamma^0(z) = (N - Mz)^{1/5}, \tag{2.170b}$$

$$v_z^0(r, z) = \frac{MC_0}{20\mu_f}(N - Mz)^{-4/5}\left((N - Mz)^{2/5} - r^2\right), \tag{2.170c}$$

$$v_r^0(r, z) = 0, \tag{2.170d}$$

for $z \in (0, L)$ and $r \in [0, \gamma^0)$, where

$$N = \left(R + \frac{P_0 - P_e}{C_0}\right)^5, \qquad M = -\frac{\left(R + \frac{P_L - P_e}{C_0}\right)^5 - N}{L}, \tag{2.171}$$

$P_0 = P\tilde{P}_0$ and $P_L = P\tilde{P}_L$. For further details on the derivation of the 0-th order solution we refer to [43]. Given the 0-th oder solution, we compute the flow as

$$\mathcal{Q}^0 = \int_{\Sigma_{lat}^f} v_z d\sigma = 2\pi \int_0^{\gamma(z)} v_r r dr = \frac{\pi M C_0}{40\mu_f}, \tag{2.172}$$

the cross-sectional area as

$$\mathcal{A}^0(z) = \pi\left(\gamma^0(z)\right)^2 = \pi(N - Mz)^{2/5}, \tag{2.173}$$

and the radial displacement as

$$U_s^0(z) = \gamma^0(z) - R = (N - Mz)^{1/5} - R. \tag{2.174}$$

The 1-st order correction of the radial velocity is obtained from (2.167) as

$$v_r^1(r, z) = \frac{M^2 C_0}{100\mu_f}\left[r^3(N - Mz)^{-9/5} - r(N - Mz)^{-7/5}\right]. \tag{2.175}$$

Comparison between techniques of model reduction

The cross-sectional averaging technique, starts from a priori assumptions that are tailored to the systems at hand, for example, the assumption that the pressure is constant on each cross-section and that $v_r = 0$. The dimensional analysis technique identifies a small parameter ε and performs a dimensional analysis of the equations to determine which terms can be neglected. Note that the choice of scaling for the physical quantities, in particular P, is critical in determining which terms can be neglected.

Using the dimensional analysis technique, with the appropriate scaling for V_z, V_r and P, we obtain that the 0-th order pressure p^0 is constant on each cross-section and that the 0-th order radial component of the velocity $v_r^0 = 0$. These are the same a-priori assumptions that are made when using the cross-sectional averaging technique. Furthermore, using the dimensional analysis technique

- we obtain that v_z^0 has a parabolic profile in the radial direction, whereas, using the cross-sectional averaging technique, the profile can be arbitrary (2.140);
- we retrieve that the radial velocity $v_r = \varepsilon v_r^1$ is not zero, whereas, using the cross-sectional averaging technique, $v_r = 0$ a priori.

Different boundary conditions are necessary to close reduced models obtained with different techniques. Using the cross-sectional averaging technique, pressure and velocity have to be known at the inlet, whereas, using the dimensional analysis technique, only pressure has to given at both inlet and outlet. Hence, depending on the specific application, one reduced model might be more appropriate to use than the other.

In conclusion, the cross-sectional averaging technique seems to be more tailored to the specific problem studied, due to the a priori assumptions. Conversely, the dimensional analysis technique might be modified and extended to study different problems, as long as we can identify a small parameter ε that characterizes the problem.

2.4.4 Test Case 2: linear elastic thick shell

In this section we derive the reduced model for the case of stationary Stokes equations 2.76 coupled with a linear elastic thick shell using the dimensional analysis technique presented in Section 2.4.2, and compare it to the linear elastic thin Koiter shell reduced model derived in Section 2.4.3.

In the stationary case, the kinematic condition (2.121) on Σ^f_{lat} can be expressed as

$$v_r = 0 \quad \text{and} \quad v_z = 0 \quad \text{for} \quad r = \gamma,\ z \in (0, L). \tag{2.176}$$

Moreover, the dynamic condition (2.129) is imposed for $s = R$ and $r = \gamma$. At the inlet and outlet fluid domain, Σ^f_0 and Σ^f_L, we require that the flow enters and leaves the domain parallel to the z axis and that the pressure are prescribed, namely

$$v_r = 0, \quad p = P_0 \qquad \text{for} \quad z = 0, \tag{2.177a}$$

$$v_r = 0, \quad p = P_L \qquad \text{for} \quad z = L. \tag{2.177b}$$

At the inlet and outlet of the solid domain Σ^w_0 and Σ^w_L, we require that the shell is clamped, namely

$$U_s = U_s = 0 \quad \text{for} \quad s = R,\ \zeta = 0, L. \tag{2.178}$$

On the external boundary of the solid domain, we impose the external pressure P_e as follows

$$\underline{\underline{\boldsymbol{S}}}\,\underline{\boldsymbol{N}} = -P_e\underline{\boldsymbol{N}} \quad \text{for} \quad s = R + h, \tag{2.179}$$

where $\underline{\boldsymbol{N}}$ is the outward normal to Σ^w_{ext}. Here, P_e is assumed to be constant.

Similarly to the thin Koiter shell case, we define the non-dimensional variables for the thick shell as

$$s = R\tilde{s}, \qquad \zeta = z = L\tilde{z}, \qquad U_s = W\tilde{U}_s, \qquad U_\zeta = W\tilde{U}_\zeta \tag{2.180}$$

and for the inlet, outlet and external pressures as

$$P_0 = P\tilde{P}_0, \qquad P_L = P\tilde{P}_L, \qquad P_e = P\tilde{P}_e. \tag{2.181}$$

In the regime of small deformations, we assume that $\delta = \dfrac{W}{R} \simeq \mathcal{O}(\varepsilon)$. Note that in this case we are not assuming a priori that U_ζ is negligible.

To choose the scaling for the pressure P, we start from the non-dimensional form of the balance of linear momentum in the direction z

$$\frac{R^2 P}{\mu_f V_z L} \frac{\partial \tilde{p}}{\partial \tilde{z}} - \Delta_{\tilde{r}} \tilde{v}_z - \varepsilon^2 \frac{\partial^2 \tilde{v}_z}{\partial \tilde{z}^2} = 0 \tag{2.182}$$

and, following [43], we choose

$$P = \frac{\mu_f V_z L}{R^2}. \tag{2.183}$$

This choice will allow us to obtain, at the 0-th order, a Poiseuille type flow.

The non-dimesionalized Stokes equations (2.158) can be written as

$$\begin{cases} \dfrac{1}{\tilde{r}} \dfrac{\partial}{\partial \tilde{r}} (\tilde{r} \tilde{v}_r) + \dfrac{\partial \tilde{v}_z}{\partial \tilde{z}} & = 0, \\ \dfrac{\partial \tilde{p}}{\partial \tilde{r}} - \varepsilon^2 \left(\Delta_{\tilde{r}} \tilde{v}_r - \dfrac{\tilde{v}_r}{\tilde{r}^2} \right) - \varepsilon^4 \dfrac{\partial^2 \tilde{v}_r}{\partial \tilde{z}^2} & = 0, \\ \dfrac{\partial \tilde{p}}{\partial \tilde{z}} - \Delta_{\tilde{r}} \tilde{v}_z - \varepsilon^2 \dfrac{\partial^2 \tilde{v}_z}{\partial \tilde{z}^2} & = 0, \end{cases} \tag{2.184}$$

for $\tilde{r} \in [0, \tilde{\gamma})$ and $\tilde{z} \in (0, 1)$. Starting from Equations (2.85) and (2.127), we can derive the non-dimensional form of the stationary balance of linear momentum for the linear elastic solid

$$\begin{cases} \left(2 + \dfrac{\lambda_w}{\mu_w}\right) \dfrac{\partial}{\partial \tilde{s}} \left[\dfrac{1}{\tilde{s}} \dfrac{\partial}{\partial \tilde{s}} \left(\tilde{s} \tilde{U}_s \right) \right] + \varepsilon \left(1 + \dfrac{\lambda_w}{\mu_w} \right) \dfrac{\partial^2 \tilde{U}_\zeta}{\partial \tilde{s} \partial \tilde{\zeta}} + \varepsilon^2 \dfrac{\partial^2 \tilde{U}_\zeta}{\partial \zeta^2} & = 0, \\ \dfrac{1}{\tilde{s}} \dfrac{\partial}{\partial \tilde{s}} \left(\tilde{s} \dfrac{\partial \tilde{U}_\zeta}{\partial \tilde{s}} \right) + \varepsilon \left(1 + \dfrac{\lambda_w}{\mu_w} \right) \dfrac{1}{\tilde{s}} \dfrac{\partial}{\partial \tilde{s}} \left(\tilde{s} \dfrac{\partial \tilde{U}_s}{\partial \tilde{\zeta}} \right) + \varepsilon^2 \left(2 + \dfrac{\lambda_w}{\mu_w} \right) \dfrac{\partial^2 \tilde{U}_\zeta}{\partial \zeta^2} & = 0, \end{cases} \tag{2.185}$$

for $\tilde{s} \in (1, 1 + h/R)$ and $\tilde{\zeta} \in (0, 1)$, and, starting from Equation (2.129), we can derive the non-dimensional form of the dynamic fluid-structure coupling condition

$$\left\{\begin{aligned}
\frac{\delta\mu_w}{RP}\left[\left(2+\frac{\lambda_w}{\mu_w}\right)\frac{\partial \tilde{U}_s}{\partial \tilde{s}} \right. & \left. +\frac{\lambda_w}{\mu_w}\frac{\tilde{U}_s}{\tilde{s}}\right] + \varepsilon\delta\frac{\lambda_w}{RP}\frac{\partial \tilde{U}_\zeta}{\partial \tilde{\zeta}} = \\
& \left(2\varepsilon^2\frac{\partial \tilde{v}_r}{\partial \tilde{r}} - \tilde{p}\right)\left(1+\delta\frac{\tilde{U}_s}{\tilde{s}}\right)\left(1+\varepsilon\delta\frac{\partial \tilde{U}_\zeta}{\partial \tilde{\zeta}}\right) \\
& -\left(\varepsilon^3\frac{\partial \tilde{v}_r}{\partial \tilde{z}} + \varepsilon\frac{\partial \tilde{v}_z}{\partial \tilde{r}}\right)\left(1+\delta\frac{\tilde{U}_s}{\tilde{s}}\right)\varepsilon\delta\frac{\partial \tilde{U}_s}{\partial \tilde{\zeta}} \\
\frac{\delta\mu_w}{RP}\left[\varepsilon\frac{\partial \tilde{U}_s}{\partial \tilde{\zeta}} + \frac{\partial \tilde{U}_\zeta}{\partial \tilde{s}}\right] & = \left(\varepsilon^3\frac{\partial \tilde{v}_r}{\partial \tilde{z}} + \varepsilon\frac{\partial \tilde{v}_z}{\partial \tilde{r}}\right)\left(1+\delta\frac{\tilde{U}_s}{\tilde{s}}\right)\left(1+\varepsilon\delta\frac{\partial \tilde{U}_\zeta}{\partial \tilde{\zeta}}\right) \\
& -\left(2\varepsilon^2\frac{\partial \tilde{v}_z}{\partial \tilde{z}} - \tilde{p}\right)\left(1+\delta\frac{\tilde{U}_s}{\tilde{s}}\right)\varepsilon\delta\frac{\partial \tilde{U}_s}{\partial \tilde{\zeta}},
\end{aligned}\right. \tag{2.186}$$

for $\tilde{s} = 1 + h/R$ and $\tilde{r} = \tilde{\gamma}$.

The 0-th approximation of fluid equations is

$$\left\{\begin{aligned}
\frac{1}{\tilde{r}}\frac{\partial}{\partial \tilde{r}}(\tilde{r}\tilde{v}_r^1) + \frac{\partial \tilde{v}_z^0}{\partial \tilde{z}} & = 0, \\
-\frac{\partial \tilde{p}^0}{\partial \tilde{r}} & = 0, \\
-\frac{\partial \tilde{p}^0}{\partial \tilde{z}} + \Delta_{\tilde{r}}\tilde{v}_z^0 & = 0,
\end{aligned}\right. \qquad \text{for} \quad \tilde{r} \in [0, \tilde{\gamma}),\ \tilde{z} \in (0, 1), \tag{2.187}$$

with the boundary conditions

$$\begin{aligned}
\tilde{p}^0 = \tilde{P}_0 \quad \tilde{v}_r = 0 \qquad & \text{for } \tilde{z} = 0, \\
\tilde{p}^0 = \tilde{P}_L \quad \tilde{v}_r = 0 \qquad & \text{for } \tilde{z} = 1.
\end{aligned} \tag{2.188}$$

The 0-th approximation of thick shell equations is

$$\left\{\begin{aligned}
\left(2+\frac{\lambda_w}{\mu_w}\right)\frac{\partial}{\partial \tilde{s}}\left(\frac{1}{\tilde{s}}\frac{\partial}{\partial \tilde{s}}\left(\tilde{s}\tilde{U}_s^0\right)\right) & = 0 \\
\frac{1}{\tilde{s}}\frac{\partial}{\partial \tilde{s}}\left(\tilde{s}\frac{\partial \tilde{U}_\zeta^0}{\partial \tilde{s}}\right) & = 0
\end{aligned}\right. \qquad \text{for} \quad \tilde{s} \in (1, 1 + h/R),\ \tilde{\zeta} \in (0, 1), \tag{2.189}$$

with the boundary conditions

$$\tilde{U}_s^0 = \tilde{U}_\zeta^0 = 0 \qquad \text{for } \tilde{\zeta} = 0, 1, \tag{2.190a}$$

$$\left(2+\frac{\lambda_w}{\mu_w}\right)\frac{\partial \tilde{U}_s^0}{\partial \tilde{s}} + \frac{\lambda_w}{\mu_w}\frac{\tilde{U}_s^0}{\tilde{s}} = -\frac{PR}{\delta\mu_w}\tilde{P}_e \qquad \text{for } \tilde{s} = 1 + h/R. \tag{2.190b}$$

They are coupled through the 0-th order kinematic interface conditions

$$\tilde{v}_r^0 = \tilde{v}_\zeta^0 = 0, \tag{2.191}$$

and dynamic interface conditions

$$\left(2 + \frac{\lambda_w}{\mu_w}\right) \frac{\partial \tilde{U}_s^0}{\partial \tilde{s}} + \frac{\lambda_w}{\mu_w} \frac{\tilde{U}_s^0}{\tilde{s}} = -\frac{PR}{\delta \mu_w} \tilde{\gamma}^0 \tilde{p}^0, \tag{2.192a}$$

$$\frac{\delta \mu_w}{RP} \frac{\partial \tilde{U}_\zeta^0}{\partial \tilde{s}} = 0, \tag{2.192b}$$

for $\tilde{s} = 1$ and $\tilde{r} = \tilde{\gamma}$. Note that Equations (2.190a) and (2.192b) imply that $\tilde{U}_\zeta^0 = 0$; hence, since $z = \zeta + U_\zeta(R, \zeta)$, we have that

$$\tilde{z} = \tilde{\zeta} + \varepsilon \cancel{\frac{\delta}{R} \tilde{U}_\zeta^0} + \mathcal{O}(\varepsilon^2) \simeq \tilde{\zeta}. \tag{2.193}$$

Following the same procedure described in [43], the dimensional solution of the 0-th order problem can be computed explicitly as

$$p^0(z) = \frac{1 - (N - Mz)^{-1/3}}{b_2}, \tag{2.194a}$$

$$\gamma^0(z) = R(1 - b_1 P_e)(N - Mz)^{1/3}, \tag{2.194b}$$

$$v_z^0(r, z) = \frac{M}{12 \mu_f b_2} (N - Mz)^{-4/3} \left(R^2 (1 - b_1 P_e)^2 (N - Mz)^{2/3} - r^2 \right), \tag{2.194c}$$

$$v_r^0(r, z) = 0, \tag{2.194d}$$

for $r \in [0, \gamma^0)$ and $z \in (0, L)$, where

$$\begin{aligned} N &= (1 - b_2 P_0)^{-3}, \quad M = \frac{N - (1 - b_2 P_L)^{-3}}{L}, \\ b_1 &= \frac{\delta}{R} (a_2 + a_3), \quad b_2 = \frac{\delta}{R} (a_1 + a_3), \end{aligned} \tag{2.195}$$

and

$$\begin{aligned} a_1 &= \frac{PR}{\delta \mu_w} \left[\frac{2h}{R} \left(2 + \frac{h}{R}\right) \left(1 + \frac{\lambda_w}{\mu_w}\right) \right]^{-1}, \\ a_2 &= a_1 \left(1 + \frac{h}{R}\right)^2, \\ a_3 &= a_1 \left(1 + \frac{\lambda_w}{\mu_w}\right) \left(1 + \frac{h}{R}\right)^2. \end{aligned} \tag{2.196}$$

Given the 0-th oder solution, we compute the flow as

$$\mathcal{Q}^0 = \frac{\pi M R^4}{24\mu_f b_2}(1 - b_1 P_e)^4, \tag{2.197}$$

the cross-sectional area as

$$\mathcal{A}^0(z) = \pi R^2 (1 - b_1 P_e)^2 (N - Mz)^{2/3}, \tag{2.198}$$

the displacement as

$$\begin{aligned} U_s^0(z) &= R(1 - b_1 P_e)(N - Mz)^{1/3} - R, \\ U_\zeta^0(z) &= 0, \end{aligned} \tag{2.199}$$

and the 1-st order correction of the radial velocity as

$$v_r^1(r, z) = \frac{M^2}{36\mu_f b_2}\left[r^3 (N - Mz)^{-7/3} - r R^2 (1 - b_1 P_e)^2 (N - Mz)^{-5/5}\right]. \tag{2.200}$$

Comparison between shell models

Contrary to Test Case 1, in Test Case 2 the shell deformation problem is not only reduced to a 0-th order fluid-structure coupling condition (2.168), but the balance of linear momentum inside the shell are non-dimensionalized (2.185) and the 0-th order problem (2.189) is solved coupled with the 0-th order Stokes equations (2.187) and the 0-th order fluid-structure coupling condition (2.192). Note that, when considering a thick shell in Test Case 2, the contribution of the external pressure acting on the external surface of the shell is treated separately as a boundary condition (2.190b) of the 0-th order structure problem. Moreover, in Test Case 2 we obtain that $U_\zeta^0 = 0$, that corresponds to the a-priori assumption made at the beginning of Section 2.4.3 in Test Case 1.

In the two Test Cases we made two different choices for the pressure scaling P, (2.164) in Test Case 1 and (2.183) in Test Case 2. These different choices were driven by the following reasons

- in Test Case 1, P was chosen in order to be able to compare the dynamic coupling condition to that used in the cross-sectional averaging method;

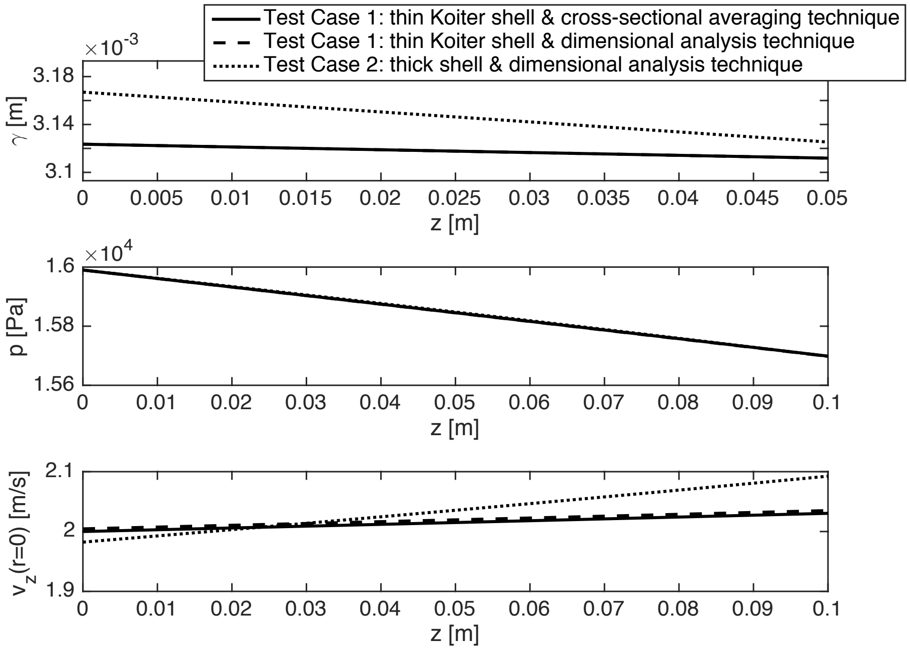

Fig. 2.8.: Comparison of the analytical solutions in Test Case 1 and Test Case 2. γ is the fluid domain deformed radius, p is the fluid pressure, $v_z(r = 0)$ is the axial fluid velocity at the centerline.

- in Test Case 2, P was chosen in order to recover Poiseuille flow.

Despite this difference, in both 0-th order solution (2.170) and (2.194), we obtain that $v_r^0 = 0$, that the pressure is constant on each cross-section, and that v_z^0 has a parabolic profile in the radial direction.

Example 4 *Comparison between Test Case 1 and Test Case 2.*

Figure 2.8 and Figure 2.9 show the deformed radius γ, fluid pressure p, axial velocity v_z and radial velocity v_r obtained in Test Case 1, using the cross-sectional average technique (2.157) (solid line) or using the dimensional analysis technique (2.170)-(2.175) (dashed line), and in Test Case 2, using the dimensional analysis technique (2.194)-(2.200) (dotted line). The solutions are obtained for $L = 0.1$ m, $R = 3.1 \times 10^{-3}$ m, $h = 0.9 \times 10^{-3}$ m, $\mu_f = 3.5 \times 10^{-3}$ kg/(m s), $\rho_f = 1050$ kg/m^3, $\lambda_w = 1.64^6$ Pa, $\mu_w = 3.35^4$ Pa, $P_0 = 15990$ Pa, $V_0 = 1$ m/s and $P_L = P_e = 15698$ Pa.

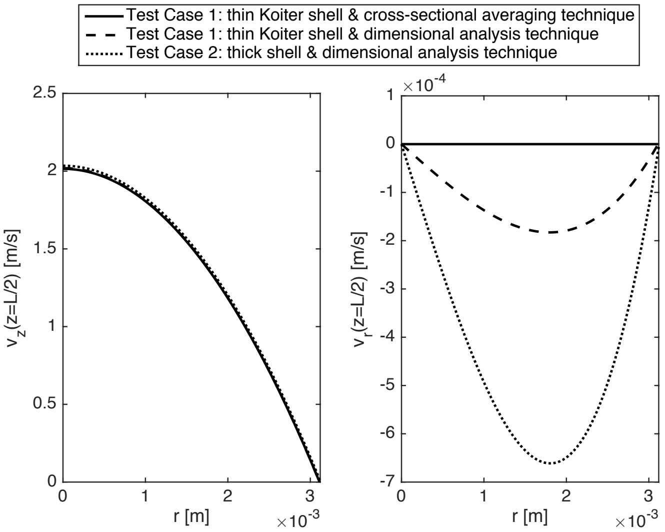

Fig. 2.9.: Comparison of the analytical solutions in Test Case 1 and Test Case 2 of the axial velocity v_z and the radial velocity v_r, evaluated at evaluated at $z = L/2$.

Comparing Test Case 1 and Test Case 2, Figure 2.8 and Figure 2.9 show that the choice of shell model and the choice of model reduction technique have

- a strong influence on the profiles of γ and v_z along the axial direction z and the profiles of v_r along the radial direction r;
- a minimal influence on the profiles of p along z and the profiles of v_z along r.

2.5 Zero-dimensional reduced model for fluid-structure interaction

In this section, we consider a zero-dimensional reduced model for fluid-structure interaction based on the analogy between vascular beds and electrical circuits. In the electrical circuit analogy model, electric potential corresponds to the fluid pressure p, current corresponds to the flow rate $\mathcal{Q}$, resistance corresponds to the *vascular resistance* $\mathcal{R}$ and capacitance corresponds to the elastic properties of the vessel, known as *compliance* $\mathcal{C}$, which is the capacity of the vessel to deform and to store fluid volume [50].

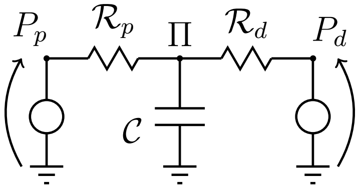

Fig. 2.10.: Three-element Windkessel model: P_p and P_d are the inlet and outlet fluid pressures, set by a generator, Π is the middle pressure, $\mathcal{R}_p$ and $\mathcal{R}_d$ are the proximal and distal resistances, and $\mathcal{C}$ is a capacitance.

The *three-element Windkessel* model, sketched in Figure 2.10, is widely used in applications to approximate fluid-structure interaction problem in hemodynamics [51–53]. In this model, a vascular segment is divided in two portions, the proximal portion and the distal portion, so that a node in the middle of the vessel is introduced and a capacitance $\mathcal{C}$ is connected to it. The fluid pressure in the middle node is denoted by Π. P_p and P_d represent the inlet and outlet fluid pressures, respectively, and $\mathcal{R}_p$ and $\mathcal{R}_d$ represent the proximal and distal resistances. Using Kirchhoff's current law, the evolution of Π in time is governed by the ordinary differential equation

$$\mathcal{C}\frac{d\Pi}{dt} = \frac{P_p - \Pi}{\mathcal{R}_p} - \frac{\Pi - P_d}{\mathcal{R}_d}. \tag{2.201}$$

Note that P_p and/or P_d could be functions of time.

There are different methods to estimate the compliance and the resistance of a vascular bed, for example, the compliance can be estimated as the product of its vascular volume and distensibility [51,54], and the resistance can be estimated using Poiseuille's law. Here we derive Poiseuille's law and the resistance formulas for rigid and compliant vessels that will be used in Chapter 3.

Consider the fluid-structure interaction problem described in Section 2.3, and assume

1. no time dependence, i.e. stationary flow;
2. negligible radial velocity, namely $v_r = 0$;
3. axial symmetry, i.e. $v_\theta = U_\vartheta = 0$ and no dependence on θ;

4. fully developed flow, namely $\dfrac{\partial v_z}{\partial z} = 0$;
5. infinitesimal displacement in the axial direction, i.e. $U_\zeta = 0$, and constant displacement in the radial direction U_s;
6. constant inlet pressure P_p and outlet pressure P_d, and a linear decrease in pressure in the axial direction z.

Under these assumptions, the Stokes equations in cylindrical coordinates (2.76) reduce to

$$\begin{cases} \dfrac{\partial p}{\partial r} = 0, \\ \dfrac{\partial p}{\partial z} = \mu_f \dfrac{1}{r}\dfrac{\partial}{\partial r}\left(r\dfrac{\partial v_z}{\partial r}\right), \end{cases} \tag{2.202}$$

where μ_f is the fluid viscosity. Note that the conservation of mass is satisfied a priori under these assumptions. The first equation of (2.202) implies that the pressure is constant on each cross-section, i.e. $p = p(z)$. Thus, assumption 6 implies that

$$\frac{\partial p}{\partial z} = \frac{dp}{dz} = \frac{P_d - P_p}{L}. \tag{2.203}$$

The second equation of (2.202) can be solved in terms of $v_z(r)$ and yields

$$v_z(r) = \frac{P_p - P_d}{4\mu_f L}(\gamma^2 - r^2), \tag{2.204}$$

where $\gamma = R + U_s$ is the deformed radius, and it is constant due to assumption 5. The corresponding flow rate $\mathcal{Q}$, which is the integral of the normal component of the velocity on the cross-section Σ, is given by

$$\mathcal{Q} = \int_\Sigma v_z d\sigma = 2\pi \int_0^\gamma \frac{P_p - P_d}{4\mu_f}(\gamma^2 - r^2) r dr = \frac{\pi\gamma^4}{8\mu_f L}(P_p - P_d), \tag{2.205}$$

hence

$$\Delta P = P_p - P_d = \frac{8\mu_f L}{\pi\gamma^4}\mathcal{Q}. \tag{2.206}$$

Equation (2.206) is known as *Poiseuille's law* and is analogous to Ohm's law for electrical circuits

$$\Delta\mathcal{V} = \mathcal{R}\mathcal{I}, \tag{2.207}$$

where $\mathcal{V}$ is the electric potential, $\mathcal{R}$ is the resistance and $\mathcal{I}$ is the current. Using this analogy, we can estimate the resistance of a vascular bed of deformed radius γ and length L as

$$\mathcal{R} = \frac{8\mu_f L}{\pi \gamma^4}. \tag{2.208}$$

Using the Windkessel model, if we assume that the vessel is rigid, then $\gamma = R$, where R is the reference radius of the fluid domain, then $\mathcal{R}_p$ and $\mathcal{R}_d$ are constant and can be approximated as

$$\mathcal{R}_p = \mathcal{R}_d \quad \text{and} \quad \mathcal{R}_p + \mathcal{R}_d = \frac{8\mu_f L}{\pi R^4}. \tag{2.209}$$

Otherwise, if we assume that the vessel is not rigid, then the deformed radius γ varies depending on the *transmural pressure difference*, which is the difference between the pressure inside the vessel and the pressure outside the vessel P_e. If the vessel walls are modeled as a thin linear elastic thin Koiter shell and if the dynamic fluid-wall interface condition (2.152) can be approximated as

$$\Pi = \tilde{C}_0 U_s + P_e, \tag{2.210}$$

where

$$\tilde{C}_0 = \frac{hE}{R^2(1-\nu^2)}, \tag{2.211}$$

then, the deformed radius γ can be written as

$$\gamma = R + U_s = R + \frac{\Pi - P_e}{\tilde{C}_0}. \tag{2.212}$$

Substituting Equation (2.212) into Equation (2.208), we obtain that $\mathcal{R}_p$ and $\mathcal{R}_d$ are variable resistances and can be approximated as

$$\mathcal{R}_p = \mathcal{R}_d \quad \text{and} \quad \mathcal{R}_p + \mathcal{R}_d = \frac{8\mu_f L}{\pi} \left(R + \frac{\Pi - P_e}{\tilde{C}_0} \right)^{-4}. \tag{2.213}$$

2.6 Multiscale coupling

When modeling a complex vasculature, such as that of the retina, it is interesting to study in detail a specific segment of the vasculature. Thus, to reduce simulations costs, a high-dimensional model can be used to simulate the segment of interest, while the rest

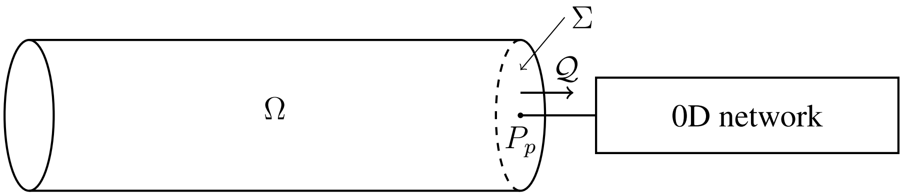

Fig. 2.11.: Sketch of multiscale coupling between a fluid domain $\Omega \subset \mathbb{R}^3$ and a zero-dimensional (0D) vascular network. Σ is the coupling surface, P_p is the nodal pressure of the network on Σ and $\mathcal{Q}$ is the flow rate in the proximal branch of the vascular network.

of the vasculature is approximated using a reduced model, such as those described in Sections 2.4 and 2.5. In this section we discuss the modeling and numerical challenges that arise when coupling the Navier-Stokes equations (2.71) in a two or three-dimensional domain to a zero-dimensional (0D) reduced model.

2.6.1 Coupling conditions

Consider a homogenous incompressible Newtonian viscous fluid in the domain $\Omega \subset \mathbb{R}^d$, with $d = 2, 3$. As described in Section 2.1.6, at any time $t \in (0, T)$ the fluid motion is described by the Navier-Stokes equations

$$\left\{ \begin{aligned} \boldsymbol{\nabla} \cdot \underline{\boldsymbol{v}} &= 0 \\ \rho \frac{\partial \underline{\boldsymbol{v}}}{\partial t} + \rho \left(\underline{\boldsymbol{v}} \cdot \boldsymbol{\nabla} \right) \underline{\boldsymbol{v}} &= \boldsymbol{\nabla} \cdot \underline{\underline{\boldsymbol{T}}} + \rho \underline{\boldsymbol{f}} \end{aligned} \right. \qquad \text{in } \Omega \times (0, T), \tag{2.214}$$

where $\underline{\underline{\boldsymbol{T}}} = -p\underline{\underline{\boldsymbol{I}}} + 2\mu\underline{\underline{\boldsymbol{D}}}$ and $\underline{\underline{\boldsymbol{D}}} = \left(\boldsymbol{\nabla}\underline{\boldsymbol{v}} + \boldsymbol{\nabla}^T\underline{\boldsymbol{v}} \right)/2$. Define $\Sigma \subset \partial\Omega$ to be the interface between the d-dimensional fluid domain and the zero-dimensional vascular network, and $P_p(t)$ to be the pressure of the vascular network at the corresponding node, as shown in Figure 2.11 for $d = 3$.

The choice of appropriate coupling conditions on Σ is essential for developing a well-posed problem that is able to reproduce the physical behavior of the system. From the physical point of view, at the interface we impose continuity of mass and of pressure.

The physical coupling conditions are translated into mathematical boundary conditions for (2.214) as follows

- the continuity of mass translates into continuity of flow, leading to the following condition on Σ
$$\int_{\Sigma} \underline{\boldsymbol{v}} \cdot \underline{\boldsymbol{n}} \, d\sigma = \mathcal{Q}, \tag{2.215}$$
where $\underline{\boldsymbol{n}}$ is the outward unit normal to Σ and $\mathcal{Q}$ is the flow rate in the proximal branch of the vascular network;

- the continuity of pressure condition requires averaging, since we are comparing the fluid pressure p, defined on $\Sigma \subset \mathbb{R}^{d-1}$, with the nodal value of pressure P_p. However, it has been shown in [55–57] that equating the average of the fluid pressure p on Σ to the nodal pressure P_p, i.e.
$$\frac{1}{|\Sigma|} \int_{\Sigma} p \, d\sigma = P_p, \tag{2.216}$$
where $|\Sigma|$ is the measure of Σ, is not sufficient to define a well-posed problem.

To derive the boundary condition that allows us to impose continuity of pressure and, at the same time, preserve the well-posedness of the Navier-Stokes equations, let us consider the contribution of the term $\boldsymbol{\nabla} \cdot \underline{\underline{\boldsymbol{T}}}$ to the variational formulation of the Navier-Stokes equations. For simplicity, let us assume that the boundary of Ω is the union of two parts, namely $\partial\Omega = \Gamma \cup \Sigma$, and that Dirichlet boundary conditions are imposed on Γ, namely

$$\underline{\boldsymbol{v}} = \underline{\boldsymbol{g}} \quad \text{on} \quad \Gamma, \tag{2.217}$$

with $\underline{\boldsymbol{g}}$ a given vectorial function of time and space. Define

$$\mathbf{V} = \mathbf{H}^1_{\Gamma}(\Omega) = \left\{ \underline{\boldsymbol{w}} \in \mathbf{H}^1(\Omega) \middle| \quad \underline{\boldsymbol{v}} = \underline{\boldsymbol{g}} \quad \text{on}\, \Gamma \right\}, \tag{2.218}$$

and

$$\mathbf{V}_0 = \mathbf{H}^1_{0,\Gamma}(\Omega) = \left\{ \underline{\boldsymbol{w}} \in \mathbf{H}^1(\Omega) \,|\quad \underline{\boldsymbol{v}} = \underline{\boldsymbol{0}} \quad \text{on}\, \Gamma \right\}. \tag{2.219}$$

For any $\underline{\boldsymbol{w}} \in \mathbf{V}_0$ we can write

$$\begin{aligned}\int_\Omega \left(\nabla \cdot \underline{\underline{\boldsymbol{T}}}\right) \cdot \underline{\boldsymbol{w}}\, d\Omega &= \int_{\partial\Omega} \underline{\boldsymbol{w}}\, \underline{\underline{\boldsymbol{T}}}\, \underline{\boldsymbol{n}}\, d\left(\partial\Omega\right) - \int_\Omega \underline{\underline{\boldsymbol{T}}} : \nabla \underline{\boldsymbol{w}}\, d\Omega \\ &= \int_\Sigma \underline{\boldsymbol{w}}\, \underline{\underline{\boldsymbol{T}}}\, \underline{\boldsymbol{n}}\, d\sigma - \int_\Omega \underline{\underline{\boldsymbol{T}}} : \nabla \underline{\boldsymbol{w}} d\Omega \\ &= \int_\Sigma \underline{\boldsymbol{w}}\, \underline{\underline{\boldsymbol{T}}}\, \underline{\boldsymbol{n}}\, d\sigma + \int_\Omega p \boldsymbol{\nabla} \cdot \underline{\boldsymbol{w}}\, d\Omega - 2\mu \int_\Omega \underline{\underline{\boldsymbol{D}}}(\underline{\boldsymbol{v}}) : \underline{\underline{\boldsymbol{D}}}(\underline{\boldsymbol{w}}) d\Omega.\end{aligned} \tag{2.220}$$

Based on (2.220), the *natural* condition to impose on Σ in order to impose continuity of pressure is

$$\underline{\underline{\boldsymbol{T}}}\, \underline{\boldsymbol{n}} = (-p\underline{\underline{\boldsymbol{I}}} + 2\mu\underline{\underline{\boldsymbol{D}}})\underline{\boldsymbol{n}} = -P_p\, \underline{\boldsymbol{n}} \quad \text{on } \Sigma. \tag{2.221}$$

Interestingly, it has been shown that this condition leads to a well-posed problem [55].

The *variational formulation* of the Navier-Stokes equations (2.214) satisfying the initial condition $\underline{\boldsymbol{v}}(t = 0) = \underline{\boldsymbol{v}}_0$ and the boundary conditions (2.217) and (2.221) can be expressed as:

Find $\underline{\boldsymbol{v}} \in L^2(0, T; \mathbf{V})$ and $p \in L^2(0, T; L^2(\Omega))$ such that for any $t \in (0, T)$

$$\begin{cases} \rho \displaystyle\int_\Omega \frac{\partial \underline{\boldsymbol{v}}}{\partial t} \cdot \underline{\boldsymbol{w}}\, d\Omega + \rho \int_\Omega \left(\underline{\boldsymbol{v}} \cdot \nabla\right) \underline{\boldsymbol{v}} \cdot \underline{\boldsymbol{w}} d\Omega - \int_\Omega p \boldsymbol{\nabla} \cdot \underline{\boldsymbol{w}}\, d\Omega + 2\mu \int_\Omega \underline{\underline{\boldsymbol{D}}}(\underline{\boldsymbol{v}}) : \underline{\underline{\boldsymbol{D}}}(\underline{\boldsymbol{w}}) d\Omega \\ \qquad\qquad = -P_p \displaystyle\int_\Sigma \underline{\boldsymbol{w}} \cdot \underline{\boldsymbol{n}}\, d\sigma + \rho \int_\Omega \underline{\boldsymbol{f}} \cdot \underline{\boldsymbol{w}} d\Omega, \\ \displaystyle\int_\Omega q \boldsymbol{\nabla} \cdot \underline{\boldsymbol{v}} d\Omega = 0, \end{cases} \tag{2.222}$$

for any $\underline{\boldsymbol{w}} \in \mathbf{V}_0$ and any $q \in L^2(\Omega)$.

Symmetric and non-symmetric formulation

In cartesian coordinates, using the incompressibility condition $\boldsymbol{\nabla} \cdot \underline{\boldsymbol{v}} = 0$, and the constitutive equation for a Newtonian fluid, the divergence of the stress tensor $\underline{\underline{\boldsymbol{T}}}$ can be expressed as

$$\nabla \cdot \underline{\underline{\boldsymbol{T}}} = \nabla \cdot (-p\underline{\underline{\boldsymbol{I}}} + 2\mu\underline{\underline{\boldsymbol{D}}}) = -\boldsymbol{\nabla} p + \mu \boldsymbol{\Delta} \underline{\boldsymbol{v}}, \tag{2.223}$$

so the Navier-Stokes equations (2.214) can be rewritten in the form

$$\left\{\begin{aligned} \boldsymbol{\nabla}\cdot\underline{\boldsymbol{v}} &= 0 \\ \rho\frac{\partial\underline{\boldsymbol{v}}}{\partial t} + \rho\left(\underline{\boldsymbol{v}}\cdot\boldsymbol{\nabla}\right)\underline{\boldsymbol{v}} &= -\boldsymbol{\nabla}p + \mu\boldsymbol{\Delta}\underline{\boldsymbol{u}} + \rho\underline{\boldsymbol{f}} \end{aligned}\right. \qquad \text{in } \Omega\times(0,T). \tag{2.224}$$

To derive the *natural* boundary condition corresponding to this new formulation, for any $\underline{\boldsymbol{w}} \in \mathbf{V}_0$, consider

$$\begin{aligned} \int_\Omega \left(-\boldsymbol{\nabla}p + \mu\boldsymbol{\Delta}\underline{\boldsymbol{v}}\right)\cdot\underline{\boldsymbol{w}}\,d\Omega = &\int_\Sigma \underline{\boldsymbol{w}}\left(-p\underline{\underline{\boldsymbol{I}}} + \mu\boldsymbol{\nabla}\underline{\boldsymbol{v}}\right)\underline{\boldsymbol{n}}\,d\sigma \\ &+ \int_\Omega p\boldsymbol{\nabla}\cdot\underline{\boldsymbol{w}}\,d\Omega - \mu\int_\Omega \boldsymbol{\nabla}\underline{\boldsymbol{v}} : \boldsymbol{\nabla}\underline{\boldsymbol{w}}d\Omega. \end{aligned} \tag{2.225}$$

Hence, using formulation (2.224), the natural condition on Σ to impose continuity of pressure can be expressed as

$$(-p\underline{\underline{\boldsymbol{I}}} + \mu\boldsymbol{\nabla}\underline{\boldsymbol{v}})\underline{\boldsymbol{n}} = -P_p\,\underline{\boldsymbol{n}} \quad \text{on } \Sigma. \tag{2.226}$$

Then, the *variational formulation* of the Navier-Stokes equations (2.224) satisfying the initial condition $\underline{\boldsymbol{v}}(t=0) = \underline{\boldsymbol{v}}_0$ and the boundary conditions (2.217) and (2.226) is:
Find $\underline{\boldsymbol{v}} \in L^2(0,T;\mathbf{V})$ and $p \in L^2(0,T;L^2(\Omega))$ such that for any $t \in (0,T)$

$$\left\{\begin{aligned} &\rho\int_\Omega \frac{\partial\underline{\boldsymbol{v}}}{\partial t}\cdot\underline{\boldsymbol{w}}\,d\Omega + \rho\int_\Omega \left(\underline{\boldsymbol{v}}\cdot\nabla\right)\underline{\boldsymbol{v}}\cdot\underline{\boldsymbol{w}}d\Omega - \int_\Omega p\boldsymbol{\nabla}\cdot\underline{\boldsymbol{w}}\,d\Omega + \mu\int_\Omega \boldsymbol{\nabla}\underline{\boldsymbol{v}} : \boldsymbol{\nabla}\underline{\boldsymbol{w}}d\Omega \\ &\qquad\qquad = -P_p\int_\Sigma \underline{\boldsymbol{w}}\cdot\underline{\boldsymbol{n}}\,d\sigma + \rho\int_\Omega \underline{\boldsymbol{f}}\cdot\underline{\boldsymbol{w}}d\Omega, \\ &\int_\Omega q\boldsymbol{\nabla}\cdot\underline{\boldsymbol{v}}d\Omega = 0, \end{aligned}\right. \tag{2.227}$$

for any $\underline{\boldsymbol{w}} \in \mathbf{V}_0$ and any $q \in L^2(\Omega)$.

The variational formulation (2.222) is called *symmetric* formulation, since it includes the symmetric part of the velocity gradient $\underline{\underline{\boldsymbol{D}}}$, and, as a consequence, the formulation (2.227) is called *non-symmetric*. The two formulations are equivalent at the continuous level, but not necessarily at the discretized level, since the numerical solution is not exactly divergence free. Moreover, the boundary conditions (2.221) and (2.226) can be interpreted in different ways

- the symmetric condition (2.221) has a physical interpretation, since it corresponds to imposing continuity of the normal stress, or traction, on Σ;
- the non-symmetric condition (2.226) has no direct interpretation from the physical point of view, however, under specific assumptions, condition (2.226) is equivalent to equating the average of the fluid pressure p on Σ to the nodal pressure P_p (2.216) as follows. Let $\underline{\boldsymbol{n}}$ be outward normal vector to Σ, let $\underline{\boldsymbol{\tau}} = (\underline{\boldsymbol{\tau}}_1, \ldots, \underline{\boldsymbol{\tau}}_{d-1})$ be $d-1$ vectors such that $(\underline{\boldsymbol{n}}, \underline{\boldsymbol{\tau}})$ is an orthogonal basis, and let

  $$v_n = \underline{\boldsymbol{v}} \cdot \underline{\boldsymbol{n}}, \qquad \underline{\boldsymbol{v}}_\tau = \underline{\boldsymbol{v}} - v_n \underline{\boldsymbol{n}}. \tag{2.228}$$

  Then, condition (2.226) can be expressed as

  $$\left(-p + \mu \frac{\partial v_n}{\partial n}\right) \underline{\boldsymbol{n}} + \mu \frac{\partial \underline{\boldsymbol{v}}_\tau}{\partial n} \underline{\boldsymbol{\tau}} = -P_p \underline{\boldsymbol{n}}, \tag{2.229}$$

  which simplifies to

  $$-p + \mu \frac{\partial v_n}{\partial n} = -P_p, \qquad \frac{\partial \underline{\boldsymbol{v}}_\tau}{\partial n} = 0. \tag{2.230}$$

  By averaging the first equation of (2.230) on Σ we obtain that

  $$\frac{1}{|\Sigma|} \int_\Sigma p \, d\sigma = P_p + \frac{\mu}{|\Sigma|} \int_\Sigma \frac{\partial v_n}{\partial n} d\sigma. \tag{2.231}$$

  If Σ is a perpendicular planar section of the domain Ω, i.e. the angle between Σ and Γ is $\pi/2$, then, using the relation $\boldsymbol{\nabla} \cdot \underline{\boldsymbol{v}} = 0$, the second term on the right-hand side of (2.231) vanishes and we obtain condition (2.216). This is not the case for the symmetric condition (2.221), for further details we refer to [55, 57].

Here, we will use the non-symmetric formulation of the Navier-Stokes equations.

Energy estimates

The energy identity that corresponds to the non-symmetric variational formulation (2.227) can be derived using the same procedure as that in Section 2.2.1, and can be written as

$$\begin{aligned}\frac{d}{dt}\left(\frac{\rho}{2}\|\underline{\boldsymbol{v}}\|^2_{L^2(\Omega)}\right) = -\mu\|\boldsymbol{\nabla}\underline{\boldsymbol{v}}\|^2_{L^2(\Omega)} &\overbrace{-\rho\int_\Sigma \frac{|\underline{\boldsymbol{v}}|^2}{2}\underline{\boldsymbol{v}}\cdot\underline{\boldsymbol{n}}\,d\sigma}^{\text{I}} \\ &\underbrace{-P_p\int_\Sigma \underline{\boldsymbol{v}}\cdot\underline{\boldsymbol{n}}\,d\sigma}_{\text{II}} + \int_\Omega \rho\underline{\boldsymbol{f}}\cdot\underline{\boldsymbol{v}}d\Omega.\end{aligned} \tag{2.232}$$

On the right-hand side, the first term corresponds to the viscous dissipation and the last term correspond to the body forces $\underline{\boldsymbol{f}}$. The Neumann boundary condition on Σ introduces two new terms in the energy identity

Term I: represents the flux of kinetic energy at the artificial boundary Σ, whose sign is not known a priori. Thus, this term is difficult to estimate and can be a source of numerical instabilities in the case of backward flows, i.e. $\underline{\boldsymbol{v}}\cdot\underline{\boldsymbol{n}} < 0$ [57–60];

Term II: depends on the network pressure P_p and can be bounded [57].

Possible solutions to Term I source of instability have been studied; below we summarize some of them.

- If we consider the Navier-Stokes formulation that involves the *total pressure*, also called *Bernoulli pressure*, defined as

  $$p_{tot} = p + \frac{\rho}{2}\underline{\boldsymbol{v}}^2, \tag{2.233}$$

  then the formulation can be shown to be stable [57, 60]. However, in blood flow application, the total stress is far from being constant on Σ [55];

- In the three dimensional case, in [60], the authors propose to insert a small three-dimensional compartment in between Ω and the vascular network, where ad-hoc modified Navier-Stokes equations are solved. The resulting system can be shown to be stable. However, in the artificial compartment the fluid is no longer incompressible and the Navier-Stokes equations are modified using three fitted parameters that mimic a three-element Windkessel model;

- If we consider the modified interface condition

$$(-p\underline{\underline{\boldsymbol{I}}} + \mu \boldsymbol{\nabla} \underline{\boldsymbol{v}})\underline{\boldsymbol{n}} = -P_p\, \underline{\boldsymbol{n}} - \rho\theta \underline{\boldsymbol{v}}\, (\underline{\boldsymbol{v}} \cdot \underline{\boldsymbol{n}})_- \quad \text{on } \Sigma, \tag{2.234}$$

  where

$$(\underline{\boldsymbol{v}} \cdot \underline{\boldsymbol{n}})_- = \begin{cases} -\underline{\boldsymbol{v}} \cdot \underline{\boldsymbol{n}} & \text{if } \underline{\boldsymbol{v}} \cdot \underline{\boldsymbol{n}} < 0, \\ 0 & \text{otherwise.} \end{cases} \tag{2.235}$$

  Then, for $\theta \geq 0.5$, the new formulation can be shown to be stable [61]. Moreover, if $\theta = 0.5$ the flux of kinetic energy at the artificial boundary Σ during back-flows is canceled and this could result in over-stabilizing physical back-flows [60].

- If using, operator splitting for the time discretization of the problem [62], the advection and diffusion terms of the Navier-Stokes equations can be solved in different steps. The advection problem, that is the source of instability, can be solved using the wave-like method, allowing it to be rewritten in a stable form. However, operator splitting introduces a splitting error and the unconditional stability of the advection problem is guaranteed only under some specific discretization assumptions.

2.6.2 Implicit and explicit coupling

In this section we summarize the main differences in treating the coupling between the fluid in the domain Ω and the 0D network implicitly or explicitly. For semplicity, let us consider the test case of Stokes flow in Ω coupled with the three-element Windkessel model described in Section 2.5.

Starting from the energy identity for the Navier-Stokes equations (2.232), we obtain that the energy identity of the Stokes flow in Ω can be expressed as

$$\frac{d}{dt}\left(\frac{\rho}{2}\|\underline{\boldsymbol{v}}\|^2_{L^2(\Omega)}\right) = -\mu\|\boldsymbol{\nabla}\underline{\boldsymbol{v}}\|^2_{L^2(\Omega)} - P_p \int_\Sigma \underline{\boldsymbol{v}} \cdot \underline{\boldsymbol{n}}\, d\sigma + \int_\Omega \rho \underline{\boldsymbol{f}} \cdot \underline{\boldsymbol{v}} d\Omega. \tag{2.236}$$

The energy identity for the Windkessel model can be written as

$$\frac{d}{dt}\left(\frac{\mathcal{C}}{2}\Pi^2\right) = -\mathcal{R}_p\mathcal{Q}^2 - \frac{1}{\mathcal{R}_d}\Pi^2 + P_p\mathcal{Q} + \frac{P_d}{\mathcal{R}_d}\Pi. \tag{2.237}$$

The identity (2.237) has been obtained by multiplying (2.201) by Π and by using the conservation of flow condition

$$\mathcal{Q} = \int_\Sigma \underline{\boldsymbol{v}} \cdot \underline{\boldsymbol{n}}\, d\sigma = \frac{P_p - \Pi}{R_p}. \tag{2.238}$$

Thus, the total energy of the coupled system is obtained by adding equations (2.236) and (2.237)

$$\frac{d}{dt}\mathcal{E}(t) = -\mathcal{D}(t) + \mathcal{F}(t), \tag{2.239}$$

where

$$\mathcal{E}(t) = \frac{\rho}{2}\|\underline{\boldsymbol{v}}\|^2_{L^2(\Omega)} + \frac{\mathcal{C}}{2}\Pi^2, \tag{2.240}$$

$$\mathcal{D}(t) = \mu\|\boldsymbol{\nabla}\underline{\boldsymbol{v}}\|^2_{L^2(\Omega)} + R_p\mathcal{Q}^2 + \frac{1}{R_d}\Pi^2, \tag{2.241}$$

$$\mathcal{F}(t) = \int_\Omega \rho\underline{\boldsymbol{f}} \cdot \underline{\boldsymbol{v}} d\Omega + \frac{P_d}{R_d}\Pi. \tag{2.242}$$

$\mathcal{E}(t)$ is the energy functional, $\mathcal{D}(t)$ is the dissipation functional and $\mathcal{F}(t)$ is the functional corresponding to the forcing terms. $\mathcal{E}(t)$ and $\mathcal{D}(t)$ are non-negative functions, while the sign of $\mathcal{F}(t)$ is not known a priori. Note that, when adding (2.236) and (2.237), the second term on the right-hand side of (2.236) cancels with the third term on the right-hand side of (2.237).

In order to understand the differences between implicit and explicit coupling, let us discretize the coupled problem in time and use a backward Euler method. Let Δt be the time step and define $t^n = n\Delta t$. Then the semi-discretized Stokes problem is:

Given $\underline{\boldsymbol{v}}^0 = \underline{\boldsymbol{v}}_0$ and $\Pi^0 = \Pi_0$, for any $n > 0$ find $\underline{\boldsymbol{v}}^{n+1} \in \mathbf{V}$, $p^{n+1} \in L^2(\Omega)$ and Π^{n+1} such that

$$\begin{aligned}\frac{\rho}{\Delta t}\int_\Omega \underline{\boldsymbol{v}}^{n+1} \cdot \underline{\boldsymbol{w}}\, d\Omega - \int_\Omega p^{n+1}\boldsymbol{\nabla} \cdot \underline{\boldsymbol{w}}\, d\Omega - \int_\Omega q\boldsymbol{\nabla} \cdot \underline{\boldsymbol{v}}^{n+1} d\Omega + \mu\int_\Omega \boldsymbol{\nabla}\underline{\boldsymbol{v}}^{n+1} : \boldsymbol{\nabla}\underline{\boldsymbol{w}} d\Omega \\ + \left[\Pi^* + \mathcal{R}_p\left(\int_\Sigma \underline{\boldsymbol{v}}^* \cdot \underline{\boldsymbol{n}}\, d\sigma\right)\right]\left(\int_\Sigma \underline{\boldsymbol{w}} \cdot \underline{\boldsymbol{n}}\, d\sigma\right) = \\ \int_\Omega \rho\underline{\boldsymbol{f}}^{n+1} \cdot \underline{\boldsymbol{w}} d\Omega + \frac{\rho}{\Delta t}\int_\Omega \underline{\boldsymbol{v}}^n \cdot \underline{\boldsymbol{w}}\, d\Omega,\end{aligned} \tag{2.243}$$

for any $\underline{\boldsymbol{w}} \in \mathbf{V}_0$ and any $q \in L^2(\Omega)$. Similarly, the semi-discretized Windkessel Equation (2.201) can be expressed as

$$\frac{\mathcal{C}}{\Delta t}\Pi^{n+1} = \int_{\Sigma} \underline{\boldsymbol{v}}^* \cdot \underline{\boldsymbol{n}}\, d\sigma - \frac{\Pi^{n+1} - P_d}{\mathcal{R}_d} + \frac{\mathcal{C}}{\Delta t}\Pi^n. \tag{2.244}$$

The coupling is *implicit* if

$$(\cdot)^* = (\cdot)^{n+1}, \tag{2.245}$$

leading to a monolithic approach, otherwise if

$$(\cdot)^* = (\cdot)^n, \tag{2.246}$$

the coupling is *explicit*.

From the energy point of view, if the coupling is implicit, the energy identity at the continuous level (2.242) is preserved also at the discrete level [52]. Contrary to implicit coupling, explicit coupling introduces an artificial uncontrolled term in the energy identity at the discrete level, that does not guarantee stability [52,58]. Indeed, the implicitly coupled problem is unconditionally stable, hence there are no restrictions on Δt. Conversely, the stability of the explicitly coupled scheme depends on Δt via a Courant-Friedrichs-Lewy (CFL) condition that depends on the values of resistances and compliances in the vascular network [58].

Moreover, in the finite element framework, the following term of (2.243)

$$\mathcal{R}_p \left(\int_{\Sigma} \underline{\boldsymbol{v}}^* \cdot \underline{\boldsymbol{n}}\, d\sigma \right) \left(\int_{\Sigma} \underline{\boldsymbol{w}} \cdot \underline{\boldsymbol{n}}\, d\sigma \right) \tag{2.247}$$

has different contributions to the corresponding algebraic system in the case of explicit or implicit coupling. In the explicit case, it contributes to the right-hand side of the algebraic system, while in the implicit case, it changes the pattern of the matrix of the algebraic system, namely the number of nonzero entries in each line is higher. This new matrix structure could influence the behavior of direct and iterative solvers [63].

2.6.3 Operator splitting schemes

In this section, we summarize the details of operator splitting schemes, which are designed to take advantage of linear decompositions of operators. This is the case for the multiscale coupled problems studied in Section 2.6, where the system can be decomposed into two or more subproblems, one represented by the fluid flow in the domain Ω and one represented by the zero-dimensional vascular network.

Consider the initial value problem

$$\begin{cases} \dfrac{\partial \phi}{\partial t} + \mathcal{A}(\phi, t) = 0, \\ \phi(t=0) = \phi_0, \end{cases} \tag{2.248}$$

where $\mathcal{A}$ is an operator from a Hilbert space $\mathbf{H}$ to itself and $\phi \in H$. Let us assume that $\mathcal{A}$, possibly nonlinear, can be nontrivially decomposed as $\mathcal{A} = \mathcal{A}_1 + \mathcal{A}_2$. We present below a splitting scheme that takes advantage of the decomposition of the operator $\mathcal{A}$ and is optimal in the cases where $\mathcal{A}_1$ and $\mathcal{A}_2$ have different mathematical properties. For further details on operator splitting schemes we refer to [62].

Consider the time discretization $\Delta t > 0$ and let $t^n = n\Delta t$. The *first-order* operator splitting scheme consists of sequentially solving two sub-steps as follow:
Given ϕ^0, for every $n \geq 0$

Step 1 given ϕ^n, solve the initial value problem

$$\begin{cases} \dfrac{\partial \phi}{\partial t} + \mathcal{A}_1(\phi, t) = 0 \\ \phi(t = t^n) = \phi^n \end{cases} \quad \text{in } (t^n, t^{n+1}) \tag{2.249a}$$

and set $\phi^{n+1/2} = \phi(t^{n+1})$;

Step 2 given $\phi^{n+1/2}$, solve the initial value problem

$$\begin{cases} \dfrac{\partial \phi}{\partial t} + \mathcal{A}_2(\phi, t^{n+1}) = 0 \\ \phi(t = t^n) = \phi^{n+1/2} \end{cases} \quad \text{in } (t^n, t^{n+1}) \tag{2.249b}$$

and set $\phi^{n+1} = \phi(t^{n+1})$.

Note that Step 1 and 2 are not discretized in time, hence a different time discretization scheme and a different time step might be chosen in the interval (t^n, t^{n+1}) for each sub-step. If $\mathcal{A}_1$ and $\mathcal{A}_2$ are linear operators, independent of t and commutative, then the scheme (2.249) can be shown to be exact, otherwise it is, at most, first-order accurate in time.

The splitting scheme presented above can be modified in order to reach *second-order* convergence in time in the following way:
Given ϕ^0, for every $n \geq 0$

Step 1 given ϕ^n, solve the initial value problem

$$\begin{cases} \dfrac{\partial \phi}{\partial t} + \mathcal{A}_1(\phi, t) = 0 \\ \phi(t = t^n) = \phi^n \end{cases} \quad \text{in } (t^n, t^{n+1/2}) \tag{2.250a}$$

and set $\phi^{n+1/2} = \phi(t^{n+1})$;

Step 2 given $\phi^{n+1/2}$, solve the initial value problem

$$\begin{cases} \dfrac{\partial \phi}{\partial t} + \mathcal{A}_2(\phi, t^{n+1/2}) = 0 \\ \phi(t = 0) = \phi^{n+1/2} \end{cases} \quad \text{in } (0, \Delta t) \tag{2.250b}$$

and set $\hat{\phi}^{n+1/2} = \phi(\Delta t)$;

Step 3 given $\hat{\phi}^{n+1/2}$, solve the initial value problem

$$\begin{cases} \dfrac{\partial \phi}{\partial t} + \mathcal{A}_1(\phi, t) = 0 \\ \phi(t = t^{n+1/2}) = \hat{\phi}^{n+1/2} \end{cases} \quad \text{in } (t^{n+1/2}, t^{n+1}) \tag{2.250c}$$

and set $\phi^{n+1} = \phi(t^{n+1})$.

If the dependence of $\mathcal{A}_1$ and $\mathcal{A}_2$ on ϕ and t is sufficiently smooth, and every subproblem is discretized in time with second order schemes, then this operator splitting scheme can be shown to be second order accurate in time. Since the operator $\mathcal{A}_1$ is solved twice, in Step 1 and 3, it should be chosen to be the easiest one to solve among the two operators.

The schemes presented in this sections can be easily extended to the case where the operator $\mathcal{A} = \sum_{i=1}^{k} \mathcal{A}_i$ for $k > 2$ [62]. This might be useful in the case of Navier-Stokes equations in Ω coupled with a zero-dimensional vascular network, because, besides splitting the fluid flow in Ω from the zero-dimensional network, we could also split the advective term from the diffusive term in Navier-Stokes equations [62, 64–66].

3. MATHEMATICAL MODELS OF CENTRAL RETINAL VESSELS AND RETINAL HEMODYNAMICS

In this chapter we present a mathematical model that simulates the mechanical deformation of the lamina cribrosa in combination with the blood flow through the vessels that supply and drain the retina [67–69]. A schematic representation of the system described by our mathematical model is depicted in Figure 3.1.

In Section 3.1, the lamina cribrosa is modeled as a weakly-nonlinear, homogeneous, elastic circular plate of finite thickness, which deforms under the combined action of IOP, RLTp, and tension from the sclera, in the same spirit of previous studies [25, 26, 28, 29]. In Section 3.2, the central retinal vessels (CRA and CRV) are modeled as a fluid-structure interaction system, where blood flow is modeled as the stationary Stokes flow of a Newtonian viscous fluid, and the arterial wall is modeled as a linear elastic cylindrical thick shell. The walls of the CRA and CRV deform under the action of IOP, RLTp, and the presence of the lamina cribrosa. In Section 3.3, the vessels upstream of the CRA, the vessels downstream of the CRV, and the retinal microcirculation are modeled as zero-dimensional networks of resistances via the electric analogy described in Section 2.5, as in [51]. In Section 3.5, the predictions of the mathematical model are presented and validated using four different and unrelated experimental and clinical studies. The model results elucidate the mechanisms through which changes in IOP, CSFp and mean arterial pressure (MAP) affect the hemodynamics in the central retinal artery and vein. In Section 3.6 the relevance of the model predictions to the pathophysiology of glaucoma is discussed.

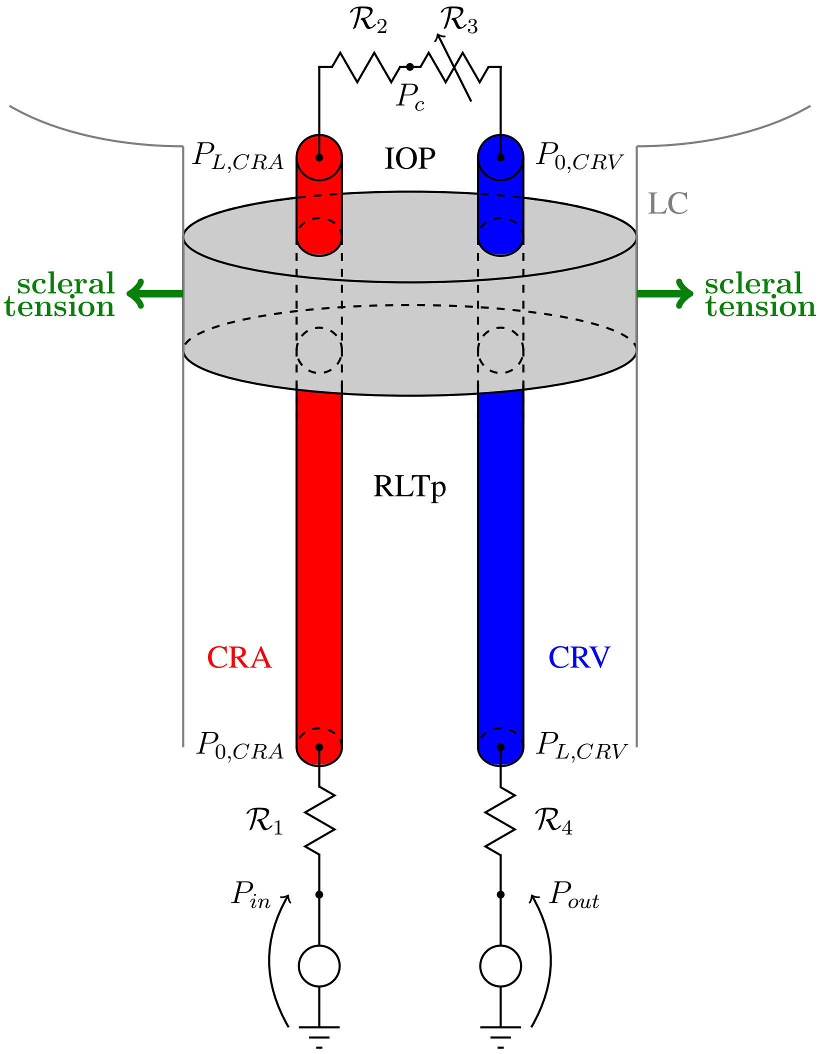

Fig. 3.1.: Schematic representation of the mathematical model that couples the deformation of the lamina cribrosa (LC) with the hemodynamics in the central retinal artery and central retinal vein (CRA and CRV). The lamina deformations are due to the intraocular pressure (IOP), the retrolaminar tissue pressure (RLTp) and the tension of the sclera. The CRA and CRV are connected to the arterial and venous systems, respectively, and to each other via a network of resistances, $\mathcal{R}_1$, $\mathcal{R}_2$, $\mathcal{R}_3$ and $\mathcal{R}_4$. P_{in} and P_{out} are the input and output pressures of the model (set by a generator), $P_{0,i}$ and $P_{L,i}$ are the inlet and outlet pressure of the central retinal vessels for $i = CRA,\ CRV$, and P_c is the outlet pressure of the retinal capillaries.

3.1 Lamina cribrosa model

The lamina cribrosa is modeled as a weakly-nonlinear, homogeneous, elastic circular plate of radius R_{LC} and finite thickness h_{LC}. In the small deformations regime, the lamina satisfies the balance of linear momentum (2.82)

$$\boldsymbol{\nabla} \cdot \underline{\underline{\boldsymbol{S}}} = \underline{\boldsymbol{0}} \quad \text{in } \Omega_{LC} \subset \mathbb{R}^3. \tag{3.1}$$

In cylindrical coordinates, the domain Ω_{LC} can be written as

$$\Omega_{LC} = \left\{ (s\cos\theta, s\sin\theta, \zeta) \in \mathbb{R}^3 \, : \, s \in [0, R_{LC}), \, \theta \in [0, 2\pi), \, \zeta \in \left(-\frac{h_{LC}}{2}, \frac{h_{LC}}{2} \right) \right\},$$

where $\{s, \theta, \zeta\}$ denote the radial, azimuthal and axial Lagrangian coordinates, respectively. A sketch of the domain is provided in Figure 3.2. We remark that our geometric representation of the lamina does not account for the central perforation which allows the passage of the central retinal vessels. However, Sigal et al. showed that this perforation has no significant effect on the stresses and strains within the lamina [30].

The elastic constitutive equation for the second Piola-Kirchhoff stress tensor (2.80) for the lamina cribrosa is given by

$$\underline{\underline{\boldsymbol{S}}}\left(\underline{\underline{\gamma}}\right) = \lambda_{LC} \operatorname{tr}\left(\underline{\underline{\gamma}}\right) \underline{\underline{\boldsymbol{I}}} + 2\mu_{LC}\, \underline{\underline{\gamma}} \tag{3.2}$$

and incorporates

1. *geometric nonlinearities*: the strain tensor $\underline{\underline{\gamma}}$, defined in (2.49), includes quadratic terms in the derivatives of the displacement, and can be decomposed as the sum of a linear part $\underline{\underline{\boldsymbol{E}}}$ and non-linear part $\underline{\underline{\boldsymbol{N}}}$ as follows

$$\underline{\underline{\gamma}}(\underline{\boldsymbol{U}}) = \underline{\underline{\boldsymbol{E}}}(\underline{\boldsymbol{U}}) + \underline{\underline{\boldsymbol{N}}}(\underline{\boldsymbol{U}}, \underline{\boldsymbol{U}}), \tag{3.3}$$

   where $\underline{\boldsymbol{U}}$ is the displacement and

$$\begin{aligned} \underline{\underline{\boldsymbol{E}}}\,(\underline{\boldsymbol{W}}) &:= \frac{1}{2}\left[\boldsymbol{\nabla}\underline{\boldsymbol{W}} + (\boldsymbol{\nabla}\underline{\boldsymbol{W}})^T \right], \\ \underline{\underline{\boldsymbol{N}}}\,(\underline{\boldsymbol{W}}, \underline{\boldsymbol{Y}}) &:= \frac{1}{4}\left[(\boldsymbol{\nabla}\underline{\boldsymbol{W}})^T\, \boldsymbol{\nabla}\underline{\boldsymbol{Y}} + (\boldsymbol{\nabla}\underline{\boldsymbol{Y}})^T\, \boldsymbol{\nabla}\underline{\boldsymbol{W}} \right]. \end{aligned} \tag{3.4}$$

   Note that $\underline{\underline{\boldsymbol{N}}}$ is symmetric with respect to $\underline{\boldsymbol{W}}$ and $\underline{\boldsymbol{Y}}$, namely

$$\underline{\underline{\boldsymbol{N}}}\,(\underline{\boldsymbol{W}}, \underline{\boldsymbol{Y}}) = \underline{\underline{\boldsymbol{N}}}\,(\underline{\boldsymbol{Y}}, \underline{\boldsymbol{W}})\,; \tag{3.5}$$

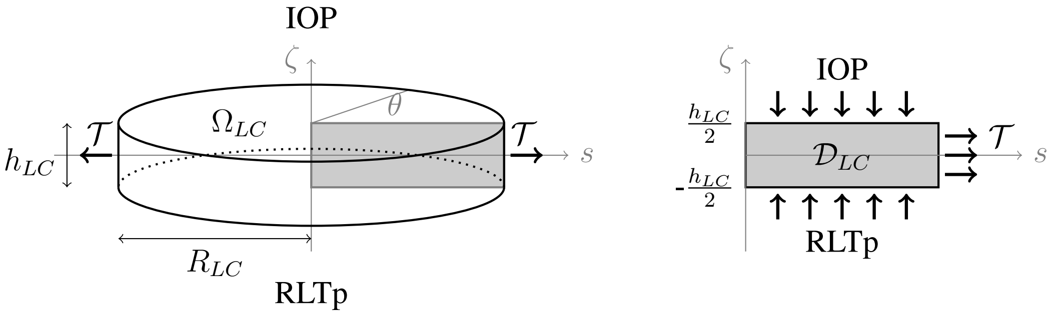

Fig. 3.2.: Schematic representation of geometry and boundary conditions of the elasticity problem for the lamina cribrosa. The lamina cribrosa domain Ω_{LC} is a circular plate of radius R_{LC} and finite thickness h_{LC}. The anterior surface ($\zeta = h_{LC}/2$) is subject to the intraocular pressure (IOP), while the posterior surface ($\zeta = -h_{LC}/2$) is subject to the retrolaminar tissue pressure (RLTp). The lateral surface ($s = R_{LC}$) is connected to the sclera and experiences the scleral tension $\mathcal{T}$. Under the assumption of axial symmetry, the domain can be restricted to the rectangular region $\mathcal{D}_{LC}$ on the right.

2. *material nonlinearities*: the Lamé parameters λ_{LC} and μ_{LC} vary with the effective stress σ_e [29, 70], as reported in Table 3.1. The effective stress is defined as

$$\sigma_e = f(\underline{\underline{\boldsymbol{S}}}) = \sqrt{\frac{3}{2}\mathrm{tr}\left(\left(\underline{\underline{\boldsymbol{S}}} - \frac{1}{3}\mathrm{tr}\left(\underline{\underline{\boldsymbol{S}}}\right)\underline{\underline{\boldsymbol{I}}}\right)\left(\underline{\underline{\boldsymbol{S}}} - \frac{1}{3}\mathrm{tr}\left(\underline{\underline{\boldsymbol{S}}}\right)\underline{\underline{\boldsymbol{I}}}\right)^{T}\right)}, \tag{3.6}$$

   and the formula

$$\lambda_{LC} = \frac{\mu_{LC}(E_{LC} - 2\mu_{LC})}{3\mu_{LC} - E_{LC}} \tag{3.7}$$

   is used to relate λ_{LC}, the Young's modulus E_{LC}, and the shear modulus μ_{LC}.

The anterior surface of the lamina cribrosa faces the eye globe and is subject to the intraocular pressure, while the posterior surface faces the optic nerve canal and is subject to the retrolaminar tissue pressure. As a result, we impose the following boundary conditions:

$$\begin{aligned} \underline{\underline{\boldsymbol{S}}}\,\underline{\boldsymbol{N}}_a &= -\mathrm{IOP}\,\underline{\boldsymbol{N}}_a \quad \text{for } \zeta = \frac{h_{LC}}{2}, \\ \underline{\underline{\boldsymbol{S}}}\,\underline{\boldsymbol{N}}_p &= -\mathrm{RLTp}\,\underline{\boldsymbol{N}}_p \quad \text{for } \zeta = -\frac{h_{LC}}{2}, \end{aligned} \tag{3.8}$$

Table 3.1.: Values of the Young's modulus E_{LC} and shear modulus μ_{LC} in the model for the lamina cribrosa as a function of the effective stress σ_e [29, 70].

E_{LC} [MPa]	μ_{LC} [MPa]	Range of σ_e [MPa]
0.358	0.12	$0.000 < \sigma_e < 0.008$
0.656	0.22	$0.008 < \sigma_e < 0.015$
1.818	0.61	$0.015 < \sigma_e$

where $\underline{\boldsymbol{N}}_a = \underline{\boldsymbol{e}}_\zeta$ and $\underline{\boldsymbol{N}}_p = -\underline{\boldsymbol{e}}_\zeta$ denote the outward normal vectors to the anterior and posterior surfaces, respectively. On its lateral surface, the lamina cribrosa is connected to the sclera and experiences the scleral tension $\mathcal{T}$, which results from the scleral inflation due to the intraocular pressure. Following [26, 29], on the lateral surface we impose that

$$\underline{\boldsymbol{N}}_l^T \, \underline{\underline{\boldsymbol{S}}} \, \underline{\boldsymbol{N}}_l = \mathcal{T} \quad \text{and} \quad U_\zeta = 0 \quad \text{for } s = R_{LC}, \tag{3.9}$$

where $\underline{\boldsymbol{N}}_l = \underline{\boldsymbol{e}}_s$ is the outward normal vector to the lateral surface, and $\mathcal{T}$ is computed using Laplace's law

$$\mathcal{T} = \frac{\text{IOP } R_s}{2h_s}, \tag{3.10}$$

where R_s and h_s are the scleral radius and thickness, respectively. Here we assume that the sclera can be modeled as a perfect sphere.

Taking advantage of the symmetry in the geometry and boundary conditions, the problem is simplified by assuming that its solutions are axial symmetric. This consists in assuming zero azimuthal displacement, i.e. $U_\theta = 0$, and radial and axial displacements independent of azimuthal angle θ, i.e. $U_s = U_s(s,\zeta)$ and $U_\zeta = U_\zeta(s,\zeta)$. Under these assumptions, the equilibrium equations (3.1) reduce to

$$\begin{aligned} \frac{S_{ss} - S_{\theta\theta}}{s} + \frac{\partial S_{ss}}{\partial s} + \frac{\partial S_{s\zeta}}{\partial \zeta} &= 0, \\ \frac{S_{\zeta s}}{s} + \frac{\partial S_{\zeta s}}{\partial s} + \frac{\partial S_{\zeta\zeta}}{\partial \zeta} &= 0, \end{aligned} \tag{3.11}$$

defined on the rectangular domain

$$\mathcal{D}_{LC} = (0, R_{LC}) \times (-h_{LC}/2, h_{LC}/2) \tag{3.12}$$

depicted in Figure 3.2 (right), with the boundary conditions

$$\begin{aligned}
&S_{\zeta\zeta} = -\text{IOP}, && S_{s\zeta} = 0 \quad \text{for} \quad s \in (0, R_{LC}),\ \zeta = \frac{h_{LC}}{2},\\
&S_{\zeta\zeta} = -\text{RLTp}, && S_{s\zeta} = 0 \quad \text{for} \quad s \in (0, R_{LC}),\ \zeta = -\frac{h_{LC}}{2},\\
&S_{ss} = \mathcal{T}, && U_{\zeta} = 0 \quad \text{for} \quad s = R_{LC},\ \zeta \in \left(-\frac{h_{LC}}{2}, \frac{h_{LC}}{2}\right),\\
&U_s = 0, && \frac{\partial U_\zeta}{\partial s} = 0 \quad \text{for} \quad s = 0,\ \zeta \in \left(-\frac{h_{LC}}{2}, \frac{h_{LC}}{2}\right).
\end{aligned} \tag{3.13}$$

The components S_{ss}, $S_{\theta\theta}$, $S_{s\zeta}$, and $S_{\zeta\zeta}$ of the stress tensor can be written in terms of the components of the linear and non-linear parts $\underline{\underline{\boldsymbol{E}}}$ and $\underline{\underline{\boldsymbol{N}}}$ of the strain tensor $\underline{\underline{\gamma}}$ as

$$\begin{aligned}
S_{ss} &= 2\mu_{LC}\left(E_{ss}(\underline{\boldsymbol{U}}) + N_{ss}(\underline{\boldsymbol{U}}, \underline{\boldsymbol{U}})\right) + \lambda_{LC}\left[\text{tr}\left(\underline{\underline{\boldsymbol{E}}}(\underline{\boldsymbol{U}})\right) + \text{tr}\left(\underline{\underline{\boldsymbol{N}}}(\underline{\boldsymbol{U}}, \underline{\boldsymbol{U}})\right)\right],\\
S_{\theta\theta} &= 2\mu_{LC}\left(E_{\theta\theta}(\underline{\boldsymbol{U}}) + N_{\theta\theta}(\underline{\boldsymbol{U}}, \underline{\boldsymbol{U}})\right) + \lambda_{LC}\left[\text{tr}\left(\underline{\underline{\boldsymbol{E}}}(\underline{\boldsymbol{U}})\right) + \text{tr}\left(\underline{\underline{\boldsymbol{N}}}(\underline{\boldsymbol{U}}, \underline{\boldsymbol{U}})\right)\right],\\
S_{\zeta\zeta} &= 2\mu_{LC}\left(E_{\zeta\zeta}(\underline{\boldsymbol{U}}) + N_{\zeta\zeta}(\underline{\boldsymbol{U}}, \underline{\boldsymbol{U}})\right) + \lambda_{LC}\left[\text{tr}\left(\underline{\underline{\boldsymbol{E}}}(\underline{\boldsymbol{U}})\right) + \text{tr}\left(\underline{\underline{\boldsymbol{N}}}(\underline{\boldsymbol{U}}, \underline{\boldsymbol{U}})\right)\right],\\
S_{\zeta s} &= S_{s\zeta} = 2\mu_{LC}\left(E_{s\zeta}(\underline{\boldsymbol{U}}) + N_{s\zeta}(\underline{\boldsymbol{U}}, \underline{\boldsymbol{U}})\right),
\end{aligned} \tag{3.14}$$

where tr $(\cdot) = (\cdot)_{ss} + (\cdot)_{\theta\theta} + (\cdot)_{\zeta\zeta}$,

$$\begin{aligned}
E_{ss}(\underline{\boldsymbol{U}}) &= \frac{\partial U_s}{\partial s}, \quad E_{\theta\theta}(\underline{\boldsymbol{U}}) = \frac{U_s}{s},\\
E_{\zeta\zeta}(\underline{\boldsymbol{U}}) &= \frac{\partial U_\zeta}{\partial \zeta}, \quad E_{s\zeta}(\underline{\boldsymbol{U}}) = \frac{1}{2}\left[\frac{\partial U_s}{\partial \zeta} + \frac{\partial U_\zeta}{\partial s}\right],
\end{aligned} \tag{3.15}$$

and

$$\begin{aligned}
N_{ss}(\underline{\boldsymbol{W}}, \underline{\boldsymbol{Y}}) &= \frac{1}{2}\left[\frac{\partial W_s}{\partial s}\frac{\partial Y_s}{\partial s} + \frac{\partial W_\zeta}{\partial s}\frac{\partial Y_\zeta}{\partial s}\right], \quad N_{\theta\theta}(\underline{\boldsymbol{W}}, \underline{\boldsymbol{Y}}) = \frac{1}{2}\left[\frac{W_s}{s}\frac{Y_s}{s}\right],\\
N_{\zeta\zeta}(\underline{\boldsymbol{W}}, \underline{\boldsymbol{Y}}) &= \frac{1}{2}\left[\frac{\partial W_s}{\partial \zeta}\frac{\partial Y_s}{\partial \zeta} + \frac{\partial W_\zeta}{\partial \zeta}\frac{\partial Y_\zeta}{\partial \zeta}\right], \quad N_{s\zeta}(\underline{\boldsymbol{W}}, \underline{\boldsymbol{Y}}) = \frac{1}{2}\left[\frac{\partial W_s}{\partial \zeta}\frac{\partial Y_s}{\partial s} + \frac{\partial W_\zeta}{\partial \zeta}\frac{\partial Y_\zeta}{\partial s}\right].
\end{aligned} \tag{3.16}$$

Let us now introduce the following functional space

$$\mathbf{V} = \left\{\underline{\boldsymbol{W}} \in \left(H^1(\mathcal{D}_{LC})\right)^2 \,:\, W_\zeta\Big|_{s=R_{LC}} = 0,\ W_s\Big|_{s=0} = 0\right\}. \tag{3.17}$$

To obtain the variational formulation of the lamina cribrosa problem, we consider the L^2 product between the balance of linear momentum (3.1) and a test function $\underline{\boldsymbol{W}} = (W_s, Y_\zeta) \in \mathbf{V}$

$$0 = \int_{\mathcal{D}_{LC}} \Big(\boldsymbol{\nabla} \cdot \underline{\underline{\boldsymbol{S}}}(\underline{\boldsymbol{U}})\Big) \cdot \underline{\boldsymbol{W}} d\mathcal{D} = -\int_{\mathcal{D}_{LC}} \underline{\underline{\boldsymbol{S}}}(\underline{\boldsymbol{U}}) : \boldsymbol{\nabla} \underline{\boldsymbol{W}} d\mathcal{D} + \int_{\partial\mathcal{D}_{LC}} \underline{\boldsymbol{W}} \cdot \underline{\underline{\boldsymbol{S}}}(\underline{\boldsymbol{U}}) \cdot \underline{\boldsymbol{N}} d(\partial\mathcal{D}), \tag{3.18}$$

where $\underline{\boldsymbol{N}}$ is the outward normal vector to the boundary of $\mathcal{D}_{LC}$.

Using the definition of $\underline{\underline{\boldsymbol{S}}}$ and its symmetry, the first term on the right-hand side of Equation (3.18) can be expressed as

$$\begin{aligned}
\int_{\mathcal{D}_{LC}} \underline{\underline{\boldsymbol{S}}}(\underline{\boldsymbol{U}}) : \boldsymbol{\nabla} \underline{\boldsymbol{W}} d\mathcal{D} &= \int_{\mathcal{D}_{LC}} \lambda_{LC} \operatorname{tr}\Big(\underline{\underline{\boldsymbol{E}}}(\underline{\boldsymbol{U}}) + \underline{\underline{\boldsymbol{N}}}(\underline{\boldsymbol{U}}, \underline{\boldsymbol{U}})\Big) \underline{\underline{\boldsymbol{I}}} : \boldsymbol{\nabla} \underline{\boldsymbol{W}} d\mathcal{D} \\
&+2 \int_{\mathcal{D}_{LC}} \mu_{LC} \Big(\underline{\underline{\boldsymbol{E}}}(\underline{\boldsymbol{U}}) + \underline{\underline{\boldsymbol{N}}}(\underline{\boldsymbol{U}}, \underline{\boldsymbol{U}})\Big) : \boldsymbol{\nabla} \underline{\boldsymbol{W}} d\mathcal{D} \\
&= \int_0^{R_{LC}} \int_{-\frac{h_{LC}}{2}}^{\frac{h_{LC}}{2}} \lambda_{LC} \operatorname{tr}\Big(\underline{\underline{\boldsymbol{E}}}(\underline{\boldsymbol{U}}) + \underline{\underline{\boldsymbol{N}}}(\underline{\boldsymbol{U}}, \underline{\boldsymbol{U}})\Big) \underline{\underline{\boldsymbol{I}}} : \underline{\underline{\boldsymbol{E}}}(\underline{\boldsymbol{W}}) \; s \, ds \, d\zeta \\
&+2 \int_0^{R_{LC}} \int_{-\frac{h_{LC}}{2}}^{\frac{h_{LC}}{2}} \mu_{LC} \Big(\underline{\underline{\boldsymbol{E}}}(\underline{\boldsymbol{U}}) + \underline{\underline{\boldsymbol{N}}}(\underline{\boldsymbol{U}}, \underline{\boldsymbol{U}})\Big) : \underline{\underline{\boldsymbol{E}}}(\underline{\boldsymbol{W}}) \; s \, ds \, d\zeta,
\end{aligned} \tag{3.19}$$

and, using the boundary conditions (3.13), the second term on the right-hand side of Equation (3.18) can be expressed as

$$\begin{aligned}
\int_{\partial\mathcal{D}_{LC}} \underline{\boldsymbol{W}} \cdot \underline{\underline{\boldsymbol{S}}}(\underline{\boldsymbol{U}}) \cdot \underline{\boldsymbol{N}} d(\partial\mathcal{D}) &= -\int_0^{R_{LC}} \text{IOP}\, W_\zeta \Big|_{\zeta = h_{LC}/2} s \, ds \\
&+ \int_0^{R_{LC}} \text{RLTp}\, W_\zeta \Big|_{\zeta = -h_{LC}/2} s \, ds \\
&+ \int_{-\frac{h_{LC}}{2}}^{\frac{h_{LC}}{2}} R_{LC} \, \mathcal{T} \, W_s \Big|_{s = R_{LC}} d\zeta.
\end{aligned} \tag{3.20}$$

Then, we obtain the *variational formulation* of the lamina cribrosa problem:
Find $\underline{\boldsymbol{U}} = (U_s, U_\zeta) \in \mathbf{V}$ such that

$$
\begin{aligned}
&\int_0^{R_{LC}} \int_{-\frac{h_{LC}}{2}}^{\frac{h_{LC}}{2}} \lambda_{LC} \mathrm{tr} \left(\underline{\underline{\boldsymbol{E}}}(\underline{\boldsymbol{U}}) + \underline{\underline{\boldsymbol{N}}}(\underline{\boldsymbol{U}}, \underline{\boldsymbol{U}}) \right) \underline{\underline{\boldsymbol{I}}} : \underline{\underline{\boldsymbol{E}}}(\underline{\boldsymbol{W}}) \; s \, ds \, d\zeta \\
&+2 \int_0^{R_{LC}} \int_{-\frac{h_{LC}}{2}}^{\frac{h_{LC}}{2}} \mu_{LC} \left(\underline{\underline{\boldsymbol{E}}}(\underline{\boldsymbol{U}}) + \underline{\underline{\boldsymbol{N}}}(\underline{\boldsymbol{U}}, \underline{\boldsymbol{U}}) \right) : \underline{\underline{\boldsymbol{E}}}(\underline{\boldsymbol{W}}) \; s \, ds \, d\zeta = \\
&- \int_0^{R_{LC}} \mathrm{IOP} \, W_\zeta \Big|_{\zeta = h_{LC}/2} s \, ds + \int_0^{R_{LC}} \mathrm{RLTp} \, W_\zeta \Big|_{\zeta = -h_{LC}/2} s \, ds \\
&+ \int_{-\frac{h_{LC}}{2}}^{\frac{h_{LC}}{2}} R_{LC} \, \mathcal{T} \, W_s \Big|_{s = R_{LC}} d\zeta \qquad\qquad \forall \underline{\boldsymbol{W}} = (W_s, Y_\zeta) \in \mathbf{V}.
\end{aligned}
\tag{3.21}
$$

3.2 Central retinal vessels model

The central retinal vessels are modeled as a fluid-structure interaction system; the same model is used for the central retinal artery and for the central retinal vein. The model for the compliant wall of the vessel is described in Section 3.2.1, and the model for the blood flow inside the vessel is described in Section 3.2.2, where the dimensional analysis reduction modeling technique described in Sections 2.4.2 and 2.4.4 is used. The subscript $i = CRA, CRV$ used in the following sections corresponds to the central retinal artery case and the central retinal vein case, respectively.

3.2.1 Vessel wall model

The reference configuration of the vessel wall is a hollow circular cylinder of internal radius R_i, thickness h_i and length L, see Figure 3.3, described by

$$
\Omega_i^w = \left\{ (\eta \cos\phi, \eta \sin\phi, z) \in \mathbb{R}^3 \, : \, \eta \in (R_i, R_i + h_i), \, \phi \in [0, 2\pi), \, z \in (0, L) \right\},
$$

where $\{\eta, \phi, z\}$ are the radial, azimuthal, and axial Lagrangian coordinates, respectively. The superscript w indicates that the domain Ω_i^w represents the wall of the vessel, for $i = CRA, CRV$. The central retinal artery and vein are assumed to have the same length L, as reported in [11].

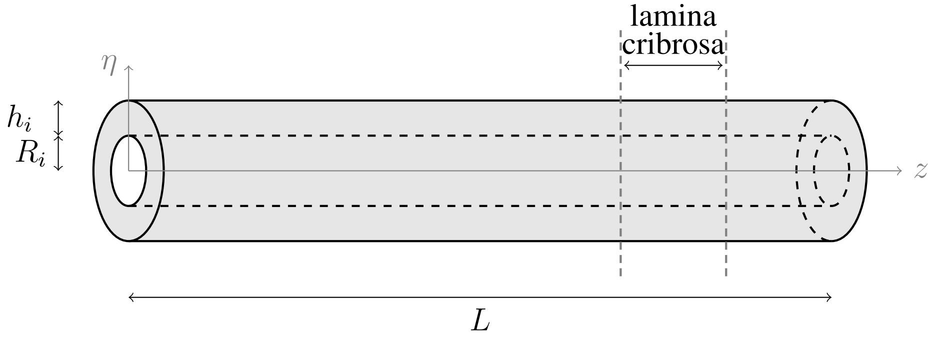

Fig. 3.3.: Representation of the wall of the central retinal vessels (shaded). The reference configuration of the vessel wall is a hollow circular cylinder of internal radius R_i and thickness h_i, for $i = CRA, CRV$. The vertical dashed lines indicate the location of the lamina cribrosa with respect to the vessel axis.

The equilibrium equation for the arterial wall is reduced to

$$\frac{\partial}{\partial \eta}\left[\frac{1}{\eta}\frac{\partial}{\partial \eta}(\eta \mathsf{U}_{\eta,i})\right] = 0 \quad \text{for} \;\; (\eta, z) \in (R_i, R_i + h_i) \times (0, L), \tag{3.22}$$

where $\mathsf{U}_{\eta,i} = \mathsf{U}_{\eta,i}(\eta, z)$ denotes the radial displacement for $i = CRA, CRV$, under the following assumptions

1. the deformation of the arterial wall obeys the linear theory of elasticity;
2. the axial displacement is negligible with respect to the radial displacement;
3. geometry, loading and solutions are axially symmetric.

Equation (3.22) necessitates boundary conditions for the external and internal cylindrical surfaces located at $\eta = R_i + h_i$ and $\eta = R_i$, respectively.

On the external surface located at $\eta = R_i + h_i$, as in (2.190b), we prescribe the normal stress through the condition

$$\left[\lambda_i \frac{\mathsf{U}_{\eta,i}}{\eta} + (2\mu_i + \lambda_i)\frac{\partial \mathsf{U}_{\eta,i}}{\partial \eta}\right]_{\eta = R_i + h_i} = -P_{e,i}(z), \tag{3.23}$$

where λ_i and μ_i are Lamé constants which are related to the Young modulus E_i and the Poisson ratio ν_i by

$$\lambda_i = \frac{E_i \nu_i}{(1+\nu_i)(1-2\nu_i)} \quad \text{and} \quad \mu_i = \frac{E_i}{2(1+\nu_i)}. \tag{3.24}$$

The external pressure $P_{e,i}(z)$ varies along the length of the vessel and accounts for the action of the intraocular pressure, retrolaminar tissue pressure, and the presence the lamina cribrosa. More precisely, we write $P_{e,CRA}(z)$ as

$$P_{e,CRA}(z) = \begin{cases} \text{RLTp} & \text{for} \quad 0 \le z < z_{LC,c}, \\ -S_{ss}(0, t(z)) & \text{for} \quad z_{LC,c} \le z \le z_{LC}, \\ \text{IOP} & \text{for} \quad z_{LC} < z < L, \end{cases} \tag{3.25}$$

where S_{ss} represents the compression exerted by the lamina cribrosa on the wall of the central retinal artery, the coordinate $z = z_{LC}$ indicates the relative position of the anterior surface of the lamina cribrosa with respect to the CRA axis, and the coordinate $z = z_{LC,c}$ indicates the lower end of the compressive region in the lamina, as shown in Figure 3.4. More precisely, we define $z_{LC,c}$ as

$$z_{LC,c} = \min\{z \in (z_{LC} - h_{LC}, z_{LC}) \,:\, -S_{ss}(0, t(z)) \ge \text{RLTp}\}, \tag{3.26}$$

where $t(z) = z - z_{LC} + h_{LC}/2$. $P_{e,CRV}$ can be expressed as the reflection of $P_{e,CRA}$ with respect to the axis $z = \frac{L}{2}$, namely

$$P_{e,CRV}(z) = P_{e,CRA}(L - z) \quad \text{for} \quad z \in [0, L]. \tag{3.27}$$

Following [11, 71], the segments of the CRA and the CRV post lamina cribrosa for

$$z_{LC} < z < L \tag{3.28}$$

are approximately 1 mm long, thus $z_{LC} = L - 1$ mm.

Note that the radial stress along the central axis of the lamina cribrosa is given by S_{ss} evaluated at $s = 0$. Radial compressive stress corresponds to negative values of S_{ss}, which translate into a positive contribution to the external pressures $P_{e,CRA}$ and $P_{e,CRV}$ (3.25) and (3.27).

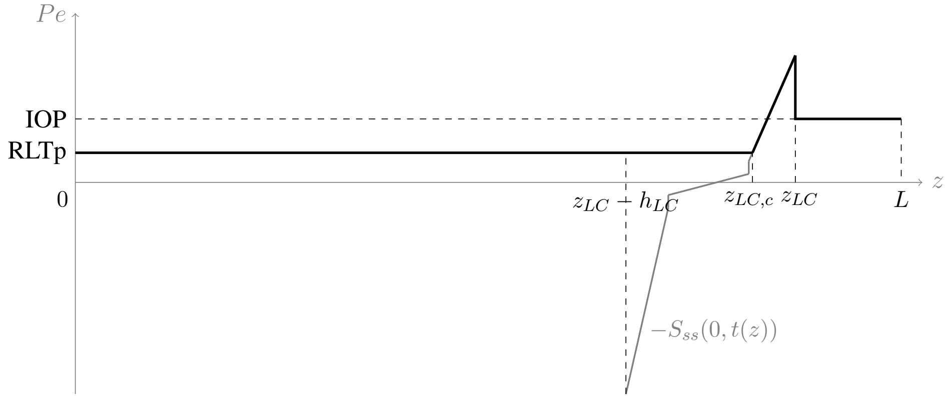

Fig. 3.4.: Representation of the external pressure $P_{e,CRA}$ acting on the wall of the central retinal artery. $P_{e,CRA}$ varies along the length of the central retinal artery, accounting for the intraocular pressure (IOP), retrolaminar tissue pressure (RLTp), and the compression from the lamina cribrosa $S_{ss}(0, t(z))$.

At the blood-wall interface $\eta = R_i$ we impose the dynamic condition

$$\left[\lambda_i \frac{\mathsf{U}_{\eta,i}}{\eta} + (2\mu_i + \lambda_i)\frac{\partial \mathsf{U}_{\eta,i}}{\partial \eta}\right]_{\eta = R_i} = -\Psi_i(z), \tag{3.29}$$

where $\Psi_i(z)$ is the function describing the action of blood flow on the vessel wall and is defined in Equation (3.34).

3.2.2 Blood flow model

The domain Ω_i^b occupied by the blood inside the vessel is shown in Figure 3.5 and is defined as

$$\Omega_i^b = \left\{(r\cos\phi, r\sin\phi, z) \in \mathbb{R}^3 \,:\, r \in [0, \gamma_i(z)),\, \phi \in [0, 2\pi),\, z \in (0, L)\right\},$$

where $\{r, \phi, z\}$ are the radial, azimuthal, and axial Eulerian coordinates, respectively. Here $\gamma_i(z)$ describes the blood-wall interface in Eulerian coordinates for $i = CRA, CRV$ and is related to the radial displacement of the wall by

$$\gamma_i(z) = R_i + \mathsf{U}_{\eta,i}(R_i, z). \tag{3.30}$$

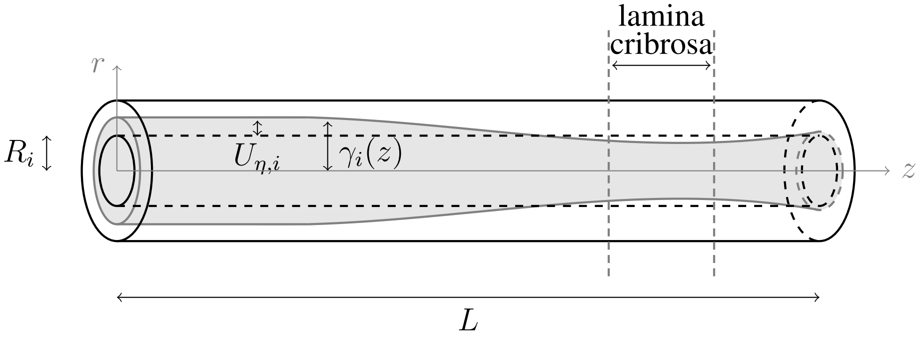

Fig. 3.5.: Domain occupied by the blood flowing inside the central retinal vessels (shaded). The function $\gamma_i(z)$ describes the wall-blood interface in eulerian coordinates, R_i is the reference radius of the vessel, and $U_{\eta,i}$ is the radial displacement of the vessel wall for $i = CRA, CRV$. The vertical dashed lines indicate the location of the lamina cribrosa with respect to the vessel axis.

We remark here that we are using the same azimuthal and axial coordinates ϕ and z for both the Lagrangian and Eulerian frameworks since we assume axial symmetry and neglect wall displacement in the axial direction (see Section 2.4.4 and Equation (2.193)).

Under the assumptions that

1. the blood can be described as a Stokes flow of a Newtonian incompressible viscous fluid;
2. the pressure depends only on z;
3. the radial velocity is negligible in the balance of axial momentum;
4. geometry, loading and solutions are axially symmetric;

the equations of conservation of mass and balance of axial momentum describing blood flow in the central retinal vessels reduce to

$$\frac{1}{r}\frac{\partial}{\partial r}(rv_{r,i}) + \frac{\partial v_{z,i}}{\partial z} = 0, \tag{3.31a}$$

$$\mu_{b,i}\frac{1}{r}\frac{\partial}{\partial r}\left(r\frac{\partial v_{z,i}}{\partial r}\right) = \frac{dp_i}{dz}, \tag{3.31b}$$

for $(r,z) \in [0,\gamma_i(z)) \times (0,L)$, where $v_{r,i} = v_{r,i}(r,z)$ and $v_{z,i} = v_{z,i}(r,z)$ denote the radial and axial components of the blood velocity, respectively, $p_i = p_i(z)$ denotes the pressure, and $\mu_{b,i}$ denotes the blood (effective) viscosity for $i = CRA,\ CRV$. Stokes flow is assumed in the CRA and CRV because the Reynolds number is less than 5. The fluid in the CRA is assumed to be Newtonian since a nearly parabolic profile is reported for the blood velocity in retinal arteries of diameter larger than 100μm [72]. We also assume that the fluid is Newtonian in the CRV.

System (3.31) must be completed with boundary conditions in both radial and axial directions. At the inlet and outlet sections of the CRA and CRV, we prescribe

$$\begin{aligned} p_i &= P_{0,i} \quad \text{for } z = 0, \\ p_i &= P_{L,i} \quad \text{for } \ z = L, \end{aligned} \qquad \text{for } i = CRA, CRV. \tag{3.32}$$

At the blood-wall interface, we impose the kinetic condition

$$v_{r,i} = 0 \quad \text{and} \quad v_{z,i} = 0 \quad \text{for} \ \ r = \gamma_i(z), \tag{3.33}$$

and the dynamic condition (3.29), where the function $\Psi_i(z)$ is given by

$$\Psi_i(z) = \frac{\gamma_i(z)p_i(z)}{R_i}. \tag{3.34}$$

In (3.34) we assume that the effect of shear stress is negligible in comparison to pressure. It is worth noticing that the function Ψ_i does not simply equal p_i, but it involves the product of p_i and γ_i. This is due to the nonlinear coupling between Lagrangian and Eulerian coordinates at the blood-wall interface.

3.2.3 Analytical solution

System (3.22)-(3.34) can be solved analytically following a procedure similar to the one presented in [43] and implemented in Section 2.4.4. The main difference is that the external pressure $P_{e,i}$, for $i = CRA,\ CRV$, varies along the axial coordinate.

The radial displacement of the arterial wall is computed as the solution of equation (3.22) with the boundary conditions (3.23) and (3.29), leading to

$$\mathsf{U}_{\eta,i}(\eta,z) = \Big(a_{1,i}\gamma_i(z)p_i(z) - a_{2,i}P_{e,i}(z)\Big)\eta + \left(\frac{\gamma_i(z)p_i(z)}{R_i} - P_{e,i}(z)\right)\frac{a_{3,i}}{\eta}, \tag{3.35}$$

where

$$\begin{aligned} a_{1,i} &= \frac{1}{2(\lambda_i+\mu_i)}\frac{R_i}{h_i(h_i+2R_i)}, \\ a_{2,i} &= a_{1,i}\frac{(h_i+R_i)^2}{R_i}, \\ a_{3,i} &= a_{2,i}\left(1+\frac{\lambda_i}{\mu_i}\right)R_i(h_i+R_i)^2. \end{aligned} \tag{3.36}$$

Using the geometric relation (3.30), we obtain

$$\begin{aligned} \gamma_i(z) &= R_i + U_{\eta,i}(R_i,z) \\ &= \Big(1+a_{1,i}\gamma_i(z)p_i(z) - a_{2,i}P_{e,i}(z)\Big)R_i + \left(\frac{\gamma_i(z)p_i(z)}{R_i} - P_{e,i}(z)\right)\frac{a_{3,i}}{R_i}. \end{aligned} \tag{3.37}$$

Solving (3.37) for $\gamma_i(z)$ we obtain

$$\gamma_i(z) = R_i\,\frac{1-b_{1,i}\;P_{e,i}(z)}{1-b_{2,i}\;p_i(z)}, \tag{3.38}$$

where

$$b_{1,i} = a_{2,i} + \frac{a_{3,i}}{R_i^2} \quad \text{and} \quad b_{2,i} = a_{1,i}R_i + \frac{a_{3,i}}{R_i^2}. \tag{3.39}$$

Let us now consider the equations describing blood flow. By integrating equation (3.31b) with respect to r, we obtain

$$v_{z,i}(r,z) = \frac{1}{4\mu_{b,i}}\left[r^2 - (\gamma_i(z))^2\right]\frac{dp_i}{dz}. \tag{3.40}$$

By integrating equation (3.31a) with respect to r, using (3.33) and (3.40), we obtain

$$\frac{d}{dz}\left[(\gamma_i(z))^4\frac{dp_i}{dz}(z)\right] = 0. \tag{3.41}$$

Now equations (3.38) and (3.41) form a system in the unknowns $\gamma_i(z)$ and $p_i(z)$ that can be solved to obtain

$$p_i(z) = \frac{1}{b_{2,i}}\left[1-\left(N_i - M_i\int_0^z(1-b_{1,i}P_{e,i}(t))^{-4}dt\right)^{-1/3}\right], \tag{3.42}$$

and

$$\gamma_i(z) = R_i\Big(1-b_{1,i}P_{e,i}(z)\Big)\left(N_i - M_i\int_0^z(1-b_{1,i}P_{e,i}(t))^{-4}dt\right)^{1/3}, \tag{3.43}$$

where $P_{e,i}(z)$ are given by (3.25) and (3.27) and the integration constants M_i and N_i can be determined using the boundary conditions (3.32)

$$M_i = \frac{N_i - (1 - b_{2,i} P_{L,i})^{-3}}{\displaystyle\int_0^L (1 - b_{1,i} P_{e,i}(t))^{-4} dt} \quad \text{and} \quad N_i = (1 - b_{2,i} P_{0,i})^{-3}. \tag{3.44}$$

Moreover, the blood flow rate $\mathcal{Q}_i$ can be expressed as

$$\mathcal{Q}_i = 2\pi \int_0^{\gamma_i(z)} v_{z,i}(r, z)\, r\, dr = \frac{\pi M_i R^4}{24 \mu_{b,i} b_{2,i}}. \tag{3.45}$$

3.3 Retinal circulation model

The vasculature upstream of the CRA and downstream of the CRV, and the retinal vasculature inside the eye are modeled as a zero-dimensional network of resistances using the electric analogy described in Section 2.5, Figure 3.1. Here we summarize the main assumptions for the zero-dimensional model. For more details on the derivation we refer to [51].

Vasculature upstream of the CRA: The vascular resistance between the ophthalmic artery and the inlet of the CRA is defined as $\mathcal{R}_1$ and corresponds to the pressure drop from the system inlet pressure (P_{in}) to the inlet pressure of the CRA ($P_{0,CRA}$). P_{in} is related to the MAP in the following way

$$P_{in} = \frac{2}{3}\text{MAP}. \tag{3.46}$$

The factors of $2/3$ accounts for the pressure drop from the brachial artery, where the MAP is measured, to the eye [73]. $\mathcal{R}_1$ is assumed to be constant and its value is estimated via Poiseuille's law (2.209).

Retinal arterioles and capillaries: The vascular resistance of the retinal arterioles and capillaries is defined as $\mathcal{R}_2$ and corresponds to the pressure drop from the outlet pressure of the CRA ($P_{L,CRA}$) to the outlet pressure of the capillaries (P_c). $\mathcal{R}_2$ is assumed to be constant and its value is estimated using the retinal network model proposed in [40] and Poiseuille's law (2.209).

Retinal venules: The vascular resistance of retinal venules is defined as $\mathcal{R}_3$ and corresponds to the pressure drop from the outlet pressure of the capillaries (P_c) to the inlet pressure of the CRV ($P_{0,CRV}$). The retinal venules are exposed to an external pressure equal to the IOP. Thus, $\mathcal{R}_3$ is assumed to be a variable resistance: $\mathcal{R}_3 = \mathcal{R}_3(IOP, P_c, P_{0,CRV})$. $\mathcal{R}_3$ is modeled using the retinal network model proposed in [40] and Equation (2.213), where $P_e = IOP$ and $\Pi = \dfrac{P_c + P_{0,CRV}}{2}$.

Vasculature downstream of the CRV: $\mathcal{R}_4$ represents the vascular resistance between the outlet of the CRV and the venous systems, that corresponds to the pressure drop from outlet pressure of the CRV ($P_{L,CRV}$) to the venous pressure (P_{out}). The venous pressure can be approximated by 14 mmHg, since it is usually considered to be approximately equal to the intraocular pressure [74]. $\mathcal{R}_4$ is assumed to be constant and its value is estimate via Poiseuille's law (2.209).

The computed values of the constant resistances $\mathcal{R}_1$, $\mathcal{R}_2$ and $\mathcal{R}_4$ are reported in Table 3.2. Note that, since we are considering the steady state regime, no capacitances are included in the vascular circuit.

The application of Kirchhoff's laws to the vascular network in Figure 3.1 leads to the following system of nonlinear algebraic equations

$$\begin{cases} P_{in} - P_{0,CRA} = & \mathcal{R}_1 \mathcal{Q}_{CRA}, \\ P_{L,CRA} - P_c = & \mathcal{R}_2 \mathcal{Q}_{CRA}, \\ P_c - P_{0,CRV} = & \mathcal{R}_3(IOP, P_c, P_{0,CRV}) \mathcal{Q}_{CRV}, \\ P_{L,CRV} - P_{out} = & \mathcal{R}_4 \mathcal{Q}_{CRV}, \end{cases} \tag{3.47}$$

where $\mathcal{Q}_{CRA}$ and $\mathcal{Q}_{CRV}$ depend on the CRA and CRV velocities through Equation (3.45). By the conservation of flow

$$\mathcal{Q}_{CRA} = \mathcal{Q}_{CRV}. \tag{3.48}$$

Table 3.2.: Values of the resistances in the retinal circulation model [51]: $\mathcal{R}_1$ represents the vascular resistance upstream of the CRA, $\mathcal{R}_2$ represents the vascular resistance of retinal arterioles and capillaries, and $\mathcal{R}_4$ represents the vascular resistance downstream of the CRV.

Parameter	Values	Unit
$\mathcal{R}_1$	2.25×10^4	[mmHg s/ml]
$\mathcal{R}_2$	2.25×10^4	[mmHg s/ml]
$\mathcal{R}_4$	5.74×10^3	[mmHg s/ml]

3.4 Solution Procedure

The model described in Sections 3.1, 3.2 and 3.3 is solved in three steps:

Step 1 solve system (3.11)-(3.13) to calculate the stress in the lamina cribrosa;

Step 2 determine $P_{e,CRA}$ and $P_{e,CRV}$ in (3.25) and (3.27), given the stress from Step 1;

Step 3 solve the systems for the CRA and the CRV (3.35)-(3.45) coupled with the system of the retinal microcirculation (3.47)-(3.48) to calculate blood velocity, blood pressure, radial deformation, deformed radius and blood flow in the central retinal artery and central retinal vein.

A schematic representation of the solution procedure is reported in Figure 3.6, additional details for Step 1 and Step 3 are given below.

Step 1

System (3.11)-(3.13) includes: material nonlinearities, as shown in Equation (3.6) and Table 3.1, and geometric nonlinearities, as shown in Equations (3.3)-(3.5). To address these nonlinearities, we designed the iterative algorithm described below.

Given IOP and RLTp, let σ_e^0 (and therefore λ_{LC}^0 and μ_{LC}^0) be given. For $n \geq 1$ proceed as follows:

1. compute $\underline{\boldsymbol{U}}^n$ via the fixed point iterations:
   let $\underline{\boldsymbol{W}}^0$ be given (equal to $\underline{\boldsymbol{U}}^{n-1}$ if $n > 1$, equal to $\underline{\mathbf{0}}$ otherwise), for $j \geq 1$:

   (a) compute $\underline{\boldsymbol{W}}^j$ as the solution of the linearized variational problem (3.21)

   $$\begin{aligned}
   &\int_0^{R_{LC}} \int_{-\frac{h_{LC}}{2}}^{\frac{h_{LC}}{2}} \lambda_{LC}^{n-1} \mathrm{tr}\left(\underline{\underline{\boldsymbol{E}}}\left(\underline{\boldsymbol{W}}^j\right) + \underline{\underline{\boldsymbol{N}}}\left(\underline{\boldsymbol{W}}^j, \underline{\boldsymbol{W}}^{j-1}\right)\right) \underline{\underline{\boldsymbol{I}}} : \underline{\underline{\boldsymbol{E}}}(\underline{\boldsymbol{Y}})\; s\, ds\, d\zeta \\
   &+2 \int_0^{R_{LC}} \int_{-\frac{h_{LC}}{2}}^{\frac{h_{LC}}{2}} \mu_{LC}^{n-1} \left(\underline{\underline{\boldsymbol{E}}}\left(\underline{\boldsymbol{W}}^j\right) + \underline{\underline{\boldsymbol{N}}}\left(\underline{\boldsymbol{W}}^j, \underline{\boldsymbol{W}}^{j-1}\right)\right) : \underline{\underline{\boldsymbol{E}}}(\underline{\boldsymbol{Y}})\; s\, ds\, d\zeta = \\
   &- \int_0^{R_{LC}} \mathrm{IOP}\, Y_\zeta \Big|_{\zeta = h_{LC}/2} s\, ds + \int_0^{R_{LC}} \mathrm{RLTp}\, Y_\zeta \Big|_{\zeta = -h_{LC}/2} s\, ds + \\
   &+ \int_{-\frac{h_{LC}}{2}}^{\frac{h_{LC}}{2}} R_{LC}\, \mathcal{T}\, Y_s \Big|_{s = R_{LC}} d\zeta \qquad \forall \underline{\mathbf{Y}} = (Y_s, Y_\zeta) \in \mathbf{V}.
   \end{aligned} \tag{3.49}$$

   (b) test for convergence:
   if $\dfrac{\|\underline{\boldsymbol{W}}^j - \underline{\boldsymbol{W}}^{j-1}\|_{L^2(\Omega)}}{\|\underline{\boldsymbol{W}}^j\|_{L^2(\Omega)}} < \varepsilon_1$ set $\underline{\boldsymbol{U}}^n = \underline{\boldsymbol{W}}^j$ and go to point 2,
   otherwise set $\underline{\boldsymbol{W}}^{j-1} = \underline{\boldsymbol{W}}^j$ and go back to point (a).

2. compute $\underline{\underline{\boldsymbol{S}}}^n = \lambda_{LC}^{n-1} \mathrm{tr}\left(\underline{\underline{\boldsymbol{E}}}(\underline{\boldsymbol{U}}^n) + \underline{\underline{\boldsymbol{N}}}(\underline{\boldsymbol{U}}^n, \underline{\boldsymbol{U}}^n)\right) \underline{\underline{\boldsymbol{I}}} + 2\mu_{LC}^{n-1} \left(\underline{\underline{\boldsymbol{E}}}(\underline{\boldsymbol{U}}^n) + \underline{\underline{\boldsymbol{N}}}(\underline{\boldsymbol{U}}^n, \underline{\boldsymbol{U}}^n)\right)$;

3. compute $\sigma_e^n = f(\underline{\underline{\boldsymbol{S}}}^n)$ (3.6);

4. test for convergence:
   if $\|\sigma_e^n - \sigma_e^{n-1}\|_{L^\infty(\Omega)} < \varepsilon_2$ go to point 5,
   otherwise set $\sigma_e^{n-1} = \sigma_e^n$, update λ_{LC}^n and μ_{LC}^n via Table 3.1 and Equation (3.7), set $\lambda_{LC}^{n-1} = \lambda_{LC}^n$ and $\mu_{LC}^{n-1} = \mu_{LC}^n$ and go back to point 1.

5. set the solution of the system to be $\underline{\boldsymbol{U}} = \underline{\boldsymbol{U}}^n$ and $\underline{\underline{\boldsymbol{S}}} = \underline{\underline{\boldsymbol{S}}}^n$.

This algorithm has been implemented in FreeFem++, a Finite Element Method-based software for the solution of PDEs [75], using quadratic finite elements on a regular and uniform

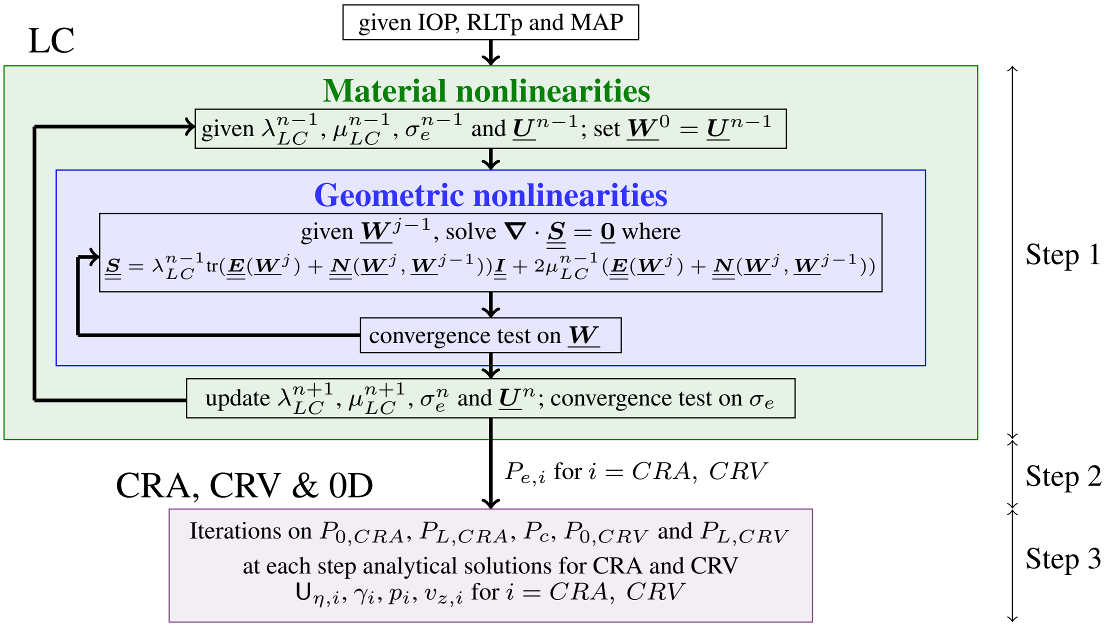

Fig. 3.6.: Sketch of the solution procedure for the lamina cribrosa, central retinal vessels and retinal circulation coupled model.

50×100 triangulation, with $\varepsilon_1 = \varepsilon_2 = 10^{-5}$. We remark that the linearized variational problem (3.49) holds since the non-linear part of the strain tensor $\underline{\underline{\boldsymbol{N}}}(\underline{\boldsymbol{W}}, \underline{\boldsymbol{Y}})$ is symmetric with respect to $\underline{\boldsymbol{W}}$ and $\underline{\boldsymbol{Y}}$ (3.4)-(3.5).

Step 3

The resolution of Step 3 has been implemented in MATLAB, a numerical computing environment. Given the external pressures $P_{e,CRA}$ and $P_{e,CRV}$ from Step 2, the integrals in Equations (3.42)- (3.44) are estimated using the trapezoidal rule. Then, given MAP, the system (3.35)- (3.45), for $i = CRA,\ CRV$, coupled with system (3.47)- (3.48), is solved using the non-linear solver *fsolve*.

3.5 Results

In this section we present and validate the predictions of the mathematical model using three different and unrelated experimental and clinical studies. The aim of the simulations presented here is to elucidate the mechanisms through which changes in IOP, CSFp and MAP affect the hemodynamics in the central retinal artery and vein.

3.5.1 Lamina cribrosa deformation and stresses

The displacement of the lamina cribrosa predicted by our mathematical model for different values of IOP and retrolaminar tissue pressure has been compared with the experimental data obtained by Morgan et al [76]. Here, the anterior chamber and lateral ventricles of the eyes of eight mixed-breed dogs were cannulated to sequentially increase IOP and CSFp.

Confocal scanning laser tomography was performed at each level of IOP and CSFp to measure the depth of the optic disc surface, which reflects the underlying anterior laminar movement. Starting from baseline (corresponding to IOP$=15$ mmHg and CSFp$=0$ mmHg), IOP was elevated up to an average of 32 mmHg, via steps between 3 and 5 mmHg. A second set of experiments were performed in which, starting from baseline, CSFp was elevated up to an average of 12 mmHg, via steps between 2 and 4 mmHg. Morgan et al. report their results using the quantity ΔMaxD, which represents the difference in the maximum disc depth with respect to baseline. Experimental data are shown in Figure 3.7.

In order to compare the predictions of our mathematical model with the experimental data, we used the following linear relation between CSFp and RLTp (in mmHg), derived by Morgan et al. in a previous work [18]

$$\mathrm{RLTp} = \begin{cases} 0.07\,\mathrm{CSFp} + 2.9200 & \text{for} \quad \mathrm{CSFp} \leq 1.33, \\ 0.82\,\mathrm{CSFp} + 1.9225 & \text{for} \quad \mathrm{CSFp} > 1.33. \end{cases} \tag{3.50}$$

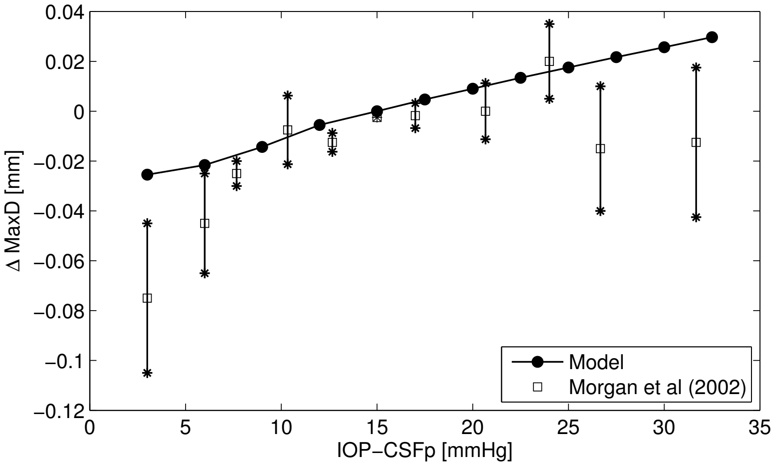

Fig. 3.7.: Comparison between model predictions and experimental measurements of the anterior lamina displacement. Increments of maximum disc depth ΔMaxD with respect to the baseline IOP-CSFp= 15 mmHg are reported as a function of the IOP-CSFp difference. The predictions of the mathematical model (solid line) are compared with experimental data by Morgan et al. [76].

Then, we solved Step 1, described in Section 3.4, with RLTp= 2.92 mmHg, which corresponds to CSFp= 0 mmHg via Equation (3.50), and with IOP varying between 15 mmHg and 32.5 mmHg. Next, we solved Step 1 with IOP= 15 mmHg, and with RLTp varying in the range that corresponds to CSFp between 0 mmHg and 12 mmHg via Equation (3.50). Since geometric and elastic properties of the eyes examined in [76] are not reported in the article, we chose physiologically representative values, see Tables 3.1 and 3.3. The maximum disc depth ΔMaxD measured by Morgan et al. is compared with the anterior laminar displacement computed via our mathematical model, namely U_ζ at $s = 0$ and $\zeta = h_{LC}/2$. The comparison between model predictions and experimental data is reported in Figure 3.7.

The mathematical model is also used to calculate the radial stress component S_{ss} arising in the lamina cribrosa for different IOP values. The results are reported in Figure 3.8

Table 3.3.: Values of the parameters in the model for the lamina cribrosa: R_{LC} and h_{LC} are the lamina cribrosa radius and thickness, respectively, R_s and h_s are scleral radius and thickness, respectively.

Parameter	Values	Unit	Source
R_{LC}	0.75	[mm]	[77]
h_{LC}	0.2	[mm]	[78,79]
R_s	12	[mm]	[78,80]
h_s	1	[mm]	[79,80]

and they show regions of radial compressive stress in the lamina cribrosa, corresponding to negative values of S_{ss}. These regions become more pronounced as IOP is elevated.

The value of S_{ss} along the central axis of the lamina is of particular interest here, since it affects the pressure acting on the external wall of the central retinal vessels via Equations (3.25) and (3.27). Figure 3.9 shows the behavior of S_{ss} for $s = 0$ as a function of the axial coordinate ζ across the thickness of the lamina, for different IOP values. The significance of compressive regions, corresponding to negative values of S_{ss}, increases with IOP both in terms of magnitude and depth penetration in the thickness of the lamina.

IOP elevation also induces an increase in scleral tension, as dictated by Laplace's law (3.10). This increase in scleral tension relieves some (but not all) of the radial compression in the lamina cribrosa, as shown in Figure 3.10. The solid lines correspond to the case where the scleral tension varies with IOP according to Laplace's law, while the dashed lines correspond to the case where the scleral tension is held constant at its value for IOP = 20 mmHg.

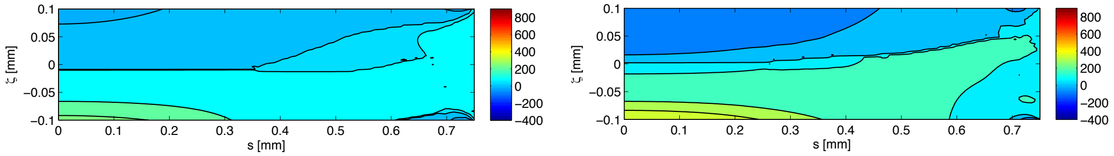

(a) IOP = 15 mmHg

(b) IOP = 20 mmHg

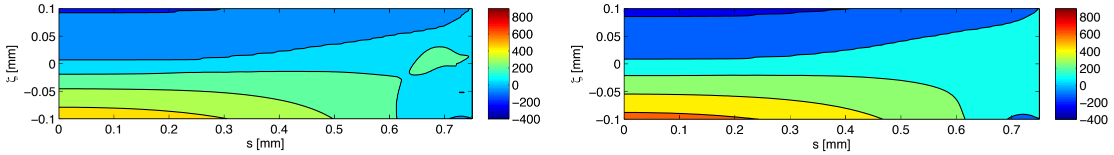

(c) IOP = 25 mmHg

(d) IOP = 30 mmHg

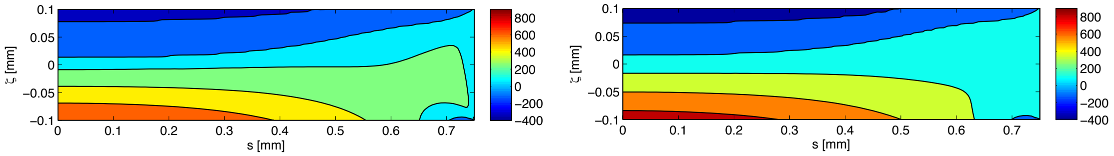

(e) IOP = 35 mmHg

(f) IOP = 40 mmHg

Fig. 3.8.: Lamina cribrosa radial stress S_{ss} [mmHg]. Distribution of the radial stress in the lamina cribrosa for different IOP values. Regions of radial compressive stress correspond to negative values of S_{ss}.

3.5.2 Effect of IOP elevation on CRA hemodynamics

The IOP-induced reduction in the CRA blood velocity predicted by our mathematical model has been compared to the clinical data reported by two independent studies, namely Harris et al [22] and Findl et al [23]. Since the studies do not report geometrical and material properties of the central retinal artery, we have used physiologically representative values summarized in Table 3.4.

In the study by Harris et al., the IOP was artificially elevated in eleven healthy individuals using suction opthalmodynamometry, from a baseline near 14 mmHg to approximately 45 mmHg in 3-4 increments. At each IOP level, peak systolic and end diastolic velocities

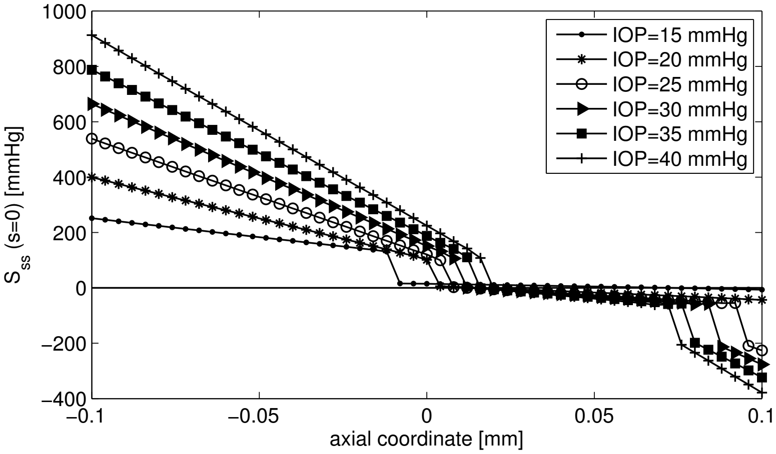

Fig. 3.9.: Effect of IOP elevation on the lamina cribrosa radial stress S_{ss}. The radial stress S_{ss} along the central axis of the lamina ($s = 0$) is reported as a function of the axial coordinate ζ across the thickness of the lamina, for different IOP values.

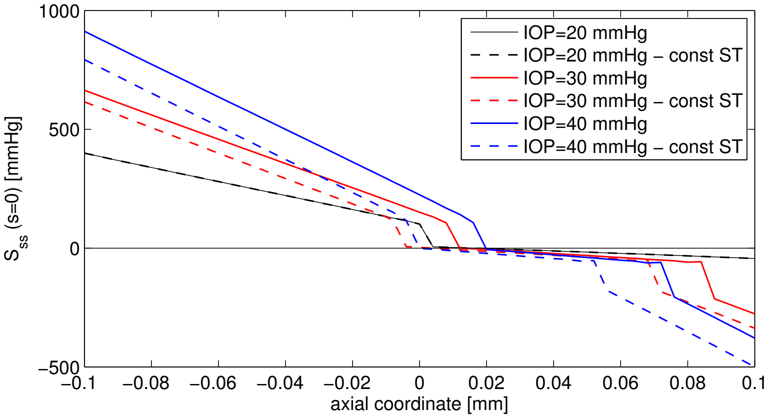

Fig. 3.10.: Effect of the scleral tension on the lamina cribrosa radial stress S_{ss}. The radial stress S_{ss} along the central axis of the lamina ($s = 0$) is reported as a function of the axial coordinate ζ across the lamina's thickness, for different IOP values and with the scleral tension increasing with IOP via the Laplace law (solid lines) or with scleral tension held constant at its value for IOP=20 mmHg (dashed lines).

Table 3.4.: Values of the parameters in the model for the CRA and CRV.

Parameter	CRA		CRV		Unit
	Value	Source	Value	Source	
radius, R	87	[81]	119	[40, 51]	[μm]
thickness, h	40	[82]	12	[83]	[μm]
length, L	10	[11]	10	[11]	[mm]
Young's modulus, E	0.3	[84–86]	0.9	[87]	[MPa]
Poisson's ratio, ν	0.49	[84–86]	0.49	[51]	[1]
blood viscosity, μ_b	3.0×10^{-3}	[86, 88]	3.2×10^{-3}	[40, 51]	[Pa s]

(PSV and EDV) were measured in the central retinal artery using Color Doppler Imaging. The measurements were performed approximately 3 mm behind the optic disc.

We solve the model by setting MAP $= 93.33$ mmHg, RLTp $= 7$ mmHg, and varying IOP between 15 and 40 mmHg. We remark that MAP is defined as

$$\text{MAP} = \frac{2}{3}\text{DP} + \frac{1}{3}\text{SP}, \tag{3.51}$$

where DP and SP are the diastolic and systolic blood pressure at the level of the brachial artery. The baseline value of MAP is obtained from the baseline values of DP$= 80$ mmHg and SP$= 120$ mmHg.

The lamina is approximately 1 mm behind the optic disc [11] and the segment of the central retinal artery that runs through the lamina is very narrow, namely $h_{LC}/L = 0.02$ using the physiological representative values reported in Tables 3.3 and 3.4. Considering the measurement error and the high variability among individuals, the clinical CRA blood velocities reported in [22] are compared to the model predicted CRA blood velocity at the centerline right before the lamina at $z = z_{LC} - h_{LC}$ (pre LC) and right after the lamina cribrosa at $z = z_{LC}$ (post LC) in Figure 3.11. Even though our stationary model provides only a mean value of the velocity, the model predictions fall nicely in the band between the values of peak systolic and end diastolic velocities measured *in vivo*. Both model

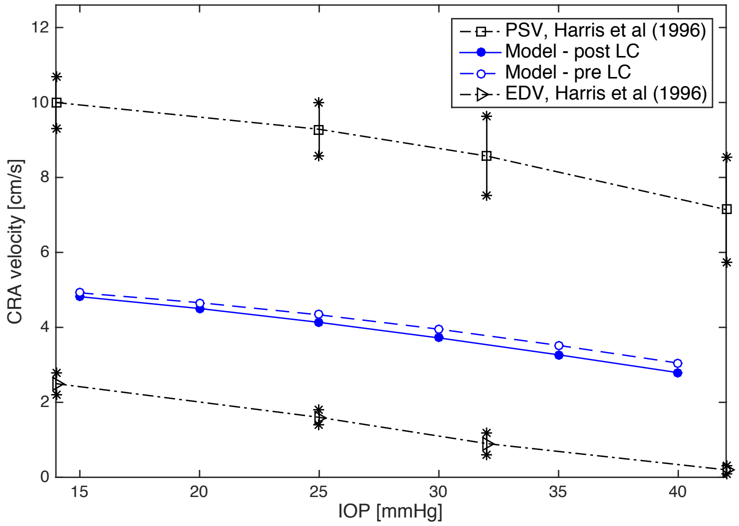

Fig. 3.11.: Effect of IOP elevation on the peak systolic velocity (PSV) and end diastolic velocity (EDV) of the blood flow in the CRA. Comparison between in vivo measurements by [22](black) and model predictions obtained before (blue, dashed line) or after (blue, solid line) the lamina cribrosa.

predictions of CRA velocity before and after the lamina cribrosa show similar behavior as the measurements, with a noticeable decrease in velocity as IOP increases from 15 to 40 mmHg. Thus, we will compare the clinical results in [22,23] with the CRA velocity before the lamina cribrosa.

In order to assess whether or not the radial compressive stress in the lamina cribrosa and the variable venular resistance $\mathcal{R}_3$ are contributing to the observed decrease in CRA blood velocity, we simulate in four different cases

a) *No LC effect and* $\mathcal{R}_3$ *constant*: the radial compressive stress of the lamina on the CRA and CRV is not taken into account and effect of IOP on the retinal venules is not taken into account;

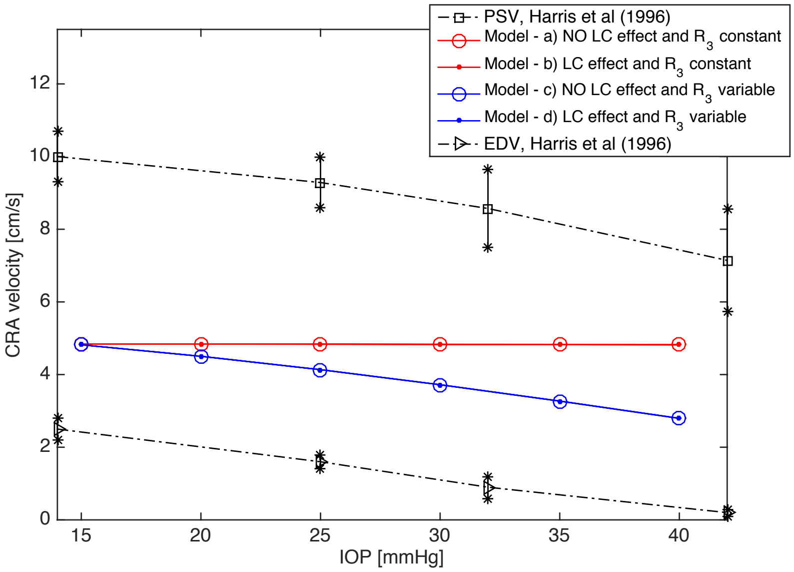

Fig. 3.12.: Comparison between in vivo measurements by [22] (black) and model predictions obtained by taking (cases b) and d)) or not taking into account the lamina compression on the CRA (cases a) and c)), and by taking (cases c) and d)) and not taking into account the effect of IOP on $\mathcal{R}_3$ (case a) and b)).

b) *LC effect and $\mathcal{R}_3$ constant*: the radial compressive stress of the lamina on the CRA and CRV is taken into account and effect of IOP on the retinal venules is not taken into account;

c) *No LC effect and $\mathcal{R}_3$ variable*: the radial compressive stress of the lamina on the CRA and CRV is not taken into account and effect of IOP on the retinal venules is taken into account;

d) *LC effect and $\mathcal{R}_3$ variable*: the radial compressive stress of the lamina on the CRA and CRV is into account and effect of IOP on the retinal venules is not taken into account.

Figure 3.12 shows the CRA blood velocity predicted by our mathematical model compared to the clinical data reported by Harris et al [22] in cases a), b), c) and d). In cases b) and d), where the radial compressive stress has been taken into account, $P_{e,CRA}$ vary as in Equation (3.25), and, in cases a) and c), where the radial compressive stress has not been taken into account, $P_{e,CRA} =$ RLTp up to z_{LC}. In all the cases, the IOP is acting directly on the post-laminar segment of the CRA, since $P_{e,CRA} =$ IOP for $z > z_{LC}$, and $P_{e,CRV}(z) = P_{e,CRA}(L - z)$. In cases c) and d), where the effect of IOP on the retinal venules has been taken into account, the venular resistance varies with IOP as described in Section 3.3, namely $\mathcal{R}_3 = \mathcal{R}_3(IOP, P_c, P_{0,CRV})$. In cases a) and b), where the effect of IOP on the retinal venules has not been taken into account, the venular resistance is constant and equal to $\mathcal{R}_3 = 6.22 \times 10^3$ mmHg s/ml. Its value has been estimated via Poiseuille's law (2.209) in [51]. The model predictions obtained by taking into account the effect of IOP on the retinal venules (cases c) and d)) show a similar behavior as the measurements, with a noticeable decrease in velocity as IOP increases from 15 to 40 mmHg. The decrease is not present in the other cases.

In the study by Findl et al. [23], the CRA blood velocity was measured by Doppler sonography on 10 healthy individuals, while IOP was elevated artificially using a suction cup. In each subject, the IOP was increased by 10 mmHg and 20 mmHg with respect to its baseline value, and the mean velocity of the CRA blood flow was measured at approximately 3 mm behind the optic disc surface. This study reported a decrease in the CRA blood flow velocity following IOP elevation. The decrease was $-5 \pm 3\%$ at $+10$ mmHg and $-14 \pm 5\%$ at $+20$ mmHg ($p < 0.005$).

In order to compare the predictions of our mathematical model with the data by Findl et al., we solve the model setting MAP $= 93.33$ mmHg, RLTp $= 7$ mmHg, and for IOP equal to 11.3 mmHg (mean value of the baseline IOP in Findl et al.), 21.3 mmHg and 31.3 mmHg, in cases a), b), c) and d). Figure 3.13 shows the comparison between the percent change of the centerline CRA velocity predicted by our mathematical model (blue and red histograms) and measured in vivo by Findl et al. (gray histograms). If the effect of IOP on the retinal venules is taken into account, our model predicts a significant decrease in the CRA velocity. Otherwise, if only the radial compressive stress of the lamina on the CRA and CRV is taken into account, the CRA velocity decrease is infinitesimal (less than 0.1%).

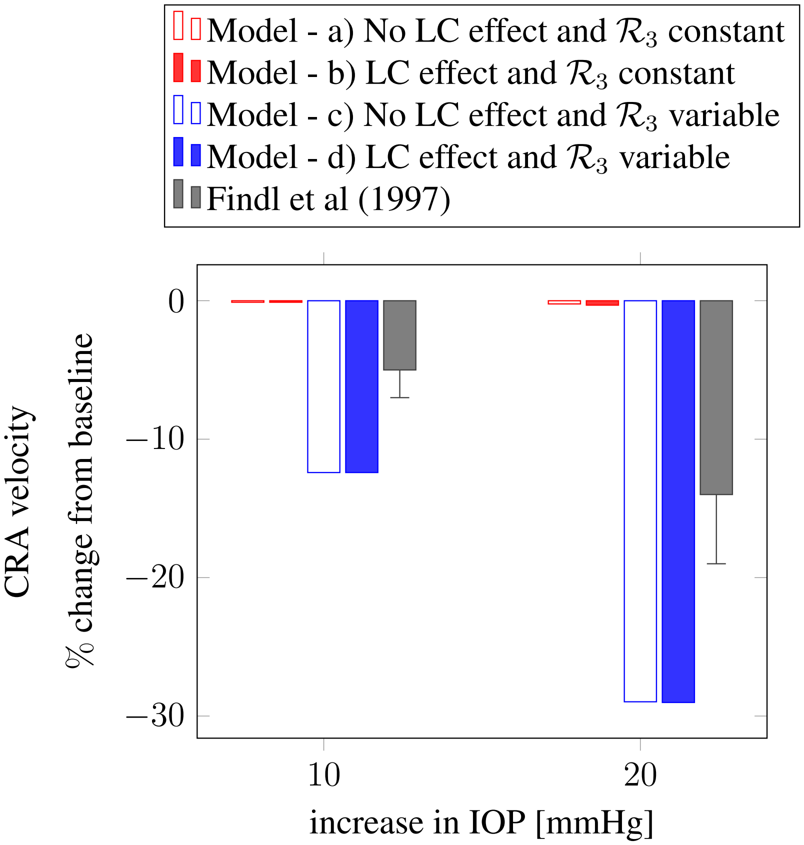

Fig. 3.13.: Comparison of percent decrease in the mean CRA centerline velocity with IOP elevation. Comparison between in vivo measurements by Findl e al. [23] (gray) and model predictions obtained by taking (cases b) and d)) or not taking into account the lamina compression on the CRA (cases a) and c)), and by taking (cases c) and d)) and not taking into account the effect of IOP on $\mathcal{R}_3$ (case a) and b)).

3.5.3 Effect of CSFp alteration on central retinal vessels hemodynamics

The CSFp-induced variations in the CRA and CRV blood velocities predicted by our mathematical model have been compared to the clinical data reported by Querfurth et al. [24]. Since the study does not report geometrical and material properties of the CRA and CRV, we have used physiologically representative values summarized in Table 3.4.

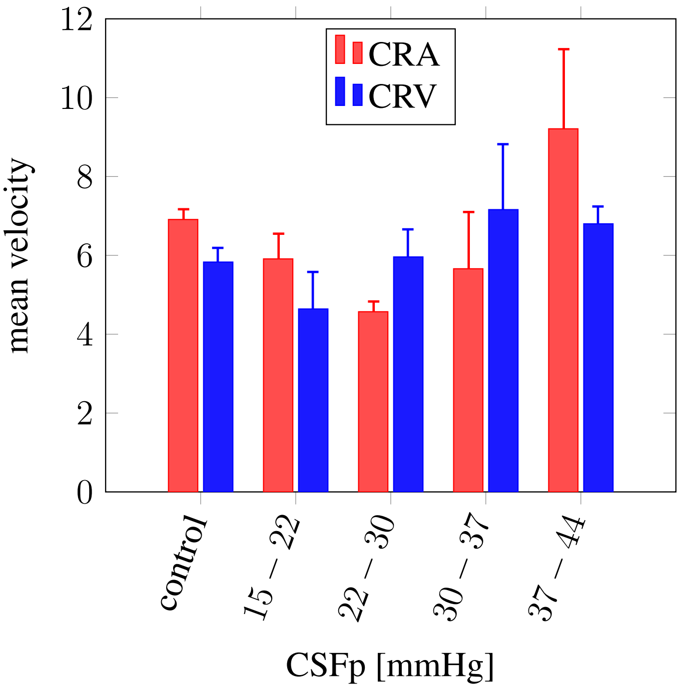

Fig. 3.14.: In vivo measurements reported by Querfurth et al. [24] of CSFp and mean CRA and CRV blood velocities in healthy individuals (control) and ICH patients

In the study by Querfurth et., the CSFp was measured by standard lumbar puncture in healthy individuals and chronic intracranial hypertension (ICH) patients. Healthy individuals represent the control group and ICH patients were divided into groups depending on their CSFp. None of the subjects in the study had an IOP greater than 20 mmHg. The mean central retinal artery and central retinal vein blood velocities were measured using Color Doppler Imaging at approximately 2 mm behind the optic disc. This study reported a bimodal behavior in the CRA and CRV blood velocities as CSFp increases, compared to the control group. In particular, there is a first decrease in velocity, followed by an unexpected increase in velocity, see Figure 3.14.

In order to compare the predictions of our mathematical model with the data by Querfurth et al., we solve the model by setting MAP$= 93.33$ mmHg, IOP $= 15$ mmHg, varying CSFp from 1 to 44mmHg and assuming RLTp$\simeq$CSFp. Figure 3.15 shows the centerline

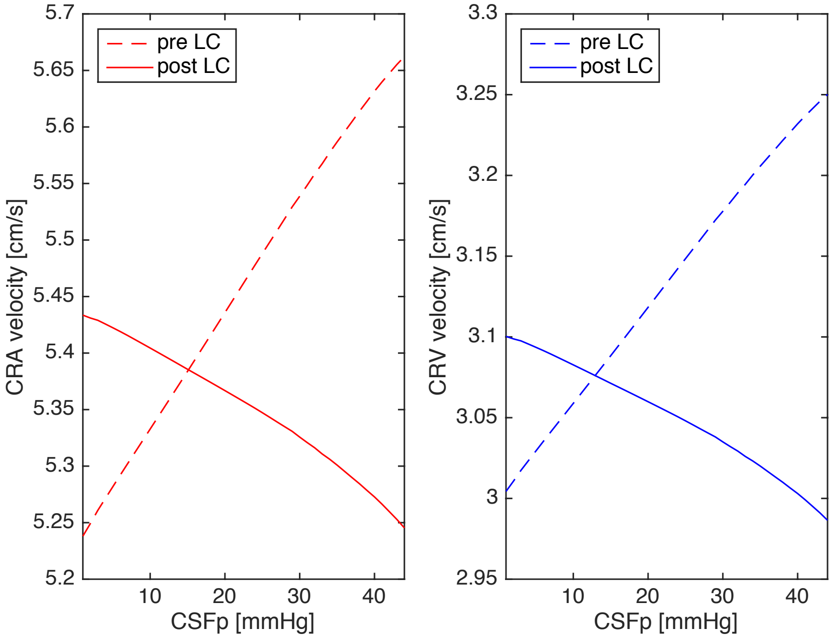

Fig. 3.15.: Model predictions of CRA and CRV velocity at the centerline before (dashed line) and after (solid line) the lamina cribrosa as CSFp varies.

CRA and CRV blood velocities predicted by our mathematical model right before the lamina (pre LC) and right after the lamina cribrosa (post LC). The predicted velocity before the lamina, in CRA and CRV, shows an increase as CSFp increases, and, conversely, the predicted velocity after the lamina in CRA and CRV shows a decrease as CSFp increases. In Table 3.5 are reported the percentage variations of CRA and CRV velocities, with respect to the control group, measured in vivo [24] and predicted by our mathematical model, before and after the lamina.

Model predictions are in qualitative agreement with the clinical data, as shown in Table 3.5; the quantitative agreement is not obtained. Note that in [24], CRA and CRV blood velocities were not measured in the same patients while CSFp was artificially elevated. Rather, CRA and CRV velocities and CSFp were measured in healthy individuals and ICH patients, and then the velocities measurements were divided in groups depending on their corresponding CSFp value. The differences between measured and predicted values re-

Table 3.5.: Percentage of CRA and CRV blood velocities variations with respect to the control group measured in vivo [24] and predicted by our mathematical model, before and after the lamina.

	% variation CRA velocity			% variation CRV velocity		
CSFp [mmHg]	Measured	Predicted		Measured	Predicted	
		pre LC	post LC		pre LC	post LC
$15-22$	-15%	$+1.6\%$	-0.2%	-20%	$+0.6\%$	-0.2%
$22-30$	-34%	$+2.0\%$	-0.7%	$+2\%$	$+2.0\%$	-0.8%
$30-37$	-18%	$+3.5\%$	-1.3%	$+23\%$	$+3.4\%$	-1.4%
$37-44$	$+33\%$	$+4.6\%$	-2.0%	$+16\%$	$+4.6\%$	-2.2%

ported in Table 3.5 might be due to the influence of MAP on hemodynamics, neglected here since MAP measurements were not reported in [24]. This motivates the investigation presented in Section 3.5.4, which combines the interaction among IOP, CSFp and MAP.

3.5.4 Combined effect of IOP, CSFp and MAP on central retinal vessels hemodynamics

In this section we use the mathematical model presented in Sections 3.1-3.3 to estimate, quantify and compare the influence of changes in IOP, CSFp and MAP on retinal hemodynamics [69], under the assumption that RLTp $\simeq$ CSFp.

The model predicted values of the blood velocity in the pre-laminar segment of the CRA and CRV, denoted by

$$V_{CRA} = v_{z,CRA}(r=0, z=L/2), \qquad V_{CRV} = v_{z,CRV}(r=0, z=L/2), \tag{3.52}$$

respectively, and the flow rate Q are compared for different theoretical cases where IOP and CSFp vary independently or in association with changes in MAP as described below.

Case 1 : IOP and CSFp vary independently

(1a) IOP varies in the range from 15 to 50 mmHg, and CSFp is constant, equal to the baseline value of 7 mmHg;

(1b) IOP is constant, equal to the baseline value of 15 mmHg, and CSFp varies between 1 and 15 mmHg;

(1c) IOP is constant, equal to the baseline value of 15 mmHg, and CSFp varies between 15 and 60 mmHg;

while MAP is constant, equal to the baseline value of 93.33 mmHg.

Case 2 : IOP and CSFp change with MAP

(2a) MAP varies from 62.22 to 108.89 mmHg, CSFp varies as a function of MAP via

$$\text{CSFp} = 0.324\frac{\text{MAP}}{7} + 8.6 \text{ mmHg}, \tag{3.53}$$

and IOP is constant, equal to the baseline value of 15 mmHg;

(2b) MAP varies from 62.22 to 108.89 mmHg, CSFp varies as a function of MAP via Equation (3.53) and IOP varies as a function of MAP via

$$\text{IOP} = 0.243\frac{\text{MAP}}{7} + 11.76 \text{ mmHg}. \tag{3.54}$$

The relations between CSFp and MAP in Equation (3.53), and between IOP and MAP in Equation (3.53) have been extracted from the clinical measurements reported in [20] and [89], respectively. The values of geometric and elastic properties of the CRA and CRV are summarized in Table 3.4 and the values of the constant resistances in Table 3.2.

Figure 3.16 shows the variations of velocities V_{CRA} and V_{CRV} in the pre-laminar segment and variations of retinal blood flow Q as a function of the absolute value of the TLpD, for the cases (1a), (1b) ad (1c). The model predicts that, for a given value of the trans-laminar pressure difference TLpD, IOP affects retinal blood flow more than CSFp. For example, for $|\text{TLpD}| = 33$ mmHg (solid black line), when IOP $= 40$ mmHg and CSFp $= 7$ mmHg (case (1a) red curve) the flow rate Q is reduced by 38% compared to baseline, whereas for IOP $= 15$ mmHg and CSFp $= 48$ mmHg (case (1c) blue curve) Q is

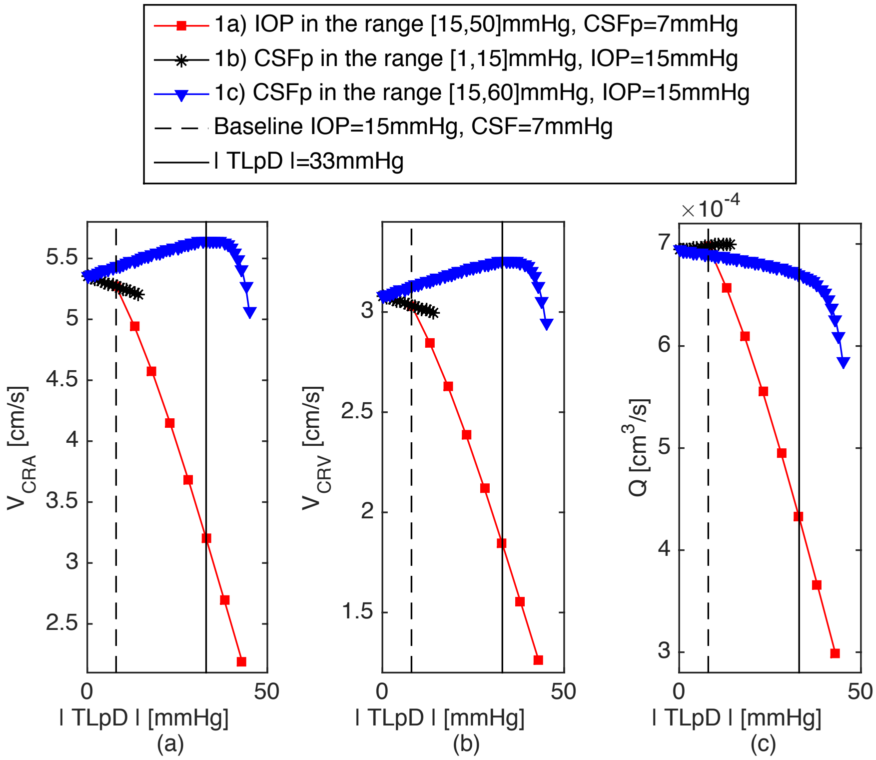

Fig. 3.16.: Variations of CRA and CRV mean velocity V_{CRA} (a) and V_{CRV} (b) in the pre-laminar segment, and variations of retinal blood flow Q (c) as functions of the absolute value of TLpD in cases (1a), (1b) and (1c). The black dashed line corresponds to the baseline case IOP $= 15$ mmHg and CSFp $= 7$ mmHg, and the black solid line corresponds to an absolute value of TLpD equal to 33 mmHg.

only reduced by 4% compared to baseline. Interestingly, flow rate reductions correspond to reductions in V_{CRA} and V_{CRV} in case (1a) and to increases in V_{CRA} and V_{CRV} in case (1c).

Figure 3.17 shows the variations of velocities V_{CRA} and V_{CRV} in the pre-laminar segment and variations of retinal blood flow Q as a function of CSFp, for case (2a) and (2b). The predictions in case (1b) are reported as baseline values. The model predicts that a decrease in CSFp from 13.64 to 11.48 mmHg due to MAP variations induces a decrease in V_{CRA}, V_{CRV} and Q of 55%, 57% and 57%, respectively. The differences between the model predictions corresponding to cases (2a) and (2b) are minimal (less than 2%).

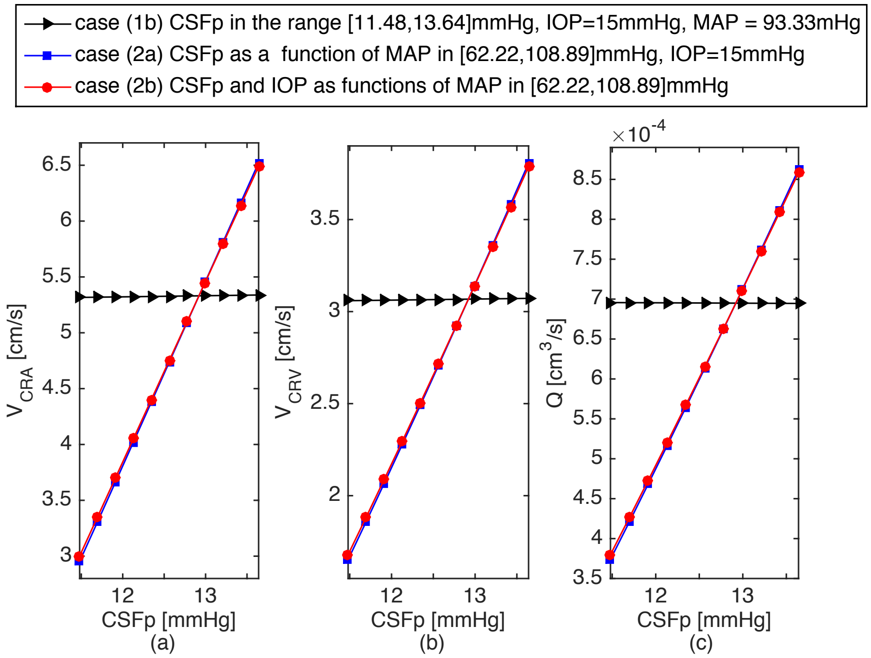

Fig. 3.17.: Variations of CRA and CRV mean velocity V_{CRA} (a) and V_{CRV} (b) in the prelaminar segment, and variations of retinal blood flow $\mathcal{Q}$ (c) as functions of CSFp in case (2a) and (2b). Case (1b) is reported as reference.

3.6 Discussion

The models results presented in Figures 3.8, 3.9 and 3.10 suggest the presence of a compressive region in the lamina cribrosa, which gets more pronounced as IOP increases. The presence of compressive regions in the lamina cribrosa has been suggested previously [18,90–92]. Nevertheless, the question of whether or not compressive stress arises in vivo in the lamina cribrosa of humans for some IOP levels is still controversial since stress distributions in the ocular tissues cannot be measured directly.

The agreement between model predictions and experimental measurements [22,23] is satisfactory when the effect of IOP on the retinal venules is taken into account, Figures 3.12 and 3.13. The mathematical model suggests that regions of radial compressive stress in the lamina cribrosa may indeed increase the vascular resistance of the central retinal vessels. However, this increase in vascular resistance is not enough to explain the decrease in the

CRA blood velocity induced by IOP elevation measured *in vivo* in humans by Harris et al. [22] and Findl et al. [23]. Instead, the model suggests that this decrease might be due to the IOP-induced increase in vascular resistance of the retinal venules.

The model results presented in Figures 3.15 suggest that CRA and CRV blood velocities in the pre-lamina and post-lamina segments behave differently as CSFp increases. Precisely, the predicted velocity in the pre-lamina segment shows an increase as CSFp increases, and, conversely, the predicted velocity in the post-lamina segment shows a decrease as CSFp increases. However, the agreement between model predictions and experimental measurements [24] is only qualitative (Table 3.5). This might be due to influence of MAP on CSFp and on retinal hemodynamics, neglected here.

The theoretical investigation of the effect of IOP and CSFp on central retinal vessels hemodynamics (Figure 3.16 assuming RLTp $\simeq$ CSFp), suggests that the relationship between measurements of blood velocity in the central retinal vessels and total retinal blood flow could have a different interpretation depending on whether IOP or CSFp is altered. Moreover, the mathematical model predictions suggest that changes in IOP have a stronger effect on retinal hemodynamics than changes in CSFp, even though these changes lead to the same TLpD. This might be due to the fact that, unlike CSFp, IOP acts directly on the intraocular retinal vessels, i.e. retinal venules resistance $\mathcal{R}_3$, thereby altering the vascular resistance of the microcirculation. Our model also suggests that the CSFp influence on retinal hemodynamics might be mediated by associated changes in MAP, see Figure 3.17.

The model is based on numerous simplifying assumptions. In particular, the lamina cribrosa is assumed to be homogeneous and the central perforation allowing the passage of the central retinal vessels is neglected. Also, the sclera affects the lamina cribrosa via the lateral tension computed by Laplace's law, but the sclera is not affected by the presence of the lamina. Similarly, the lamina cribrosa affects the CRA and CRV via the radial compression acting on a portion of the vessels external walls, but the lamina is not affected by the presence of the vessels. Moreover, one-dimensional and zero-dimensional reduced models have been used to study the hemodynamics in the central retinal vessels and in the retina, where the vessels walls have been assumed to be linear elastic thick shells and in the regime of small deformations, and the effect of IOP on retinal arterioles and capillaries has been neglected.

To assess the validity of such assumptions, we have used experimental and clinical studies. The model for the lamina cribrosa has been validated against the data obtained in dogs by Morgan et al. [18, 76]. The model for the coupling between the lamina cribrosa, the CRA, CRV and retina hemodynamics has been validated against three different sets of clinical data, namely those by Harris et al. [22], those by Findl et al. [23] and those by Querfurth et al. [24]. The agreement between the model predictions and the experimental/clinical data from these three different and unrelated studies is satisfactory, as shown in Figures 3.7, 3.12, 3.13 and Table 3.5, and this provides a good validation of our model.

4. OPERATOR SPLITTING APPROACH FOR MULTISCALE COUPLED SYSTEMS

As a first step in expanding the model presented in Chapter 3 to account for a three-dimensional description of the central retinal vessels, we derive in this Chapter a novel technique based on operator splitting for the time discretization of coupled systems of partial and ordinary differential equations. This technique allows to solve potential non-linearities in separate steps and ensures overall stability of the numerical method, giving, at the same time, flexibility in choosing the numerical method and discretization approach of each sub-step.

In Section 4.1 the general multiscale coupled problem is presented. We consider a non-stationary Stokes flow in a rigid domain $\Omega \subset \mathbb{R}^d$, with $d = 2, 3$ coupled with a zero-dimensional network via a *RC buffer*, as in [56]. In Section 4.2 the energy based operator splitting scheme is presented, and its solution procedure is described in Section 4.3. Stability and convergence of the scheme are tested in Section 4.4 in the case of $\Omega \subset \mathbb{R}^2$, and the numerical results are discussed in Section 4.5.

4.1 Coupled problem

Consider a non-stationary Stokes flow in a rigid domain $\Omega \subset \mathbb{R}^d$, with $d = 2, 3$, coupled with a 0D network via a RC buffer composed by a resistor characterized by a constant resistance $\mathcal{R}_p$ and by a capacitor characterized by a constant capacitance $\mathcal{C}_p$, as depicted in Figure 4.1 for the case $d = 3$. Let

$$\partial\Omega = \Sigma_0 \cup \Sigma_w \cup \Sigma_L, \tag{4.1}$$

where Σ_0 represents the inlet surface, Σ_w the lateral surface and Σ_L the outlet surface.

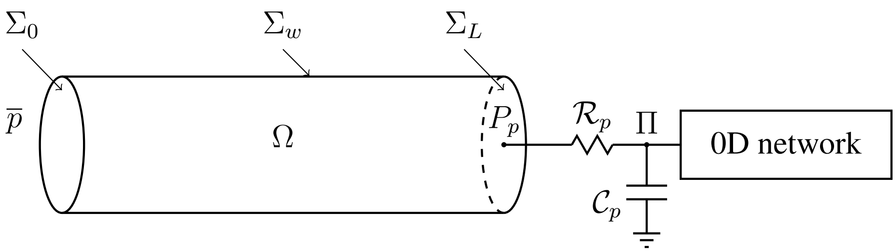

Fig. 4.1.: Sketch of a coupled problem between a fluid flow in Ω and a zero-dimensional (0D) network. The coupling occurs via a RC buffer of resistance $\mathcal{R}_p$ and capacitance $\mathcal{C}_p$. P_p is the nodal pressure at the interface Σ_L between Ω and the RC buffer and Π is the pressure at the interface between the RC buffer and the 0D network.

4.1.1 Stokes flow

We can write the Stokes equations (2.73) in Ω as

$$\boldsymbol{\nabla} \cdot \underline{\boldsymbol{v}} = 0 \qquad \text{in } \Omega \times (0, T), \tag{4.2a}$$

$$\rho \frac{\partial \underline{\boldsymbol{v}}}{\partial t} = -\boldsymbol{\nabla} p + \mu \boldsymbol{\Delta} \underline{\boldsymbol{v}} + \rho \underline{\boldsymbol{f}} \qquad \text{in } \Omega \times (0, T), \tag{4.2b}$$

where p is the fluid pressure, $\underline{\boldsymbol{v}}$ is the fluid velocity, ρ and μ are positive constants representing the fluid density and viscosity, respectively, and $\underline{\boldsymbol{f}}$ are given body forces per unit of mass. Note that we are considering the non-symmetric formulation of Stokes equations (for more details about the difference between symmetric and non-symmetric formulation please refer to Section 2.6.1). This system is equipped with the initial condition

$$\underline{\boldsymbol{v}}(t = 0) = \underline{\boldsymbol{v}}_0 \qquad \text{in } \Omega \tag{4.3}$$

and the boundary conditions

$$\underline{\boldsymbol{v}} = \underline{\boldsymbol{0}} \qquad \text{on } \Sigma_w \times (0, T), \tag{4.4a}$$

$$\left(-p \underline{\underline{\boldsymbol{I}}} + \mu \boldsymbol{\nabla} \underline{\boldsymbol{v}} \right) \underline{\boldsymbol{n}} = -\overline{p} \underline{\boldsymbol{n}} \qquad \text{on } \Sigma_0 \times (0, T), \tag{4.4b}$$

where $\underline{\underline{\boldsymbol{I}}}$ is the identity matrix, $\underline{\boldsymbol{n}}$ is the outward unit normal vector and $\overline{p} = \overline{p}(t)$ is a given function of time. Note that, contrary to Section 2.6.1, we are considering Neumann boundary conditions on the surface Σ_0, since in many application it is more natural to impose a pressure rather than a velocity profile. However, other choices may be possible as required by the specific application. On the coupling interface Σ_L, we impose continuity of flow and pressure, as discussed in 2.6.1, namely

$$\left(-p\underline{\underline{\boldsymbol{I}}} + \mu\boldsymbol{\nabla}\underline{\boldsymbol{v}}\right)\underline{\boldsymbol{n}} = -P_p\underline{\boldsymbol{n}} \qquad \text{on } \Sigma_L \times (0,T), \tag{4.5a}$$

$$\int_{\Sigma_L} \underline{\boldsymbol{v}} \cdot \underline{\boldsymbol{n}} d\sigma = \frac{P_p - \Pi}{\mathcal{R}_p} \qquad \text{in } (0,T), \tag{4.5b}$$

where $P_p = P_p(t)$ and $\Pi = \Pi(t)$ are the unknown pressures at the nodes of the RC buffer that couple the Stokes flow with the flow in the 0D network.

4.1.2 Zero-dimensional network

The application of Kirchhoff's law to the RC buffer and the 0D network can be expressed as the following system of ordinary differential equations

$$\frac{d\underline{\boldsymbol{y}}}{dt} = \underline{\underline{\boldsymbol{N}}}(\underline{\boldsymbol{y}}, t) + \underline{\boldsymbol{r}}(\underline{\boldsymbol{y}}, t) \quad \text{in } (0,T), \tag{4.6}$$

where $\underline{\boldsymbol{y}}$ is the vector of state variables, $\underline{\underline{\boldsymbol{N}}}$ is a matrix and $\underline{\boldsymbol{r}}$ is a vector, which both might depend on $\underline{\boldsymbol{y}}$ and on time t.

Here, we focus on the particular case in which $\underline{\boldsymbol{y}}$ can be expressed as

$$\underline{\boldsymbol{y}} = \underline{\underline{\boldsymbol{C}}}\,\underline{\boldsymbol{\Pi}} = \underline{\underline{\boldsymbol{C}}}\begin{bmatrix} \Pi \\ \underline{\boldsymbol{\mathcal{P}}} \end{bmatrix}, \tag{4.7}$$

where $\underline{\boldsymbol{\Pi}} \in \mathbb{R}^{m+1}$ is the column vector of unknown pressures at the nodes of the RC buffer and the 0D network, $\underline{\boldsymbol{\mathcal{P}}} \in \mathbb{R}^m$ is the column vector of the unknown pressures at the m nodes of the 0D network and $\underline{\underline{\boldsymbol{C}}} \in \mathbb{R}^{(m+1)\times(m+1)}$ is the matrix that represents capacitive connections in the RC buffer and the 0D network. Then, Equation 4.6 can be reformulated as follows

$$\frac{d\left(\underline{\underline{\boldsymbol{C}}}\,\underline{\boldsymbol{\Pi}}\right)}{dt} = -\underline{\underline{\boldsymbol{R}}}(\underline{\boldsymbol{\Pi}})\underline{\boldsymbol{\Pi}} + (P_p - \Pi)\underline{\boldsymbol{h}} + \underline{\boldsymbol{g}}(\underline{\boldsymbol{\Pi}}, t) \quad \text{in } (0,T). \tag{4.8}$$

The matrix $\underline{\underline{\boldsymbol{R}}} \in \mathbb{R}^{(m+1)\times(m+1)}$ represents the resistive connections in the RC buffer and the 0D network; $\underline{\underline{\boldsymbol{R}}}$ might include a nonlinear dependence on $\underline{\boldsymbol{\Pi}}$. The vector $\underline{\boldsymbol{h}} \in \mathbb{R}^{m+1}$ is defined as

$$\underline{\boldsymbol{h}} = \left[\frac{1}{\mathcal{R}_p}, \underline{\mathbf{0}}\right]^T \in \mathbb{R}^{m+1}, \tag{4.9}$$

and the vector $\underline{\boldsymbol{g}} \in \mathbb{R}^{m+1}$ contains the forcing terms of the 0D network. Moreover, we assume that $\underline{\underline{\boldsymbol{C}}}$ can be expressed as

$$\underline{\underline{\boldsymbol{C}}} = \begin{bmatrix} \mathcal{C}_p & \underline{\mathbf{0}}^T \\ \underline{\mathbf{0}} & \underline{\underline{\boldsymbol{\mathcal{C}}}} \end{bmatrix} \in \mathbb{R}^{(m+1)\times(m+1)}, \tag{4.10}$$

where $\underline{\underline{\boldsymbol{\mathcal{C}}}} \in \mathbb{R}^{m\times m}$ is the matrix representing the capacitive connections in the 0D network. In particular, (4.10) implies that no other capacitors, except for $\mathcal{C}_p$, are connected to the RC buffer. System (4.8) is equipped with the initial condition

$$\underline{\boldsymbol{\Pi}}(t=0) = \underline{\boldsymbol{\Pi}}_0 = [\Pi_0, \underline{\boldsymbol{\mathcal{P}}}_0]. \tag{4.11}$$

4.1.3 Energy identity

The energy identity of the Stokes problem can be obtained by considering the L^2 product of the conservation of linear momentum in (4.2b) and $\underline{\boldsymbol{v}}$, as in Sections 2.6.1 and 2.6.2. Utilizing the divergence free condition, the boundary conditions (4.4) and the interface conditions (4.5), we obtain

$$\frac{d}{dt}\left(\frac{\rho}{2}\|\underline{\boldsymbol{v}}\|^2_{L^2(\Omega)}\right) + \mu\|\boldsymbol{\nabla}\underline{\boldsymbol{v}}\|^2_{L^2(\Omega)} = -\overline{p}\int_{\Sigma_0}\underline{\boldsymbol{v}}\cdot\underline{\boldsymbol{n}}\,d\sigma - P_p\int_{\Sigma_L}\underline{\boldsymbol{v}}\cdot\underline{\boldsymbol{n}}\,d\sigma + \int_{\Omega}\rho\underline{\boldsymbol{f}}\cdot\underline{\boldsymbol{n}}d\Omega. \tag{4.12}$$

The energy identity of the RC buffer and the 0D network can be obtained by multiplying Equation 4.8 by $\underline{\boldsymbol{\Pi}}$, yielding

$$\frac{1}{2}\frac{d}{dt}\left(\underline{\boldsymbol{\Pi}}^T\underline{\underline{\boldsymbol{C}}}\,\underline{\boldsymbol{\Pi}}\right) + \underline{\boldsymbol{\Pi}}^T\underline{\underline{\boldsymbol{R}}}\,\underline{\boldsymbol{\Pi}} + \mathcal{R}_p\left(\int_{\Sigma_L}\underline{\boldsymbol{v}}\cdot\underline{\boldsymbol{n}}\,d\sigma\right)^2 = P_p\int_{\Sigma_L}\underline{\boldsymbol{v}}\cdot\underline{\boldsymbol{n}}\,d\sigma + \underline{\boldsymbol{g}}\cdot\underline{\boldsymbol{\Pi}}. \tag{4.13}$$

Now adding Equations (4.12) and (4.13), we obtain the following energy identity of the coupled problem

$$\frac{d}{dt}\mathcal{E}(t) + \mathcal{D}(t) = \mathcal{F}(t) \quad \text{in } (0,T), \tag{4.14}$$

where

$$\begin{aligned}
\mathcal{E}(t) &= \frac{\rho}{2}\|\underline{\boldsymbol{v}}\|^2_{L^2(\Omega)} + \frac{1}{2}\underline{\boldsymbol{\Pi}}^T \underline{\underline{\boldsymbol{C}}}\,\underline{\boldsymbol{\Pi}}, \\
\mathcal{D}(t) &= \mu\|\boldsymbol{\nabla}\underline{\boldsymbol{v}}\|^2_{L^2(\Omega)} + \underline{\boldsymbol{\Pi}}^T \underline{\underline{\boldsymbol{R}}}\,\underline{\boldsymbol{\Pi}} + \mathcal{R}_p\left(\int_{\Sigma_L} \underline{\boldsymbol{v}}\cdot\underline{\boldsymbol{n}}\,d\sigma\right)^2, \\
\mathcal{F}(t) &= -\overline{p}\int_{\Sigma_0} \underline{\boldsymbol{v}}\cdot\underline{\boldsymbol{n}}\,d\sigma + \int_{\Omega} \rho\underline{\boldsymbol{f}}\cdot\underline{\boldsymbol{n}}d\Omega + \underline{\boldsymbol{g}}\cdot\underline{\boldsymbol{\Pi}}.
\end{aligned} \tag{4.15}$$

$\mathcal{E}(t)$ is a non-negative functional describing the energy of the coupled system and is given by the sum of the kinetic energy of the fluid in Ω and the potential energy stored in the capacitors of the RC buffer and the 0D network. $\mathcal{D}(t)$ is a non-negative functional describing the dissipation of the coupled system and is given by the sum of the viscous dissipation of the fluid in Ω and the resistive dissipation in the RC buffer and the 0D network. The functional $\mathcal{F}(t)$ does not have a definite sign a priori and is given by the sum of the coupled problem forcing terms. If all the forcing terms are zero, then the coupled system is a dissipative system, as described in Section 2.2, namely

$$\mathcal{E}(t) \leq \mathcal{E}(0) \quad \forall t \in (0,T). \tag{4.16}$$

4.2 Splitting scheme

In this section we describe a splitting scheme for the coupled problem presented in Section 4.1. The scheme is based on the first-order operator splitting scheme described in Section 2.6.3. Consider the time discretization Δt and let $t^n = n\Delta t$. Given

$$\underline{\boldsymbol{v}}^0 = \underline{\boldsymbol{v}}(t=0) = \underline{\boldsymbol{v}}_0 \qquad \text{and} \qquad \underline{\boldsymbol{\Pi}}^0 = \underline{\boldsymbol{\Pi}}(t=0) = \underline{\boldsymbol{\Pi}}_0, \tag{4.17}$$

for any $n \geq 0$, compute $\underline{\boldsymbol{v}}^{n+1}$ and $\underline{\boldsymbol{\Pi}}^{n+1}$ as follows

Step 1 Given $\underline{\boldsymbol{v}}^n$ and $\underline{\boldsymbol{\Pi}}^n$, solve

$$\boldsymbol{\nabla}\cdot\underline{\boldsymbol{v}} = 0 \qquad \text{in } \Omega\times(t^n,t^{n+1}), \tag{4.18a}$$

$$\rho\frac{\partial\underline{\boldsymbol{v}}}{\partial t} = -\boldsymbol{\nabla}p + \mu\boldsymbol{\Delta}\underline{\boldsymbol{v}} + \rho\underline{\boldsymbol{f}} \qquad \text{in } \Omega\times(t^n,t^{n+1}), \tag{4.18b}$$

$$\underline{\underline{\boldsymbol{C}}}\frac{d\underline{\boldsymbol{\Pi}}}{dt} = (P_p - \Pi)\underline{\boldsymbol{h}} \qquad \text{in } (t^n,t^{n+1}), \tag{4.18c}$$

with initial conditions

$$\underline{\boldsymbol{v}}(t^n) = \underline{\boldsymbol{v}}^n \qquad \text{in } \Omega, \tag{4.18d}$$

$$\underline{\boldsymbol{\Pi}}(t^n) = \underline{\boldsymbol{\Pi}}^n, \tag{4.18e}$$

boundary conditions

$$\underline{\boldsymbol{v}} = \underline{\boldsymbol{0}} \qquad \text{on } \Sigma_w \times (t^n, t^{n+1}), \tag{4.18f}$$

$$\left(-p\underline{\underline{\boldsymbol{I}}} + \mu\boldsymbol{\nabla}\underline{\boldsymbol{v}}\right)\underline{\boldsymbol{n}} = -\bar{p}\underline{\boldsymbol{n}} \qquad \text{on } \Sigma_0 \times (t^n, t^{n+1}), \tag{4.18g}$$

and interface conditions

$$\left(-p\underline{\underline{\boldsymbol{I}}} + \mu\boldsymbol{\nabla}\underline{\boldsymbol{v}}\right)\underline{\boldsymbol{n}} = -P_p\underline{\boldsymbol{n}} \qquad \text{on } \Sigma_L \times (t^n, t^{n+1}), \tag{4.18h}$$

$$\int_{\Sigma_L} \underline{\boldsymbol{v}} \cdot \underline{\boldsymbol{n}} d\sigma = \frac{P_p - \Pi}{\mathcal{R}_p} \qquad \text{in } (t^n, t^{n+1}). \tag{4.18i}$$

Set

$$\underline{\boldsymbol{v}}^{n+\frac{1}{2}} = \underline{\boldsymbol{v}}(t^{n+1}), \qquad \underline{\boldsymbol{\Pi}}^{n+\frac{1}{2}} = \underline{\boldsymbol{\Pi}}(t^{n+1}), \tag{4.18j}$$

$$p^{n+1} = p(t^{n+1}) \qquad P_p^{n+1} = \mathcal{R}_p \int_{\Sigma_L} \underline{\boldsymbol{v}}(t^{n+1}) \cdot \underline{\boldsymbol{n}} d\sigma + \Pi(t^{n+1}). \tag{4.18k}$$

Step 2 Given $\underline{\boldsymbol{v}}^{n+\frac{1}{2}}$ and $\underline{\boldsymbol{\Pi}}^{n+\frac{1}{2}}$, solve

$$\rho\frac{\partial\underline{\boldsymbol{v}}}{\partial t} = \underline{\boldsymbol{0}} \qquad \text{in } \Omega \times (t^n, t^{n+1}), \tag{4.19a}$$

$$\underline{\underline{\boldsymbol{C}}}\frac{d\underline{\boldsymbol{\Pi}}}{dt} = -\underline{\underline{\boldsymbol{R}}}(\underline{\boldsymbol{\Pi}})\underline{\boldsymbol{\Pi}} + \underline{\boldsymbol{g}}(\underline{\boldsymbol{\Pi}}, t) \qquad \text{in } (t^n, t^{n+1}), \tag{4.19b}$$

with initial conditions

$$\underline{\boldsymbol{v}}(t^n) = \underline{\boldsymbol{v}}^{n+\frac{1}{2}} \qquad \text{in } \Omega, \tag{4.19c}$$

$$\underline{\boldsymbol{\Pi}}(t^n) = \underline{\boldsymbol{\Pi}}^{n+\frac{1}{2}}. \tag{4.19d}$$

Set

$$\underline{\boldsymbol{v}}^{n+1} = \underline{\boldsymbol{v}}(t^{n+1}), \qquad \underline{\boldsymbol{\Pi}}^{n+1} = \underline{\boldsymbol{\Pi}}(t^{n+1}). \tag{4.19e}$$

Note that each step of the splitting scheme is not discretized in time and space, however it is solved in the discrete time interval (t^n, t^{n+1}). Hence, the splitting scheme described above allows for different choices for the numerical scheme and discretization approach used in each sub-step. In Step 2, Equation (4.19a) implies that the velocity $\underline{\boldsymbol{v}}$ is not updated, namely

$$\underline{\boldsymbol{v}}^{n+1} = \underline{\boldsymbol{v}}^{n+\frac{1}{2}}. \tag{4.20}$$

Note that, in Step 2, also p and P_p are not updated. Here, we have considered the forcing term $\underline{\boldsymbol{g}}$ as part of Step 2. However, depending on what is more convenient for the particular 0D network, $\underline{\boldsymbol{g}}$ can be included either in Step 1 (4.18c) or in Step 2 (4.19b).

The scheme presented here is, at most, first-order in time, provided that in each sub-step the numerical method used to discretize the time derivative is al least of first order. In the next section we will study the stability of the scheme by looking at the energy identities of the sub-steps.

4.2.1 Energy identities

Following the same steps as in Section 4.1.3, the energy identities in each sub-step of the splitting scheme can be obtained.

Step 1 The energy identity of Step 1 can be expressed as

$$\frac{d}{dt}\mathcal{E}_1(t) + \mathcal{D}_1(t) = \mathcal{F}_1(t) \quad \text{in } (t^n, t^{n+1}), \tag{4.21a}$$

where

$$\mathcal{E}_1(t) = \frac{\rho}{2}\|\underline{\boldsymbol{v}}\|^2_{L^2(\Omega)} + \frac{1}{2}\underline{\boldsymbol{\Pi}}^T \underline{\underline{\boldsymbol{C}}}\, \underline{\boldsymbol{\Pi}}, \tag{4.21b}$$

$$\mathcal{D}_1(t) = \mu\|\boldsymbol{\nabla}\underline{\boldsymbol{v}}\|^2_{L^2(\Omega)} + \mathcal{R}_p\left(\int_{\Sigma_L} \underline{\boldsymbol{v}} \cdot \underline{\boldsymbol{n}}\, d\sigma\right)^2, \tag{4.21c}$$

$$\mathcal{F}_1(t) = -\overline{p}\int_{\Sigma_0} \underline{\boldsymbol{v}} \cdot \underline{\boldsymbol{n}}\, d\sigma + \int_{\Omega} \rho \underline{\boldsymbol{f}} \cdot \underline{\boldsymbol{n}} d\Omega. \tag{4.21d}$$

Step 2 The energy identity of Step 2 can be expressed as

$$\frac{d}{dt}\mathcal{E}_2(t) + \mathcal{D}_2(t) = \mathcal{F}_2(t) \quad \text{in } (t^n, t^{n+1}), \tag{4.22a}$$

where

$$\mathcal{E}_2(t) = \frac{\rho}{2}\|\underline{\boldsymbol{v}}\|^2_{L^2(\Omega)} + \frac{1}{2}\underline{\boldsymbol{\Pi}}^T \underline{\underline{\boldsymbol{C}}}\, \underline{\boldsymbol{\Pi}}, \tag{4.22b}$$

$$\mathcal{D}_2(t) = \underline{\boldsymbol{\Pi}}^T \underline{\underline{\boldsymbol{R}}}\, \underline{\boldsymbol{\Pi}}, \tag{4.22c}$$

$$\mathcal{F}_2(t) = \underline{\boldsymbol{g}} \cdot \underline{\boldsymbol{\Pi}}. \tag{4.22d}$$

In the absence of forcing terms $\mathcal{F}_1 = \mathcal{F}_2 = 0$, it follows that

$$\mathcal{E}_1(t^{n+1}) \leq \mathcal{E}_1(t^n) \quad \text{and} \quad \mathcal{E}_2(t^{n+1}) \leq \mathcal{E}_2(t^n) \quad \forall n \geq 0. \tag{4.23}$$

Due to the choice of initial conditions for the sub-steps, we have that

$$\mathcal{E}_2(t^{n+1}) \leq \mathcal{E}_2(t^n) = \mathcal{E}_1(t^{n+1}) \leq \mathcal{E}_1(t^n) \quad \forall n \geq 0, \tag{4.24}$$

from which it follows that our scheme is unconditionally stable in time. This implies that the choice of numerical methods and discretization in each sub-step will affect only the accuracy of the solution, but it will not affect the stability of the scheme. Note that the stability of the scheme does not depend on whether $\underline{\boldsymbol{g}}$ is included in Step 1 or in Step 2.

4.3 Solution procedure

Here we describe the solution procedure implemented to obtain the results presented in Section 4.4. Precisely, we describe the approach utilized for the discretization in time and space and for the assembly of the matrices in the algebraic system.

Step 1

Let

$$\mathbf{V} = \mathbf{H}^1_{\Sigma_w}(\Omega) = \left\{ \underline{\boldsymbol{w}} \in \mathbf{H}^1(\Omega) \,|\, \quad \underline{\boldsymbol{v}} = \underline{\mathbf{0}} \quad \text{on } \Sigma_w \right\}. \tag{4.25}$$

For any $n \geq 0$, the variational formulation in Step 1 (4.18) is:

Find $\underline{\boldsymbol{v}} \in L^2(t^n, t^{n+1}; \mathbf{V})$, $p \in L^2(t^n, t^{n+1}; L^2(\Omega))$ and $\underline{\boldsymbol{\Pi}} \in \left[C^1(t^n, t^{n+1})\right]^{m+1}$, i.e. the space of continuos vectorial function in (t^n, t^{n+1}), such that

$$\begin{aligned}\rho \int_\Omega \frac{\partial \underline{\boldsymbol{v}}}{\partial t} \cdot \underline{\boldsymbol{w}}\, d\Omega - \int_\Omega p \boldsymbol{\nabla} \cdot \underline{\boldsymbol{w}}\, d\Omega - \int_\Omega q \boldsymbol{\nabla} \cdot \underline{\boldsymbol{v}} d\Omega + \mu \int_\Omega \boldsymbol{\nabla} \underline{\boldsymbol{v}} : \boldsymbol{\nabla} \underline{\boldsymbol{w}} d\Omega \\ + \mathcal{R}_p \left(\int_{\Sigma_L} \underline{\boldsymbol{v}} \cdot \underline{\boldsymbol{n}}\, d\sigma \right) \left(\int_{\Sigma_L} \underline{\boldsymbol{w}} \cdot \underline{\boldsymbol{n}}\, d\sigma \right) + \Pi \int_{\Sigma_L} \underline{\boldsymbol{w}} \cdot \underline{\boldsymbol{n}}\, d\sigma \\ = -\overline{p} \int_{\Sigma_0} \underline{\boldsymbol{w}} \cdot \underline{\boldsymbol{n}}\, d\sigma + \rho \int_\Omega \underline{\boldsymbol{f}} \cdot \underline{\boldsymbol{w}} d\Omega \\ \forall \underline{\boldsymbol{w}} \in \mathbf{V} \quad \forall q \in L^2(\Omega) \quad \forall t \in (t^n, t^{n+1}), \quad \text{(4.26a)}\end{aligned}$$

$$\mathcal{C}_p \frac{d\Pi}{dt} = \int_{\Sigma_L} \underline{\boldsymbol{v}} \cdot \underline{\boldsymbol{n}}\, d\sigma \qquad \forall t \in (t^n, t^{n+1}), \qquad \text{(4.26b)}$$

Let us define the following linear and bilinear variational forms:

$$\begin{array}{lrrcl} & a: & \mathbf{V} \times \mathbf{V} & \to & \mathbb{R} \\ & & (\underline{\boldsymbol{v}}, \underline{\boldsymbol{w}}) & \mapsto & a(\underline{\boldsymbol{v}}, \underline{\boldsymbol{w}}) = \mu \int_\Omega \boldsymbol{\nabla} \underline{\boldsymbol{v}} : \boldsymbol{\nabla} \underline{\boldsymbol{w}} d\Omega, \\ & b: & L^2(\Omega) \times \mathbf{V} & \to & \mathbb{R} \\ & & (p, \underline{\boldsymbol{w}}) & \mapsto & b(p, \underline{\boldsymbol{w}}) = -\int_\Omega p \boldsymbol{\nabla} \cdot \underline{\boldsymbol{w}} d\Omega, \\ \text{for } i = 0, L & d_i: & \mathbf{V} & \to & \mathbb{R} \\ & & \underline{\boldsymbol{w}} & \mapsto & d_i(\underline{\boldsymbol{w}}) = \int_{\Sigma_i} \underline{\boldsymbol{w}} \cdot \underline{\boldsymbol{n}}\, d\sigma, \\ & e: & \mathbf{V} \times \mathbf{V} & \to & \mathbb{R} \\ & & (\underline{\boldsymbol{v}}, \underline{\boldsymbol{w}}) & \mapsto & e(\underline{\boldsymbol{v}}, \underline{\boldsymbol{w}}) = \mathcal{R}_p d_L(\underline{\boldsymbol{v}}) d_L(\underline{\boldsymbol{w}}), \\ & m: & \mathbf{V} \times \mathbf{V} & \to & \mathbb{R} \\ & & (\underline{\boldsymbol{v}}, \underline{\boldsymbol{w}}) & \mapsto & m(\underline{\boldsymbol{v}}, \underline{\boldsymbol{w}}) = \rho \int_\Omega \underline{\boldsymbol{v}} \cdot \underline{\boldsymbol{w}} d\Omega. \end{array} \qquad \text{(4.27)}$$

Then, Equation (4.26a) can be expressed as

$$\begin{aligned} m\left(\frac{\partial \underline{\boldsymbol{v}}}{\partial t}, \underline{\boldsymbol{w}}\right) + b(p, \underline{\boldsymbol{w}}) + b(q, \underline{\boldsymbol{v}}) + a(\underline{\boldsymbol{v}}, \underline{\boldsymbol{w}}) + e(\underline{\boldsymbol{v}}, \underline{\boldsymbol{w}}) + \Pi d_L(\underline{\boldsymbol{w}}) \\ = -\overline{p} d_0(\underline{\boldsymbol{w}}) + m(\underline{\boldsymbol{f}}, \underline{\boldsymbol{w}}), \quad \text{(4.28)}\end{aligned}$$

and Equation (4.26b) can be expressed as

$$\mathcal{C}_p \frac{d\Pi}{dt} = d_L(\underline{\boldsymbol{v}}). \tag{4.29}$$

For a fixed $n \geq 0$, consider the time discretization Δt_1 for the time interval (t^n, t^{n+1}) and let $t^k = t^n + k\Delta t_1$. Then the semi-discretized version of Step 1 (4.26) can be written as:

Given $\underline{\boldsymbol{v}}^0 = \underline{\boldsymbol{v}}(t^n)$, $p^0 = p(t^n)$ and $\underline{\boldsymbol{\Pi}}^0 = \underline{\boldsymbol{\Pi}}(t^n)$, for any k find $\underline{\boldsymbol{v}}^{k+1} \in \mathbf{V}$, $p^{k+1} \in L^2(\Omega)$ and $\underline{\boldsymbol{\Pi}}^{k+1}$ such that

$$\begin{aligned} \frac{1}{\Delta t_1} m\left(\underline{\boldsymbol{v}}^{k+1}, \underline{\boldsymbol{w}}\right) + b(p^{k+1}, \underline{\boldsymbol{w}}) + b(q, \underline{\boldsymbol{v}}^{k+1}) + a(\underline{\boldsymbol{v}}^{k+1}, \underline{\boldsymbol{w}}) + e(\underline{\boldsymbol{v}}^{k+1}, \underline{\boldsymbol{w}}) \\ + \Pi^{k+1} d_L(\underline{\boldsymbol{w}}) = -\overline{p}^{k+1} d_0(\underline{\boldsymbol{w}}) + m(\underline{\boldsymbol{f}}^{k+1}, \underline{\boldsymbol{w}}) + \frac{1}{\Delta t_1} m\left(\underline{\boldsymbol{v}}^{k}, \underline{\boldsymbol{w}}\right) \\ \forall \underline{\boldsymbol{w}} \in \mathbf{V} \quad \forall q \in L^2(\Omega), \end{aligned} \tag{4.30a}$$

$$\frac{\mathcal{C}_p}{\Delta t_1} \Pi^{k+1} - d_L(\underline{\boldsymbol{v}}^{k+1}) = \frac{\mathcal{C}_p}{\Delta t_1} \Pi^{k}, \tag{4.30b}$$

where a backward Euler method has been used to discretize the time derivatives. Note that equations (4.26a) and (4.26b) have been coupled implicitly in order to avoid possible instabilities, as discussed in Section 2.6.2.

Let us now consider the spatial discretization of Ω and let T_h be a regular triangulation of Ω, where h is defined as

$$h = \max_{K \in \mathsf{T}_h} h_K, \tag{4.31}$$

where K is any triangle in T_h and h_K is its diameter. Let $\mathbf{V}_h \subset \mathbf{V}$ and $Q_h \subset L^2(\Omega)$ be two finite element spaces of dimensions

$$N_v = \text{dim}\mathbf{V}_h < \infty, \qquad N_p = \text{dim}Q_h < \infty. \tag{4.32}$$

Let $\left\{\underline{\boldsymbol{\psi}}_j\right\}_{j=1}^{N_v}$ be a vectorial basis for $\mathbf{V}_h$ and let $\{\phi_i\}_{i=1}^{N_p}$ be a scalar basis for Q_h. Then, $\underline{\boldsymbol{v}}_h$ and p_h can be expressed as

$$\underline{\boldsymbol{v}}_h = \sum_{j=1}^{Nv} v_j \underline{\boldsymbol{\psi}}_j, \qquad p_h = \sum_{i=1}^{Np} p_i \phi_i. \tag{4.33}$$

Then, the *Galerkin problem* corresponding to (4.30) can be expressed as:

Given $\underline{\boldsymbol{v}}_h^0$, p_h^0 and $\underline{\boldsymbol{\Pi}}^0$, for any k, find $\underline{\boldsymbol{v}}_h^{k+1} \in \mathbf{V}_h$, $p_h^{k+1} \in Q_h$ and Π^{k+1} such that

$$
\begin{aligned}
\frac{1}{\Delta t_1} m\left(\underline{\boldsymbol{v}}_h^{k+1}, \underline{\boldsymbol{w}}_h\right) + b(p_h^{k+1}, \underline{\boldsymbol{w}}_h) + b(q_h, \underline{\boldsymbol{v}}_h^{k+1}) + a(\underline{\boldsymbol{v}}_h^{k+1}, \underline{\boldsymbol{w}}_h) + e(\underline{\boldsymbol{v}}_h^{k+1}, \underline{\boldsymbol{w}}_h) \\
+ \Pi^{k+1} d_L(\underline{\boldsymbol{w}}_h) = -\overline{p}_h^{k+1} d_0(\underline{\boldsymbol{w}}_h) + m(\underline{\boldsymbol{f}}^{k+1}, \underline{\boldsymbol{w}}_h) + \frac{1}{\Delta t_1}\left(\underline{\boldsymbol{v}}_h^k, \underline{\boldsymbol{w}}_h\right) \\
\forall \underline{\boldsymbol{w}}_h \in \mathbf{V}_h \quad \forall q_h \in Q_h, \quad \text{(4.34a)}
\end{aligned}
$$

$$
\frac{\mathcal{C}_p}{\Delta t_1}\Pi^{k+1} - d_L(\underline{\boldsymbol{v}}_h^{k+1}) = \frac{\mathcal{C}_p}{\Delta t_1}\Pi^k. \tag{4.34b}
$$

Now, if we substitute (4.33) into the Galerkin problem (4.34) and we choose $\underline{\boldsymbol{w}}_h = \underline{\boldsymbol{\psi}}_j$ and $q_h = \phi_i$ we obtain the following algebraic system

$$
\begin{bmatrix}
\frac{1}{\Delta t_1}\underline{\underline{\boldsymbol{M}}} + \underline{\underline{\boldsymbol{A}}} + \underline{\underline{\boldsymbol{E}}} & \underline{\underline{\boldsymbol{B}}} & \underline{\boldsymbol{d}}_L \\
\underline{\underline{\boldsymbol{B}}}^T & \underline{\underline{\boldsymbol{0}}} & \underline{\boldsymbol{0}} \\
-\underline{\boldsymbol{d}}_L^T & \underline{\boldsymbol{0}}^T & \frac{\mathcal{C}_p}{\Delta t_1}
\end{bmatrix}
\begin{bmatrix}
\underline{\boldsymbol{V}}^{k+1} \\
\underline{\boldsymbol{P}}^{k+1} \\
\Pi^{k+1}
\end{bmatrix}
=
\begin{bmatrix}
-\overline{p}^{k+1}\underline{\boldsymbol{d}}_0 + \underline{\boldsymbol{F}} + \frac{1}{\Delta t_1}\underline{\underline{\boldsymbol{M}}}\,\underline{\boldsymbol{V}}^k \\
\underline{\boldsymbol{0}} \\
\frac{\mathcal{C}_p}{\Delta t_1}\Pi^k
\end{bmatrix},
\tag{4.35}
$$

where $\underline{\boldsymbol{V}}^{k+1}, \underline{\boldsymbol{V}}^k \in \mathbb{R}^{N_v}$ are the column vectors of the components of $\underline{\boldsymbol{v}}_h^{k+1}$ and $\underline{\boldsymbol{v}}_h^k$ in the basis $\left\{\underline{\boldsymbol{\psi}}_j\right\}_{j=1}^{N_v}$, respectively, and $\underline{\boldsymbol{P}}^{k+1} \in \mathbb{R}^{N_p}$ is the column vector of the components of p_h^{k+1} in the basis $\{\phi_i\}_{i=1}^{N_p}$. The elements of the matrices $\underline{\underline{\boldsymbol{M}}}, \underline{\underline{\boldsymbol{A}}} \in \mathbb{R}^{N_v \times N_v}$ are defined as

$$
M_{ij} = \left(\underline{\boldsymbol{\psi}}_j, \underline{\boldsymbol{\psi}}_i\right) = \int_\Omega \underline{\boldsymbol{\psi}}_j \cdot \underline{\boldsymbol{\psi}}_i d\Omega, \qquad A_{ij} = a\left(\underline{\boldsymbol{\psi}}_j, \underline{\boldsymbol{\psi}}_i\right), \tag{4.36}
$$

the elements of the column vectors $\underline{\boldsymbol{d}}_0, \underline{\boldsymbol{d}}_L \in \mathbb{R}^{N_v}$ are defined as

$$
d_{0,j} = d_0(\underline{\boldsymbol{\psi}}_j), \qquad d_{L,j} = d_L(\underline{\boldsymbol{\psi}}_j), \tag{4.37}
$$

the matrix $\underline{\underline{\boldsymbol{E}}} \in \mathbb{R}^{N_v \times N_v}$ is defined as

$$
\underline{\underline{\boldsymbol{E}}} = \underline{\boldsymbol{d}}_L \, \underline{\boldsymbol{d}}_L^T, \tag{4.38}
$$

and the elements of the matrix $\underline{\underline{\boldsymbol{B}}} \in \mathbb{R}^{N_v \times N_p}$ are defined as

$$
B_{ji} = b(\phi_i, \underline{\boldsymbol{\psi}}_j). \tag{4.39}
$$

On the right-hand side of (4.35), the elements of the column vector $\underline{\boldsymbol{F}} \in \mathbb{R}^{N_v}$ are defined as

$$F_j = m\left(\underline{\boldsymbol{f}}^{k+1}, \underline{\boldsymbol{\psi}}_j\right). \tag{4.40}$$

As discussed in Section 2.6.2, the choice of an implicit coupling changes the pattern of the global algebraic matrix in (4.35). Indeed, the global matrix has more non-zero entries than the explicit case and it is not symmetric. For more details on the Galerkin finite element method we refer to [93].

Step 2

For a fixed $n \geq 0$, consider the time discretization Δt_2 for the time interval (t^n, t^{n+1}) and let $t^l = t^n + l\Delta t_2$. Then the discretized version of Step 2 (4.19) can be written as: Given $\underline{\boldsymbol{\Pi}}^0 = \underline{\boldsymbol{\Pi}}(t^n)$, for any l find $\underline{\boldsymbol{\Pi}}^{l+1}$ such that

$$\frac{1}{\Delta t_2}\underline{\underline{\boldsymbol{C}}}\,\underline{\boldsymbol{\Pi}}^{l+1} + \underline{\underline{\boldsymbol{R}}}(\underline{\boldsymbol{\Pi}}^*)\underline{\boldsymbol{\Pi}}^{l+1} = \underline{\boldsymbol{g}}(\underline{\boldsymbol{\Pi}}^{l+1}, t^{l+1}) + \frac{1}{\Delta t_2}\underline{\underline{\boldsymbol{C}}}\,\underline{\boldsymbol{\Pi}}^{l} \tag{4.41}$$

where $(\cdot)^*$ might be equal to $(\cdot)^{l+1}$ or $(\cdot)^l$, depending on how we choose to treat nonlinearities. Recall that in Step 2 (4.19) the fluid velocity $\underline{\boldsymbol{v}}$ is not updated.

4.4 Results

Here we will the splitting scheme introduced in Section 4.2 and the solution procedure presented in Section 4.3 in three test cases

Test 1: stationary Stokes flow coupled with a resistor, to test the effect of the matrix $\underline{\underline{\boldsymbol{E}}}$ in (4.35) on the order of convergence of the finite element discretization;

Test 2: non-stationary Stokes flow coupled with the RC buffer, to test the stability of the solution procedure of Step 1;

Test 3: non-stationary Stokes flow coupled with a non-linear 0D network via a RC buffer, to test the stability and convergence of the splitting scheme proposed.

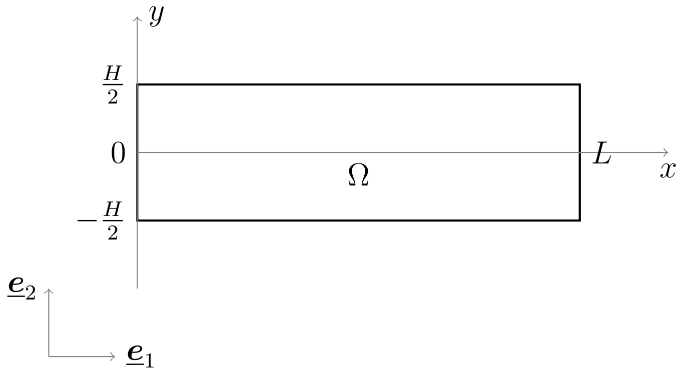

Fig. 4.2.: Sketch of the two-dimensional rectangular Stokes flow domain Ω of height H and length L.

The splitting scheme has been implemented in FreeFem++ [75] and the algebraic systems have been solved using the UMFPACK library with a tolerance of 10^{-12}.

In all the test cases we consider the two-dimensional domain Ω sketched in Figure 4.2 and defined as

$$\Omega = (0, L) \times \left(-\frac{H}{2}, \frac{H}{2}\right) \subset \mathbb{R}^2. \tag{4.42}$$

The Stokes equations are written as

$$\boldsymbol{\nabla} \cdot \underline{\boldsymbol{v}} = 0 \qquad \text{in } \Omega \times (0, T), \tag{4.43a}$$

$$\rho \frac{\partial \underline{\boldsymbol{v}}}{\partial t} + \boldsymbol{\nabla} p - \mu \boldsymbol{\Delta} \underline{\boldsymbol{v}} = +\rho \underline{\boldsymbol{f}} \qquad \text{in } \Omega \times (0, T), \tag{4.43b}$$

and are equipped with the initial condition

$$\underline{\boldsymbol{v}}(t = 0) = \underline{\boldsymbol{v}}_0 \qquad \text{in } \Omega, \tag{4.43c}$$

the boundary conditions

$$\underline{\boldsymbol{v}} = \underline{\boldsymbol{0}} \qquad \text{for } y = \pm\frac{H}{2},\ t \in (0, T), \tag{4.43d}$$

$$\left(-p\underline{\underline{\boldsymbol{I}}} + \mu \boldsymbol{\nabla} \underline{\boldsymbol{v}}\right) \underline{\boldsymbol{e}}_1 = -\overline{p} \underline{\boldsymbol{e}}_1 \qquad \text{for } x = 0,\ t \in (0, T), \tag{4.43e}$$

and the interface conditions

$$\left(-p\underline{\underline{\boldsymbol{I}}} + \mu\boldsymbol{\nabla}\underline{\boldsymbol{v}}\right)\underline{\boldsymbol{e}}_1 = -P_p\underline{\boldsymbol{e}}_1 \qquad \text{for } x = L,\ t \in (0,T), \tag{4.43f}$$

$$\int_{-H/2}^{H/2} \underline{\boldsymbol{v}} \cdot \underline{\boldsymbol{n}}\big|_{x=L} dy = \frac{P_p - \Pi}{\mathcal{R}_p} \qquad \text{for } t \in (0,T). \tag{4.43g}$$

For each test case, we compute an exact solution that can be used for comparison with the numerical results. We look for an exact solution where the fluid velocity $\underline{\boldsymbol{v}}(x,y,t) = v_1\underline{\boldsymbol{e}}_1 + v_2\underline{\boldsymbol{e}}_2$ can be written as

$$v_1(x,y,t) = s(t)\mathscr{V}(y), \qquad v_2(x,y,t) = 0, \tag{4.44}$$

and the fluid pressure can be written as

$$p(x,y,t) = s(t)\mathscr{P}(x). \tag{4.45}$$

Therefore, in order to have (4.44) and (4.45) as a solution of (4.43), the body forces $\rho\underline{\boldsymbol{f}}(x,y,t) = f_1\underline{\boldsymbol{e}}_1 + f_2\underline{\boldsymbol{e}}_2$ must satisfy

$$f_1(x,y,t) = \rho\frac{ds(t)}{dt}\mathscr{V}(y) - \mu s(t)\frac{d^2\mathscr{V}(y)}{dy^2} + s(t)\frac{d\mathscr{P}(x)}{dx}, \tag{4.46}$$

$$f_2(x,y,t) = 0. \tag{4.47}$$

Note that, under these assumptions, and due to the fact that we are using the non-symmetric formulation of Stokes equations, conditions (4.43e) and (4.43f) can be written as

$$p(x=0) = \overline{p}, \qquad p(x=L) = P_p. \tag{4.48}$$

They imply that $\overline{p}$ and P_p satisfy

$$\overline{p}(t) = s(t)\mathscr{P}(0), \qquad P_p(t) = s(t)\mathscr{P}(L). \tag{4.49}$$

If we consider condition (4.43g), the left-hand side can be expressed as

$$\int_{-H/2}^{H/2} \underline{\boldsymbol{v}} \cdot \underline{\boldsymbol{n}}\big|_{x=L} dy = s(t)\int_{-H/2}^{H/2} \mathscr{V}(y)dy = \alpha s(t), \tag{4.50}$$

where α is a constant, equal to the integral of $\mathscr{V}$. If we solve (4.43g) for Π and use (4.50), we obtain the following expression for Π

$$\Pi(t) = s(t)\left(\mathscr{P}(L) - \alpha\mathcal{R}_p\right). \tag{4.51}$$

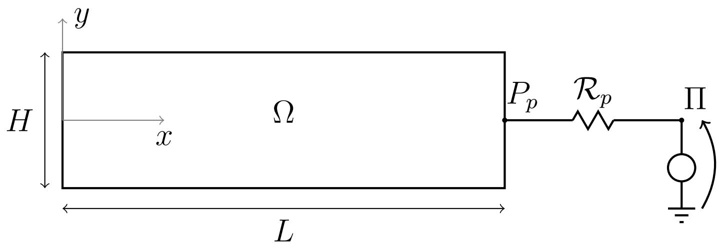

Fig. 4.3.: Test 1: stationary Stokes in Ω coupled with a resistor $\mathcal{R}_p$. P_p is the nodal pressure at the interface $x = L$ and Π is the pressure at the end of the resistor, set by the generator.

4.4.1 Test 1

In Test 1 we consider the case of stationary Stokes flow in Ω coupled with a resistor $\mathcal{R}_p$ (Figure 4.3). Let

$$\mathscr{V}(y) = V_0 \cos^2\left(\frac{\pi}{H}y\right), \qquad \mathscr{P}(x) = a_0 \exp(-kx) + a_1, \tag{4.52}$$

where V_0, a_0, a_1 and k are all positive constants, and let $s(t) = 1$ since the problem is stationary. This implies that

$$\alpha = \frac{V_0 H}{2}. \tag{4.53}$$

Given (4.52) and (4.53), the following expressions for f_1, $\overline{p}$, P_p and Π can be derived using (4.46)-(4.51)

$$f_1 = 2\mu V_0 \left(\frac{\pi}{H}\right)^2 \cos\left(\frac{2\pi}{H}y\right) - ka_0 \exp(-kx), \tag{4.54a}$$

$$\overline{p} = a_0 + a_1, \tag{4.54b}$$

$$P_p = a_0 \exp(-kL) + a_1, \tag{4.54c}$$

$$\Pi = a_0 \exp(-kL) + a_1 - \mathcal{R}_p \frac{V_0 H}{2}. \tag{4.54d}$$

Figure 4.4 shows the order of the spatial discretization error in Test 1 as a function of the mesh size h. The results presented are obtained in the case of $H = 2$ cm, $L = 10$ cm, $\mathbb{P}_2/\mathbb{P}_1$ Taylor-Hood elements for velocity and pressure, a regular $n \times m$ triangular mesh of Ω, where

$$n = 5(2^i), \qquad m = 5 * n \qquad i = 1, 2, 3, 4, \tag{4.55}$$

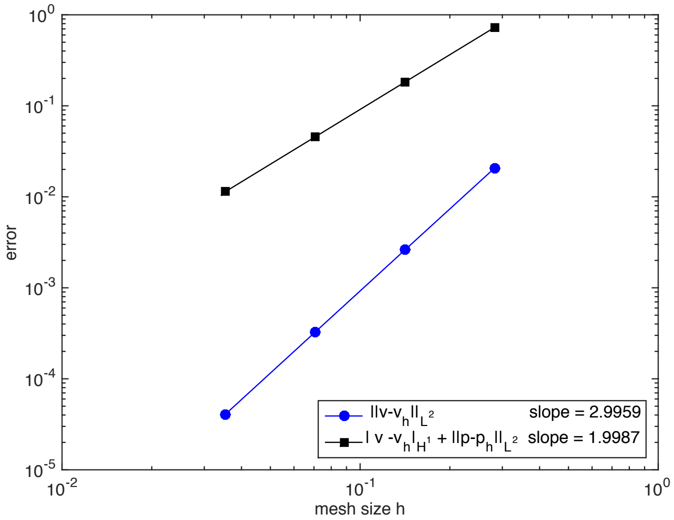

Fig. 4.4.: Test 1: logarithmic plot of the norm of the discretization error as a function of the mesh size h.

$\mu = 1$ g/(cm s), $\mathcal{R}_p = 100$ g/(cm^3 s), $V_0 = 10$ cm/s, $a_0 = 10$ Pa, $a_1 = 2$ Pa and $k = 0.01$ cm^{-1}. We are able to achieve the following orders of convergence

$$\|\underline{\boldsymbol{v}} - \underline{\boldsymbol{v}}_h\|_{L^2(\Omega)} \sim \mathcal{O}(h^3), \tag{4.56}$$

$$|\underline{\boldsymbol{v}} - \underline{\boldsymbol{v}}_h|_{H^1(\Omega)} + \|p - p_h\|_{L^2(\Omega)} \sim \mathcal{O}(h^2). \tag{4.57}$$

The results obtained are confirmed by literature, since the same orders of convergence have been proven to hold in the case of two-dimensional Stokes flow with homogenous Dirichlet boundary conditions and approximated by $\mathbb{P}_2$/$\mathbb{P}_1$ Taylor-Hood elements [94]. Figure 4.5 shows the numerical solution of pressure and velocity using a regular 40×200 triangular mesh of Ω. Note that v_2 is not exactly equal to zero, however, it is really small, of the order of 10^{-6}.

4.4.2 Test 2

In Test 2 we consider the case of non-stationary Stokes flow coupled with the RC buffer, see Figure 4.6. Problem (4.43) is coupled with Kirchhoff's law

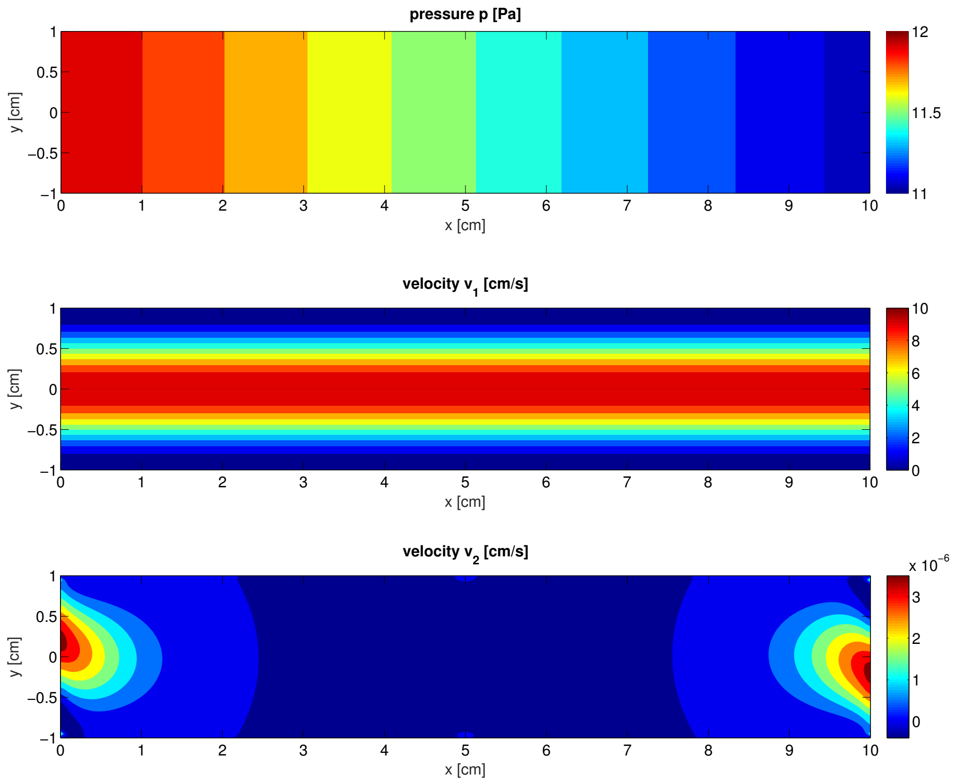

Fig. 4.5.: Test 1: numerical solution of fluid pressure p and velocity $\underline{\boldsymbol{v}}$ in Ω using $\mathbb{P}_2$/$\mathbb{P}_1$ Taylor-Hood elements and a regular 40×200 triangular mesh. v_1 is the horizontal component of the velocity and v_2 is the vertical components of the velocity.

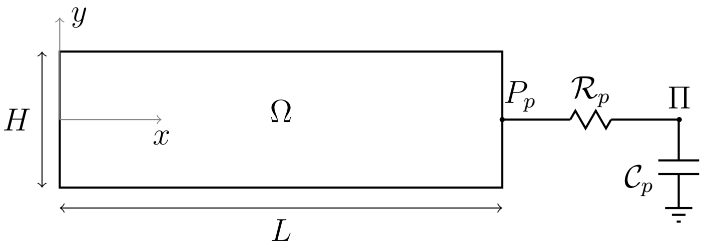

Fig. 4.6.: Test 2: non-stationary Stokes in Ω coupled with a RC buffer of resistor $\mathcal{R}_p$ and capacitor $\mathcal{C}_p$. P_p is the nodal pressure at the interface $x = L$ and Π is the pressure at the node in between the resistor and the capacitor.

$$\mathcal{C}_p \frac{d\Pi(t)}{dt} = \frac{P_p - \Pi}{\mathcal{R}_p}, \tag{4.58}$$

that is just a particular case of (4.8), where $m = 0$, $\underline{\underline{\boldsymbol{C}}} = \left[\mathcal{C}_p\right]$, $\underline{\boldsymbol{\Pi}} = [\Pi]$, $\underline{\boldsymbol{h}} = \left[1/\mathcal{R}_p\right]$ and $\underline{\boldsymbol{g}} = [0]$.

In this case the function $s(t)$ cannot be chosen a priori, because using Equations (4.58), (4.43g) and (4.50), we obtain that

$$\mathcal{C}_p \frac{d\Pi(t)}{dt} = \mathcal{C}_p \frac{ds(t)}{dt} \left(\mathscr{P}(L) - \alpha \mathcal{R}_p\right) = \frac{P_p - \Pi}{\mathcal{R}_p} = \alpha s(t). \tag{4.59}$$

As a consequence, $s(t)$ has to satisfy the following differential equation

$$\frac{ds(t)}{dt} = \frac{\alpha}{\mathcal{C}_p \left(\mathscr{P}(L) - \alpha \mathcal{R}_p\right)} = \beta s(t), \tag{4.60}$$

meaning that it can only be an exponential function of t

$$s(t) = s_0 \exp(\beta t), \tag{4.61}$$

where s_0 is an arbitrary constant. Let us consider in Test 2 the same expressions for $\mathscr{V}$ and $\mathscr{P}$ as in Test 1. Using (4.52)-(4.53) and (4.61), the following expressions for f_1, $\overline{p}$, P_p and Π can be derived from (4.46)-(4.51)

$$f_1 = s_0 \exp(\beta t) \left[\rho \beta V_0 \cos^2\left(\frac{\pi}{H} y\right) + 2\mu V_0 \left(\frac{\pi}{H}\right)^2 \cos\left(\frac{2\pi}{H} y\right) - k a_0 \exp(-kx)\right], \tag{4.62a}$$

$$\overline{p} = s_0 \exp(\beta t) \left(a_0 + a_1\right), \tag{4.62b}$$

$$P_p = s_0 \exp(\beta t) \left(a_0 \exp(-kL) + a_1\right), \tag{4.62c}$$

$$\Pi = s_0 \exp(\beta t) \left(a_0 \exp(-kL) + a_1 - \mathcal{R}_p \frac{V_0 H}{2}\right). \tag{4.62d}$$

Figure 4.7 shows the comparison between the exact solutions of $P_p(t)$ and $\Pi(t)$ and the corresponding numerical solutions for $t \in (0, 4]$ for two time steps $\Delta t = \Delta t_1 = 0.1, 0.01$. The following normalized errors are computed

$$\mathrm{err}_v(\Delta t) = \max_{t^n \in (0,4]} \frac{\|\underline{\boldsymbol{v}}(t^n) - \underline{\boldsymbol{v}}_h^n\|_{H^1(\Omega)}}{\|\underline{\boldsymbol{v}}(t^n)\|_{H^1(\Omega)}} \tag{4.63a}$$

$$\mathrm{err}_p(\Delta t) = \max_{t^n \in (0,4]} \frac{\|p(t^n) - p_h^n\|_{L^2(\Omega)}}{\|p(t^n)\|_{L^2(\Omega)}}, \qquad t^n = t^{n-1} + \Delta t \tag{4.63b}$$

$$\mathrm{err}_{0\mathrm{D}}(\Delta t) = \max_{t^n \in (0,4]} \frac{|\Pi(t^n) - \Pi^n|}{|\Pi(t^n)|} \tag{4.63c}$$

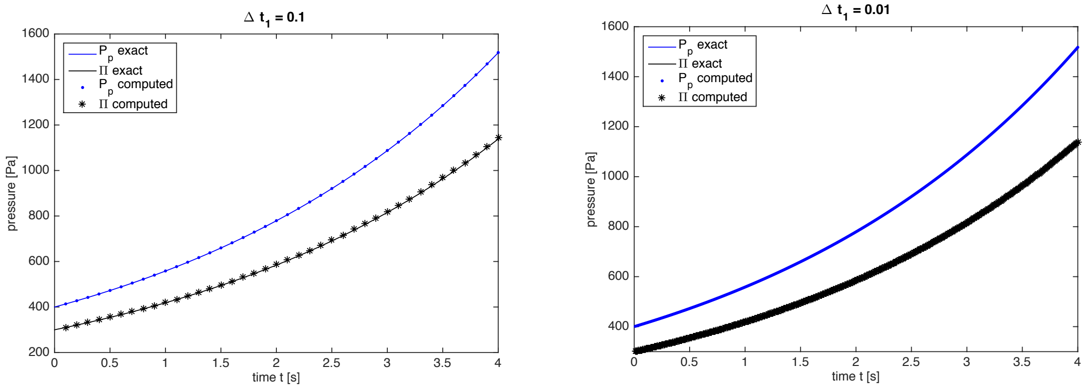

Fig. 4.7.: Test 2: comparison between the exact solution of $P_p(t)$ and $\Pi(t)$ and the corresponding numerical approximation for $t \in (0, 4]$ for two time steps $\Delta t_1 = 0.1, 0.01$.

Table 4.1.: Test 2: normalized errors for two different time steps.

Δt_1	err_v	err_p	$\mathrm{err}_{0\mathrm{D}}$
0.1	7.3×10^{-3}	8.2×10^{-8}	3.3×10^{-3}
0.01	3.5×10^{-3}	0.2×10^{-8}	0.3×10^{-3}

and reported in Table 4.1 for the two different time steps considered. The results presented are obtained in the case of $H = 2$ cm, $L = 10$ cm, $\mathbb{P}_2/\mathbb{P}_1$ Taylor-Hood elements, a regular 40×200 triangular mesh of Ω, $\rho = 1$ g/cm^3, $\mu = 1$ g/(cm s), $\mathcal{R}_p = 100$ g/(cm^3 s), $\mathcal{C}_p = 0.01$ (cm^3 s^2)/g, $V_0 = 10$ cm/s, $a_0 = 50$ Pa, $a_1 = 400$ Pa, $k = 1$ cm^{-1}, $s_0 = 1$ and $\beta = 1/3$ s^{-1}.

4.4.3 Test 3

In Test 3 we consider the case of a non-stationary Stokes flow coupled with a non-linear 0D network via a RC buffer, as depicted in Figure 4.8.

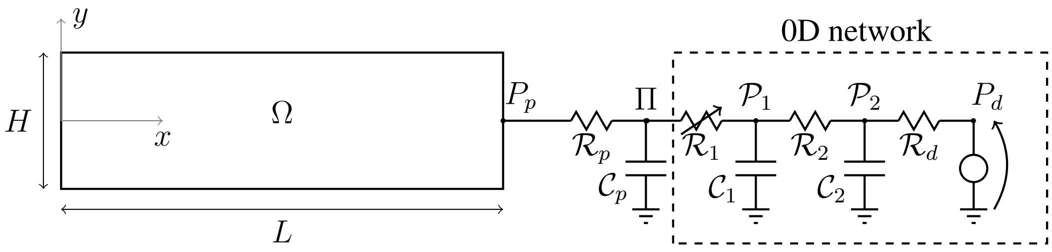

Fig. 4.8.: Test 3: non-stationary Stokes in Ω coupled with a non-linear 0D network via a RC buffer. $\mathcal{R}_p$, $\mathcal{C}_p$ and Π are the resistance, capacitance and nodal pressure in the RC buffer, and $\mathcal{R}_1$, $\mathcal{R}_2$, $\mathcal{R}_d$, $\mathcal{C}_1$, $\mathcal{C}_2$, $\mathcal{P}_1$, $\mathcal{P}_2$ and P_d are the resistances, capacitances and nodal pressures in the 0D network.

Problem (4.43) is coupled with Kirchhoff's laws

$$\mathcal{C}_p \frac{d\Pi}{dt} = \frac{P_p - \Pi}{\mathcal{R}_p} - \frac{\Pi - \mathcal{P}_1}{\mathcal{R}_1(\Pi)}, \tag{4.64a}$$

$$\mathcal{C}_1 \frac{d\mathcal{P}_1}{dt} = \frac{\Pi - \mathcal{P}_1}{\mathcal{R}_1(\Pi)} - \frac{\mathcal{P}_1 - \mathcal{P}_2}{\mathcal{R}_2}, \tag{4.64b}$$

$$\mathcal{C}_2 \frac{d\mathcal{P}_2}{dt} = \frac{\mathcal{P}_1 - \mathcal{P}_2}{\mathcal{R}_2} - \frac{\mathcal{P}_2 - P_d}{\mathcal{R}_d}, \tag{4.64c}$$

where the resistance $\mathcal{R}_1$ depends on the pressure Π. This system of ordinary differential equations can be expressed in the general form (4.8) for $m = 2$, $\underline{\boldsymbol{\mathcal{P}}}(t) = [\mathcal{P}_1(t), \mathcal{P}_2(t)]^T$, $\underline{\boldsymbol{\Pi}}(t) = [\Pi(t), \underline{\boldsymbol{\mathcal{P}}}(t)]^T \in \mathbb{R}^3$,

$$\underline{\underline{\boldsymbol{C}}} = \begin{bmatrix} \mathcal{C}_p & 0 & 0 \\ 0 & \mathcal{C}_1 & 0 \\ 0 & 0 & \mathcal{C}_2 \end{bmatrix}, \qquad \underline{\underline{\boldsymbol{R}}}(\Pi) = \begin{bmatrix} \frac{1}{\mathcal{R}_1(\Pi)} & -\frac{1}{\mathcal{R}_1(\Pi)} & 0 \\ -\frac{1}{\mathcal{R}_1(\Pi)} & \frac{1}{\mathcal{R}_1(\Pi)} + \frac{1}{\mathcal{R}_2} & -\frac{1}{\mathcal{R}_2} \\ 0 & -\frac{1}{\mathcal{R}_2} & \frac{1}{\mathcal{R}_2} + \frac{1}{R_p} \end{bmatrix}, \tag{4.65}$$

$$\underline{\boldsymbol{b}} = \left[\frac{1}{\mathcal{R}_d}, 0, 0\right]^T \quad \text{and} \quad \underline{\boldsymbol{g}}(t) = \left[0, 0, \frac{P_d(t)}{\mathcal{R}_d}\right]^T. \tag{4.66}$$

Using (4.46)-(4.51) and (4.64), let us derive the expression for the pressures of the network. If we solve Equation (4.64a) for $\mathcal{P}_1$, we obtain

$$\mathcal{P}_1(t) = \mathcal{R}_1(\Pi(t)) \left(\mathcal{C}_p \frac{d\Pi(t)}{dt} - \alpha s(t) \right) + \Pi(t). \tag{4.67}$$

Hence, given the expression for Π in (4.51), we can differentiate it and find the expression for $\mathcal{P}_1$ using (4.67). Recursively, $\mathcal{P}_2$ can be derived from $\mathcal{P}_1$ and its derivative by solving Equation (4.64b) for $\mathcal{P}_2$

$$\mathcal{P}_2(t) = \mathcal{R}_2 \left(\mathcal{C}_1 \frac{d\mathcal{P}_1(t)}{dt} - \alpha s(t) + \mathcal{C}_p \frac{d\Pi(t)}{dt} \right) + \mathcal{P}_1(t), \tag{4.68}$$

and P_d can be derived from $\mathcal{P}_2$ and its derivative by solving Equation (4.64c) for P_d

$$P_d(t) = \mathcal{R}_d \left(\mathcal{C}_2 \frac{d\mathcal{P}_2(t)}{dt} - \frac{\mathcal{P}_1(t) - \mathcal{P}_2(t)}{\mathcal{R}_2} \right) + \mathcal{P}_2(t). \tag{4.69}$$

Note that, since $\mathcal{R}_1$ is nonlinear, $\mathcal{P}_2$ and P_d depend on its time derivatives.

In this test case we do not have constraints on the choice of $s(t)$, so we consider the periodic function

$$s(t) = s_0 \sin(\omega t) + s_1, \tag{4.70}$$

where s_0, s_1 and ω are positive constants. We assume that $\mathcal{R}_1$ varies as function of Π via the sigmoidal function

$$\mathcal{R}_1(\Pi) = \overline{\mathcal{R}_1} + \frac{b_0}{1 + b_1 \exp(-b_2 \Pi(t))}, \tag{4.71}$$

where $\overline{\mathcal{R}_1}$, b_0, b_1 and b_2 are positive constants. Let us consider in Test 3 the same expressions for $\mathscr{V}$ and $\mathscr{P}$ as in Test 1 and 2. Using (4.52)-(4.53) and (4.70)- (4.71),f_1, $\overline{p}$, P_p, $\underline{\mathbf{\Pi}}$ and P_d can be derived from (4.46)-(4.51) and (4.67)-(4.69).

In Test 3, given the periodic function $s(t)$, the coupled systems is solved in time until periodicity is reached. Once the periodicity is reached, the following normalized errors are computed

$$\mathrm{err}_v(\Delta t) = \max_{t^n \in \text{ period}} \frac{\|\underline{\boldsymbol{v}}(t^n) - \underline{\boldsymbol{v}}_h^n\|_{H^1(\Omega)}}{\|\underline{\boldsymbol{v}}(t^n)\|_{H^1(\Omega)}} \tag{4.72a}$$

$$\mathrm{err}_p(\Delta t) = \max_{t^n \in \text{ period}} \frac{\|p(t^n) - p_h^n\|_{L^2(\Omega)}}{\|p(t^n)\|_{L^2(\Omega)}} \qquad t^n = t^{n-1} + \Delta t. \tag{4.72b}$$

$$\mathrm{err}_{0\mathrm{D}}(\Delta t) = \max_{t^n \in \text{ period}} \frac{|\underline{\mathbf{\Pi}}(t^n) - \mathbf{\Pi}^n|}{|\underline{\mathbf{\Pi}}(t^n)|} \tag{4.72c}$$

Figure 4.9 shows the order of convergence of the errors defined in (4.72). A first-order convergence in time is obtained for every error considered. Figure 4.10 shows the

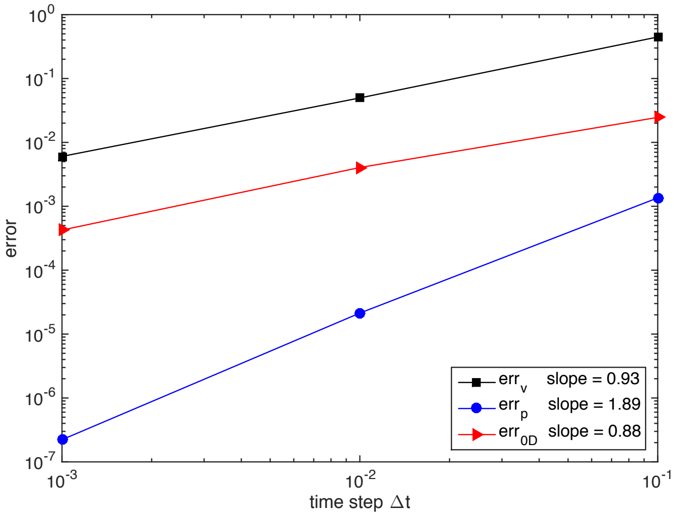

Fig. 4.9.: Test 3: logarithmic plot of the errors defined in (4.72) as a function of the time step.

comparison between the exact solution and the numerical solution over one period, once periodicity has been reached. The numerical solution is reported for two different time steps $\Delta t = 0.1, 0.01$. The results presented are obtained in the case of $H = 2$ cm, $L = 10$ cm, $\mathbb{P}_2/\mathbb{P}_1$ Taylor-Hood elements for velocity and pressure, a regular 20×100 triangular mesh of Ω, and the time discretization $\Delta t_1 = \Delta t$ and $\Delta t_2 = \Delta t/20$. Moreover, the parameter values used in the simulations are $\rho = 1$ g/cm^3, $\mu = 1$ g/(cm s), $\mathcal{R}_p = \mathcal{R}_2 = \mathcal{R}_d = 10$ g/(cm^3 s), $\mathcal{C}_p = 0.01$ (cm^3 s^2)/g, $\mathcal{C}_1 = \mathcal{C}_2 = 0.001$ (cm^3 s^2)/g, $V_0 = 10$ cm/s, $a_0 = 300$ Pa, $a_1 = 50$ Pa, $k = 0.1$ cm^{-1}, $s_0 = 1$, $s_1 = 2$, $\omega = \pi$ rad/s, $\overline{\mathcal{R}_1} = 10$ g/(cm^3 s), $b_0 = 10$ g/(cm^3 s), $b_1 = 1$, $b_2 = 0.001$ Pa^{-1}.

4.5 Discussion

In this Chapter we have studied Stokes equations in truncated domains coupled with a 0D network via a RC buffer, as previously considered in [56]. We have proposed a new energy-based operator slipping scheme that is stable, like the coupling schemes presented in [41, 52, 56], and, moreover,

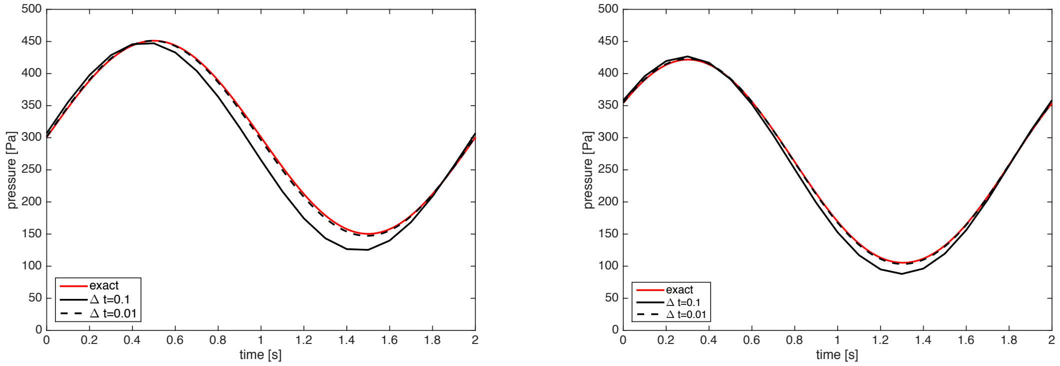

(a) $\Pi(t)$ (b) $\mathcal{P}_1(t)$

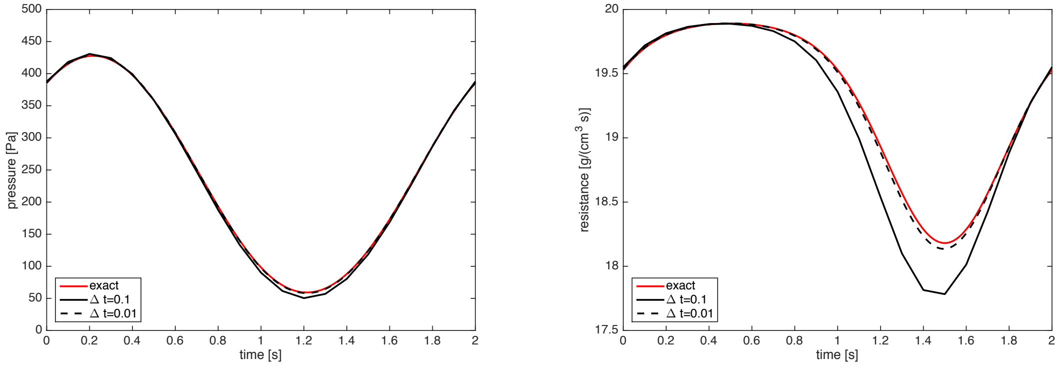

(c) $\mathcal{P}_2(t)$ (d) $\mathcal{R}_1(\Pi(t))$

Fig. 4.10.: Test 3: comparison between the exact solution and the numerical approximation of $\underline{\mathbf{\Pi}}$ in (a), (b) and (c), and comparison between the computed variable resistance $\mathcal{R}_1$ and its exact expression in (d). Two different time steps are considered $\Delta t = 0.1, 0.01$.

1. allows to solve in a separate step potential nonlinearities in the 0D network;
2. is flexible on the choice of the numerical method and discretization for each sub-step;
3. is unconditionally stable, independently on the numerical method and discretization chosen in each sub-step.

The results in Section 4.4 confirm that the stability of the splitting scheme does not depend on the time step, see Figures 4.7 and 4.10, and that the first-order convergence in time is obtained in the case of a nonlinear 0D network, see Figure 4.9.

The first-order splitting scheme proposed here can be easily extended to

- a second-order scheme, as discussed in Section 2.6.3. We recall that the second-order convergence in time can be achieved only if the numerical methods used for the time discretization of each sub-step are at least of second-order;
- Navier-Stokes equations, non-Newtonian fluids equations and fluid-structure interactions in Ω by combining the proposed scheme with other operator splitting techniques already developed [62, 64–66];
- the case of Stokes flow in between two 0D networks, namely where both Σ_0 and Σ_L in Figure 4.1 are coupled to a 0D network via a RC buffer, by solving in one step the Stokes equations and the two RC buffers, in the same fashion as in Step 1 (4.18), and by solving in a separate step the two 0D networks together, in the same fashion as in Step 2 (4.19);
- more general 0D networks were the vector of state variables $\underline{\boldsymbol{y}}$ in (4.6) does not necessarily correspond to the column vector of pressures at the nodes, and were also capacitances might depend nonlinearly on pressure.

5. PATIENT-SPECIFIC THEORETICAL INTERPRETATION OF CLINICAL DATA

In this Chapter we present two studies in which mathematical models and numerical methods are used in synergy with clinical data and statistical methods to elucidate the mechanisms behind clinical correlations and to provide new explanations for clinical observations. These methods are able to identify new clinical markers than can help to distinguish between healthy individuals and glaucoma patients.

In Section 5.1, we combine clinical data and mathematical predictions to propose possible explanations for the increase in venous oxygen saturation observed in advanced glaucoma patients. In Section 5.2, we propose a computer-aided manipulation process that enables the extraction of a novel set of waveform parameters to help to characterize the disease status in glaucoma patients.

5.1 Oximetry data in advanced glaucoma patients

5.1.1 Introduction

Despite evidence linking blood flow alterations with glaucoma, it is still unknown whether vascular changes occur primary or secondary to retinal ganglion cell loss. In [95–97], patients with advanced glaucoma (visual field mean defect (MD) ≥ 10 dB) exhibited higher venous oxygen saturation levels compared with healthy individuals and mild glaucoma patients (MD ≤ 5 dB). These observations led to the hypothesis that the decreased arteriovenous difference in the advanced glaucoma group could be due to a decrease in retinal oxygen consumption, hence suggesting that the observed increase in venous saturation is likely a secondary effect of glaucomatous atrophy and not a primary cause of glaucoma.

Additional methods are needed before definitive conclusions can be made relating blood oxygen saturation changes and the severity or type of glaucoma.

Here, we apply a previously developed theoretical model of retinal vascular wall mechanics [35] to a set of clinical oximetry data obtained from healthy individuals and glaucoma patients [96] to propose possible explanations for the increase in venous oxygen saturation observed in advanced glaucoma patients. The combined mathematical and clinical approach is used to calculate theoretical changes in blood oxygen saturation in retinal arterioles, capillaries and venules and to compute patient-specific levels of tissue oxygen demand or Krogh tissue width (herein referred to as tissue width) that would yield the measured values of venous oxygen saturation given values of MAP, IOP and arterial oxygen saturation from patients [98].

5.1.2 Methods

Experimental data

The methods of performing retinal oximetry and obtaining baseline measurements of factors such as IOP and blood pressure in glaucoma patients and healthy individuals has previously been described in detail [96]. In short, measurements from 89 healthy individuals and 74 glaucoma patients of age 40 years or older were collected. Glaucoma was defined based on the characteristic optic disc damage and on the corresponding visual field defects. Of all of the glaucoma patients considered, 45 were diagnosed with primary open angle glaucoma (POAG) and 29 were diagnosed with NTG. A diagnosis of POAG was defined by an untreated IOP > 21 mmHg. Patients with IOP measurements consistently ≤ 21 mmHg were classified as having NTG. All glaucoma patients underwent automated perimetry. A patient was defined as having mild glaucoma if the visual field MD was ≤ 5 dB and was defined as having advanced glaucoma if the visual field MD ≥ 10 dB. Of the 45 POAG patients, 20 were diagnosed with mild glaucoma and 12 were diagnosed with advanced glaucoma. Of the 29 NTG patients, 13 were diagnosed with mild glaucoma and

9 were diagnosed with advanced glaucoma. Some patients were under active treatment at the time of measurement.

Mathematical model

To determine possible explanations for measured changes in venous oxygen saturation in POAG and NTG patients [96], a simplified mathematical model of the retinal vasculature, previously developed by Arciero et al. [35], is used. The retinal vasculature downstream of the CRA and upstream of the CRV is modeled as a representative segment network, where five vessel compartments for the large arterioles (LA), small arterioles (SA), capillaries (C), small venules (SV) and large venules (LV) supplying and draining the retina are connected in series; each compartment consists of identical segments arranged in parallel (see Figure 5.1). All compartments are assumed to experience the same hemodynamic and metabolic conditions. A summary of the model equations, along with its input values and output values, is provided in Table 5.1. The subscripts used in Table 5.1 indicate if the quantity is evaluated either at the inlet (in, i), midpoint (mp, i) or outlet (out, i) of the ith compartment, where i =LA, SA, C, SV, LV. The values of the model parameters are listed in Tables 5.2, 5.3 and 5.4. In the following, the main features of the model are discussed, which are leveraged to perform the simulations reported in the Section 5.1.3. For a complete description of the model we refer to a previous study by Arciero et al. [35].

Blood flow and oxygen saturation throughout the network are predicted according to hemodynamic and mechanical principles. Retinal flow is assumed to follow Poiseuille's law (2.206), in which flow through each vessel is proportional to the fourth power of the vessel diameter. The complex blood rheology is accounted for by assigning different values of the apparent viscosity μ to vessels in each compartment according to an experimental *in vivo* relationship [99](Table 5.3). The total tension $T_{total,i}$ generated in the vessel walls of the vasoactive compartments i= LA, SA follows the law of Laplace and is modeled as the sum of passive and active tension, denoted by $T_{passive,i}$ and $T_{max.active,i}$, respectively, as detailed in Table 5.1(b). $T_{passive,i}$ results from the structural components of the vessel wall,

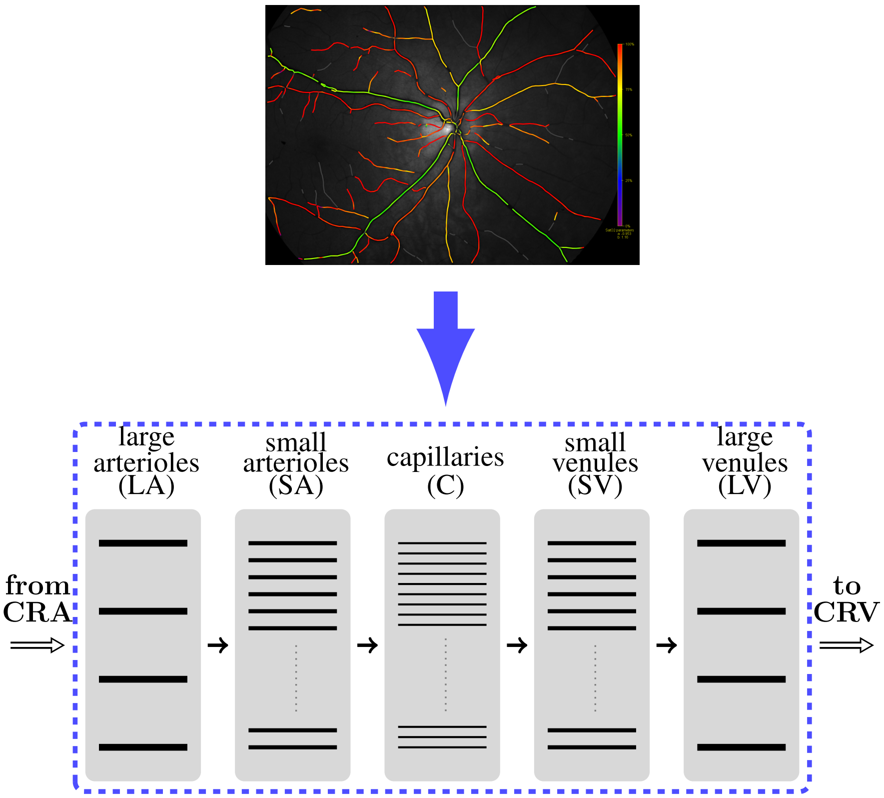

Fig. 5.1.: The retinal vasculature, as depicted in the oximetry image (top), is modeled as a representative segment network (bottom) consisting of five compartments of parallel-arranged vessels connected in series downstream of the central retinal artery (CRA) and upstream of the central retinal vein (CRV): large arterioles/arteries (LA), small arterioles (SA), capillaries (C), small venules (SV) and large venules/veins (LV).

and $T_{max.active,i}$ is generated by the contraction and dilation of smooth muscles in the LA and SA. Smooth muscle tone in LA and SA is described by the activation function $A_{total,i}$, which ranges from 0 to 1. The product of $T_{max.active,i}$ and the activation A_i yields the active tension generated in the vessel wall. Changes in $A_{total,i}$ are dictated by the stimulus function $S_{tone,i}$ which results from a linear combination of four autoregulatory mechanisms

1. *myogenic mechanism*, related to the wall tension T_i computed via the law of Laplace. Details are provided in Table 5.1(c), where ΔP_{tot} represents the total pressure drop

Table 5.1.: Summary of model [35] variables and equations (sections b-f), including input (section a) and output (section g) data.

		Input
(a)		$P_{in,LA} = \frac{2}{3}MAP - 20\text{mmHg}, \quad P_{out,LV} = IOP, \quad S(x=0) = \text{arterial oxygen saturation},$ $M_0, \quad d, \quad bCO_2(x=0) = 50\%, \quad C(x=0) = 0.5\mu M$
		Equations
(b)		$\begin{cases} \frac{dD_i}{dt} = \frac{2\lambda_i}{\tau_d}\left(T_i - T_{total,i}\right) \\ \frac{dA_i}{dt} = \frac{1}{\tau_a}\left(A_{total,i} - A_i\right) \end{cases} \quad i = \text{LA,SA}$ $T_{total,i} = T_{passive,i} + A_i T_{max.active,i}$ $\quad T_{passive,i} = C_{pass,i} \exp\left[C'_{pass,i}\left(D_i/D_{0,i} - 1\right)\right]$ $T_{max.active,i} = C_{act,i} \exp\left\{-\left[\left(D_i/D_{0,i} - C'_{act,i}\right)/C''_{act,i}\right]^2\right\}$ $\quad A_{total,i} = 1/\left(1 + \exp(-S_{tone,i})\right)$ $S_{tone,i} = C_{myo,i}T_i - C_{shear,i}\tau_i - C_{meta,i}S_{CR,i} - C_{CO_2,i}S_{CO_2,LV} + C''_{tone,i}$
(c)	*Myogenic*	$T_i = (P_{mp,i} - IOP)D_i/2 \quad i = \text{LA,SA,C,SV,LV}$ $\Delta P_{tot} = Q_{tot}R_{tot} = P_{in,LA} - P_{out,LV} \quad R_{tot} = \sum_i R_i \quad Q_{tot} = n_i Q_i$ $\Delta P_i = Q_i R_i = P_{in,i} - P_{out,i} \quad R_i = (128\mu_i L_i)/(\pi D_i^4 n_i) \quad P_{mp,i} = P_{in,i} + \frac{1}{2}\Delta P_i$
(d)	*Shear stress*	$\tau_i = (32\mu_i Q_i)/(\pi D_i^3) \quad i = \text{LA,SA,C,SV,LV}$
(e)	*Metabolic*	$S_{CR,i} = \int_{x_{mp,i}}^{x_{end,i}} \exp\left[-\left(y - x_{mp,i}\right)/L_0\right] C(y)dy \quad i = \text{LA,SA}$ $C(x) = \alpha + \beta(x - x_{in,i}) + \exp\left[\gamma(x_{in,i} - x)\right]\left(C(x_{in,i}) - \alpha\right)$ $\alpha(x) = H_T R_0\left[D_i(1 - R_1 S(x_{in,i})) - (1 - H_D)R_1 q(x)/(\pi c_0 H_D k_d)\right]/4k_d$ $\beta(x) = (D_i H_T R_0 R_1 q(x))/(4Q_i c_0 H_D k_d) \quad \gamma = k_d \pi D_i/[(1 - H_D)Q_i]$ $q(x) = M_0\pi(r_{t,i}^2 - r_{v,i}^2) \quad r_{v,i} = \frac{1}{2}D_i \quad r_{t,i} = r_{v,i} + d_i$ $S(x) = S(x_{in,i}) + q(x)(x_{in,i} - x)/(Q_i c_0 H_D)$ $PO_2(x,r) = PO_2(x, r_{v,i}) + M_0\left[(r^2 - r_{v,i}^2)/4 + r_{t,i}^2 \ln\left(r_{v,i}/r\right)/2\right]/k$
(f)	*Carbon dioxide*	$S_{CO_2,LV} = f(PCO_{2LV}, Q_{tot})$ $PCO_{2LV} = g(tCO_2(x_{mp,LV})) \quad tCO_2(x) = bCO_2(x)(1 - (-0.115Q_{tot} + 0.23))$ $bCO_2(x) = bCO_2(x_{in,i}) - 0.81q(x)(x_{in,i} - x)/(Q_i c_0 H_D)$
		Output
(g)		P_i, ΔP_i, R_i and Q_i $i = \text{LA,SA,C,SV,LV}$, $C(x)$, $S(x)$, $PO_2(r,x)$, $tCO_2(x)$, $bCO_2(x)$

Table 5.2.: Parameter values for passive tension, active tension, and vascular smooth muscle activation equations in the large arterioles (LA) and small arterioles (SA).

Constant	Value		Unit
	LA	SA	
C_{pass}	361.48	197.01	[dyn/cm]
C'_{pass}	53.69	17.60	[1]
C_{act}	2114.2	3089.6	[dyn/cm]
C'_{act}	0.93	1.02	[1]
C''_{act}	0.11	0.20	[1]
C_{myo}	0.0092	0.025	[cm/dyn]
C_{shear}	0.0258	0.0258	[cm^2/dyn]
C_{meta}	200	200	[1/(μM cm)]
C_{CO_2}	8×10^{-4}	1.31×10^{-4}	[1/mmHg]
C''_{tone}	159.26	62.27	[1]
D_0	135.59	73.9	[μm]
λ	0.0457	0.0604	[1/mmHg]

Table 5.3.: Parameter values describing vessel network geometry and viscosity.

Parameter	Value					Unit
	LA	SA	C	SV	LV	
number of segments, n	4	39	111360	39	4	[1]
segments length, L	0.807	0.583	0.088	0.583	0.807	[cm]
viscosity, μ	2.28	2.06	10.01	2.09	2.44	[cP]

Table 5.4.: Time constants for the model equations (Table 5.1(b)) and parameter values for the metabolic response (Table 5.1(e)).

Parameter	Value	Unit
time constant for diameter, τ_d	1	[s]
time constant for activation, τ_a	60	[s]
tube hematocrit, H_T	0.3	[1]
discharge hematocrit, H_D	0.4	[1]
rate of ATP degradation, k_d	2×10^{-4}	[cm/s]
maximum rate of ATP release, R_0	1.4×10^{-9}	[mol s^{-1} cm^{-3}]
effect of oxygen saturation on ATP release, R_1	0.891	[1]
oxygen capacity of red blood cells, c_0	0.5	[cm^3O_2/cm^3]
oxygen tissue diffusion coefficient, k	9.4	[cm^3O_2/(cm mmHg s)]
length constant for S_{CR}, L_0	1	[cm]

along the retinal network from the outlet of the CRA to the inlet of the CRV, and ΔP_i represents the pressure drop along each segment of the i th compartment. Similarly, Q_{tot} represents the total blood flow along the network and Q_i represents the blood flow in each segment of the i th compartment, and R_{tot} represents the resistance to flow offered by the whole retinal network and R_i represents the resistance to flow offered by a single segment of the i th compartment. The resistances R_i are computed according to Poiseuille's law;

2. *shear stress mechanism*, related to the wall shear stress τ_i computed according to Poiseuille's law. Details are provided in Table 5.1(d);
3. *metabolic mechanisms*, related to the signal $S_{CR,i}$. Details are provided in Table 5.1(e), where the signal $S_{CR,i}$ depends on the adenosine triphosphate (ATP) concentration

at each position x along the network $C(x)$, which itself depends on the blood oxygen saturation at each point in the network $S(x)$;

4. *carbon dioxide mechanism*, related to the signal $S_{CO_2,LV}$. Details are provided in Table 5.1(f), where the signal $S_{CO_2,LV}$ is given by the nonlinear function f of the partial pressure of carbon dioxide in the tissue (PCO_2) and of the total retinal blood flow (Q_{tot}). The tissue carbon dioxide content (tCO_2) is converted into PCO_2 via carbon dioxide dissociation curves, represented by the function g. The tissue carbon dioxide content and the blood carbon dioxide content (bCO_2) are assumed to be linearly related [100].

Arciero et al. [35] showed that the metabolic and carbon dioxide responses contribute most significantly to blood flow autoregulation, leading to a nearly constant blood flow over a wide range of intraluminal pressures. In the model, autoregulation is achieved through changes in the diameters D_i in the LA and SA segments, which should be interpreted as the new equilibrium state attained by the system as the input data are altered. In Section 5.1.3 simulations are also performed in the case of impaired autoregulation (IA) corresponding to the case in which metabolic and carbon dioxide mechanisms are switched off.

Since we aim to compare model-predicted and clinically measured venous saturation levels, details for the oxygen saturation model calculations are provided. Other details of flow, diameter and smooth muscle activation calculations are given previously [35] and are outlined here in Table 5.1. By the conservation of mass, the change in oxygen flux must be equal the rate of oxygen consumed by the retinal tissue

$$\frac{d}{dx}\left[Q_i c_0 H_D S(x)\right] = -q, \tag{5.1}$$

where x is the distance along the network, Q_i is the blood flow in each compartment i, c_0 is the oxygen carrying capacity of red blood cells at 100% saturation, H_D is the discharge hematocrit, $S(x)$ is the blood oxygen saturation and q is the tissue oxygen consumption per vessel length. Since the clinical data set considered does not include patient-specific hematocrit values, H_D is assumed to be constant, as specified in Table 5.4.

Oxygen consumption in the tissue is calculated using a Krogh cylinder model, in which each oxygen-delivering vessel is assumed to provide oxygen via diffusion to a cylindrical region of tissue surrounding it (see Figure 5.2(a)). In the present model, oxygen is assumed to be delivered by the large and small arterioles and capillaries; no oxygen exchange is assumed in the venules. At each position x in the retinal vascular network, the oxygen is delivered to the nearest tissue via diffusion according to

$$k\left[\frac{1}{r}\frac{d}{dr}\left(r\frac{dPO_2(x,r)}{dr}\right)\right] = M_0, \tag{5.2}$$

where k is the diffusion coefficient, PO_2 is the partial pressure of oxygen at a radial distance r within the tissue cylinder and M_0 is the tissue oxygen demand per tissue volume (assumed here to be constant). The degeneration of the retinal ganglion cells is modeled indirectly by varying the tissue oxygen demand M_0; retinal ganglion cells degeneration would correspond to a decrease in M_0. Given the architecture of this model, it is important to note that the M_0 defined here is primarily representative of the oxygen demand of the retinal ganglion cells in the inner retina [101].

The partial pressure of oxygen in the tissue along the radial direction r for a fixed position in the network x is given by

$$PO_2(x,r) = PO_2(x,r_{v,i}) + \frac{M_0}{k}\left[\frac{r^2 - r_{v,i}^2}{4} + \frac{r_{t,i}^2}{2}\ln\left(\frac{r_{v,i}}{r}\right)\right], \tag{5.3}$$

where the subscript i indicates the vessel compartment, $r_{t,i}$ denotes the radius of the tissue region and $r_{v,i}$ denotes the vessel radius, as depicted in Figure 5.2(c). Figure 5.2(b) depicts a sample solution for two positions $x_{in,SA} = 0.81$ cm (blue curve) and $x_{end,SA} = 1.39$ cm (black curve) in the small arterioles for $PO_2(x_{in,SA}, r_v) = 67.53$ mmHg, $PO_2(x_{end,SA}, r_v) = 66.67$ mmHg, $M_0 = 1.65$ cm^3 $O_2 \cdot 100$ cm^{-3} min^{-1}, $k = 9.4$ cm^3 O_2 cm^{-1} mmHg^{-1} s^{-1}, $r_v = 23.6$ μm, and $r_t = 38.6$ μm.

For a constant value of M_0, the tissue oxygen consumption per vessel length q is computed as

$$q = \int_{r_{v,i}}^{r_{t,i}} 2\pi r M_0 dr = \pi M_0\left(r_{t,i}^2 - r_{v,i}^2\right). \tag{5.4}$$

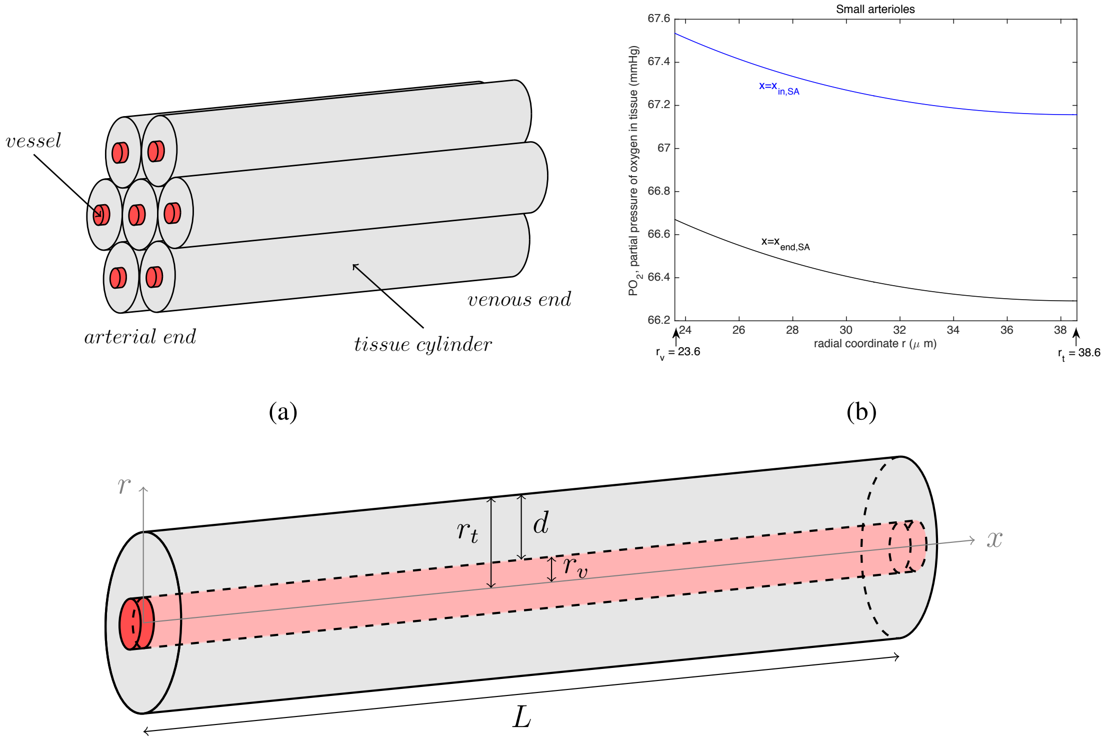

(a) (b)

(c)

Fig. 5.2.: A Krogh cylinder model is used to predict oxygen diffusion in retinal tissue. (a) Representation of a Krogh cylinder model in which vessels (red) run along the center axis of a tissue cylinder (gray). (c) Depiction of a single vessel (red) supplying a cylindrical region of tissue (gray) with oxygen, where r is the radial coordinate, x is the distance along the network, r_t is the radius of the tissue region, r_v is the radius of the vessel, d is the tissue width and L is the vessel length. (b) Distribution of the partial pressure of oxygen $PO_2(x,r)$ in the tissue surrounding the small arterioles in the radial direction at two fixed positions $x_{in,SA} = 0.81$ cm and $x_{end,SA} = 1.39$ cm.

The width of tissue surrounding each vessel is defined as

$$d_i = r_{t,i} - r_{v,i}. \tag{5.5}$$

Here, it is assumed that d_i is equal to the same value d for each oxygen-delivering vessel i=LA, SA, C and that $d_i = 0$ for the SV and LV compartments. Thus, the oxygen consumption rate q depends on both the tissue volume surrounding the vessel and on the level of functional activity of the retinal ganglion cells represented by the tissue oxygen demand M_0. In turn, changes in the oxygen consumption rate q will induce changes in the oxygen saturation within the vessel as dictated by the balance of mass in Equation (5.1).

Given the model inputs listed in Table 5.1 section (a), the steady-state values of the diameters D_i and of the vascular smooth muscle activations A_i in the LA and SA compartments are determined by integrating the system of ordinary differential equation in Table 5.1(b) until equilibrium is reached. It is important to note that the system also involves the quantities T_i, $T_{total,i}$ and $A_{total,i}$ which, as detailed in Table 5.1, are functions of the unknowns D_i and A_i. The use of a steady state model is justified since the variation in the clinical measurements of oxygen saturation due to the cardiac cycle are not large [102].

Model reference state

A reference state is defined to represent conditions typical of a healthy retina. For example, the reference state values of IOP, MAP and arterial and venous oxygen saturation are set equal to the average values of these factors measured in all of the healthy individuals in [96](see Table 5.5). The reference state value of tissue width is chosen to be $d^{ref} = 15$ μm, which corresponds to an experimental measurement of retinal intercapillary space of 30 μm [103]. In the reference state, the proportion of the tissue occupied by capillary lumens is about 2.7%, in good agreement with 2.5% measured in histological specimens [104]. Given the reference values of IOP, MAP, tissue width, and arterial oxygen saturation, the model is used to calculate the value of tissue oxygen demand ($M_0^{ref} = 1.65$ cm^3 $O_2 \cdot 100$ cm^{-3} min^{-1}) that will yield the reference venous oxygen saturation level of 54%, as measured in healthy patients. This calculated rate of oxygen demand in the reference state is close in magnitude to oxygen demand levels observed experimentally [105–107].

Model simulations

The mathematical model presented is used to conduct the following simulations.

1. *Theoretical investigation*: the model is used to predict the theoretical effect of the artificial variation of the model inputs (Table 5.1(a)) on the computed outputs (Table 5.1(g));
2. *Theoretical interpretation of clinical data*: the model is used to estimate patient-specific values of oxygen demand (simulation 2A) or tissue depth (simulation 2B) that would yield the clinically-measured value of venous oxygen saturation when patient-specific inputs are considered.

The details of the algorithms implemented to perform these novel, patient-specific simulations are provided below.

Algorithm for simulation 2A : for any individual included in the experimental study proceed as follows

- i. set the patient-specific input values for $P_{in,LA}$, $P_{out,LV}$ and $S(x = 0)$ (Table 5.1(a)) given the clinical measurements of MAP, IOP and arterial oxygen saturation;
- ii. set the input tissue depth equal to the reference state value d^{ref} (Table 5.1(a));
- iii. set the initial guess for the input oxygen demand to M_0^0 (Table 5.1(a)), for any $k \geq 0$
  - a) solve the model described in Table 5.1(b)-(f);
  - b) compute the output of the model (Table 5.1(g)), which includes oxygen saturation $S^k(x)$;

   c) test for convergence:

      if $\dfrac{|\text{ measured - predicted venous oxygen saturation }|}{|\text{ measured venous oxygen saturation }|} \leq 5 \cdot 10^{-2}$

      set $M_0 = M_0^k$, otherwise set $M_0^{k+1} = M_0^k + \delta_M$ and return to point a);

Algorithm for simulation 2B : for any individual included in the experimental study proceed as follows

i. set the patient-specific input values for $P_{in,LA}$, $P_{out,LV}$ and $S(x = 0)$ (Table 5.1(a)) given the clinical measurements of MAP, IOP and arterial oxygen saturation;

ii. set the input oxygen demand equal to the reference state value M_0^{ref} (Table 5.1(a));

iii. set the initial guess for the input tissue depth to d^0 (Table 5.1(a)), for any $k \geq 0$

   a) solve the model described in Table 5.1(b)-(f);

   b) compute the output of the model (Table 5.1(g)), which includes oxygen saturation $S^k(x)$;

   c) test for convergence:

      if $\dfrac{|\text{ measured - predicted venous oxygen saturation }|}{|\text{ measured venous oxygen saturation }|} \leq 5 \cdot 10^{-2}$

      set $d = d^k$, otherwise set $d^{k+1} = d^k + \delta_d$ and return to point a).

In step iii(c) of simulations (2A) and (2B), the values of δ_M and δ_d are determined via the MATLAB algorithm *fsolve*, which is a nonlinear least-squares algorithm. For each of the algorithms (2A) and (2B), two sets of simulations are performed corresponding to the cases of functional or impaired autoregulation.

5.1.3 Results

Experimental data

Figure 5.3 shows the scatter plot of the venous saturation data collected from healthy individuals, advanced POAG patients and advanced NTG patients [96]. Four healthy indi-

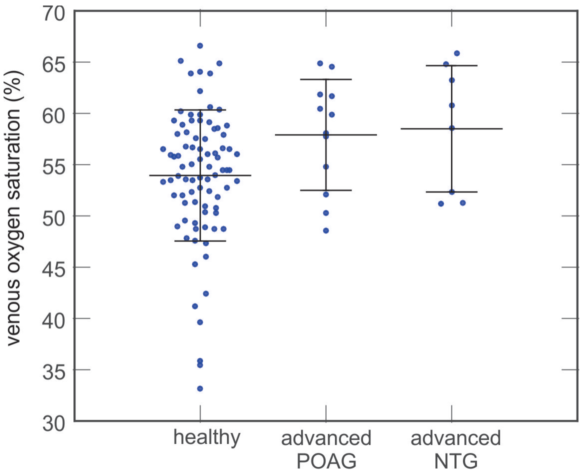

Fig. 5.3.: Venous oxygen saturation clinical data collected from healthy individuals (n=85), advanced POAG patients (n=12) and advanced NTG patients (n=8) [96] (blue dots). Black bars represent the mean and standard deviation of each group.

viduals and one advanced NTG patient were excluded since no record of MAP measurement was reported. Data for mild glaucoma patients are not included in the figure since Olafsdottir and Vandewalle et al. [96] found no statistical difference in retinal oxygen arterial and venous saturation between healthy individuals and mild glaucoma patients. The black bars represent the average value of each group and the corresponding standard deviation. In both the advanced POAG and advanced NTG patient groups, the average value of venous oxygen saturation is higher than in healthy individuals, and the average value of arteriovenous difference is lower than in healthy individuals. No statistical difference was reported in retinal oxygen saturation when mild POAG and mild NTG patients were compared, nor when advanced POAG and advanced NTG patients were compared. The average values of IOP, MAP and oxygen saturation measured in healthy individuals, advanced POAG patients and advanced NTG patients are also reported in Table 5.5.

Table 5.5.: Clinical average values of intraocular pressure (IOP, in mmHg), mean arterial pressure (MAP, in mmHg), ocular perfusion pressure (OPP, in mmHg), retinal arterial oxygen saturation and retinal venous oxygen saturation measured in healthy individuals, advanced (visual field MD$\geq$ 10 dB) primary open-angle glaucoma (POAG, IOP > 21 mmHg) patients and advanced normal tension glaucoma (NTG, IOP$\leq$21 mmHg) patients [96]. Reference state parameter values are highlighted in bold.

		Healthy (n=85)	Advanced POAG (n=12)	Advanced NTG (n=8)
Clinical data	IOP [mmHg]	**15** ± 3	15 ± 3	10 ± 3
	MAP [mmHg]	**102** ± 12	99 ± 10	109 ± 11
	OPP [mmHg]	**53** ± 8	51 ± 8	62 ± 6
	Arterial oxygen saturation [%]	**93** ± 4	95 ± 2	94 ± 3
	Venous oxygen saturation [%]	**54** ± 6	58 ± 5	58 ± 6
Reference values	M_0^{ref} [cm^3 $O_2 \cdot$ 100 cm^{-3} min^{-1}]	**1.65**		
	d^{ref} [μm]	**15**		

Theoretical investigation

Figure 5.4 shows the scatter plot of the venous oxygen saturation data collected from healthy individuals as a function of ocular perfusion pressure (OPP), defined as

$$\text{OPP} = \frac{2}{3}\text{MAP} - \text{IOP}. \tag{5.6}$$

The clinical data (blue dots) are compared to the mathematical model prediction (solid curve) of venous saturation as OPP is varied. Reference state values of IOP, MAP, arterial oxygen saturation, M_0^{ref} and d^{ref} are used to produce the model simulated curve. Since the model predictions generated by varying MAP and holding IOP constant or by varying IOP and holding MAP constant are nearly identical, only one curve is shown as OPP is varied.

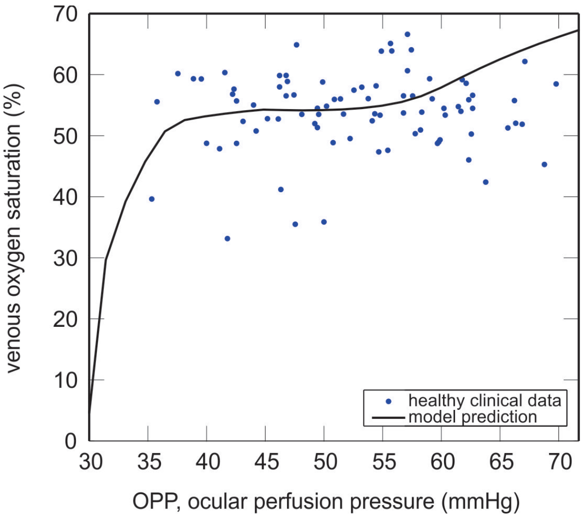

Fig. 5.4.: A scatter plot of the venous saturation clinical data (blue dots) collected from healthy individuals is compared with theoretical predictions (solid black curve) as OPP is varied. Here, a range of OPP values is generated by holding IOP constant at its reference state value (15 mmHg) while varying MAP between 67 and 130 mmHg.

Since the clinical data [96] show an increase in venous saturation in advanced glaucoma patients, the mathematical model is used to theorize three possible explanations for increased venous saturation:

Case 1 *A decrease in tissue oxygen demand* M_0: if less oxygen is consumed by the tissue, higher levels of venous oxygen saturation are predicted;

Case 2 *An impairment of blood flow autoregulation*: if the most influential autoregulation mechanisms (conducted metabolic and/or local carbon dioxide response mechanisms) are impaired, higher levels of venous oxygen saturation are predicted for certain ranges of OPP;

Case 3 *A decrease in tissue width* d: if the volume of tissue supplied by each capillary or arteriole is decreased, higher levels of venous oxygen saturation are predicted.

As shown in Figure 5.5(a), the model predicts a decrease in venous oxygen saturation as oxygen demand is increased provided that all other factors (MAP, IOP, d, arterial blood saturation and functionality of autoregulation) are not altered. Figure 5.5(b) depicts case 1 in which venous oxygen saturation is shown as a function of OPP for two different values of M_0

$$M_0^{ref} = 1.65\ \text{cm}^3\ O_2 \cdot 100\ \text{cm}^{-3}\ \text{min}^{-1} \tag{5.7}$$

for the blue curve and

$$M_0 = 1.32\ \text{cm}^3\ O_2 \cdot 100\ \text{cm}^{-3}\ \text{min}^{-1} \tag{5.8}$$

for the red curve. These curves show the effect of a 20% decrease in oxygen demand on the model predictions of venous saturation. It is interesting to observe that this decrease in oxygen demand causes variable increases in venous oxygen saturation depending on the value of OPP.

Figure 5.5(c) provides evidence for case 2, namely that an increase in venous oxygen saturation can also occur over a certain range of OPP values when autoregulation is impaired. In this case, $M_0^{ref} = 1.65\ \text{cm}^3\ O_2 \cdot 100\ \text{cm}^{-3}\ \text{min}^{-1}$ for both curves, but the metabolic and carbon dioxide autoregulation mechanisms are impaired (i.e., absent) in the black dashed curve.

Figure 5.5(d) shows that a decrease in tissue width supplied by each arteriole or capillary in the Krogh cylinder model can also lead to an increase in venous oxygen saturation, as outlined in case 3. Decreasing the tissue width leads to a decrease in the total tissue volume supplied by the retinal vasculature. Figure 5.5(d) depicts the effect of decreasing tissue width from $d^{ref} = 15\ \mu$ m (blue curve) to $d = 13\ \mu$ m (green curve).

Theoretical interpretation of clinical data

Figure 5.6 summarizes the model predicted values of oxygen demand (gray) or tissue width (blue) that will yield the clinically observed venous saturation levels (Figure 5.3) for each individual in the healthy, advanced POAG and advanced NTG populations. Model

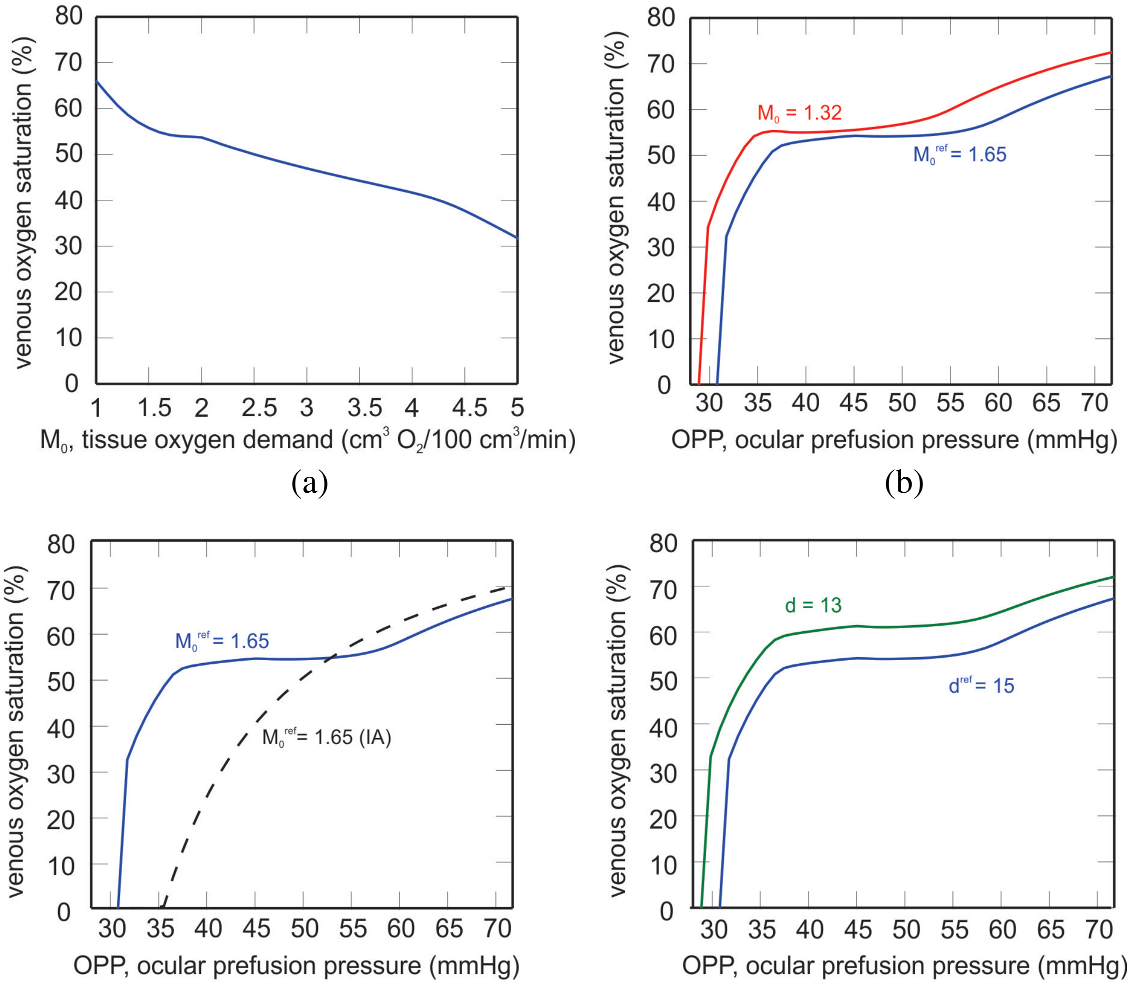

(a)

(b)

(c)

(d)

Fig. 5.5.: (a) Decrease in venous oxygen saturation as tissue oxygen demand M_0 is increased, given constant reference state values of MAP, IOP and arterial oxygen saturation. The remaining panels highlight the three-part theoretical investigation of the effects of (b) oxygen demand M_0, (c) impaired autoregulation (IA) and (d) tissue width d on model predictions of venous oxygen saturation as OPP is varied. Each scenario is compared with the model prediction of the reference state (blue curve) in which $M_0^{ref} = 1.65$ cm^3 $O_2 \cdot 100$ cm^{-3} min^{-1}, $d^{ref} = 15$ μm, and autoregulation is functional.

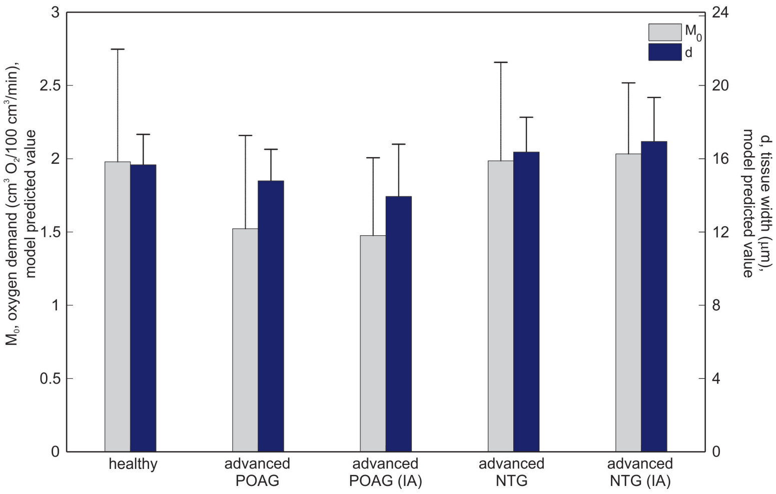

Fig. 5.6.: Model predicted levels of tissue oxygen demand M_0 and tissue width d that yield the venous saturation clinical data collected from each individual in the healthy, advanced POAG and advanced NTG populations [96]. Model predictions are also provided when autoregulation is impaired (IA) in advanced POAG and NTG patients. Black bars represent mean and standard deviation of each group.

predictions for mild POAG and NTG patient groups are not included since the venous saturation levels did not differ from healthy individuals. The model predicts that the observed increase in venous saturation in advanced POAG patients is accompanied by a decrease in oxygen demand, whereas no change in oxygen demand is predicted in advanced NTG patients. A slightly lower tissue width is predicted in POAG patients to yield increased venous saturation but not in NTG patients. These trends are observed regardless of whether autoregulation is functioning or impaired. Table 5.6 lists the mean and standard deviation of the oxygen demand and tissue width model predictions depicted in Figure 5.6. All clinical measures were used except for a few cases in which the tolerance of the optimization procedure employed to find M_0 (2 healthy patients, 1 advanced POAG patient and 1 advanced NTG patient) and d (2 healthy patients and 1 advanced NTG patient) was not achieved.

It is important to note that the average values of oxygen demand and tissue width calculated for the healthy population (reported in Table 5.6) are not equal to the reference

Table 5.6.: Model predicted levels of tissue oxygen demand M_0 and tissue width d that yield the venous saturation clinical data collected from healthy, advanced POAG and advanced NTG patients [96].

	Healthy	Advanced POAG	Advanced POAG (IA)	Advanced NTG	Advanced NTG (IA)
M_0 [cm^3 $O_2 \cdot 100$ cm^{-3} min^{-1}]	1.98 ±0.77	1.58 ±0.64	1.48 ±0.53	1.99 ±.67	2.03 ±0.48
d [μm]	15.66 ±1.66	14.79 ±1.72	13.94 ±2.85	16.36 ±1.90	16.94 ±2.40

state values of oxygen demand and tissue width (reported in Table 5.5). In Table 5.5, the values M_0^{ref} and d^{ref} are computed from average values of IOP, MAP and arterial saturation obtained from the healthy population. In Table 5.6, the values of M_0 and d are computed using the MAP, IOP and arterial saturation from each individual and then averaging the resulting values in each population.

Based on the model predictions summarized in Figure 5.6 and Table 5.6, Figure 5.7(a) shows the model predicted curves of venous oxygen saturation for $M_0 = 1.98$ cm^3 $O_2 \cdot 100$ cm^{-3} min^{-1} (blue curve) and decreased $M_0 = 1.52$ cm^3 $O_2 \cdot 100$ cm^{-3} min^{-1} (black curve) as well as the average clinical values of venous saturation and OPP in healthy individuals (asterisk) and advanced POAG patients (square). In Figure 5.7(b), $M_0 = 1.98$ cm^3 $O_2 \cdot 100$ cm^{-3} min^{-1} and $d^{ref} = 15\ \mu$ m are fixed for both curves, but autoregulation is assumed to be impaired for the black dashed curve. These model predictions are compared with average clinical values of venous saturation and OPP measured in healthy individuals (asterisk) and advanced NTG patients (square).

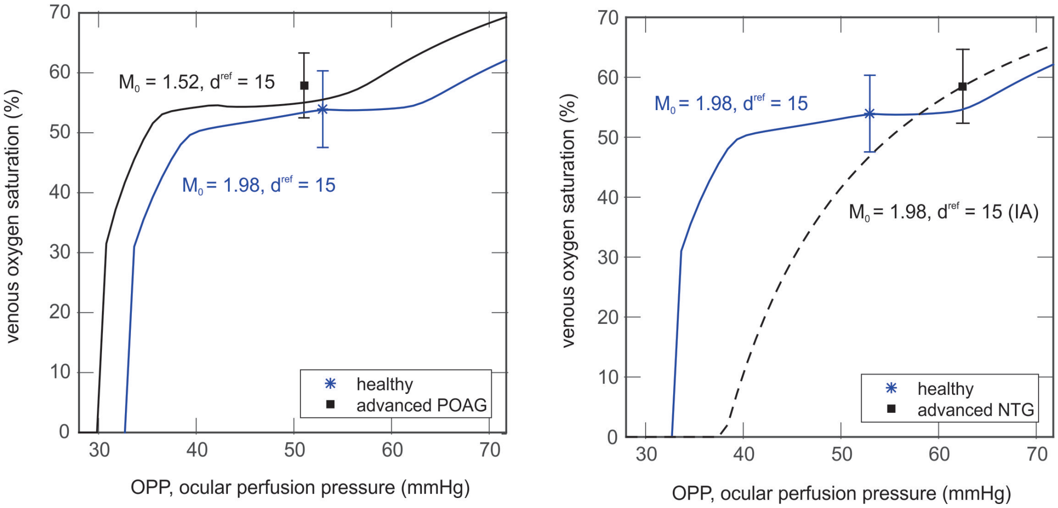

(a)

(b)

Fig. 5.7.: Model predicted curves of venous oxygen saturation as OPP is varied are shown with average values of venous oxygen saturation and OPP measured clinically. (a) The observed increase in the average venous saturation in healthy individuals (blue asterisk) and in advanced POAG patients (black square) is compared with model predicted levels of venous saturation for decreased levels of tissue demand. (b) The observed increase in the average venous saturation in healthy individuals (blue asterisk) and advanced NTG patients (black square) is compared with model predicted levels of venous saturation when autoregulation is impaired (IA).

5.1.4 Discussion

Experimental data

Retinal vessel oxygen saturation was measured in healthy individuals and glaucoma patients using a non-invasive retinal oximeter. The measurements indicated that patients with advanced glaucoma (both POAG and NTG patients) exhibited higher venous oxygen saturation (and consequently a lower arteriovenous difference in oxygen saturation) compared with healthy individuals. Other studies [108, 109] have confirmed these findings, and it has been previously hypothesized [96] that the observed increase in venous saturation is likely a secondary effect of glaucomatous atrophy and not a primary cause of glaucoma, citing the absence of hypoxia in advanced glaucoma patients as supporting evidence. However, the number of advanced glaucoma patients in these studies (including the current one) was rather small, and many patients were under active ophthalmological care. Thus, additional studies, ideally progressive in nature and conducted in patients with very high IOP and very low OPP, are needed in order to draw more definitive conclusions.

Theoretical investigation

Here, we have implemented a theoretical model based on fundamental hemodynamic and mechanical principles to predict venous oxygen saturation levels given patient-specific values of MAP, IOP and arterial oxygen saturation. The model predictions using the reference state values of these factors align well with the observed venous saturation levels collected from healthy individuals (Figure 5.4).

A Krogh cylinder model is used to describe the diffusion of oxygen into tissue; this Krogh model is applied in the classical sense in which the oxygen-supplying vessel runs along the central axis of a tissue cylinder. However, such an assumption may not be the most appropriate for retinal tissue, since the majority of the tissue that retinal vessels feed is typically located ”below” the vessels [110]. Some mathematical models have described oxygen diffusion through the retinal tissue layers [111–114] but did not consistently include a description of blood flow and autoregulation in the retinal vasculature. It would be an interesting research direction to enhance the model to include a more realistic geometric arrangement of vessels and tissue.

Theoretical interpretation of clinical data

We have used a mathematical model to offer possible explanations for the observed trends in oximetry data collected in healthy individuals and glaucoma patients. Specifically, the model shows that a decrease in oxygen demand, an impairment of autoregulation or a decrease in tissue width can all lead to increased venous saturation levels. It is important to note that although the model predictions offer each of these scenarios as a possible explanation, not all of them are physiologically relevant when describing the details of glaucoma. For example, suggesting a decrease in the Krogh cylinder tissue width as an explanation for the increased venous saturation levels observed in glaucoma is not consistent with the reduced vascularization observed in some glaucoma patients [104, 115–117]. However, the interconnection of tissue width and retinal atrophy suggests that future insight could be gained by using the model to assess the effects of altering multiple factors at once.

The patient-specific model optimizations presented (Figure 5.7) suggest that there might be different explanations for the increased venous saturation levels observed among advanced POAG patients and advanced NTG patients. Specifically, a decrease in oxygen demand may be more relevant to the increase in venous saturation observed in advanced POAG (Figure 5.7(a)), while impaired autoregulation mechanisms may be more relevant to the increase in venous saturation observed in advanced NTG (Figure 5.7(b)). This finding also suggests that vascular changes might occur primary to glaucomatous damage in NTG patients. Of note, the relation found between NTG patients and the impairment of blood flow autoregulation has been proposed previously [118, 119]. Importantly, impaired blood flow autoregulation could play a role in all advanced glaucoma patients, but to varying extents, as suggested by Figure 5.6. Additional theoretical investigations, ideally coupled with statistical methods and conducted on a wider set of glaucoma patients, are needed to confirm the model findings.

5.2 Color Doppler images in healthy individuals and glaucoma patients

5.2.1 Introduction

CDI is a consolidated noninvasive technique to measure blood velocity profile in different medical fields, such as radiology [120, 121], cardiology [122–125], obstetrics [126, 127] and ophthalmology [128–131]. Interestingly, since the arterial waveform changes as we move along the arterial tree, various waveform parameters (WPs) have been proposed in the scientific literature.

Typical WPs utilized in ophthalmology are PSV, EDV and resistive index (RI) [132]. Here we further advance the analysis of CDI measurements by proposing a computer-aided manipulation process of ophthalmic artery CDI images that enables the extraction of a novel set of WPs that might help better characterize the disease status in glaucoma [133].

5.2.2 Methods

CDI images obtained form healthy individuals and glaucoma patients are considered. 50 CDI images acquired by 4 different operators on 9 healthy individuals were collected at the University Eye Clinic, Foundation IRCCS, Policlinico San Matteo, Pavia, Italy, and CDI images of 38 glaucoma patients within the Indianapolis Glaucoma Progression Study were collected at the Eugene and Marilyn Glick Eye Institute, Indiana University School of Medicine, Indianapolis, IN, USA. The baseline characteristics of the study group are described in Table 5.7. The PSV, EDV and RI raw data are obtained directly from the ultrasound machine as an average of the values measured over at least three cardiac cycles.

An ad-hoc semi-automated image processing code was implemented in MATLAB to analyze the CDI images, detect the digitalized OA velocity waveforms and extract the WPs, Figure 5.8. The image processing consists of several steps

1. the CDI image in red-green-blue (RGB) color scale is converted into grayscale format;

2. the resulting grayscale image is analyzed to extract the time scale, velocity scale, cardiac cycle period and height of PSV (all of them measured in terms of image pixels);

3. the original grayscale image is cropped, using the previously extracted pixels values, to contain only one cardiac cycle;

4. the Sobel method [134, 135] is used to detect waveform edges;

Table 5.7.: Baseline characteristics of the healthy individuals and glaucoma patients included in the study.

	Healthy	Glaucoma
Number of patients	9	38
Females	5	19
Males	4	19
Age	24 ± 2	70 ± 13
Years of glaucoma diagnosis at the time of the visit	-	17 ± 10
Intraocular pressure [mmHg]	14 ± 3	16 ± 4
Heart rate (HR) [bpm]	-	67 ± 12
Systolic pressure (SP) [mmHg]	117 ± 7	138 ± 21
Diastolic pressure (DP) [mmHg]	70 ± 8	84 ± 11
Mean arterial pressure (MAP) [mmHg]	86 ± 7	102 ± 13
Systolic ocular perfusion pressure (SOPP) [mmHg]	103 ± 8	77 ± 15
Diastolic ocular perfusion pressure (DOPP) [mmHg]	56 ± 8	41 ± 8
Mean ocular perfusion pressure (MOPP) [mmHg]	43 ± 5	53 ± 10
Ocular medications	-	$25(66\%)$
Systemic medications	-	$22(58\%)$
Peak systolic velocity (PSV) raw [cm/s]	40 ± 7	26 ± 10
End diastolic velocity (EDV) raw [cm/s]	8 ± 2	6 ± 3
Resistive index (RI) raw[-]	0.80 ± 0.05	0.78 ± 0.7

5. the waveform edges are smoothed via local regression using weighted linear least squares and a first degree polynomial model;

6. the resulting waveform profile is then scaled from pixel units to physical units.

Once the OA waveform digitalized profile is constructed, the following WPs are extracted (Figure 1)

- PSV;
- dicrotic notch velocity (DNV);
- EDV;
- RI, defined as
$$\mathrm{RI} = \frac{\mathrm{PSV} - \mathrm{EDV}}{\mathrm{PSV}}; \tag{5.9}$$
- period of a cardiac cycle (T);
- first systolic ascending time (PSV time);
- difference between PSV time and DNV time (Dt);
- subendocardial viability ratio (SEVR) between the diastolic time interval (DTI) and the systolic time interval (STI) [136];
- area under the wave (A);
- area ratio (ϕ) defined as
$$\phi = \frac{A_w}{A_{box}} = \frac{Aw}{\mathrm{PSV}\ Dt}; \tag{5.10}$$
- normalized distance between ascending and descending limb of the wave at two thirds of the difference between PSV and EDV (DAD/T) [137].

The Shapiro-Wilk test was used to test the normal distribution of quantitative variables: as all quantitative variables were normally distributed, the results are expressed as the mean value and standard deviation (SD) were reported. Qualitative variables are summarized as counts and percentages. An analysis of concordance is performed to compare the raw values of PSV, EDV and RI with the corresponding values extracted from the digitalized OA profile using the image manipulation process detailed previously. The concordance correlation coefficient (CCC) determines how far the data deviate from the line of

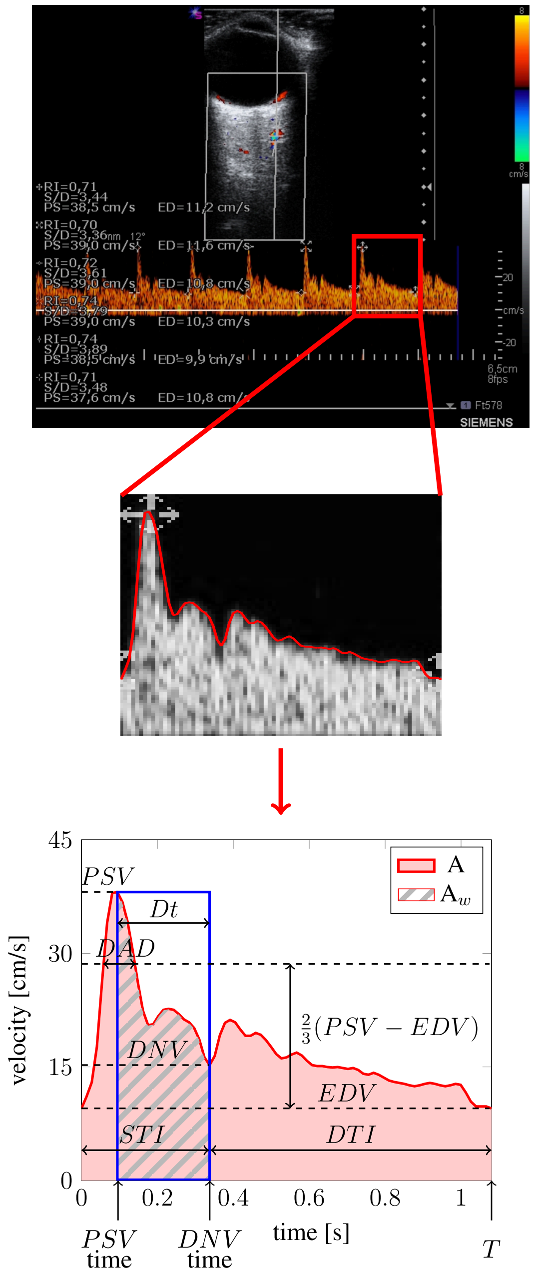

Fig. 5.8.: A summary of the semi-automated image manipulation process used to extract the ophthalmic artery waveform parameters. Starting from the CDI image (top), the digitalized OA velocity waveform is detected (center) and the corresponding waveform parameters are extracted (bottom).

perfect concordance, combining measures of precision and accuracy [138]. CCC ranges in values from 0 to 1. A CCC value of 0 indicates that most of the error originates from differences in measurements between operators. As CCC values approach 1, the measurement differences between the different operators are becoming negligible and more consistent. Inter-observer agreement was classified as poor (0.00 to 0.20), fair (0.21 to 0.40), moderate (0.41 to 0.60), good (0.61 to 0.80), excellent (0.81 to 1.00) [139]. CCCs are reported together with theirs 95% Confidence Interval (CI). To investigate the WPs differences among glaucoma patients with respect to gender and ocular medications, and between healthy subjects and glaucoma patients, a two-sample t-test for independent data is used. Moreover, the differences between healthy subjects and glaucoma patients are adjusted for age and gender fitting multivariable linear regression models. The Pearsons correlation coefficient r is computed to explore the associations among WPs and age, year of diagnosis and clinical measurements in glaucoma patients. A p-value $\mathsf{p} < 0.05$ was considered statistically significant. All tests were two-sided. The data analysis was performed with the STATA statistical package (release 14.0, 2015, Stata Corporation, College Station, Texas, USA).

5.2.3 Results

When considering all individuals included in the study, i.e. healthy individuals and glaucoma patients, the analysis showed an excellent concordance on PSV (CCC $= 0.85$; 95% CI 0.77 - 0.93), a good concordance on EDV (CCC $= 0.63$; 95% CI: 0.49 - 0.78) and a fair concordance on RI (CCC $= 0.33$; 95% CI: 0.14 - 0.52). When considering only glaucoma patients, the analysis showed a good concordance on PSV (CCC $= 0.80$; 95% CI: 0.69 - 0.91), a good concordance on EDV (CCC $= 0.62$; 95% CI: 0.46 - 0.78) and a fair concordance on RI (CCC $= 0.30$; 95% CI: 0.09 - 0.52). When considering only healthy individuals, the analysis showed an excellent concordance on PSV (CCC $= 0.99$; 95% CI: 0.97 - 1.00), a moderate concordance on EDV (CCC $= 0.45$; 95% CI: 0.15 - 0.74) and a moderate concordance on RI (CCC $= 0.58$; 95% CI: 0.31 - 0.85).

When compared to male glaucoma patients, female glaucoma patients showed statistically higher values of the ratio DAD/T ($\mathsf{p} = 0.002$), and statistically lower values of SEVR ($\mathsf{p} = 0.031$). No statistical difference was found in the remaining WPs when comparing glaucoma patients of different gender. Glaucoma patients taking ocular medications showed significantly higher values of T ($\mathsf{p} = 0.005$) and SEVR ($\mathsf{p} = 0.002$) when compared to glaucoma patients not taking ocular medications. No statistical difference was found in the remaining WPs when comparing glaucoma patients taking ocular medications with glaucoma patients not taking ocular medications.

Glaucoma patients age is positively correlated with RI ($\mathsf{r} = 0.52$; $\mathsf{p} < 0.001$) and negatively correlated with EDV ($\mathsf{r} = -0.35$; $\mathsf{p} = 0.030$). No statistical correlation was found among the remaining WPs and glaucoma patients age. The years of glaucoma diagnosis at the time of the visit is negatively correlated with T ($\mathsf{r} = -0.41$; $\mathsf{p} = 0.015$) and SEVR ($\mathsf{r} = -0.36$; $\mathsf{p} = 0.038$). No statistical correlation was found among the remaining WPs and glaucoma patients years of diagnosis at the time of the visit. Among the set of clinical measurements of heart rate (HR), SP, DP, MAP, IOP, systolic ocular perfusion pressure (SOPP), diastolic ocular perfusion pressure (DOPP) and mean ocular perfusion pressure (MOPP), HR is the only parameter that showed statistical correlations with some of the WPs in glaucoma patients: HR is negatively correlated with T ($\mathsf{r} = -0.65$), PSV time ($\mathsf{r} = -0.41$), SEVR ($\mathsf{r} = -0.39$), ϕ ($\mathsf{r} = -0.35$).

When compared to healthy individual, glaucoma patients showed significantly higher values of ϕ ($\mathsf{p} < 0.001$) and DAD/T ($\mathsf{p} < 0.001$), and statistically lower values of A ($\mathsf{p} = 0.041$), Dt ($\mathsf{p} = 0.008$), PSV ($\mathsf{p} = 0.004$) and EDV ($\mathsf{p} = 0.033$), Figure 5.9. If the comparison is adjusted by gender and age (fitting a multivariable linear regression model), then, glaucoma patients showed significantly higher values of ϕ ($\mathsf{p} < 0.001$) and DAD/T ($\mathsf{p} = 0.002$), and significantly lower values of RI ($\mathsf{p} = 0.002$) when compared with healthy individuals. No statistical difference was found in the other WPs when comparing glaucoma patients with healthy individuals.

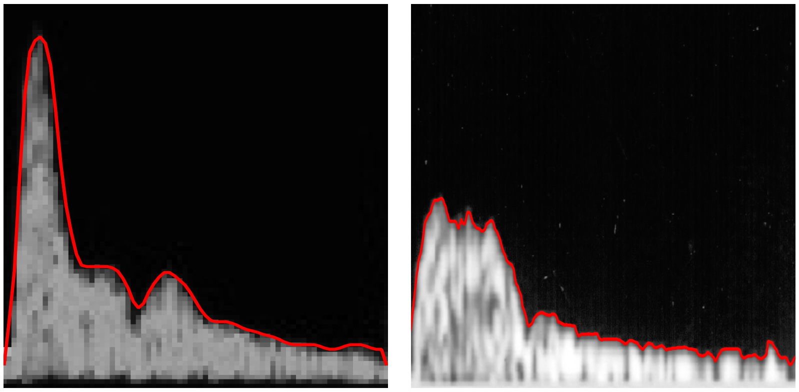
(a) healthy individual (b) glaucoma patient

Fig. 5.9.: Digitalized OA velocity profile of a healthy individual (a) and a glaucoma patient (b).

5.2.4 Discussion

We investigated whether new approaches to analyzing WPs using computer-aided manipulation of OA-CDI images could distinguish between healthy subjects and glaucoma patients. The OA-CDI images manipulation proposed here showed a higher concordance between PSV raw data and extracted PSV data than on EDV and RI data. Note that the raw PSV, EDV and RI values were obtained averaging over at least three cardiac cycles; instead the corresponding parameters extracted via the OA-CDI manipulation process correspond to just one of those cardiac cycles. Moreover, CDI PSV measurements have been found to be more reproducible and accurate then EDV and RI measurements [140–142].

There now is strong evidence that glaucoma patients have a vascular contribution to their disease [143]. We found that glaucoma patients had a statistically significant higher DAD/T than did healthy subjects. This is interesting because when Oliva and Roztocil [137] examined patients with obliterating atherosclerosis by Doppler ultrasound and then analyzed the waveform to identify P/L, which is identical to DAD/T here, they found that P/L identified the severity of the disease and the presence or absence of progression based on the variability coefficients. We also found that glaucoma patients had a statistically significant higher area ratio ϕ than did healthy individuals. Of note, ϕ represents another method to measure the shape of the wave in the systolic portion of the cardiac cycle similar to that proposed by Oliva and Roztocil. The correlation between DAD/T, vascular status, and glaucoma could prove to enhance the screening of glaucoma, and potentially serve as a marker for progression.

It has long been debated whether men or women are at higher risk of glaucoma [144–146]. We found a statistically significant increase in DAD/T in females when comparing male and female patients with glaucoma whose average age was 70 ± 13. It is well known that age is a risk factor for glaucoma [147]. We found that age correlated positively with RI and negatively with EDV. These findings suggest that, similar to other vascular beds [148], the OA is susceptible to the atherosclerotic effects of aging.

Although the correlation with DAD/T, glaucoma, and gender shows very promising results, there were, however, several limitations to the study design. The difference in mean age between healthy and glaucoma patients was 46 years. Due to the role of age on general health and disease process, future studied comparing age-matched healthy and glaucoma patients might provide closer evaluation between healthy subjects and glaucoma. The total number of enrolled subjects was 47, with 9 healthy subjects. In future studies, analysis of a larger population with equal numbers of healthy subjects and glaucoma patient would provide greater insight into the potential role of DAD/T.

6. CONCLUSIONS AND FUTURE DIRECTIONS

In this thesis we developed mathematical models to investigate the relevance of mechanical and vascular factors in the pathophysiology of glaucoma. Briefly,

- We have developed a mathematical model that combines the description of stresses and strains in the lamina cribrosa with the blood flow in the central retinal vessels and retinal microcirculation using reduced-order fluid-structure interaction models. We have validated the model predictions using three different and unrelated experimental and clinical studies.
- We have derived a novel energy-based technique for coupling partial and ordinary differential equations in blood flow using operator splitting. We have shown that the proposed splitting scheme is unconditionally stable independently of the choice of numerical method and discretization approach in each sub-step. We have numerically tested its stability and order of convergence in time in three theoretical test cases.
- We have used a previously developed model of the retinal microcirculation to predict three possible explanations for the increases in venous oxygen saturation observed in advanced glaucoma patients.
- We have proposed a novel computer-aided extraction process of ophthalmic artery waveform parameters from CDI images. We have tested the concordance between clinically measured and extracted parameters, and have identified a set of novel parameters that are statistically different between healthy subjects and glaucomatous individuals.

Using this mathematical framework we were able to provide a preliminary answer to the following open questions in ophthalmology

Is there a region of compression in the lamina cribrosa? Stress distributions in ocular tissues cannot be measured directly. The model results show regions of compressive stresses in the lamina cribrosa, that become more pronounced as IOP is elevated. The increase in scleral tension due to IOP elevation partially relieves some of the compression in the lamina.

To confirm the model findings, it would be interesting to extend the lamina cribrosa model to three-dimensional geometries, that are not necessarily axially symmetric.

What mechanism might explain the influence of IOP elevation on CRA blood velocity? The model suggests that the decrease in the CRA blood velocity induced by IOP elevation measured *in vivo* in humans might be due to the IOP-induced increase in vascular resistance of the retinal venules. Indeed, the model suggests that regions of radial compressive stress in the lamina cribrosa cause an increase in the vascular resistance of the CRA; however, this increase is minimal compared to the IOP-induced increase in resistance of the retinal venules.

To confirm these findings, higher-order time dependent fluid-structure interaction models for the CRA and CRV are needed. As a first step in this direction, we proposed an energy-based multiscale coupling technique.

Is high translaminar pressure difference (TLpD) a risk factor in glaucoma? The model predictions suggest that changes in IOP have a stronger effect on retinal hemodynamics than changes in CSFp, even though these changes lead to the same TLpD. This might be due to the fact that, unlike CSFp, IOP acts directly on the intraocular retinal venules. Our model also suggests that the CSFp influence on retinal hemodynamics might be mediated by associated changes in MAP.

Expanding the model to describe the CRV and the retinal venules as collapsible vessels (using a Starling resistor) will help to quantify the effect of IOP and CSFp on retinal blood flow and confirm the model findings.

Do blood flow alterations occur primary or secondary to glaucomatous damage? The model results suggest that there might be different explanations for the increased venous saturation levels observed among advanced POAG patients and advanced NTG patients: a decrease in oxygen demand in advanced POAG, and impaired autoregulation in advanced NTG. This finding also suggests that vascular changes might occur secondary to the loss of retinal ganglion cells in advanced POAG patients, since those cells would no longer require oxygen, and might occur primary in advanced NTG patients, suggesting that impaired autoregulation might lead to tissue damage with subsequent vision loss.

Additional theoretical investigations, ideally coupled with statistical methods and conducted on a wider set of glaucoma patients, are needed to confirm the model findings.

Can velocity profiles be used to characterize the disease status in glaucoma? The computer-aided analysis of OA-CDI images suggests that glaucoma patients have a statistically significant higher normalized distance between ascending and descending limb of the wave (DAD/T) than healthy subjects. Moreover, we found a statistically significant higher DAD/T in females than male glaucoma patients.

In future analyses, DAD/T should be examined in relationship to longitudinal data of glaucoma patients to investigate the potential to predict severity and progression.

Is it possible to relate clinical measurements to the patient risk of developing glaucoma? Glaucoma is a multifactorial disease, hence clinical interpretation of flow and velocity measurements is extremely challenging. Statistical methods are widely used to estimate correlations between clinical factors and retinal hemodynamics, such as IOP and CSFp. However, the mechanisms behind these correlations are still elusive. In this thesis, we have shown that mathematical modeling predictions, used in synergy with clinical data and statistical methods, help elucidate these mechanisms and estimate the contribution of each factor, ultimately aiding the future development of individualized medicine in glaucoma.

REFERENCES

REFERENCES

[1] J. B. Jonas and N. Wang, "Association between arterial blood pressure, cerebrospinal fluid pressure and intraocular pressure in the pathophysiology of optic nerve head diseases," *Clinical & experimental ophthalmology*, vol. 40, no. 4, pp. e233–e234, 2012.

[2] F. Hollows and P. Graham, "Intra-ocular pressure, glaucoma, and glaucoma suspects in a defined population." *The British journal of ophthalmology*, vol. 50, no. 10, p. 570, 1966.

[3] R. Shah and R. Wormald, "Glaucoma," *BMJ Clinical Evidence*, Jun. 2011.

[4] L. A. Pinto, E. Vandewalle, E. De Clerck, C. Marques-Neves, and I. Stalmans, "Ophthalmic artery doppler waveform changes associated with increased damage in glaucoma patientscdi analysis of the oa in glaucoma patients," *Investigative ophthalmology & visual science*, vol. 53, no. 4, pp. 2448–2453, 2012.

[5] C. Akarsu and M. Y. K. Bilgili, "Color doppler imaging in ocular hypertension and open-angle glaucoma," *Graefe's archive for clinical and experimental ophthalmology*, vol. 242, no. 2, pp. 125–129, 2004.

[6] Z. Butt, C. O'Brien, G. McKillop, P. Aspinall, and P. Allan, "Color doppler imaging in untreated high-and normal-pressure open-angle glaucoma." *Investigative ophthalmology & visual science*, vol. 38, no. 3, pp. 690–696, 1997.

[7] P. Rojanapongpun, S. Drance, and B. Morrison, "Ophthalmic artery flow velocity in glaucomatous and normal subjects." *British Journal of Ophthalmology*, vol. 77, no. 1, pp. 25–29, 1993.

[8] L. A. Tobe, A. Harris, R. M. Hussain, G. Eckert, A. Huck, J. Park, P. Egan, N. J. Kim, and B. Siesky, "The role of retrobulbar and retinal circulation on optic nerve head and retinal nerve fibre layer structure in patients with open-angle glaucoma over an 18-month period," *British Journal of Ophthalmology*, pp. bjophthalmol–2014, 2014.

[9] J. Caprioli, A. L. Coleman *et al.*, "Blood pressure, perfusion pressure, and glaucoma," *American journal of ophthalmology*, vol. 149, no. 5, pp. 704–712, 2010.

[10] Jmarchn - Own work, CC BY-SA 3.0, via Wikipedia Commons https://commons.wikimedia.org/w/index.php?curid=34828874.

[11] A. Harris, C. Jonescu-Cuypers, L. Kagemann, T. Ciulla, and G. Krieglstein, *Atlas of ocular blood flow*. Butterworth-Heinemann, 2010.

[12] D. Moore, A. Harris, D. WuDunn, N. Kheradiya, and B. Siesky, "Dysfunctional regulation of ocular blood flow: A risk factor for glaucoma?" *Clinical ophthalmology (Auckland, NZ)*, vol. 2, no. 4, p. 849, 2008.

[13] A. Harris, L. Kagemann, R. Ehrlich, C. Rospigliosi, D. Moore, and B. Siesky, “Measuring and interpreting ocular blood flow and metabolism in glaucoma,” *Canadian Journal of Ophthalmology/Journal Canadien d’Ophtalmologie*, vol. 43, no. 3, pp. 328–336, 2008.

[14] R. N. Weinreb and A. Harris, *Ocular blood flow in glaucoma.* Kugler Publications, 2009, vol. 6.

[15] S. H. Hardarson, “Retinal oximetry,” *Acta ophthalmologica*, vol. 91, p. 489490, 2013.

[16] R. Ren, N. Wang, X. Zhang, T. Cui, and J. B. Jonas, “Trans-lamina cribrosa pressure difference correlated with neuroretinal rim area in glaucoma,” *Graefe’s Archive for Clinical and Experimental Ophthalmology*, vol. 249, no. 7, pp. 1057–1063, 2011.

[17] B. Marek, A. Harris, P. Kanakamedala, E. Lee, A. Amireskandari, L. Carichino, G. Guidoboni, L. A. Tobe, and B. Siesky, “Cerebrospinal fluid pressure and glaucoma: regulation of trans-lamina cribrosa pressure,” *British Journal of Ophthalmology*, pp. bjophthalmol–2013, 2013.

[18] W. H. Morgan, D.-Y. Yu, V. A. Alder, S. J. Cringle, R. L. Cooper, P. H. House, and I. J. Constable, “The correlation between cerebrospinal fluid pressure and retrolaminar tissue pressure.” *Investigative ophthalmology & visual science*, vol. 39, no. 8, pp. 1419–1428, 1998.

[19] J. B. Jonas, “Role of cerebrospinal fluid pressure in the pathogenesis of glaucoma,” *Acta ophthalmologica*, vol. 89, no. 6, pp. 505–514, 2011.

[20] R. Ren, X. Zhang, N. Wang, B. Li, G. Tian, and J. B. Jonas, “Cerebrospinal fluid pressure in ocular hypertension,” *Acta ophthalmologica*, vol. 89, no. 2, pp. e142–e148, 2011.

[21] J. P. Berdahl, M. P. Fautsch, S. S. Stinnett, and R. R. Allingham, “Intracranial pressure in primary open angle glaucoma, normal tension glaucoma, and ocular hypertension: a case–control study,” *Investigative ophthalmology & visual science*, vol. 49, no. 12, pp. 5412–5418, 2008.

[22] A. Harris, K. Joos, M. Kay, D. Evans, R. Shetty, W. E. Sponsel, and B. Martin, “Acute iop elevation with scleral suction: effects on retrobulbar haemodynamics.” *British journal of ophthalmology*, vol. 80, no. 12, pp. 1055–1059, 1996.

[23] O. Findl, K. Strenn, M. Wolzt, R. Menapace, C. Vass, H.-G. Eichler, and L. Schmetterer, “Effects of changes in intraocular pressure on human ocular haemodynamics,” *Current eye research*, vol. 16, no. 10, pp. 1024–1029, 1997.

[24] H. Querfurth, W.-D. Lagrèze, T. Hedges, and P. Heggerick, “Flow velocity and pulsatility of the ocular circulation in chronic intracranial hypertension,” *Acta neurologica scandinavica*, vol. 105, no. 6, pp. 431–440, 2002.

[25] C. F. Burgoyne, J. C. Downs, A. J. Bellezza, J.-K. F. Suh, and R. T. Hart, “The optic nerve head as a biomechanical structure: a new paradigm for understanding the role of iop-related stress and strain in the pathophysiology of glaucomatous optic nerve head damage,” *Progress in retinal and eye research*, vol. 24, no. 1, pp. 39–73, 2005.

[26] H. Dongqi and R. Zeqin, "A biomathematical model for pressure-dependent lamina cribrosa behavior," *Journal of biomechanics*, vol. 32, no. 6, pp. 579–584, 1999.

[27] M. E. Edwards and T. A. Good, "Use of a mathematical model to estimate stress and strain during elevated pressure induced lamina cribrosa deformation," *Current eye research*, vol. 23, no. 3, pp. 215–225, 2001.

[28] J. Morgan-Davies, N. Taylor, A. Hill, P. Aspinall, C. OBrien, and A. Azuara-Blanco, "Three dimensional analysis of the lamina cribrosa in glaucoma," *British journal of ophthalmology*, vol. 88, no. 10, pp. 1299–1304, 2004.

[29] T. Newson and A. El-Sheikh, "Mathematical modeling of the biomechanics of the lamina cribrosa under elevated intraocular pressures," *Journal of biomechanical engineering*, vol. 128, no. 4, pp. 496–504, 2006.

[30] I. A. Sigal, J. G. Flanagan, I. Tertinegg, and C. R. Ethier, "Finite element modeling of optic nerve head biomechanics," *Investigative ophthalmology & visual science*, vol. 45, no. 12, pp. 4378–4387, 2004.

[31] I. A. Sigal, H. Yang, M. D. Roberts, J. L. Grimm, C. F. Burgoyne, S. Demirel, and J. C. Downs, "Iop-induced lamina cribrosa deformation and scleral canal expansion: independent or related?" *Investigative ophthalmology & visual science*, vol. 52, no. 12, pp. 9023–9032, 2011.

[32] I. A. Sigal, R. A. Bilonick, L. Kagemann, G. Wollstein, H. Ishikawa, J. S. Schuman, and J. L. Grimm, "The optic nerve head as a robust biomechanical systemthe onh as a robust system," *Investigative ophthalmology & visual science*, vol. 53, no. 6, pp. 2658–2667, 2012.

[33] I. A. Sigal and J. L. Grimm, "A few good responses: Which mechanical effects of iop on the onh to study? pca of onh biomechanics," *Investigative ophthalmology & visual science*, vol. 53, no. 7, pp. 4270–4278, 2012.

[34] I. A. Sigal, J. G. Flanagan, K. L. Lathrop, I. Tertinegg, and R. Bilonick, "Human lamina cribrosa insertion and age," *Investigative ophthalmology & visual science*, vol. 53, no. 11, pp. 6870–6879, 2012.

[35] J. Arciero, A. Harris, B. Siesky, A. Amireskandari, V. Gershuny, A. Pickrell, and G. Guidoboni, "Theoretical analysis of vascular regulatory mechanisms contributing to retinal blood flow autoregulationmechanisms contributing to retinal autoregulation," *Investigative ophthalmology & visual science*, vol. 54, no. 8, pp. 5584–5593, 2013.

[36] P. Ganesan, S. He, and H. Xu, "Development of an image-based network model of retinal vasculature," *Annals of biomedical engineering*, vol. 38, no. 4, pp. 1566–1585, 2010.

[37] ——, "Analysis of retinal circulation using an image-based network model of retinal vasculature," *Microvascular research*, vol. 80, no. 1, pp. 99–109, 2010.

[38] ——, "Development of an image-based model for capillary vasculature of retina," *Computer methods and programs in biomedicine*, vol. 102, no. 1, pp. 35–46, 2011.

[39] ——, "Modelling of pulsatile blood flow in arterial trees of retinal vasculature," *Medical engineering & physics*, vol. 33, no. 7, pp. 810–823, 2011.

[40] T. Takahashi, T. Nagaoka, H. Yanagida, T. Saitoh, A. Kamiya, T. Hein, L. Kuo, and A. Yoshida, “A mathematical model for the distribution of hemodynamic parameters in the human retinal microvascular network,” *Journal of biorheology*, vol. 23, no. 2, pp. 77–86, 2009.

[41] A. Quarteroni and A. Veneziani, “Analysis of a geometrical multiscale model based on the coupling of ode and pde for blood flow simulations,” *Multiscale Modeling & Simulation*, vol. 1, no. 2, pp. 173–195, 2003.

[42] S. Canic, J. Tambaca, G. Guidoboni, A. Mikelic, C. J. Hartley, and D. Rosenstrauch, “Modeling viscoelastic behavior of arterial walls and their interaction with pulsatile blood flow,” *SIAM Journal on Applied Mathematics*, vol. 67, no. 1, pp. 164–193, 2006.

[43] A. Mikelic, G. Guidoboni, and S. Canic, “Fluid-structure interaction in a pre-stressed tube with thick elastic walls i: the stationary stokes problem,” *Networks and Heterogeneous Media*, vol. 2, no. 3, p. 397, 2007.

[44] A. C. Eringen, “Mechanics of continua,” *Huntington, NY, Robert E. Krieger Publishing Co., 1980. 606 p.*, vol. 1, 1980.

[45] A. Hazel, “Continuum mechanics lecture notes 2015,” Retrived from: http://www.maths.manchester.ac.uk/ ahazel/MATH45061/MATH45061.html.

[46] P. G. Ciarlet and V. Lods, “Asymptotic analysis of linearly elastic shells:generalized membrane shells,” *Journal of Elasticity*, vol. 43, no. 2, pp. 147–188, 1996.

[47] ——, “Asymptotic analysis of linearly elastic shells. iii. justification of koiter’s shell equations,” *Archive for rational mechanics and analysis*, vol. 136, no. 2, pp. 191–200, 1996.

[48] A. Quarteroni and L. Formaggia, “Mathematical modelling and numerical simulation of the cardiovascular system,” Retrived from:https://www.mate.polimi.it/biblioteca/add/qmox/mox01.pdf, 2002.

[49] L. Formaggia, D. Lamponi, and A. Quarteroni, “One-dimensional models for blood flow in arteries,” *Journal of engineering mathematics*, vol. 47, no. 3-4, pp. 251–276, 2003.

[50] K. Hayashi, H. Ishikawa, M. Tanaka, and T. Adachi, *Computational biomechanics*. Springer, 1996.

[51] G. Guidoboni, A. Harris, S. Cassani, J. Arciero, B. Siesky, A. Amireskandari, L. Tobe, P. Egan, I. Januleviciene, and J. Park, “Intraocular pressure, blood pressure, and retinal blood flow autoregulation: A mathematical model to clarify their relationship and clinical relevanceeffects of iop, bp, and ar on retinal hemodynamics,” *Investigative ophthalmology & visual science*, vol. 55, no. 7, pp. 4105–4118, 2014.

[52] C. Bertoglio, A. Caiazzo, and M. A. Fernández, “Fractional-step schemes for the coupling of distributed and lumped models in hemodynamics,” *SIAM Journal on Scientific Computing*, vol. 35, no. 3, pp. B551–B575, 2013.

[53] V. Chabannes, M. Ismail, C. Prud'Homme, and M. Szopos, "Hemodynamic simulations in the cerebral venous network: A study on the influence of different modeling assumptions," *Journal of Coupled Systems and Multiscale Dynamics*, vol. 3, no. 1, pp. 23–37, 2015.

[54] W. D. Lakin, S. A. Stevens, B. I. Tranmer, and P. L. Penar, "A whole-body mathematical model for intracranial pressure dynamics," *Journal of mathematical biology*, vol. 46, no. 4, pp. 347–383, 2003.

[55] J. G. Heywood, R. Rolf, and T. Stefan, "Artificial boundaries and flux and pressure conditions for the incompressible navier-stokes equations," *International Journal for Numerical Methods in Fluids*, vol. 22, pp. 325–352, 1996.

[56] A. Quarteroni, S. Ragni, and A. Veneziani, "Coupling between lumped and distributed models for blood flow problems," *Computing and Visualization in Science*, vol. 4, no. 2, pp. 111–124, 2001.

[57] J. Fouchet-Incaux, "Artificial boundaries and formulations for the incompressible navier–stokes equations: applications to air and blood flows," *SeMA Journal*, vol. 64, no. 1, pp. 1–40, 2014.

[58] J. Fouchet-Incaux, C. Grandmont, and S. Martin, "Numerical stability of coupling schemes in the 3d/0d modelling of airflows and blood flows," Retrived from:https://hal.inria.fr/hal-01095960, 2015.

[59] J. Fouchet-Incaux, "Modélisation, analyse numérique et simulations autour de la respiration," Ph.D. dissertation, Paris 11, 2015.

[60] G. Arbia, "Multiscale modeling of blood flow in the context of congenital heart disease," Ph.D. dissertation, Université Pierre et Marie Curie, 2014.

[61] Y. Bazilevs, J. Gohean, T. Hughes, R. Moser, and Y. Zhang, "Patient-specific isogeometric fluid–structure interaction analysis of thoracic aortic blood flow due to implantation of the jarvik 2000 left ventricular assist device," *Computer Methods in Applied Mechanics and Engineering*, vol. 198, no. 45, pp. 3534–3550, 2009.

[62] R. Glowinski, *Handbook of Numerical Analysis : Numerical methods for Fluids (Part 3), Philippe G. Ciarlet and Jacques-Louis Lions(Eds)*. North-Holland, 2003, vol. IX.

[63] B. Maury, *The respiratory system in equations*. Springer Science & Business Media, 2013, vol. 7.

[64] G. Guidoboni, R. Glowinski, N. Cavallini, S. Canic, and S. Lapin, "A kinematically coupled time-splitting scheme for fluid–structure interaction in blood flow," *Applied Mathematics Letters*, vol. 22, no. 5, pp. 684–688, 2009.

[65] G. Guidoboni, R. Glowinski, N. Cavallini, and S. Canic, "Stable loosely-coupled-type algorithm for fluid–structure interaction in blood flow," *Journal of Computational Physics*, vol. 228, no. 18, pp. 6916–6937, 2009.

[66] G. Guidoboni, R. Glowinski, and M. Pasquali, "Operator splitting for the numerical solution of free surface flow at low capillary numbers," *Journal of computational and applied mathematics*, vol. 232, no. 1, pp. 72–81, 2009.

[67] G. Guidoboni, A. Harris, J. C. Arciero, B. A. Siesky, A. Amireskandari, A. L. Gerber, A. H. Huck, N. J. Kim, S. Cassani, and L. Carichino, “Mathematical modeling approaches in the study of glaucoma disparities among people of african and european descents,” *Journal of coupled systems and multiscale dynamics*, vol. 1, no. 1, p. 1, 2013.

[68] G. Guidoboni, A. Harris, L. Carichino, Y. Arieli, and B. A. Siesky, “Effect of intraocular pressure on the hemodynamics of the central retinal artery: a mathematical model.” *Mathematical biosciences and engineering: MBE*, vol. 11, no. 3, pp. 523–546, 2014.

[69] L. Carichino, G. Guidoboni, B. Siesky, A. Amireskandari, I. Januleviciene, and A. Harris, “Effect of intraocular pressure and cerebrospinal fluid pressure on the blood flow in the central retinal vessels,” *Integrated Multidisciplinary Approaches in the Study and Care of the Human Eye Kugler Publications*, pp. 59–66, 2014.

[70] S.-Y. Woo, A. Kobayashi, W. Schlegel, and C. Lawrence, “Nonlinear material properties of intact cornea and sclera,” *Experimental Eye Research*, vol. 14, no. 1, pp. 29–39, 1972.

[71] E. J. Lee, T.-W. Kim, and R. N. Weinreb, “Variation of lamina cribrosa depth following trabeculectomy,” *Investigative ophthalmology & visual science*, vol. 54, no. 8, pp. 5392–5399, 2013.

[72] C. J. Pournaras, E. Rungger-Brändle, C. E. Riva, S. H. Hardarson, and E. Stefansson, “Regulation of retinal blood flow in health and disease,” *Progress in retinal and eye research*, vol. 27, no. 3, pp. 284–330, 2008.

[73] A. Strauss and A. Kedra, “Experiences with a new procedure for the measurement of the ophthalmic artery pressure: ophthalmomanometry-doppler.” *Medical instrumentation*, vol. 21, no. 5, pp. 255–261, 1987.

[74] J. W. Kiel, “The ocular circulation,” in *Colloquium Series on Integrated Systems Physiology: From Molecule to Function*, vol. 3, no. 1. Morgan & Claypool Life Sciences, 2011, pp. 1–81.

[75] F. Hecht, O. Pironneau, A. Le Hyaric, and K. Ohtsuka, “Freefem++,” *Numerical Mathematics and Scientific Computation. Laboratoire JL Lions, Université Pierre et Marie Curie, http://www. freefem. org/ff+*, vol. 3, 2012.

[76] W. H. Morgan, B. C. Chauhan, D.-Y. Yu, S. J. Cringle, V. A. Alder, and P. H. House, “Optic disc movement with variations in intraocular and cerebrospinal fluid pressure,” *Investigative ophthalmology & visual science*, vol. 43, no. 10, pp. 3236–3242, 2002.

[77] J. Jonas, C. Y. Mardin, U. Schlötzer-Schrehardt, and G. Naumann, “Morphometry of the human lamina cribrosa surface.” *Investigative ophthalmology & visual science*, vol. 32, no. 2, pp. 401–405, 1991.

[78] J. B. Jonas and L. Holbach, “Central corneal thickness and thickness of the lamina cribrosa in human eyes,” *Investigative ophthalmology & visual science*, vol. 46, no. 4, pp. 1275–1279, 2005.

[79] R. Ren, N. Wang, B. Li, L. Li, F. Gao, X. Xu, and J. B. Jonas, "Lamina cribrosa and peripapillary sclera histomorphometry in normal and advanced glaucomatous chinese eyes with various axial length," *Investigative ophthalmology & visual science*, vol. 50, no. 5, pp. 2175–2184, 2009.

[80] R. E. Norman, J. G. Flanagan, S. M. Rausch, I. A. Sigal, I. Tertinegg, A. Eilaghi, S. Portnoy, J. G. Sled, and C. R. Ethier, "Dimensions of the human sclera: thickness measurement and regional changes with axial length," *Experimental eye research*, vol. 90, no. 2, pp. 277–284, 2010.

[81] G. T. Dorner, E. Polska, G. Garhöfer, C. Zawinka, B. Frank, and L. Schmetterer, "Calculation of the diameter of the central retinal artery from noninvasive measurements in humans," *Current eye research*, vol. 25, no. 6, pp. 341–345, 2002.

[82] D. Baleanu, M. Ritt, J. Harazny, J. Heckmann, R. E. Schmieder, and G. Michelson, "Wall-to-lumen ratio of retinal arterioles and arteriole-to-venule ratio of retinal vessels in patients with cerebrovascular damage," *Investigative ophthalmology & visual science*, vol. 50, no. 9, pp. 4351–4359, 2009.

[83] E. Wetterer, R. Bauer, and T. Pasch, "Arteriensystem," in *Lehrbuch der Physiologie in Einzeldarstellungen*. Springer, 1971, pp. 1–66.

[84] R. L. Armentano, J. G. Barra, J. Levenson, A. Simon, and R. H. Pichel, "Arterial wall mechanics in conscious dogs assessment of viscous, inertial, and elastic moduli to characterize aortic wall behavior," *Circulation Research*, vol. 76, no. 3, pp. 468–478, 1995.

[85] Y. C. Fung, *Biomechanics: mechanical properties of living tissues*, 2nd ed. Springer Science & Business Media, 1993.

[86] A. Quarteroni, M. Tuveri, and A. Veneziani, "Computational vascular fluid dynamics: problems, models and methods," *Computing and Visualization in Science*, vol. 2, no. 4, pp. 163–197, 2000.

[87] X. Deng and R. Guidoin, "Arteries, veins and lymphatic vessels," in *Handbook of Biomaterial Properties*. Springer, 1998, pp. 81–105.

[88] Y. C. Fung, *Biomechanics: circulation*, 2nd ed. Springer Science & Business Media, 1997.

[89] S. Deokule and R. N. Weinreb, "Relationships among systemic blood pressure, intraocular pressure, and open-angle glaucoma," *Canadian Journal of Ophthalmology/Journal Canadien d'Ophtalmologie*, vol. 43, no. 3, pp. 302–307, 2008.

[90] Y. Agoumi, G. P. Sharpe, D. M. Hutchison, M. T. Nicolela, P. H. Artes, and B. C. Chauhan, "Laminar and prelaminar tissue displacement during intraocular pressure elevation in glaucoma patients and healthy controls," *Ophthalmology*, vol. 118, no. 1, pp. 52–59, 2011.

[91] I. A. Sigal, J. G. Flanagan, I. Tertinegg, and C. R. Ethier, "Predicted extension, compression and shearing of optic nerve head tissues," *Experimental eye research*, vol. 85, no. 3, pp. 312–322, 2007.

[92] ——, "Modeling individual-specific human optic nerve head biomechanics. part i: Iop-induced deformations and influence of geometry," *Biomechanics and modeling in mechanobiology*, vol. 8, no. 2, pp. 85–98, 2009.

[93] A. Quarteroni, *Numerical models for differential problems.* Springer Science & Business Media, 2010, vol. 2.

[94] V. Girault and P.-A. Raviart, *Finite element methods for Navier-Stokes equations: theory and algorithms.* Springer Science & Business Media, 2012, vol. 5.

[95] O. B. Olafsdottir, S. H. Hardarson, M. S. Gottfredsdottir, A. Harris, and E. Stefánsson, "Retinal oximetry in primary open-angle glaucoma," *Investigative ophthalmology & visual science*, vol. 52, no. 9, pp. 6409–6413, 2011.

[96] O. B. Olafsdottir, E. Vandewalle, L. A. Pinto, A. Geirsdottir, E. De Clerck, P. Stalmans, M. S. Gottfredsdottir, J. V. Kristjansdottir, J. Van Calster, T. Zeyen *et al.*, "Retinal oxygen metabolism in healthy subjects and glaucoma patients," *British Journal of Ophthalmology*, vol. 98, no. 3, pp. 329–333, 2014.

[97] E. Vandewalle, L. Abegão Pinto, O. B. Olafsdottir, E. De Clerck, P. Stalmans, J. Van Calster, T. Zeyen, E. Stefánsson, and I. Stalmans, "Oximetry in glaucoma: correlation of metabolic change with structural and functional damage," *Acta ophthalmologica*, vol. 92, no. 2, pp. 105–110, 2014.

[98] L. Carichino, A. Harris, G. Guidoboni, B. A. Siesky, E. Vandewalle, O. B. Olafsdottir, S. H. Hardarson, K. Van Keer, I. Stalmans, E. Stefánsson *et al.*, "A theoretical investigation of the increase in venous oxygen saturation levels in advanced glaucoma patients," *Journal for Modeling in Ophthalmology*, vol. 1, no. 1, pp. 64–87, 2016.

[99] A. Pries, T. Secomb, T. Gessner, M. Sperandio, J. Gross, and P. Gaehtgens, "Resistance to blood flow in microvessels in vivo." *Circulation research*, vol. 75, no. 5, pp. 904–915, 1994.

[100] G.-F. Ye, T. W. Moore, D. G. Buerk, and D. Jaron, "A compartmental model for oxygen-carbon dioxide coupled transport in the microcirculation," *Annals of biomedical engineering*, vol. 22, no. 5, pp. 464–479, 1994.

[101] P. Causin, G. Guidoboni, F. Malgaroli, R. Sacco, and A. Harris, "Blood flow mechanics and oxygen transport and delivery in the retinal microcirculation: multiscale mathematical modeling and numerical simulation," *Biomechanics and modeling in mechanobiology*, pp. 1–18, 2015.

[102] O. Palsson, A. Geirsdottir, S. H. Hardarson, O. B. Olafsdottir, J. V. Kristjansdottir, and E. Stefánsson, "Retinal oximetry images must be standardized: A methodological analysisretinal oximetry images must be standardized," *Investigative ophthalmology & visual science*, vol. 53, no. 4, pp. 1729–1733, 2012.

[103] G. Michelson, J. Welzenbach, I. Pal, and J. Harazny, "Functional imaging of the retinal microvasculature by scanning laser doppler flowmetry," in *Laser Scanning: Update 1.* Springer, 2001, pp. 145–153.

[104] H. A. Quigley, "Neuronal death in glaucoma," *Progress in retinal and eye research*, vol. 18, no. 1, pp. 39–57, 1999.

[105] C. J. Medrano and D. A. Fox, "Oxygen consumption in the rat outer and inner retina: light-and pharmacologically-induced inhibition," *Experimental eye research*, vol. 61, no. 3, pp. 273–284, 1995.

[106] R. D. Braun, R. A. Linsenmeier, and T. K. Goldstick, “Oxygen consumption in the inner and outer retina of the cat.” *Investigative ophthalmology & visual science*, vol. 36, no. 3, pp. 542–554, 1995.

[107] N. D. Wangsa-Wirawan and R. A. Linsenmeier, “Retinal oxygen: fundamental and clinical aspects,” *Archives of ophthalmology*, vol. 121, no. 4, pp. 547–557, 2003.

[108] D. Mordant, I. Al-Abboud, G. Muyo, A. Gorman, A. Harvey, and A. McNaught, “Oxygen saturation measurements of the retinal vasculature in treated asymmetrical primary open-angle glaucoma using hyperspectral imaging,” *Eye*, vol. 28, no. 10, pp. 1190–1200, 2014.

[109] L. Ramm, S. Jentsch, S. Peters, R. Augsten, and M. Hammer, “Investigation of blood flow regulation and oxygen saturation of the retinal vessels in primary open-angle glaucoma,” *Graefe’s Archive for Clinical and Experimental Ophthalmology*, vol. 252, no. 11, pp. 1803–1810, 2014.

[110] J. Kur, E. A. Newman, and T. Chan-Ling, “Cellular and physiological mechanisms underlying blood flow regulation in the retina and choroid in health and disease,” *Progress in retinal and eye research*, vol. 31, no. 5, pp. 377–406, 2012.

[111] S. J. Cringle and D.-Y. Yu, “A multi-layer model of retinal oxygen supply and consumption helps explain the muted rise in inner retinal po 2 during systemic hyperoxia,” *Comparative Biochemistry and Physiology Part A: Molecular & Integrative Physiology*, vol. 132, no. 1, pp. 61–66, 2002.

[112] L. M. Haugh, R. A. Linsenmeier, and T. K. Goldstick, “Mathematical models of the spatial distribution of retinal oxygen tension and consumption, including changes upon illumination,” *Annals of biomedical engineering*, vol. 18, no. 1, pp. 19–36, 1990.

[113] J. C. Lau and R. A. Linsenmeier, “Oxygen consumption and distribution in the long-evans rat retina,” *Experimental eye research*, vol. 102, pp. 50–58, 2012.

[114] M. W. Roos, “Theoretical estimation of retinal oxygenation during retinal artery occlusion,” *Physiological measurement*, vol. 25, no. 6, p. 1523, 2004.

[115] Y. Jia, J. C. Morrison, J. Tokayer, O. Tan, L. Lombardi, B. Baumann, C. D. Lu, W. Choi, J. G. Fujimoto, and D. Huang, “Quantitative oct angiography of optic nerve head blood flow,” *Biomedical optics express*, vol. 3, no. 12, pp. 3127–3137, 2012.

[116] Y. Jia, O. Tan, J. Tokayer, B. Potsaid, Y. Wang, J. J. Liu, M. F. Kraus, H. Subhash, J. G. Fujimoto, J. Hornegger *et al.*, “Split-spectrum amplitude-decorrelation angiography with optical coherence tomography,” *Optics express*, vol. 20, no. 4, pp. 4710–4725, 2012.

[117] Y. Jia, E. Wei, X. Wang, X. Zhang, J. C. Morrison, M. Parikh, L. H. Lombardi, D. M. Gattey, R. L. Armour, B. Edmunds *et al.*, “Optical coherence tomography angiography of optic disc perfusion in glaucoma,” *Ophthalmology*, vol. 121, no. 7, pp. 1322–1332, 2014.

[118] L. Abegão Pinto, E. Vandewalle, E. De Clerck, C. Marques-Neves, and I. Stalmans, “Lack of spontaneous venous pulsation: possible risk indicator in normal tension glaucoma?” *Acta ophthalmologica*, vol. 91, no. 6, pp. 514–520, 2013.

[119] A. Oettli, K. Gugleta, A. Kochkorov, R. Katamay, J. Flammer, and S. Orgul, "Rigidity of retinal vessel in untreated eyes of normal tension primary open-angle glaucoma patients," *Journal of glaucoma*, vol. 20, no. 5, pp. 303–306, 2011.

[120] J. Leoniuk, A. Łukasiewicz, M. Szorc, I. Sackiewicz, J. Janica, and U. Łebkowska, "Doppler ultrasound detection of preclinical changes in foot arteries in early stage of type 2 diabetes," *Polish Journal of Radiology*, vol. 79, p. 283, 2014.

[121] H. R. Tahmasebpour, A. R. Buckley, P. L. Cooperberg, and C. H. Fix, "Sonographic examination of the carotid arteries 1," *Radiographics*, vol. 25, no. 6, pp. 1561–1575, 2005.

[122] M. Correale, A. Totaro, R. Ieva, A. Ferraretti, F. Musaico, and M. Di Biase, "Tissue doppler imaging in coronary artery diseases and heart failure," *Current cardiology reviews*, vol. 8, no. 1, pp. 43–53, 2012.

[123] K. K. Kadappu and L. Thomas, "Tissue doppler imaging in echocardiography: value and limitations," *Heart, Lung and Circulation*, vol. 24, no. 3, pp. 224–233, 2015.

[124] J. Choi, R. Heo, G.-R. Hong, H.-J. Chang, J. M. Sung, S. H. Shin, I. J. Cho, C.-Y. Shim, and N. Chung, "Differential impact of three-dimensional color doppler echocardiography for the quantification of mitral regurgitation according to the severity and characteristics," *Circulation: Cardiovascular Imaging*, pp. CIRCIMAGING–113, 2014.

[125] N. C. Wunderlich, R. Beigel, and R. J. Siegel, "Management of mitral stenosis using 2d and 3d echo-doppler imaging," *JACC: Cardiovascular Imaging*, vol. 6, no. 11, pp. 1191–1205, 2013.

[126] J. He and G. Yan, "Research on ovary blood flow before and after uterine artery embolization with the application of color doppler blood imaging." *The Journal of reproductive medicine*, vol. 60, no. 11-12, pp. 513–520, 2014.

[127] A. P. Saini, S. Ural, and L. B. Pauliks, "Quantitation of fetal heart function with tissue doppler velocity imagingreference values for color tissue doppler velocities and comparison with pulsed wave tissue doppler velocities," *Artificial organs*, vol. 38, no. 1, pp. 87–91, 2014.

[128] V. P. Costa, A. Harris, D. Anderson, R. Stodtmeister, F. Cremasco, H. Kergoat, J. Lovasik, I. Stalmans, O. Zeitz, I. Lanzl *et al.*, "Ocular perfusion pressure in glaucoma," *Acta ophthalmologica*, vol. 92, no. 4, pp. e252–e266, 2014.

[129] A. P. Cherecheanu, G. Garhofer, D. Schmidl, R. Werkmeister, and L. Schmetterer, "Ocular perfusion pressure and ocular blood flow in glaucoma," *Current opinion in pharmacology*, vol. 13, no. 1, pp. 36–42, 2013.

[130] M. Yanagi, R. Kawasaki, J. J. Wang, T. Y. Wong, J. Crowston, and Y. Kiuchi, "Vascular risk factors in glaucoma: a review," *Clinical & experimental ophthalmology*, vol. 39, no. 3, pp. 252–258, 2011.

[131] D. Schmidl, G. Garhofer, and L. Schmetterer, "The complex interaction between ocular perfusion pressure and ocular blood flow–relevance for glaucoma," *Experimental eye research*, vol. 93, no. 2, pp. 141–155, 2011.

[132] L. Pourcelot, “Applications cliniques de l’examen doppler transcutane,” *Velocimetrie Ultrasonore Doppler*, vol. 34, pp. 780–785, 1974.

[133] L. Carichino, G. Guidoboni, A. C. Verticchio Vercellin, G. Milano, C. A. Cutolo, C. Tinelli, A. De Silvestri, S. Lapin, J. C. Gross, B. Siesky, and A. Harris, “Computer-aided identification of novel ophthalmic artery waveform parameters in healthy subjects and glaucoma patients,” *Journal for Modeling in Ophthalmology*, officially accepted May 2016.

[134] J. R. Parker, *Algorithms for image processing and computer vision.* John Wiley & Sons, 2010.

[135] J. S. Lim, “Two-dimensional signal and image processing,” *Englewood Cliffs, NJ, Prentice Hall, 1990, 710 p.*, vol. 1, 1990.

[136] M. T. Savage, C. J. Ferro, S. J. Pinder, and C. R. Tomson, “Reproducibility of derived central arterial waveforms in patients with chronic renal failure,” *Clinical Science*, vol. 103, no. 1, pp. 59–65, 2002.

[137] I. Oliva and K. Roztocil, “Toe pulse wave analysis in obliterating atherosclerosis,” *Angiology*, vol. 34, no. 9, pp. 610–619, 1983.

[138] I. Lawrence and K. Lin, “A concordance correlation coefficient to evaluate reproducibility,” *Biometrics*, pp. 255–268, 1989.

[139] D. G. Altman, *Practical statistics for medical research.* CRC press, 1990.

[140] P. Founti, A. Harris, D. Papadopoulou, P. Emmanouilidis, B. Siesky, V. Kilintzis, E. Anastasopoulos, A. Salonikiou, T. Pappas, and F. Topouzis, “Agreement among three examiners of colour doppler imaging retrobulbar blood flow velocity measurements,” *Acta ophthalmologica*, vol. 89, no. 8, pp. e631–e634, 2011.

[141] A. Harris, T. H. Williamson, B. Martin, J. A. Shoemaker, R. C. Sergott, G. L. Spaeth, J. L. Katz *et al.*, “Test/retest reproducibility of color doppler imaging assessment of blood flow velocity in orbital vessels.” *Journal of glaucoma*, vol. 4, no. 4, pp. 281–286, 1995.

[142] L. Quaranta, A. Harris, F. Donato, M. Cassamali, F. Semeraro, G. Nascimbeni, E. Gandolfo, and C. A. Quaranta, “Color doppler imaging of ophthalmic artery blood flow velocity: a study of repeatability and agreement,” *Ophthalmology*, vol. 104, no. 4, pp. 653–658, 1997.

[143] L. Abegão Pinto, K. Willekens, K. Van Keer, A. Shibesh, G. Molenberghs, E. Vandewalle, and I. Stalmans, “Ocular blood flow in glaucoma–the leuven eye study,” *Acta ophthalmologica*, 2016.

[144] V. V. Kapetanakis, M. P. Chan, P. J. Foster, D. G. Cook, C. G. Owen, and A. R. Rudnicka, “Global variations and time trends in the prevalence of primary open angle glaucoma (poag): a systematic review and meta-analysis,” *British Journal of Ophthalmology*, pp. bjophthalmol–2015, 2015.

[145] T. S. Vajaranant, S. Nayak, J. T. Wilensky, and C. E. Joslin, “Gender and glaucoma: what we know and what we need to know,” *Current opinion in ophthalmology*, vol. 21, no. 2, p. 91, 2010.

[146] D. Schmidl, L. Schmetterer, G. Garhöfer, and A. Popa-Cherecheanu, “Gender differences in ocular blood flow,” *Current eye research*, vol. 40, no. 2, pp. 201–212, 2015.

[147] E. K. Akpek and R. A. Smith, “Overview of age-related ocular conditions,” *Am J Managed Care*, vol. 19, no. 5, pp. s67–s75, 2013.

[148] J. C. Wang and M. Bennett, “Aging and atherosclerosis mechanisms, functional consequences, and potential therapeutics for cellular senescence,” *Circulation Research*, vol. 111, no. 2, pp. 245–259, 2012.

VITA

VITA

Lucia Carichino

EDUCATION

- Doctor of Philosophy, August 2016

  Purdue University, Applied Mathematics

  Multiscale mathematical modeling of ocular blood flow and oxygenation and their relevance to glaucoma.

  Major Advisor: Giovanna Guidoboni, IUPUI.

  Co-Advisors: Alon Harris, Indiana University; Julia Arciero, IUPUI.

- Master of Science, December 2010

  Politecnico di Milano, Mathematical Engineering

  Computational Models for Power Electronics Cooling Systems.

  Advisors: Riccardo Sacco, Politecnico di Milano; Francesco Agostini, ABB, Switzerland.

- Bachelor of Science, March 2008

  Polytechnico di Milano, Mathematical Engineering

  Elliptic Restricted 3-*Body Problem: analysis of branches of periodic orbits with varying eccentricity.*

  Advisor: Gianni Arioli, Politecnico di Milano.

AWARDS AND HONORS

- Elite 50 Graduate and Professional Students Award, April 2015

  The Graduate and Professional Student Government at IUPUI, Indianapolis, IN

- Yuri Abramovich Memorial Scholarship, April 2015
  Department of Mathematical Sciences IUPUI, Indianapolis, IN
- 2014-2015 STEM Chateaubriand Fellowship, May 2014
  Office for Science and Technology of the Embassy of France in the United States
- Outstanding Advanced (post-Qualifying Exams) Graduate Student Award in Mathematics, April 2014
  Department of Mathematical Sciences IUPUI, Indianapolis, IN
- Outstanding IUPUI SIAM Chapter Officer Award, April 2014
- Poster Award - 1st Place, October 2013
  The Fourth Annual Eugene & Marilyn Glick Eye Institute Vision Research Symposium, Indianapolis, IN
- Member in Training Poster Award - Finalist, May 2012
  Association for Research in Vision and Ophthalmology(ARVO) 2012 Annual Meeting, Fort Lauderdale, FL

SELECTED PUBLICATIONS

- *Computer-aided identification of novel ophthalmic artery waveform parameters in healthy subjects and glaucoma patients*, L. Carichino, G. Guidoboni, A. C. Verticchio Vercellin, G. Milano, C. A. Cutolo, C. Tinelli, A. De Silvestri, S. Lapin, J. C. Gross, B. Siesky, A. Harris, JMO, officially accepted May 18, 2016.
- *A theoretical investigation of the increase in venous oxygen saturation levels in glaucoma patients*, L. Carichino, A. Harris, G. Guidoboni, B.A. Siesky, L.A. Pinto, E. Vandewalle, O.B. Olafsdottir, S.H. Hardarson, K. Van Keer, I. Stalmans, E. Stefansson, J.C. Arciero, JMO, Vol. 1 (2016) 64-87.
- *A multiscale Thermo-Fluid Computational Model for a Two-Phase Cooling System*, R. Sacco, L. Carichino, C. de Falco, M. Verri, A. Francesco and T. Gradinger, CMAME, Vol. 282 (2014) 239-268.
- *Effect of intraocular pressure and cerebrospinal fluid pressure on the blood flow in the central retinal vessels*, L. Carichino, G. Guidoboni, B.A. Siesky, A. Amireskandari,

I. Januleviciene and A. Harris, Integrated Multidisciplinary Approaches in the Study and Care of the Human Eye, P. Causin, G. Guidoboni, R. Sacco and A. Harris (Eds), (pp. 59-66), Kugler Publications, 2014.

- *Effect of intraocular pressure on the hemodynamics of the central retinal artery: a mathematical model*, G. Guidoboni, A. Harris, L. Carichino, Y. Arieli and BA. Siesky, MBE, Vol. 11(3) (2014) 523-546.
- *Mathematical modeling approaches in the study of glaucoma disparities among people of African and European descents*, G. Guidoboni, A. Harris, J.C. Arciero, B.A. Siesky, A. Amireskandari, A.L. Gerber, A.H. Huck, N.J. Kim, S. Cassani and L. Carichino, J. Coupled Syst. Multiscale Dyn., Vol. 1(1) (2013) 1-21.

RESEARCH EXPERIENCES

- January-December 2015, Université de Strasbourg, Labex IRMA, France.
  Research project: *Eye2Brain: the eye as a window on the brain.*
  Supervisors: Giovanna Guidoboni, IUPUI, Christophe Prud'homme, IRMA and Marcela Szopos, IRMA.
- March 2014 and 2016, SQuaREs (Structured Quartet Research Ensembles), American Institute of Mathematics.
  Research project: *Ocular blood flow and its role in development of glaucoma.*
  Sergey Lapin, Giovanna Guidoboni, Julia Arciero, Alon Harris, Lucia Carichino, Simone Cassani.
- August-December 2011, Short-term Scholar, IUPUI.
  Research project: *Mathematical modeling of the ocular blood flow*.
  Supervisors: Giovanna Guidoboni, IUPUI, Alon Harris, IU School of Medicine.

TEACHING EXPERIENCES

- Primary instructor MATH 17100: Multidimensional Mathematics, Summer 2015, Coordinator S. Klimek, IUPUI.
- Primary instructor MATH 15300: Algebra and Trigonometry I, Fall 2013 and Fall 2014, Coordinator S. Rangazas, IUPUI.

- Primary instructor MATH 15400: Algebra and Trigonometry II, Spring 2014, Coordinator S. Rangazas, IUPUI.
- Recitation instructor MATH 16600: Integrated Calculus and Analytic Geometry II, Fall 2014, Primary instructor J. Miller, IUPUI.
- Recitation instructor MATH 16500: Integrated Calculus and Analytic Geometry I, Fall 2012, Primary instructor J. Watt, IUPUI.
- Tutor at the Mathematics Assistance Center (MAC), IUPUI, 2012-2016.

CONFERENCES

- The ARVO Annual Meetings, May 2012, 2013, 2014, 2015 and 2016, USA.
- The International Congress of Advanced Technologies and Treatments for Glaucoma, October 2015, Milano, Italy.
- SMAI Congress 2015, June 2015, Les Karellis, France.
- 11th World Congress on Computational Mechanics, July 2014, Barcelona, Spain.
- 2nd Annual Midwest Women in Mathematics Symposium, April 2014, South Bend, IN, USA.
- Integrated Multidisciplinary approaches in the study and Care of the Human Eye, Clinical Experience - Mathematical Modeling - New Technologies, June 2013, Milano, Italy.
- 13th INFORMS Computing Society Conference, January 2013, Santa Fe, NM, USA.
- The Third and Fourth Annual Eugene & Marilyn Glick Eye Institute Vision Symposium, October 2013 and November 2012, Indianapolis, IN, USA.